

DISS. ETH NO. 21994

# Investigation of the heat transfer patterns on the vane endwall of an axial turbine

A thesis submitted to attain the degree of  
DOCTOR OF SCIENCES of ETH ZURICH  
(Dr. sc. ETH Zurich)

presented by

Benoit Edouard LAVEAU

Master of Science - Aeronautical Engineering  
ISAE - Ensica, Toulouse, France

born on November 28, 1985  
citizen of France

accepted on the recommendation of  
Prof. Dr. Reza S. Abhari, examiner  
Prof. Dr. Michael Crawford, co-examiner

2014





# Abstract

In order to continue increasing the efficiency of gas turbines, an important effort is made on the thermal management of the turbine stage. In particular understanding and accurately estimating the thermal loads in a vane passage is of primary interest to engine designers looking to optimize the cooling requirements and ensure the integrity of the components. The latest development in turbine aerodynamics, driven by the improvement of numerical predictions technique, have achieved a reduction of aerodynamic losses by using non-axisymmetric modification of the endwall shape. The modification of flow structure due to the contouring has been covered intensively in the last decade but the consequence on the thermal loads distribution are not yet fully understood. This study focuses on the measurement of heat transfer on cylindrical and contoured endwall in a vane passage with advanced 3D airfoils in an axial turbine steady state facility.

In a preliminary phase, the experimental methods and procedure are adapted or improved to provide high resolution and high accuracy heat transfer data on the endwall of a vane passage. The work is performed in a test bench facility LAVAL, equipped with a thermally managed flat plate. A linear cascade composed of NACA symmetric airfoils is installed in the test section and provide a configuration similar to the turbine configuration. The measurements are performed using an infrared camera traversed by a multi-axis traversing system accessing the surface through Zinc Selenide windows. The measurement technique is based on a quasi-isothermal boundary condition obtained with circulating water impinging on a thick copper plate covered with an insulating Kapton layer. The adiabatic wall temperature and the heat transfer coefficient, are deduced from multiple measurements performed at different solid temperature. The small aspect ratio of the channel requires multiple position and access for the camera to cover the complete passage. The geometrical calibration of the camera allow the reconstruction of the complete passage. The measurements are performed on two endwall configurations, flat and contoured, at different flow conditions providing a variation of Reynolds number of 38%. A numerical study helps clarifying the link between the change in the heat transfer quantities and in the flow field due to the endwall contouring. Finally predicted heat transfer data are compared to the experimental data and the significant difference in the measured heat transfer coefficient between flat and contoured endwalls, is under-predicted numerically.

A heat transfer platform composed of four vanes is designed, assembled and integrated to the axial turbine facility. The heat transfer measurement technique is adapted from the flat plate configuration, and uses circulating water in multiple channels drilled through the aluminum core part of the platform. The mechanical and thermal design

are optimized using 3D numerical tools (CAD, CFD, FEM). A distribution system is designed and used to individually feed and control the flow through the different channels. The accessibility of the passage endwall is granted through small Zinc Selenide windows designed using ray tracing scripts and tested on a bench. Due to the limited size of the view ports, a 6 axis robot arm provides an automatic traversing of the camera.

Experimental measurements of heat transfer quantities are performed on the cylindrical endwall of the nozzle guide vane passage in the turbine facility. The heat transfer quantities are derived from measurements at 14 different isothermal temperature accomplished in a single measurement day. Two different flow conditions obtained by varying the mass flow through the turbine: measurements at the design point ( $Re_{C_{ax}}=700k$  and at a reduced mass flow rate ( $Re_{C_{ax}}=520k$ ). The repeatability of the measurements is shown to be better than  $\pm 5\%$ . The comparison of the measured data to flat plate correlation shows matching values obtained in the inlet portion of the segment where the flow acceleration and the impact of secondary flow structures are limited. The experimental data are supplemented with numerical predictions that are deduced from a set of adiabatic and diabatic simulations. In addition, the predicted flow field in the passage is used to highlight the link between the heat transfer patterns measured and the vortical structures present in the passage. Comparison of predicted and measured data along streamlines highlight the difficulty for CFD codes to predict the heat transfer coefficient levels.

The surface properties of the measurements platform are measured and quantified in terms of roughness. A high resolution 3D scan of the surface is also performed to provide an equivalent sand-grain roughness based on the elements distribution, which is used for numerical simulations. A roughness model is implemented in the in-house code Multi3 and the comparison of aerodynamic losses and heat transfer between smooth and rough surfaces are performed.

In a second measurement campaign, a turbine geometry with contoured endwall is integrated to the facility. The measurements of heat transfer quantities are performed on the contoured endwall for the same operating conditions as the cylindrical case. The extreme curvature encountered on the endwall prevented an ideal attachment of the Kapton layer and micro air bubble of the order of  $50\mu m$  thickness have been trapped underneath. The affected regions have been identified and an experimental procedure is developed to quantify the change in the local thermal resistance due to the presence of air. The calibration procedure helped to recover the data in regions covered with the micro bubbles. The data from the contoured endwall are compared finally to the cylindrical case. Numerical predictions performed with the in-house code Multi3 provides more insight into the flowfield modification due to the endwall contouring. The change in the horseshoe vortex behavior is highlighted as well as the change in wall shear stress distribution in the downstream part of the passage.

# Résumé

Afin de poursuivre l'amélioration de l'efficacité des turbines à gaz, les efforts de recherche se concentrent principalement sur la gestion des échanges de chaleur dans l'étage de turbine. En effet, l'augmentation de la température à la sortie de la chambre de combustion est la voie privilégiée aujourd'hui pour accomplir cette tâche. La compréhension des phénomènes physiques gérant les transferts thermiques et leur estimation est essentielle pour les ingénieurs définissant les composants et flux d'air requis pour protéger et refroidir les pièces et s'assurer du maintien de leur intégrité mécanique tout au long de leur utilisation. D'un point de vue aérodynamique, l'amélioration des techniques de simulation numérique a permis de réduire les pertes grâce à l'utilisation de formes non-axisymétrique pour les carter d'aubes de turbine. Les changements introduits par ces modifications sur le flux d'air ont été étudié de façon intensive dans la dernière décennie. En revanche l'impact de ces modifications sur les échanges thermiques reste méconnu. Cette étude concerne donc la mesure des échanges thermiques dans un passage d'aube de turbine ayant une géométrie complexe tri-dimensionnelle et équipée de carter cylindrique ou tri-dimensionnels. Dans une première partie, les méthodes expérimentales et les procédures de mesures sont adaptées et améliorées afin d'obtenir des mesures à haute résolution avec une précision accrue. Ce travail est effectué dans une soufflerie à section rectangulaire équipée, dans la section de test, d'une plaque plane contrôlée thermiquement. Trois profils symétrique sont installés dans la section de test afin de simuler une configuration aube-carter similaire à ce qui se trouve dans une turbine. Les mesures expérimentales sont effectuées par thermographie infrarouge à travers un accès optique fait en cristal de Zinc Selenium. La technique de mesure employée utilise une plaque de cuivre contrôlée thermiquement par circulation d'eau et recouverte d'une structure isolante à base de Kapton, fournissant ainsi une condition aux limites quasi-isotherme. La température adiabatique de surface et le coefficient d'échange de chaleur sont obtenus grâce à plusieurs mesures à des températures de plaque différentes. La forme étirée de la section de test requiert l'utilisation de multiples positions et accès pour la caméra infrarouge. Les données acquises sur l'ensemble du passage sont reconstruites grâce à une calibration géométrique du système. Deux configuration de carters sont également utilisées, avec des surfaces planes et tri-dimensionnelles. Les mesures sont effectuées pour deux conditions d'opérations, permettant une variation du nombre de Reynolds de l'ordre de 38%. Une étude numérique fournit le lien entre les changements de transferts de chaleur mesurés et les changement d'écoulement du flux d'air. Enfin les échanges de chaleur sont également prédits numériquement et comparés aux données expérimentales. La principale différence réside dans la sous estimation des échanges de chaleur prédite.

Dans une seconde phase, une plate-forme de mesures composée de quatre aubes de distributeur est conçue pour permettre les mesures de transfert thermique dans la turbine axiale LISA. La méthode de mesure, utilisée dans la configuration plaque plane, est adaptée et utilise également la circulation d'eau à travers plusieurs canaux dans le segment fabriqué en aluminium. La conception mécanique et thermique est réalisée grâce à des outils numériques de CAD, CFD et FEM, en trois dimensions. La circulation d'eau à travers chaque canal est contrôlée grâce à un système de distribution. L'accès optique pour la caméra infrarouge est obtenu à travers multiples éléments en Zinc Selenium. Un robot six axes est utilisé pour manipuler la caméra et offrir une couverture complète du passage entre deux aubes de distributeurs. Les mesures expérimentales sont ensuite effectuées sur le moyeu du distributeur dans la turbine axiale LISA. Les coefficients d'échanges thermiques sont obtenus grâce à l'utilisation de quatorze températures de solide, obtenus au cours d'une unique journée de mesure. Les tests sont effectués pour deux conditions (nominales avec  $Re_{Cax} = 700k$  et réduite  $Re_{Cax} = 520k$ ) de fonctionnement obtenues en variant le flux d'air à travers la section de test. Un test de répétabilité des mesures montre des différences inférieures à  $\pm 5\%$ . Les coefficients d'échange de chaleur mesurés à l'entrée du passage, où les structures secondaires sont limitées, sont en accord avec les corrélations pour plaque plane. Des simulations numériques sont également utilisées pour identifier les liens entre les variations d'échanges thermiques dans le passage et les spécificités d'écoulement du flux d'air. La comparaison des données le long des lignes d'écoulement montre la difficulté des simulations numériques à prédire les coefficients d'échanges thermiques. La rugosité de la surface de la plate-forme de mesures est mesurée avec un profilomètre et un système de mesure optique permettant d'obtenir des données tri-dimensionnelles à haute résolution. La réduction des données obtenues permet d'obtenir une rugosité équivalente de type "grain de sable" qui est utilisée dans les modèles numériques. Un modèle de rugosité est ajouté au code numérique Multi3 et utilise la mesure de rugosité pour prédire les pertes aérodynamiques et les échanges de chaleur dans le distributeur. Enfin, une géométrie de moyeu non-axisymétrique est installée et testée dans la turbine. Les mesures d'échanges de chaleur sont effectuées sur les parois tri-dimensionnelles, dans les mêmes conditions de fonctionnement que les mesures sur parois cylindriques. L'installation de la couche isolante de Kapton est rendue délicate par la courbure des surfaces du moyeu et des micro bulles d'air, de l'ordre de  $50\mu m$  sont présentes sous la couche, ce qui altère les mesures. Afin de corriger les données mesurées dans les régions affectées par ces bulles d'air, une procédure de calibration utilisant la réponse transitoire en température de la surface à une impulsion d'un laser est développée. Les données recouvrées sur les surfaces complexes sont ensuite comparées aux données mesurées dans la configuration à parois cylindriques. Le code Multi3 est utilisé à nouveau et fournit des indications sur la modification des écoulements des flux d'air due à la déformation des parois. En particulier, des changements de comportement du vortex de bord d'attaque sont observés ainsi que les variations de coefficient de friction de paroi dans la seconde partie du passage.

# Acknowledgments

This thesis presents the outcome of the work accomplished in the 5 years spent at the Laboratory for Energy Conversion of ETH Zurich. Despite ups and downs encountered along the "PhD journey", the personal evolution and the pleasure to successfully lead a research project is immense. This achievement would not have been possible without a number of people from the Lab, former colleagues and friends.

I would like to thank first Professor Dr. Reza Abhari for the chance he gave me to work with him on this interesting and challenging research project. I am grateful for the continuous support and advice throughout the time on this project. Above all, the lessons about management, leadership, negotiation learnt during internal or industry meetings and his permanent quest for excellence, are (now!) truly appreciated. At last, I would like to thank Prof. Abhari for his attention in providing a fulfilling work environment, with people from different part of the world, different way of living, different culture.

Special thanks should go to my colleagues from the heat transfer team of the project, Dr. Michael Crawford and Dr. Ewald Lutum. The continuous support provided throughout the project and their experience are gratefully appreciated. Finally I would like to thank my co-examiner Dr. Michael Crawford for accepting the role and coming all the way from the United States to attend my oral examination.

I would also like to thank Dr. Anestis Kalfas for his technical guidance and the numerous discussions on various aspect of the project. His support and confidence are greatly appreciated.

Dr Ndaona Chokani, thank you for reading and correcting the different articles and above all thanks for all the useful comments on how to make a proper presentation.

I would like to specially thank my project colleague Kai Regina, who dealt with the aerodynamic side of the project. His help in organizing the manufacturing of the parts and in running the facility during my measurements made is profoundly acknowledged. This work would not have been possible without him.

Without the help of the workshop team, this work would not have been achieved with the same quality. Ein riesige Dankeschön für Thomas Künzle und Rolf Rüttiman, ohne Ihre Beratung, würde dieses Projekt kein Erfolg sein. Many thanks to Flori Alickaj who helped me build the electronic system and shared with me his knowledge of acquisition systems.

I would like to thank all my colleagues working at LEC for the great time we had and for the support I received during my time in the laboratory. I would like to thank Dr Vipluv Aga for providing me the tools to build up this research work. Many thanks go to the team developing the instrumentation, Dr. Michel Mansour, Dr. Christian Lenherr,

Ilias Bosdas for the numerous ideas, the interesting discussions and the long working hours shared in clean room. I would like also to thank the office colleagues I had along these years, Dr. Samira Jafari, Dr. Bob Rollinger and Dr. Altug Basol in particular, for the very intense exchange of ideas and discussions about our respective fields. Altug, thanks for introducing me to Multi3, and thank you for all the technical discussions we had and the knowledge you shared with me in the last few years.

Last but not least, I would like to gratefully thank Marlene Hegner for helping me going through the administrative matters, thanks for the supporting smiles and discussion before and after every meeting.

Special thanks go to Dr. Oran Morris and Dr. Armin Zemp first for sharing their technical knowledge and for the discussions but mainly for their friendship. Their support during the hard time will not be forgiven. Armin, the great times spent in coffee breaks are truly missed.

Finally, I wish to thank my sister and my parents for all their support during this time. Thanks for making me who I am today...

# Contents

|          |  |           |
|----------|--|-----------|
| <b>1</b> | <b>Introduction</b>  | <b>1</b>  |
| 1.1      | Motivation . . . . .   | 1         |
| 1.2      | Literature Review . . . . .  | 7         |
| 1.2.1    | Flow structures in a turbine stator row. . . . .   | 7         |
| 1.2.2    | Endwall heat transfer. . . . .   | 10        |
| 1.3      | Research Objectives . . . . .  | 14        |
| 1.4      | Thesis outline . . . . .   | 15        |
| <b>2</b> | <b>Experimental Methods</b>  | <b>17</b> |
| 2.1      | Temperature measurement . . . . .  | 17        |
| 2.1.1    | Basis of radiation applied to thermal imaging. . . . .   | 20        |
| 2.1.2    | Infrared thermography for heat transfer measurements . . . . .   | 28        |
| 2.2      | Image processing techniques . . . . .  | 33        |
| 2.2.1    | General model of a camera . . . . .  | 34        |
| 2.2.2    | Calculation of the camera matrix . . . . .   | 35        |
| 2.2.3    | Blurring and focusing of the camera . . . . .  | 36        |
| 2.2.4    | Complete passage reconstruction. . . . .   | 38        |
| 2.2.5    | Use of images as a measurement or a positioning tool . . . . .   | 40        |
| <b>3</b> | <b>Experimental investigation of heat transfer on the endwall of a linear cascade with symmetric airfoils.</b> | <b>45</b> |
| 3.1      | Experimental facility LAVAL . . . . .  | 45        |
| 3.1.1    | Description of the wind tunnel . . . . .   | 45        |
| 3.1.2    | Water network . . . . .  | 49        |
| 3.1.3    | Traversing system . . . . .  | 50        |
| 3.1.4    | Setup for heat transfer measurements . . . . .   | 50        |
| 3.2      | Linear cascade geometry . . . . .  | 52        |
| 3.3      | Measurement procedure and data reduction . . . . .   | 56        |
| 3.3.1    | Measurement procedure . . . . .  | 56        |
| 3.4      | Numerical setup . . . . .  | 57        |
| 3.5      | Experimental Uncertainty Analysis . . . . .  | 59        |
| 3.6      | Experimental Results and comparison to numerical predictions . . . . .   | 61        |
| 3.6.1    | Flat plate heat transfer . . . . .   | 61        |
| 3.6.2    | Measurements in the cascade on flat and contoured endwall . . . . .  | 62        |
| 3.6.3    | Effect of the vanes mounted on a flat endwall. . . . .   | 63        |

|          |  |            |
|----------|--|------------|
| 3.6.4    | Results from predictions and comparison to the experiments . . .                                 | 65         |
| 3.6.5    | Overall effect of contouring on heat transfer. . . . .   | 70         |
| 3.6.6    | Effect of a variation of Reynolds number for the two endwall geometry. . . . .                   | 71         |
| 3.7      | Conclusions . . . . .  | 71         |
| <b>4</b> | <b>Integration of a heat transfer measurement platform into the turbine axial facility LISA.</b> | <b>75</b>  |
| 4.1      | Axial turbine facility LISA . . . . .  | 75         |
| 4.1.1    | Description of the wind tunnel . . . . .   | 75         |
| 4.2      | Redesign of the test section to house a heat transfer measurement platform                       | 81         |
| 4.3      | Design of the heat transfer platform. . . . .  | 82         |
| 4.3.1    | Thermal design of the platform using 3D thermal analysis. . . . .                                | 83         |
| 4.4      | Design of the optical access to the endwall for the infrared camera . . . .                      | 85         |
| 4.5      | Mechanical design, manufacturing and assembly of the heat transfer platform. . . . .             | 88         |
| 4.5.1    | Hub platform. . . . .  | 90         |
| 4.5.2    | Connection to the water network. . . . .   | 93         |
| 4.6      | Water network . . . . .  | 95         |
| 4.7      | Design of a traversing system to manipulate the infrared camera . . . . .                        | 99         |
| <b>5</b> | <b>Measurements of heat transfer on the cylindrical hub endwall of an axial turbine.</b>         | <b>105</b> |
| 5.1      | Measurement procedure . . . . .  | 105        |
| 5.2      | Experimental Uncertainty Analysis . . . . .  | 108        |
| 5.3      | Computational Setup . . . . .  | 112        |
| 5.4      | Experimental results . . . . .   | 113        |
| 5.5      | Comparison with numerical predictions. . . . .   | 118        |
| 5.6      | Effect of temperature non-uniformity on heat transfer coefficient . . . . .                      | 121        |
| 5.7      | Conclusions . . . . .  | 123        |
| <b>6</b> | <b>Numerical predictions of heat transfer on rough surfaces.</b>                                 | <b>125</b> |
| 6.1      | Surface roughness measurements . . . . .   | 125        |
| 6.1.1    | Measurement of integral roughness quantities . . . . .   | 125        |
| 6.1.2    | Determination of an equivalent sand grain roughness using a 3D scan of the surface. . . . .      | 126        |
| 6.2      | Numerical model . . . . .  | 128        |
| 6.2.1    | Modeling of rough walls . . . . .  | 128        |
| 6.2.2    | Mesh of the vane passage . . . . .   | 129        |
| 6.2.3    | Judgment of convergence of a calculation . . . . .   | 130        |
| 6.3      | Results from numerical predictions . . . . .   | 131        |
| 6.3.1    | Effect of roughness on aerodynamic losses . . . . .  | 131        |
| 6.3.2    | Effect of roughness on heat transfer quantities . . . . .  | 133        |
| 6.4      | Summary . . . . .  | 137        |



|          |  |            |
|----------|--|------------|
| <b>7</b> | <b>Measurements of heat transfer on contoured endwall</b>  | <b>139</b> |
| 7.1      | Adaptation of the platform design to a contoured endwall configuration. . . . .                            | 139        |
| 7.1.1    | Changes in the mechanical design. . . . .  | 139        |
| 7.1.2    | Attachment of the Kapton layer on the contoured endwall. . . . .   | 140        |
| 7.1.3    | Measurements of roughness levels through the passage. . . . .  | 143        |
| 7.2      | Calibration for thermal resistance non-uniformity of the multilayer at-<br>tached to the platform. . . . . | 144        |
| 7.2.1    | Transient heat transfer measurements in LISA . . . . .   | 145        |
| 7.2.2    | Surface thermal response measurements using a laser pulse and the<br>infrared camera . . . . .             | 145        |
| 7.3      | Experimental results . . . . .   | 153        |
| 7.3.1    | Operating conditions . . . . .   | 153        |
| 7.3.2    | Heat transfer data calculation . . . . .   | 155        |
| 7.3.3    | Uncertainty analysis . . . . .   | 156        |
| 7.3.4    | Results . . . . .  | 158        |
| 7.3.5    | Effect of the contouring on the thermal loads. . . . .   | 161        |
| 7.4      | Effect of the endwall contouring on the flow structure. . . . .  | 162        |
| 7.5      | Summary . . . . .  | 166        |
| <b>8</b> | <b>Detailed analysis of the results and discussions</b>  | <b>169</b> |
| 8.1      | Impact of the formation of vortices in the leading edge region . . . . .                                   | 171        |
| 8.1.1    | Influence of the endwall contouring on the flow structure close to<br>the leading edge. . . . .            | 175        |
| 8.2      | Effect of roughness in the accelerating boundary layer close to the vane<br>pressure side . . . . .        | 179        |
| 8.2.1    | Impact of endwall contouring on the pressure side close to the<br>trailing edge . . . . .                  | 183        |
| <b>9</b> | <b>Summary, Conclusions and Outlook</b>  | <b>187</b> |
| 9.1      | Contribution of the current work . . . . .   | 187        |
| 9.1.1    | Experimental Setup and Methods . . . . .   | 187        |
| 9.1.2    | High resolution measurements of heat transfer on cylindrical and<br>contoured endwall . . . . .            | 188        |
| 9.1.3    | Numerical setup and methods for predictions on rough surfaces. . . . .                                     | 189        |
| 9.1.4    | Concluding remarks . . . . .   | 190        |
| 9.2      | Future perspective . . . . .   | 192        |
|          | <b>Bibliography</b>  | <b>202</b> |
|          | <b>A Nomenclature</b>  | <b>203</b> |
|          | <b>B List of Publications</b>  | <b>205</b> |
|          | <b>C Curriculum Vitae</b>  | <b>207</b> |



# Chapter 1

## Introduction

### 1.1 Motivation

In the last two decades, the emergence of the new industrial countries BRICS (Brazil, Russia, India, China, South Africa) led by China and India has increased by 45% the global demand of energy and it is expected to see another 50% increase till 2040. The growth of the population and the fast economic development in Asia & Oceania have led to an increase of their energy consumption of 150% since 1990 while it remained fairly constant in North America and Europe. The transformation of the historical bipolar economy into a more Global market also requires an ever growing need for transportation of person and goods. In the last 10 years, an averaged annual growth of 4-4.5% of freight and passenger air traffic was measured, and the trend is expected to intensify leading to a doubling of the current levels in 15 years. Both fields of power generation and transportation relies massively on the combustion of fossil fuel (oil, coal, natural gas) to produce energy, which leads to a contribution of fossil fuels of 88% to the World energy consumption. The recent concerns about oil and natural gas reserves, the need for technological development to exploit new resources and the rising interests in Global Warming and  $CO_2$  emissions have strongly impacted the price level of these resources. In 2012, the fuel cost reported by IATA represented 32% of the total operating costs for an airline, and has forced companies to focus on fuel savings policy and invest on energy efficient aircrafts. Most of the energy production and aircraft propulsion is based on a thermal cycle transforming heat into mechanical work, used then to produce electricity or thrust. Because of their high power density, axial turbomachines are widely used to fulfill these tasks and most of the increase in their efficiency can be accomplished by improving the efficiency of the components in the "hot part". A diagram of a turbomachine is shown in Fig. 1.1, while Fig. 1.4&1.5 show real engines used for energy production and aircraft propulsion respectively.

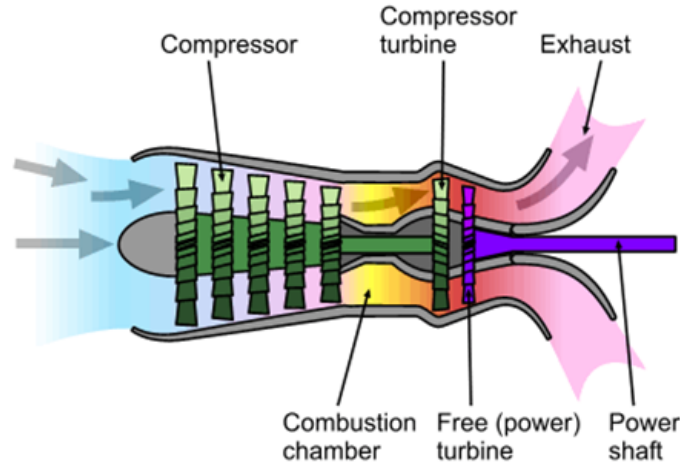


Figure 1.1: Schematic of a typical turbomachine composed of a gas generator and a power turbine.

A typical turbomachine is divided into a gas generator, which is composed of three main parts, namely the compressor, the combustion chamber and the turbine, and a power turbine. The role of every component is as follows:

- **the compressor** generally composed of multiple stages, comprising a row of rotating airfoils followed by stationary ones, accelerates the flow and increase its pressure and temperature
- **the combustion chamber** where the fuel is injected, mixed with the air and burnt, this is where the most intense heat release is observed in the engine
- **the turbine** composed of multiple stages as well (stators followed by rotor) which serves to extract and recover work from the fluid to entrain the compressor stage which is mounted on the same shaft
- **the free or power turbine** is used to extract the remaining work from the fluid but it is mounted on a separated shaft which transfer the recovered work to a fan stage in case of a turbofan type of aircraft engine or to a generator for electricity generation

The thermodynamic ideal cycle corresponding to this succession of operations is known as the Brayton cycle. The expression of the cycle efficiency is shown in Eq. 1.1, and is only dependent on the compressor pressure ratio. In real engines, components are not ideal and the processes are not isentropic, the efficiency becomes then dependent to the compressor pressure ratio but mainly to the highest cycle temperature, which is the turbine entry temperature TET as shown in Fig. 1.2. The figure shows the evolution of the cycle efficiency for a non-ideal machine and different TET.

$$\eta_B = 1 - \frac{1}{PR^{(\gamma-1)/\gamma}} \quad (1.1)$$

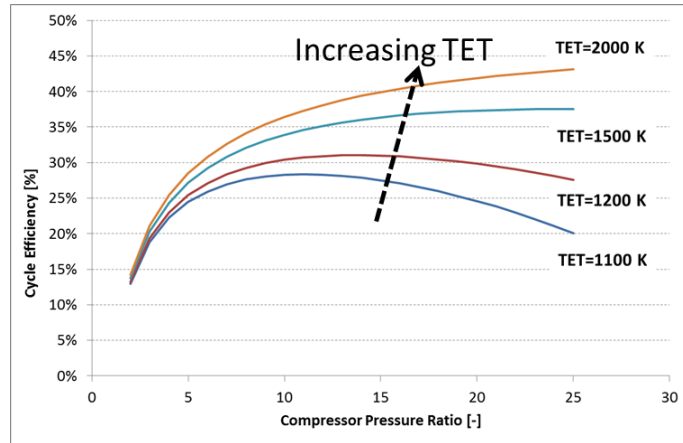


Figure 1.2: Simple cycle thermal efficiency variation with TET for a generator with non-ideal components:  $\eta_{compressor} = .87$  and  $\eta_{turbine} = 0.85$ .

The application of the gas turbine becomes then a factor in deciding which factor is to be increased. In fact, increasing the compressor pressure ratio is done usually by adding more stages, which leads to higher machine weight. For land based gas turbines, typically used for power generation, this is not a limiting factor and a higher count of compressor stages are used as shown in Fig. 1.5. On the other hand, the weight of an aircraft engine is critical to the aircraft overall performance and the compressor cannot be extended indefinitely. A typical turbofan engines, shown in Fig. 1.4, has a multi-stage compressor located on different shafts to optimize the overall pressure ratio while limiting its weight.

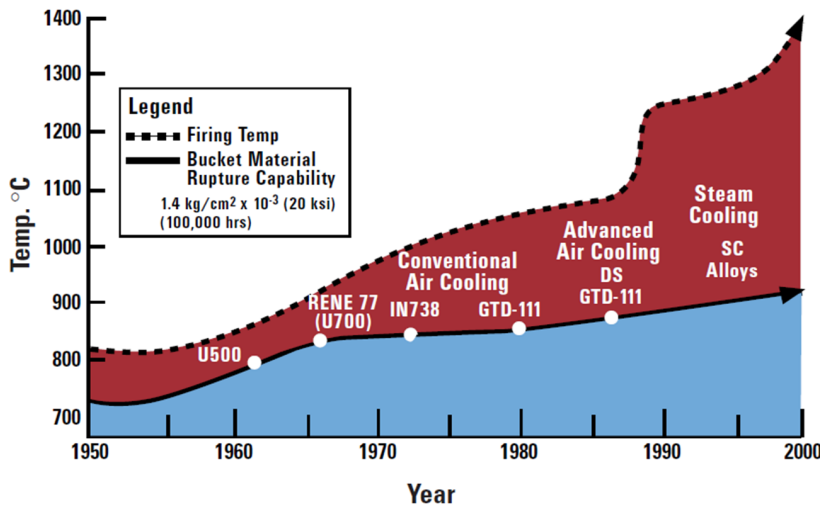


Figure 1.3: Turbine inlet temperature and blade metal temperature trends with cooling technologies and material capabilities. The materials are materials used in General Electric engines [78]

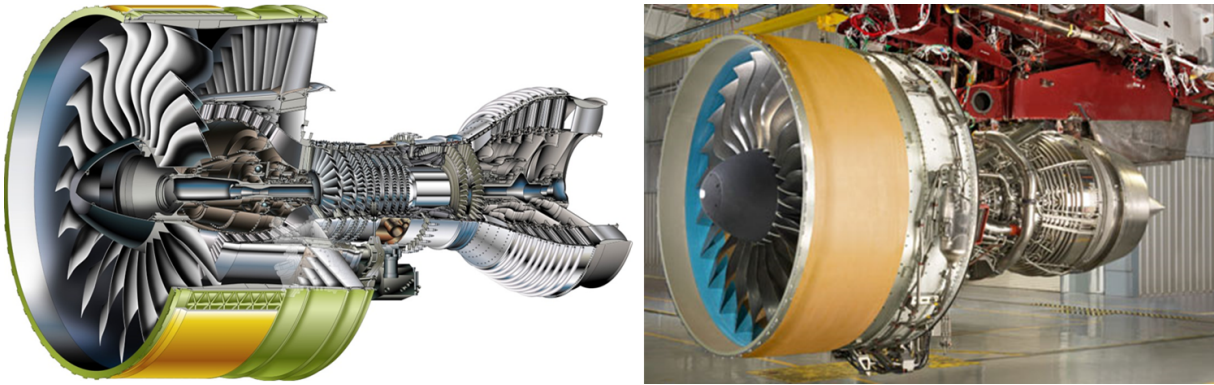


Figure 1.4: Cut-away view and picture of an assembled GP7000 Turbofan, aircraft engine for the A380 manufactured by MTU and their partners.

The complexity is also reduced and thus the maintenance costs, that are another critical budget for airlines. The remaining degree of freedom to further increase a cycle efficiency is the increase in turbine entry temperature, and this is proven to be the most effective criteria, as shown in Fig. 1.2.

A major limitation in increasing the flow temperature at the inlet of the turbine is the availability of materials able to withstand the harsh conditions in a turbine stage. In fact, the high temperature environment combined to the mechanical stresses from the rotation and the aerodynamic loading requires the strongest and most resilient engineered materials. The improvement of materials and manufacturing technique on one hand and from protection and cooling techniques on the other are now allowing turbine

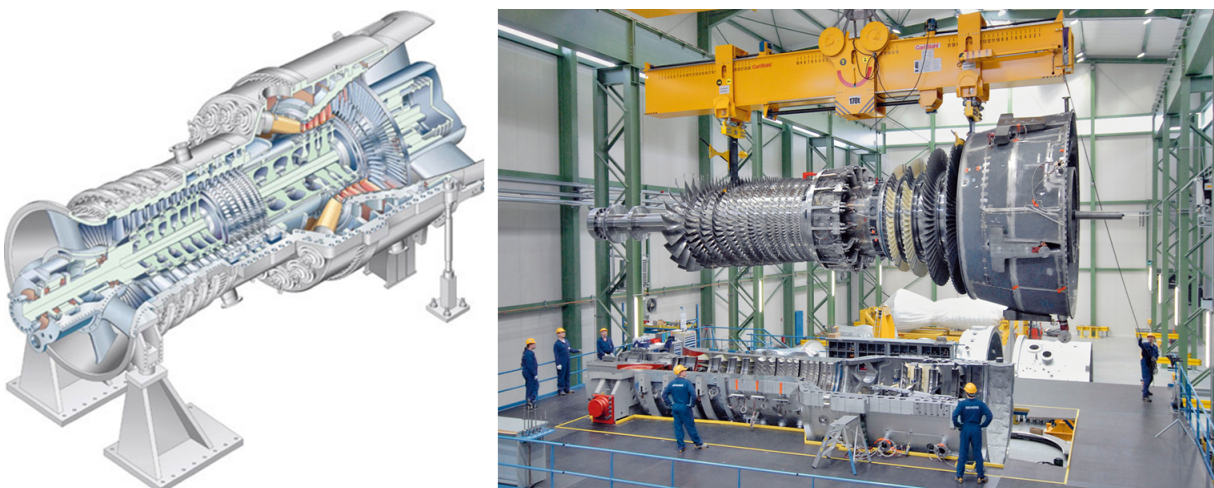


Figure 1.5: Cut-away schematic and picture of the rotor assembly of a SGT5-800H, Siemens's most powerful gas turbine.

inlet temperature 300K above the material melting temperature. Figure 1.3 shows the increase of blade metal temperature with the improvements of the material properties and the increase of turbine inlet temperature to reach higher efficiency. The graphs also highlights the importance of cooling techniques using bypassed air from the compressor stages to cool down the turbine components. The improvement of the techniques allowed a TET increase of 250K between "simple" internal convection cooling and the implementation of advanced film cooling techniques. On the other side, the material improvements helped only for 100K. In a film cooled turbine stage, the cold air is injected in the main flow through single holes and this air is used as a gas curtain to prevent hot fluid from reaching the metal of the endwall and the airfoils. The injection of the cooling fluid along the endwall and airfoil is however generating additional aerodynamic losses due the mixing with the mainstream. In addition to the internal and external cooling of the first turbine rows, part of the coolant air is used to prevent hot gas ingestion to the core of the engine where the seals, disks, bearings and other parts made of less resistant material would immediately melt. This purge flow is injected from cavities between rows and has an impact on the aerodynamic performance. In fact, because of the swirl present in the cavity, the purge flow is injected with a different momentum and direction compared to the main stream generating additional mixing losses. The amount of coolant air has to be minimized since it reduces the working fluid and the overall performance. The compromise stands in achieving a TET increase that overcome for the extra losses and further increase the cycle efficiency. In the design phase of an engine, the coolant requirements for every part are assessed based on the thermal loads and the desired lifetime of the components. As mentioned in Han et al. [37], an error of 50K in the prediction of the metal blade temperature can reduce the lifetime up to 50% and therefore highly accurate predictions are of interest for the engineers. Experimental validation of the design is commonly used by gas turbine manufacturers to ensure the safe operation of the system, but due to their costs only optimized geometry are tested. The recent advances in Computational Fluid Dynamics (CFD) in both software and hardware provides now tools to predict the loads in a reduced lead time and therefore further optimize the designs. However CFD tools have to be used wisely by the designer who should be aware of their limitations. Denton [25] provides a summary of the sources of error in Turbomachinery CFD and divide them based on their origin, modeling, numerical models and boundary conditions. In fact, the strong requirements in the prediction accuracy is a challenge when considering the complexity of the flow physics in a turbine stage (three dimensional, unsteady, wakes propagation and mixing,...) and the many sources of errors that can arise (modeling, numerical smoothing, grid sensitivity,...). In order to further understand the limits of heat transfer predictions and reduce the number of tests for real engine parts, there is a need for high resolution, high accuracy experimental data that can be directly compared to predictions.

Although the component efficiency in a gas turbine can exceed 90% for a turbine stage, there is still room for improvement. The innovation in material science, manufacturing techniques, computer aided design (CAD) and flow predictions (CFD) capabilities have recently pushed the limits in terms of design space for airfoils and their integration in a compressor or a turbine environment. With the goal of reducing the complexity of the machine, the number of stages and airfoils per stage is kept to a minimum, leading to a higher loading per airfoil. A direct consequence on the aerodynamic performance is the increase in secondary flow losses and methods to reduce these losses are of great value. It has been shown in the 1990s by Rose [75] that the secondary flow losses also interact with the purge flow and that a correct combination of these can improve the stage performance. The computer aided design methods (CAD, CFD, optimization algorithms) have helped in designing complex airfoils geometry to reduce the secondary flow losses and then shape the endwall to benefit from their interaction with the purge flows. The use of non-axisymmetric endwall contouring has shown great potential in achieving the latter. However the impact of endwall contouring on the thermal loads is less understood. In addition, the use of complex 3D shapes makes the task of the thermal designer more complex since empirical models used for loads estimation and lifetime prediction do not apply anymore. The comparison of well defined experimental test cases (geometry, boundary conditions, operating conditions) with predictions for the same case is essential to further understand the differences and bound the uncertainty relative to the use of CFD for design purpose. The ability to reduce the safety factor applied during the designs and the limitations of the experimental campaigns will lead to substantial increase in performance and a significant decrease of the costs.

The thermal management of a vane passage endwall or a blade hub platform is critical for the safe operation of a turbine. In fact, as shown in Fig. 1.6, the platforms are often extended elements with low thickness over length aspect ratio. The effect of thermal loads and centrifugal stresses combines and acts as a bending moment for the extremity of the platforms. Low cycle fatigue and creep are then limiting the part lifetime. The already mentioned geometry and the large pressure gradients on the endwall are further limiting the use of cooling techniques. In fact, the pressure gradient observed on the passage endwall requires a well controlled feeding arrangement for film cooling holes, which is difficult to achieve within the geometrical constraints. The variation of the static pressure field at the exit of holes fed by a unique cavity leads to large variation of jet momentum flux across the passage, resulting in lifted jets and high aerodynamic losses for reduced cooling effectiveness. Difficulties due to the accessibility for machining are further limiting the cooling possibilities. In fact, film cooling holes are drilled with laser techniques due to their small diameter (0.4-1mm), a line of sight is then required to machine the holes. The high turning encountered in vane passages is limiting the accessibility for the laser especially close to the junction of the pressure side with the endwall along in the aft portion of the passage (throat, close to the trailing edge). The film cooling holes are



therefore located in regions accessible for manufacturing, and where the pressure field is rather uniform and remains constant through the engine operating phases. The cooling of the endwall is therefore often achieved with impingement cooling or convective cooling, that are less efficient techniques. The limitations of the loads on the endwall and a correct estimation of their magnitude is then a significant parameter for the engine hot gas path design. When combined with non-axisymmetric endwall contouring, the geometry of the platform is further constraining the cooling possibilities. In addition the effect of endwall contouring on the thermal loads distribution is not yet completely understood. There is therefore a need for an experimental investigation of the effect of endwall contouring on the heat transfer coefficient and adiabatic wall temperature patterns.

The thermal design of components in the hot gas path is generally performed using 3D thermal and structural FEM models, in which the temperature fields and von Mises equivalent stress levels are predicted. For turbine components, the local variation of the thermal boundary conditions can have a critical effect on the thermal stresses in particular. For example, a error in the local prediction of temperature of 10degrees, can lead to a wrong estimation of the thermal stress by  $\delta\sigma = E\alpha dt = 20\text{MPa}$  for a typical turbine component. When combined with existing loads, thermal, centrifugal or due to the gas bending, this error can lead to an early failure of the part.

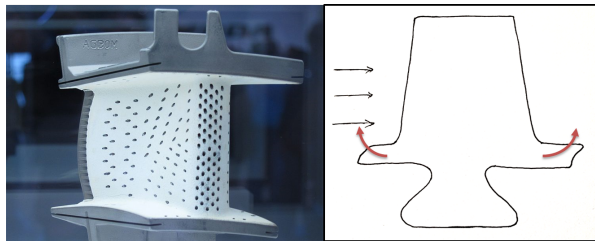


Figure 1.6: Left - Film cooled gas turbine vane from the V2500. Right - Schematic of a blade with hub platform and the bending moment on the platform.

The current work lies at the intersection of these different fields and deals with the measurement of heat transfer on cylindrical and contoured hub endwall of a vane passage in an axial turbine.

## 1.2 Literature Review

### 1.2.1 Flow structures in a turbine stator row.

The aerodynamic losses are commonly divided in profiles losses and endwall losses. The endwall losses or "secondary flow" losses contributes between 30 to 50% of the overall aerodynamic losses as stated by Sharma and Butler [83]. Because of this importance, research in the field has been quite extensive and a clear review is provided by Langston

[50]. An important number of studies performed in linear or annular cascades have helped to develop models for the formation and migration of the secondary flow structures.

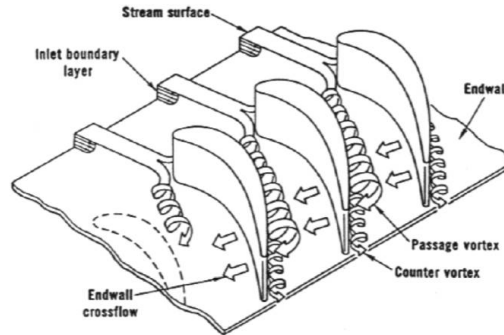


Figure 1.7: Secondary flow model by Langston [51]

**Formation of secondary flow structures.** Secondary flow structures are named "secondary" because they are not aligned with the mainstream. They are dominated by a system of vortical structure that are interacting with each other. In a turbine stator row and according to the model shown in Fig.1.7 from Langston et al. [51], the Horseshoe Vortex (HV) and Passage Vortex (PV) are the most significant. The HV originates at the leading edge of a junction between an endwall and a bluff body. The incoming boundary layer is decelerated by the adverse pressure gradient due to the presence of the airfoil and, after separation, rolls up and creates a vortex. After its formation, the HV is stretched around the leading edge of the airfoil and split in two legs following the pressure and suction sides of the airfoil. The formation of a HV occurs in general for any bluff body such as cylinder, symmetric airfoils, vanes, rotor blades, etc. The passage vortex develops due to the pressure gradient between the pressure and suction sides of the passage. The low-momentum fluid from the endwall boundary layer is entrained by the pressure gradient towards the suction side of the passage. Within the passage, the pressure side leg of the HV and the PV interact and merge forming a stronger passage vortex. The suction side leg of the HV, follows the suction side of the airfoil and rotates in the opposite direction compared to the PV. It interacts also with the passage vortex and appears as a satellite vortex to the bigger passage vortex. The development of these flow structures and the resulting migration of low momentum fluid in the mainstream explains the strong impact of these structures on the aerodynamic losses.

Other model of secondary flow structures have been developed based on measurements and basically add complexity to the vortical system previously described. Sharma and Butler [83] observed the wrapping of the HV suction side leg around the PV. Wang et al. [90] identified more vortices, especially close to the leading edges where the HV structure is duplicated, and also multiple corner vortices developing at the airfoil endwall junction along the passage.

**Reduction of secondary secondary flow losses to increase aerodynamic efficiency of a turbine stage.** In the last two decades, both passive and active techniques have been developed and tested to reduce the secondary flow losses.

Three dimensional airfoil shapes with lean and compound lean have been developed to manage the endwall and profile losses. A leaned airfoil is composed of span-wise sections not aligned radially but shifted circumferentially, with a linear distribution for simple lean or parabolic in the case of compound lean. The major intent is to reduce the forces acting on the formation of the HV and PV and therefore limiting the strength and migration of the structure. Harrisson [39] performed experimental measurements of aerodynamic losses downstream of prismatic, leaned and compound leaned airfoils. While the overall losses were marginally increased by lean or unchanged by compound lean, the major outcome of the 3D shape was the resulting flow field at the exit of the row. In fact the airfoil shape modified the flow turning distribution and reduced its non-uniformity. The impact of the 3D shape has then to be considered within a multi-row turbine where it will be positive in terms of mixing losses and turbine efficiency.

The modification of the airfoil leading edge also received an important interest in the last decade. In fact, adding a sort of bulb close at the junction between the airfoil and the endwall helped reducing the aerodynamic losses by up to 50% as shown by Sauer et al. [77]. The suction side leg of the HV is intensified but the interaction with the passage vortex (counter-rotating) leads to a loss reduction. The later numerical study by Zess et al. [92] presented a leading edge modification leading to an elimination of the horseshoe vortex and delaying the development of the passage vortex.

Another passive control method of the secondary flows using three-dimensional shaping of the endwall was developed and successfully tested in recent years. The principle is based on changing the endwall curvature to locally control the static pressure field. A convex surface will lead to a flow acceleration as the cross section changes and therefore a decrease in static pressure whereas the opposite effect is observed for a concave curvature. First introduced by Rose [75], their performance was studied, both in real engines by Brennan et al. [19] and in research facilities (Ingram et al. [43], Schuepbach et al. [82]). In his numerical work, Rose [75] showed the benefit of endwall contouring to reduce the static pressure non-uniformity by 70% at the exit of a passage. The technique can be used then to reduce the requirements in purge air. Harvey [41] showed later the benefit of endwall contouring on the secondary flow losses. The reduction of the cross passage pressure gradient limited the formation of the passage vortex and reduce the losses. More recently, an increase in stage efficiency of  $1\% \pm 0.4\%$  was measured in the LISA research turbine facility by Schuepbach et al. [82]. The optimized configuration included endwall contouring on both stator and rotor rows of a highly loaded turbine stage. A change in the sensitivity to purge flow of the stage efficiency was also measured for the different configurations. The endwall geometry is generally modified using hills and troughs in an axisymmetric or non-axisymmetric manner, as described in Germain et al. [31]. Both

usually result from a complex optimization process using three-dimensional numerical fluid predictions. The objective is to tune the position of the protrusions or valleys to shape the static pressure field on the endwall. The optimization goals can be various and different studies showed the usefulness of endwall contouring in reducing the non-uniformity of the turbine exit flow angle, reducing the migration of the passage vortex across the passage, in Schuepbach et al. [81] and shaping the static pressure distribution profile at the exit of the passage to control a purge flow, in Schuepbach et al. [82].

### 1.2.2 Endwall heat transfer.

The heat transfer coefficient distribution on the endwall of a vane passage has received constant interest over the years. The work of Blair [14] and the more detailed works of Graziani et al. [34] and Goldstein and Spores [33] provided a detailed description of heat transfer patterns and studied links to the vortical flow structure evolving in the passage. Different methods were used providing different measurement resolution but the major conclusions were the following:

- the highest heat transfer rate is observed in the leading edge region where the horseshoe vortex forms,
- a wedged shaped area located at the entrance of the passage and pointing towards the passage shows a uniform heat transfer level similar to the level measured in the incoming boundary layer,
- the passage vortex has an impact on the heat transfer distribution,
- the migration of this vortex along the separation line shows two regions of high (upstream) and low (downstream) heat transfer coefficients. The sharp decrease originates from the formation of a new boundary layer, after the inlet boundary layer has been swept into the horseshoe vortex.

The intimate link between secondary flows and heat transfer rates was clearly stated in these studies and led many later studies to focus on the leading edge-endwall junction where the vortices are created. The work of Gaugler and Russell [29] linked the peak of Stanton number with the peak activity of the horseshoe vortex. The combined high resolution measurements of flow structure and heat transfer in the work of Kang et al. [47] highlighted also the link between the down wash of the vortical structure and the peak level of heat transfer coefficient.

**Heat transfer in a cascade with symmetric airfoils.** A limited number of studies have focused on heat transfer at a blade-endwall junction (illustrated in Fig. 1.8) with symmetric airfoils. Most of these studies focus on the leading edge area of a blade-endwall junction to understand the physical mechanism leading to elevated levels of heat transfer in the junction region. The work of Lewis and Simpson [55] presented heat transfer coefficient data around the leading edge of a NACA 0015 and a NACA 0020 symmetric airfoil mounted on a flat plate. Time resolved measurements of heat transfer

were obtained and related to previous measurements of the flow [26]. An augmentation of the heat transfer coefficient of 200% was observed near the leading edge compared to the level measured in the approaching boundary layer. The influence of the wing shape was also highlighted. A blunt leading edge led to a more upstream position for the horseshoe vortex and therefore a reduced heat transfer close to the body. Two more recent studies by Praisner and Smith [73] and Hada et al. [35] also focused on the leading edge region of an airfoil-endwall junction with NACA symmetric profiles. Both studies linked time resolved measurement of flow-field and heat transfer close to the junction. A complex flow structure was identified upstream of the leading edge with four distinct vortices (horseshoe, secondary, tertiary and corner vortices). An increase in the heat transfer coefficient of 250% compared to the upstream boundary layer was reported. A high thermal unsteadiness observed in this region showed heat transfer rms variation of  $\pm 25\%$  compared to the time average value.

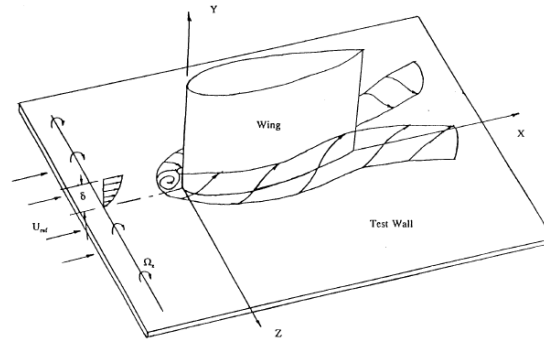


Figure 1.8: Sketch of an airfoil-endwall junction including the horseshoe vortex. (from [55]).

**Impact of leading edge or endwall modifications on thermal loads.** Following the work on leading edge modifications improving the aerodynamic performance, the impact on heat loads were also assessed. Lethander [54] integrated an optimizer to a CFD tool and generated a leading edge shape reducing the averaged adiabatic wall temperature by 6.3%. Also the use of a fillet reduces the total surface (airfoil and endwall) requiring cooling. In their work, Han and Goldstein [38] use the naphthalene technique to measure the changes in mass transfer due to the leading edge modification mentioned in Zess and Thole [92]. The influence of the modified leading edge show a reduction of the observed mass transfer upstream of the leading edge and the high mass transfer related to the passage vortex in a case without fillet is not observed when the fillets are used. However corner vortices are created at the junction of the leading edge with the fillet and further downstream along the suction side near the trailing edge.

The computational work of Saha and Acharya [76] is one of the first work using endwall contouring and showing a reduction of Nusselt number levels due to endwall modification. A reduction of a factor three is predicted locally close to the leading edge while reduction around 15-20% are predicted within the passage. Overall, a 8% reduction of the area averaged Nusselt number is predicted.

On the experimental side, few studies were performed on contoured endwall. Mahmood and Acharya [60] performed one of the first study. The geometry combined leading edge modification and endwall contouring. The measurements showed a 20-30% reduction in Nusselt number for the contoured case compared to a flat endwall. The changes are observed primarily upstream of the throat where the effect of the passage vortex is important in the flat endwall case. While the overall area averaged Nusselt number is reduced with endwall contouring, higher values are locally observed downstream of the throat where corner vortices form. The more recent study of Lynch et al. [58] provides detailed measurements of the heat transfer coefficient in a blade cascade with non-axisymmetric endwall. The measurements were performed in a low speed linear cascade using an iso-heat flux boundary condition and an infrared imaging device. Even though the area averaged heat transfer for the contoured case showed a reduction of 3.1% compared to a flat endwall, large increases (up to 20-30%) in the heat transfer coefficient were observed locally.

As it can be seen in this short survey, the number of works providing heat transfer data on contoured endwall is very limited. Also most of the studies highlighted previously are performed in cascade environment and are related to both nozzle guide vane and rotor configurations. The major reason is the strong requirements in terms of setup to perform accurate heat transfer measurements.

**Heat transfer on rough surfaces** In real engines, the surface quality of the parts is changing during the lifetime of the engine. In particular, the parts located downstream of the combustion chamber are especially affected by the deposition of residuals of combustion, ash, or by the erosion of the thermal barrier coating. This result in varying changes in roughness level between the manufactured part and its end of life. Also the distribution of the roughness elements on the vane endwall is not uniform. The work of Bons [17] provides a review of roughness studies performed in a gas turbine environment. The current study does not aim to provide heat transfer data on rough surfaces, but the experimental setup used showed level of roughness that will have an impact on the measurements.

Barlow et al. [10] performed heat transfer measurements on a flat plate with zero pressure gradient and equipped with rough surfaces composed of different element shapes and densities. The measurements showed an increase in heat transfer by up to 120% compared to the smooth plate, depending on the element shape and distribution.

Blair [15] studied the effect of surface roughness on heat transfer for the endwall and the blade surface. The experiments were performed for two surfaces with black paint (smooth) or grit (rough). On the vane surface, increase of the heat transfer coefficient as high as 100% is reported close to the leading edge. On the endwall, the heat transfer patterns is similar between the two configuration but an increase in heat transfer levels is measured and can be as high as 75% at the passage exit.

Stripf et al. [86] and Lorenz et al. [56] performed heat transfer and aerodynamic loss measurements in the linear cascade of Karlsruhe Institute of Technology (KIT). The two studies present measurements using arrays of deterministic roughness elements with varying height, shape, spacing, eccentricity, anisotropy, etc. Heat transfer coefficients are increased by up to 50% compared to the smooth configuration. The study of anisotropic roughness elements on the surface vane concluded that the stream wise stretched roughness shows lower level of heat transfer increase than the spanwise stretched elements.

Most of the correlation developed for heat transfer coefficient or skin friction are based on deterministic roughness as tested in the studies cited before. The origin is located in the definition of a single parameter to account for surface roughness by Nikuradse [68], who defined the equivalent sand grain roughness parameter  $k_s$  by comparing the pressure drop in rough pipes to the same quantity in pipes roughened with known sand paper. However most of the roughness shape due to deposition, spray of TBC coating, ash or chemical deposition, is not following a deterministic distribution.

The work of Bons [16] focused on the scaling of real roughness measured on actual engine parts and the testing on a flat plate. The results are compared intensively with correlation for skin friction and Stanton number, which are seen to under predict the effect of roughness in the transitionally rough regime ( $Re_k = \frac{k_s u_\tau}{\nu} < 70$ ). A new correlation for  $k_s$  based on the rms of the slope of the roughness element is also provided.

The need for a single parameter to characterize the surface roughness comes from the use of correlation or models to predict the 3D flow field on rough surfaces. In most of the CFD code, a sand grain equivalent roughness parameter is used to alter the turbulent eddy viscosity  $\mu_t$  at the wall. New approaches using a discrete element model are used, such as in McClain et al. [64] but these are not yet applicable to turbomachinery flow because of their 2D formulation. The complete discretization of the roughness element is the "brute force" approach and is at the moment limited due the computational cost involved.

**Heat transfer measurements in a turbine environment.** Different methods have been developed to measure heat transfer coefficients either using a steady state or a transient principle, a comparison of the methods is made in O'Dowd et al. [69]. Also the experimental facility can itself be a blow-down facility as in Abhari [4] or continuously running. The evolution of measurement techniques from discrete measurement points using thermocouples in Graziani [34] or heat flux gages in Abhari [4] and more recently

Haldemann et al. [36] to 2D field measurements using CCD camera and liquid crystal in Giel et al. [32] or thermal imaging devices in Lorenz et al. [56], helped improving the resolution of the acquired data.

Another critical aspect in measuring heat transfer data is the need of either a precisely known isothermal or an iso-energetic (incl. adiabatic) boundary condition. The following issues have to be overcome to successfully measure heat transfer quantities on a passage endwall

- creating a uniform boundary condition,
- shaping and attaching the heating device or insulating element to the airfoil and the endwall (potentially a non-developable surface),
- measuring using high resolution imaging devices on complex geometries with limited accessibility (view angle, geometrical reconstruction, distortion).

A certain number of flow conditions cannot be reproduced with a high fidelity in simplified configurations such as flat plate or cascade experiments. For example the unsteady flow field, the annular flow behavior, the free stream turbulence level and its distribution, the wakes, fluid injection and swirling flows cannot always be simulated and their effect may not be individually investigated. There is therefore a need for high resolution experimental data measured in a rotating axial turbine facility.

An important requirement for the designer is to have access to data that are independent to the configuration and that can be applied to complex (non optimum) cases. As the driving temperature in heat transfer processes, Moffat [66] proposed a definition of the heat transfer coefficient based on the use of the adiabatic wall temperature. Following studies, such as Anderson et al. [8], demonstrated that this definition leads to a heat transfer coefficient independent of the thermal boundary conditions.

### 1.3 Research Objectives

The objective of this work is to investigate the influence of advanced blade geometry and endwall contouring on the thermal loads and provide design guidelines to improve endwall contouring design methodology from a thermal loads perspective. The sensitivity of the contoured endwall to a change in operating conditions and the consequences on the thermal loads is also investigated and compared to the cylindrical endwall case.

For this purpose, a heat transfer measurement setup is designed and integrated in the axial turbine test rig LISA to allow the measurements of heat transfer coefficient and adiabatic wall temperature on the hub endwall of the first vane row. To reach this objective the following milestones have been achieved:

- adapt the heat transfer measurements technique to an airfoil-endwall configuration
- design and integrate a vane segment to the axial turbine facility allowing heat transfer measurements on the hub endwall



- perform heat transfer measurements on cylindrical hub endwall for different turbine operating conditions
- perform heat transfer measurements on a contoured endwall for the same turbine operating conditions
- use the experimental data to provide explanation for the physical phenomena influencing the thermal loads on the endwall of a vane passage

The experimental results are complemented with numerical predictions to enhance the knowledge about the flow behavior close to the endwall and the link between heat transfer patterns and flow structures.

## 1.4 Thesis outline

**Chapter 1:** The motivation for the current work and a literature review highlighting the major studies and findings made in the field is provided. In particular, a description of the flow structure in a turbine vane passage, methods to reduce secondary flows and their impact on thermal loads are presented. Also, an overview of turbine heat transfer measurement studies is provided.

**Chapter 2:** This chapter describes the theoretical basis for the experimental methods used in this work. The infrared thermography technique and the image processing techniques are in particular detailed.

**Chapter 3:** The preliminary study performed in the flat plate research facility LAVAL is presented in this chapter. The focus of this work is to adapt the heat transfer measurement technique and extend the measurement know-how to a vane endwall configuration.

**Chapter 4:** The design of the heat transfer measurement platform to be integrated in the axial turbine facility is described in this chapter. The boundary conditions are described and the different design procedure are explained. The design and use of the different equipments involved in the measurement chain are also extensively covered.

**Chapter 5:** This chapter presents the results of the measurements of heat transfer quantities performed on the cylindrical hub endwall of the nozzle guide vane row in the turbine facility LISA. The measurement procedure is described and a precise uncertainty analysis is provided. The measurements at two operating conditions are shown and a comparison with numerically predicted data is achieved.

**Chapter 6:** In this chapter, the surface roughness is characterized and the effect of the roughness is numerically investigated using the in-house solver Multi3, modified with

a newly implemented roughness model.

**Chapter 7:** The heat transfer measurements performed on the contoured endwall configuration are presented in this chapter. This chapter details also the experimental methods used to map the thermal resistance non-uniformity over the passage and the procedure used to correct the heat transfer data accordingly.

**Chapter 8:** The measurements for both cylindrical and contoured endwall are analyzed in combination with work from the literature and numerical predictions. This chapter provides a more detailed explanation of the secondary flow structure encountered in the cylindrical endwall case and the impact of the contouring on the flow structure and heat transfer patterns.

Finally, the last chapter summarizes the work and identifies design recommendations and guidelines for future work.

# Chapter 2

## Experimental Methods

This chapter introduces the different experimental techniques involved in the current work. Their theoretical bases are covered as well as practical application to situations encountered in the course of this work. The measure of heat transfer quantities cannot be performed directly and a combination of multiple temperature or heat flux measurements is required. The measurement techniques used in the current work to provide surface and solid temperatures data are introduced in this chapter. The infrared imaging technique is especially described in this section. The goal of the current study was to provide data covering a complete vane endwall. Due to the limited accessibility of the facility as well as the cost of transparent materials, this could only be done using multiple positions of the imaging device. The image reconstruction procedure used for the measurements is described in this chapter. In addition, the current work relies intensively on imaging devices capturing in the visible or infrared ranges and the collected images are used for positioning purpose. A specific description of the methodology used for this purpose is made in the last section.

### 2.1 Temperature measurement

Different methods can be used in order to measure temperature on a surface. Single point measurements are usually performed using thermocouples, when size is an issue, or thermistors, when accuracy is an issue. The Seebeck effect is used in thermocouples, which provides a difference of potential between two points at different temperature. A junction at a reference temperature is therefore required to obtain an accurate temperature data. On the other hand the thermistor uses the known linear variation of a material resistivity, commonly platinum. When fed by a constant current, the voltage measure across the thermistor is directly linked to the temperature of the element. The most common type of thermistor is the PT100 which is also used for solid temperature measurements in this work. Both types, shown in Fig. 2.1, require therefore a dedicated

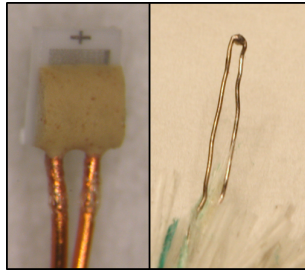


Figure 2.1: Miniature PT 100 (1.6x1.2x0.8mm) used in the current work (manufacturer IST AG). On the left a typical K-type thermocouple junction measuring 0.5mm in diameter is shown.

setup (reference junction, current source) to provide a measure of temperature at a single point, which make them not suitable for temperature field analysis over a large area.

While the single point data are acquired using common voltage or current measuring devices, 2D measurement techniques rely on imaging devices and can provide, generally quickly, a large quantity of data points spread over an area of interest. The major difference is then the non-intrusive nature of the 2D measurement techniques. This is a clear advantage as sensor installation effects can sometime disturb the measured phenomenon and corrupt the acquired data.

One area based technique use thermo chromic liquid crystal, shown in Fig. 2.2, that is applied in the form of paint or sheet to a surface of interest. The orientation of the molecules changes because of the temperature, which affects the reflection of an incident light by limiting it to certain wavelength. When the illumination is uniform, the colors observed in the surface are related then to the local temperature. More information related to the working principle and the use of this technique can be found in Smith et al. [85]. However the range of color change for a single TLC is often limited to 10-15degC and different TLC combination are required to cover a broader range of temperature.



Figure 2.2: Example of a sheet of ThermoChromic Liquid Crystal reacting to the temperature of the hand holding it.

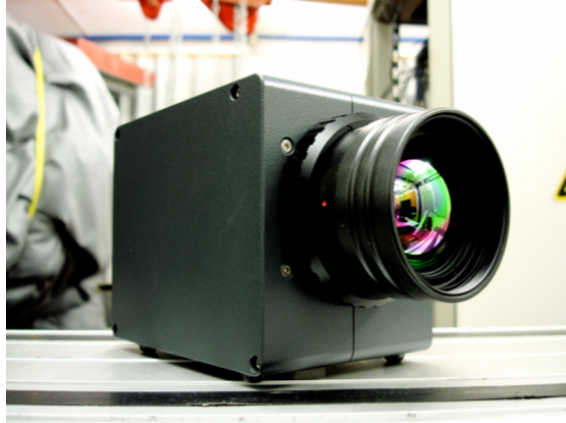


Figure 2.3: Infrared camera operating in the LWIR range used in this study.

More recently, technique using temperature sensitive paint (TSP) have emerged. In this case the surface is painted with a mixture of luminescent molecules and a polymer binder. The principle is based on fluorescence, where molecules are excited by incoming light radiation and then transition back to the original state by emitting light at a higher wavelength. The intensity of TSP fluorescence is inversely proportional to the local molecule temperature. An illumination at a single wavelength is needed then to capture accurate surface temperature. More details can be found in Lee et al. [53]. The major limiting factors are the need for an uniform illumination and the reduced lifetime of the coated surface. Lee et al. advise to re-coat every two weeks the surface which is critical when installed in a complex measurement facility with limited access. Both TLC or TSP technique require CCD camera operating in the visible range to acquire high resolution data on the surface. The color or light intensity on the surface is changing with its temperature and the temperature is recovered using a calibration curve.

The developments made in the field of infrared sensor manufacturing over the last ten years are now making infrared imaging systems suitable for quantitative measurements of temperature. An infrared imaging system, as shown in Fig. 2.3 is now able to provide temperature data at a high resolution (up to 640x512 pixels on the sensors of a Long Wavelength infrared camera) and within a limited set up time. Infrared imaging can also be used in situation where conventional measuring devices could not be installed such as:

- electrically conductive materials,
- gaseous medias,
- high temperature or aggressive environments,
- small or moving targets,...

However, infrared measurement devices able to provide repeatable, quantitative temperature measurements are nonetheless complex and expensive systems and require careful setup and calibration procedures.

### 2.1.1 Basis of radiation applied to thermal imaging.

The interested reader is referred to Vollmer [89] for a further detailed description of the theory of infrared imaging and its application.

#### Electromagnetic wave

A thermal imaging system is basically collecting radiation from the surface located in front of its lens and then transforming this radiation into an electrical signal that can be converted into an temperature value. The values sensed by an array of pixels can then form an image with a color scale corresponding to the temperature.

Every body at a temperature exceeding the absolute  $0K$  ( $-273.15\text{degC}$ ) emits a radiation in the form of electromagnetic waves. A body will emit a certain amount of energy with a certain spectral distribution depending on its temperature, its properties (material, surface properties,...) and the surrounding environment. This emission can be discretized as a generation of a quantity of photons having an energy  $W$  related to the wavelength  $\lambda$  of the radiation, the Planck's constant  $h_p = 6.6 \times 10^{-34} \text{m}^2/\text{kg}/\text{s}$  and the speed of light  $c$  according to Eq. 2.1

$$W = \frac{h_p c}{\lambda} \quad (2.1)$$

On Fig.2.4 the complete spectrum of electromagnetic radiation is shown. The infrared range starts around 1micrometer wavelength and ends around 1 millimeter. In infrared thermography this band is divided in

- the Near InfraRed (NIR) or the Short Wavelength InfraRed (SWIR) from 700nm to  $1\mu m$
- the Mid Wavelength InfraRed (MWIR) from  $1\mu m$  to  $5\mu m$
- and the Long Wavelength InfraRed (LWIR) from  $8\mu m$  to  $20\mu m$

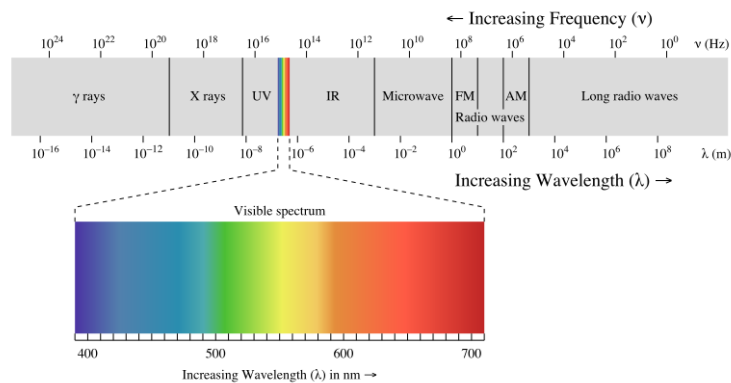


Figure 2.4: Spectrum of electromagnetic radiation.

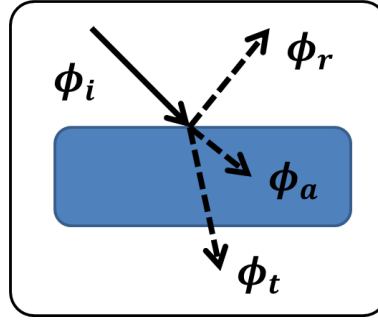


Figure 2.5: Energy conservation law.

As each and every object is able to emit radiation, an exchange process between the multiple medium involved in a scene is taking place. The energy conservation law Eq. 2.2 requires that the incident radiation ( $\phi_i$ ) on an object is either reflected ( $\phi_r$ ), transmitted through the object ( $\phi_t$ ) or absorbed ( $\phi_a$ ) within the object, as shown in Fig. 2.5. By taking the ratio of these terms with the incident radiation, three properties namely the absorptivity  $\alpha$ , the reflectance  $\rho$  and the transmittance  $\tau$  of a medium are then derived and translate the ability of the object to perform these tasks. The sum of these parameters reduces then to unity as shown in Eq. 2.3.

$$\phi_i = \phi_r + \phi_t + \phi_a \quad (2.2)$$

$$\alpha + \rho + \tau = 1 \quad (2.3)$$

The theory of radiation then relies on the specific case of a blackbody which is an ideal object absorbing every incident radiation ( $\alpha = 1$ ) regardless of wavelength and direction. Therefore no surface can emit more than a blackbody at a given temperature and wavelength. The emitted radiation depends on the wavelength but is independent on the direction. The Planck's law then define the emissive power of a blackbody in thermal equilibrium at a defined temperature  $T$  placed in vacuum in the wavelength interval  $[\lambda; \lambda + d\lambda]$  according to Eq. 2.4. The integral of this distribution over the complete spectrum is given by the Stefan-Boltzmann law Eq. 2.5.

$$M_\lambda(T)d\lambda = \frac{2\pi h_p c^2}{\lambda^5} \frac{1}{e^{\frac{h_p c}{\lambda k T}} - 1} d\lambda \quad (2.4)$$

$$M(T) = \int_0^\infty M_\lambda(T)d\lambda = \sigma T^4 \quad (2.5)$$

where  $\lambda$  is the wavelength,  $\sigma$  the Stefan-Boltzmann constant,  $h_p$  the Plank's constant,  $k$  the Boltzman's constant and  $c$  the speed of light.

The Fig 2.6 shows the spectral distribution of emittance (or emissive power) according to the Planck's law for different blackbody temperature. The magnitude increase and

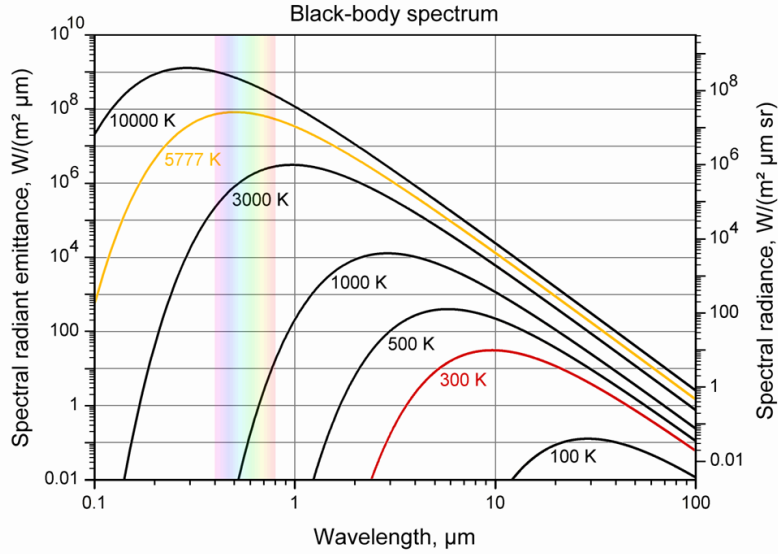


Figure 2.6: Spectral distribution of emittance according to Planck's law.

shift towards shorter wavelength of the peak can be observed with increasing temperature. The location of the peak can be calculated according to the Wien's displacement law given by Eq. 2.6.

$$\lambda_{max}T = 2897.8[\mu\text{m}] \quad (2.6)$$

For a blackbody, the body temperature can then be deduced from the measure of the radiation emitted by the body at every wavelength. However a real body does not satisfy the assumption of complete absorption of an incident radiation, only the fraction  $\alpha$  is effectively absorbed and affects the body temperature at equilibrium. The Kirchoff's law then states that the amount of radiation absorbed by any object is equal to the amount of radiation emitted by this object. A parameter called emissivity is defined and is equal to the absorbance, Eq. 2.7. It compares the emitted radiation of a real body the one of a blackbody at the same temperature. A blackbody can be considered as a perfect "absorber" or a perfect "emitter".

$$\epsilon = \alpha \quad (2.7)$$

For a non-ideal opaque surface  $\tau = 0$  and according to Eq. 2.3, the following relation is obtained  $\epsilon = 1 - \rho$ . For an object placed in vacuum, the radiation coming from the object observed by the camera is then the sum of the object emission, which is a function of its temperature, and a reflected radiation coming from the environment. When performing measurements outside of vacuum, the medium (gas) surrounding the object and the optical access (windows) are also participating. The radiation emitted by the object is then undergoing an absorption-reflection-transmission process through the gas and the optical access. The properties ( $\alpha, \rho, \tau$ ) of gases and windows are strongly wavelength dependent and specific care should be taken to select appropriate materials



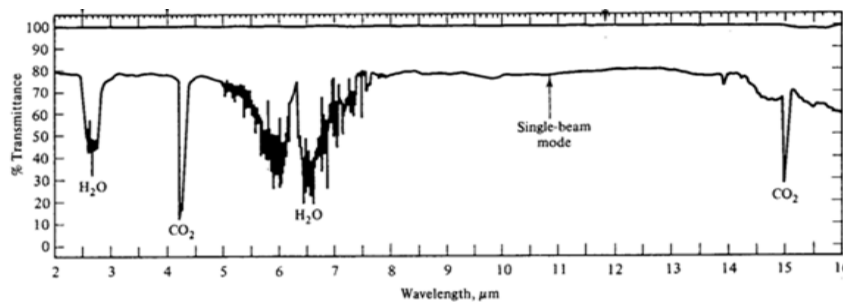


Figure 2.7: Air transmission spectrum.

for temperature measurements using an infrared imaging device. Figure 2.7 show the transmission spectrum for air, the bands where  $CO_2$  or  $H_2O$  are absorbing radiation are identified clearly. In the far infrared however the transmission is shown to be constant around 80%. The properties of Makrolon (physical name PMMA but also known as Plexiglas), water and Sodium Chloride (NaCl) are shown in Fig. 2.8. The first graph shows the transmission properties of PMMA, which is commonly used as an optical access in the visible range (400 to 800 nm wavelength) due to the 90% transmission level. However this material is clearly opaque above 2200nm which corresponds to the start of the MWIR range. The properties of water in the infrared range are shown in the second graph (B.), this illustrates the fact that an infrared camera cannot detect the radiation from a body immersed in water, the water surface temperature is acquired instead. However, when only a thin layer ( $1\mu m$ ) of water is present an object temperature can be acquired. Finally in the third graph (C.), the properties of NaCl are shown. It is a relatively cheap infrared transparent material that is used to make view ports. The balance between transmission, reflection and absorption for NaCl is seen to be dependent on the wavelength and the importance of the absorption above  $12\mu m$  is highlighted.

### Infrared imaging system

A thermal imaging system is composed of the following elements:

- the detector that is the core of the system: it is a sensing element composed of multiple pixels which properties are changing depending on the incoming radiation level
- an electronic circuit reading the data collected on the detector
- a lens collecting radiation coming from the scene and focusing it onto the detector
- a thermoelectric cooler controlling the temperature of the detector and ensuring its operating temperature as low as 77K

Two types of detectors are commonly used, thermal and photonics sensors. The thermal sensors are similar to an array of thermistors, where the thermal effect of the incoming radiation changes the resistance of the pixel element. Systems operating with such sensors produced out of Vanadium pentoxide are called bolometers or micro-bolometers.

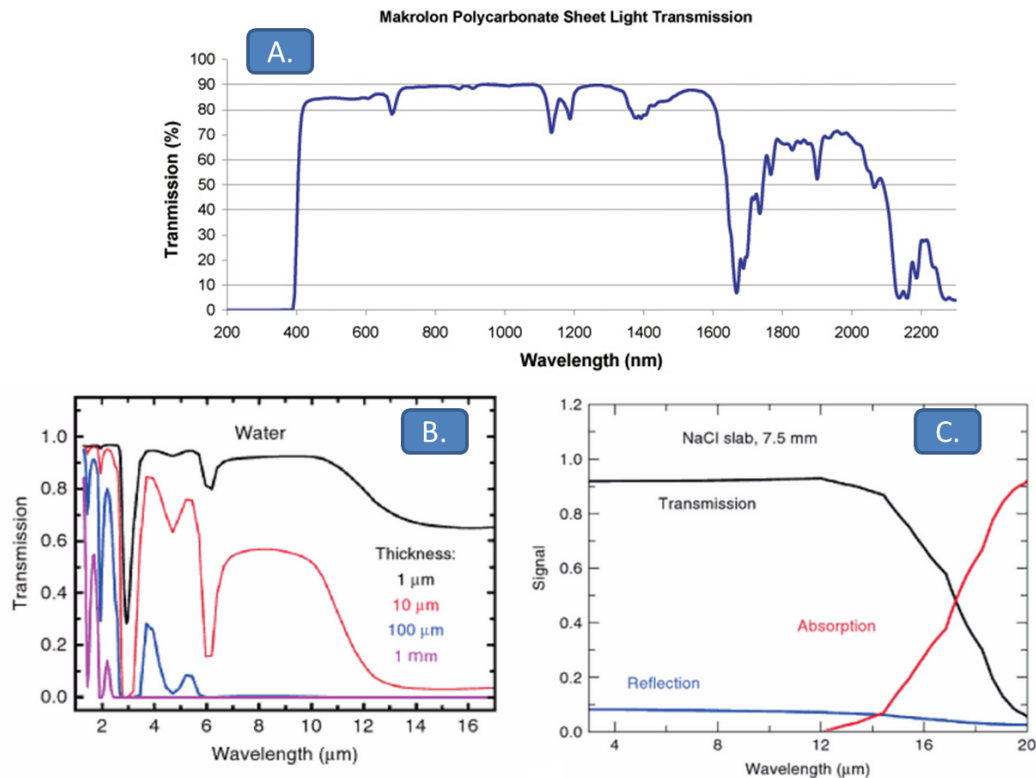


Figure 2.8: A - transmission curve for PMMA (brand name Makrolon) in the visible and NIR ranges. B - transmission properties of water layers of different thicknesses. C - properties of the infrared transparent material Sodium Chloride and the share of transmission, reflection and absorption relative to the wavelength.

The photo detectors operate based on the photo-conductive or photo-voltaic modes and are brought to very low temperature using a thermoelectric cooler. Ideally a sensor sensitive over the complete infrared spectrum should be used to integrate the emitted radiation at every wavelength and obtain a direct relation to the object temperature using Eq2.5. However no material used in the semi conductor industry can offer this ability. Therefore materials sensitive over large bands of the spectrum are used to produce the sensors:

- Indium gallium arsenide (InGaAs) for SWIR sensors
- Indium antimonide (InSb) for MWIR sensors
- Mercury cadmium telluride (HgCdTe) for LWIR sensors.

Due to the Wien's displacement law Eq.2.6 and the responsivity of a material at a certain wavelength, a type of detector can only be used for certain wavelengths and therefore their use is optimized for limited temperature ranges. Fig. 2.9 shows the detectivity of different detectors as a function of their wavelength.

The measurements performed within this project cover the temperature range between 10 and 100 degC. The wavelength range corresponding to the peak of the Planck's

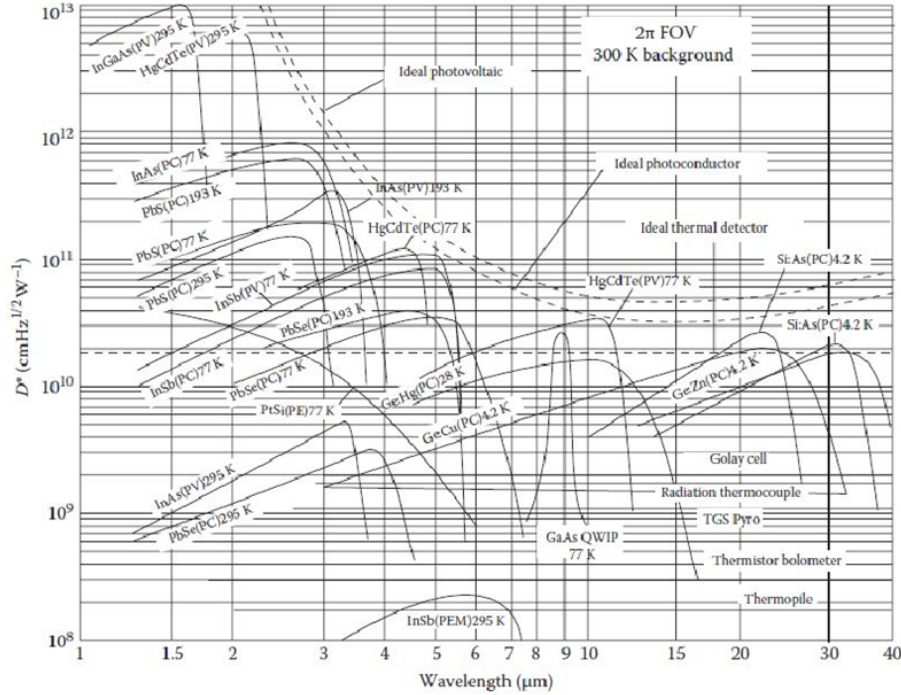


Figure 2.9: Specific spectral detectivity  $D_\lambda$  of multiple type of thermal and photons detector for IR radiation. The theoretical curve is also shown for ideal detectors.

distribution for this range is between  $7.7\mu m$  and  $10.5\mu m$ . Micro-bolometers and MCT detectors are the preferred sensors operating in this range.

MCT systems are high end systems used in situation where the sensitivity of the detector, the achievable frame rate or the integration time are critical, such as fast moving objects. The micro-bolometer systems are cheaper while providing image frame rates up to 50Hz. The system used in the current study, shown in Fig. 2.3, is a micro-bolometer based uncooled camera known as VarioCam and manufactured by the company Infratec. The spectral response band of the camera detector is  $7.5\mu m$  to  $14\mu m$ . The images provided have a dimension of 288x384 pixels (0.1 Megapixels). The picture is acquired in a "line-by-line" scanning mode where the values of every pixels are successively collected after an integration time of 7ms, corresponding to the thermal constant of the pixel. The complete picture acquisition and transfer is performed in minimum 20ms which is equivalent to a 50Hz maximum frame rate.

### Infrared transmitting material.

In order to image a surface located inside a wind tunnel, one or multiple viewports are required and they should be manufactured out of a material transparent in the wavelength range matching the sensitive range of the camera. For the  $7.5\mu m$  to  $14\mu m$  range the most common materials used are Sapphire, Germanium and Zinc Selenide.

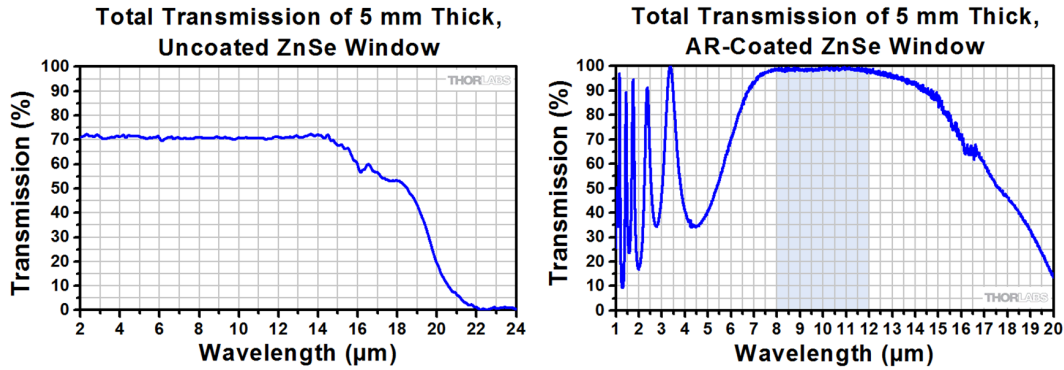


Figure 2.10: Transmission properties of 5mm thick ZnSe windows without coating (left) and with an anti-reflective (AR) coating applied (right). The target range for the anti-reflective coating is  $8 - 12\mu\text{m}$ . This data are taken from Thorlabs' website [3].

|                        |                                 |
|------------------------|---------------------------------|
| Density                | 5270 kg/m <sup>3</sup>          |
| Melting Point          | 1525 degC                       |
| Thermal conductivity   | 18 W/m/K                        |
| Thermal Expansion      | $7.1 \times 10^{-6} / \text{K}$ |
| Hardness Knoop         | 120                             |
| Young Modulus (E)      | 67.2 Gpa                        |
| Bulk Modulus (K)       | 40 Gpa                          |
| Apparent Elastic Limit | 55.1 MPa                        |
| Refractive Index       | 2.403                           |

Figure 2.11: Physical, thermal, mechanical and optical properties of Zinc Selenide material.

The material used in the present study is Zinc Selenide. The transmission property of the material is enhanced by coating both faces of the window with anti-reflective (AR) coating matching again the wavelength range. The coating brings the transmission level from 72% to 98% transmission, as shown in Fig. 2.10 where the transmission curves are shown for two 5mm thick ZnSe samples with and without AR coating.

Zinc Selenide is a rare material in nature but can be grown as a crystal and polished to achieve the desired shape. The thermal and mechanical properties of ZnSe are summarized in Fig. 2.11. These properties constrain its use and make it very expensive:

- difficulty to grow large pieces of high quality ZnSe crystal
- ZnSe dust generated during polishing is a highly toxic compound requiring extensive safety precautions
- its mechanical fragility requires very controlled and cautious polishing process as well as careful handling and protection measures while being assembled and stored
- moderate thermal expansion factor requires specific care for its integration in facilities with large thermal gradients

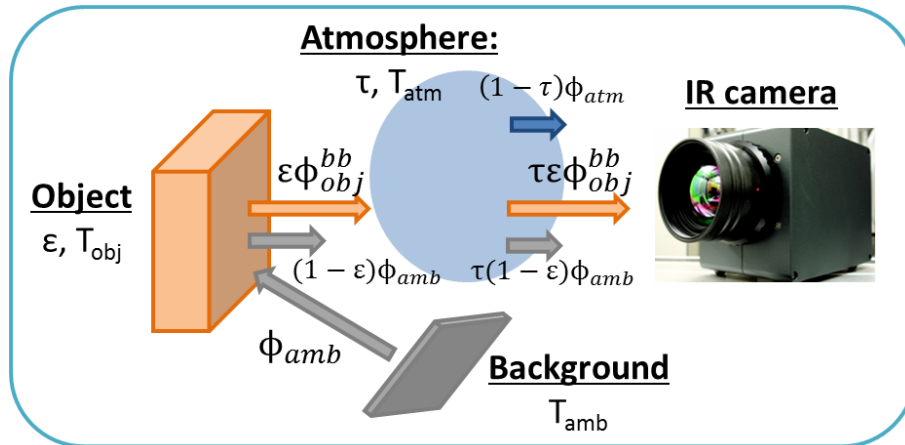


Figure 2.12: Schematic view of the complete radiometric chain. The object, background and atmosphere radiation fluxes are detailed and routed until they reach the infrared camera.

### Camera calibration

As a detector is sensitive to an incident radiation, it does not measure directly an object temperature. A calibration is therefore required. Blackbodies are held at constant temperature and imaged with the camera to obtain a calibration curve linking the incident radiation to the camera and the blackbody temperature. Practically a blackbody is made using a cavity with an aperture through which the camera can image. Radiation from the environment cannot enter the enclosure and therefore the effective emissivity of the opening is equal to unity.

As most surfaces are not ideal blackbodies, the temperature given by the camera is not equal to the object real temperature. When the emissivity of the surface, the environment temperature, and the transmission along the line of sight are known, the camera can correct for the reflection and transmission losses and provide a correct measure of the real temperature. If one of these parameters is non-uniform or not known, an in-situ calibration of the measurement chain is required. Figure 2.12 shows the entire radiometric chain with the different radiation fluxes and their modification due to the emissivity or transmission properties. The radiation captured by the camera is clearly a combination of fluxes in which the radiation coming from the object is a fraction.

The emissivity of a surface can be increased by painting it with a high emissivity paint. In the current project the black Nextel Velvet coating 811-21 manufactured by 3M is used. The properties of the paint have been quite extensively studied due to the common use of this paint for space related applications. In particular, the emissivity distribution over the LWIR wavelength range is shown in Fig. 2.13. The directional emissivity of this paint is shown in Fig. 2.13, and it can be noted that the emissivity drops dramatically after 70 degree. This will be a limiting factor for measurements on

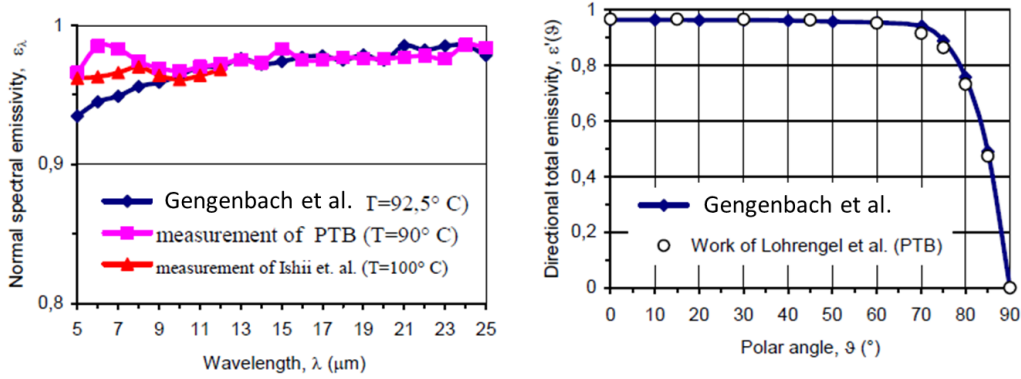


Figure 2.13: Left - Normal spectral emissivity of Nextel Velvet Coating measured normal to radiating surface. Right - Directional total emissivity of Nextel Velvet Coating measured at different emission angles. From Gengenbach et al. [30]

complex surface shapes. In fact the camera must be positioned accordingly to prevent the angle between the surface normal and the camera from exceeding this threshold.

## 2.1.2 Infrared thermography for heat transfer measurements

As we have seen in the previous section, an infrared imaging system can provide direct temperature measurements when used in combination with a very well known measurement setup or when a calibration is performed in-situ.

The convective heat flux from a fluid to a surface is expressed according to Eq. 2.8 where  $T$  is the temperature in the fluid and  $n$  is the normal to the surface.

$$q_{conv} = -k_{fluid} \frac{\partial T}{\partial n} \quad (2.8)$$

Due to the difficulty in experimental heat transfer to measure the gradient of temperature very close to the wall, the definition of convective heat flux using a heat transfer coefficient  $h$  and the difference between the wall temperature and a driving temperature is commonly used. The driving temperature used in this work is the adiabatic wall temperature as shown in Eq. 2.9.

$$q_{conv} = h(T_w - T_{ad}) \quad (2.9)$$

In a turbine stage the local recovery temperature is usually greatly varying due mainly to the large variation of flow Mach number. The use of a mainstream temperature or any mean temperature can be criticized. Moffat [66] discussed extensively the use of the adiabatic wall temperature in the definition of  $h$ . As mentioned in Moffat [66]: "It is an invariant descriptor of the convective process. Its values are a function of the geometry, the flow field, and the fluid properties."

The adiabatic wall temperature is also known in aerodynamics as the recovery temperature which is defined in Eq 2.10 where  $T_{stag}$  is the flow stagnation temperature,  $u_\infty$  the main flow velocity and  $r$  the recovery coefficient. On flat plate, the recovery coefficient is usually estimated using  $r = Pr^{1/2}$  in laminar cases and  $r = Pr^{1/3}$  for a turbulent boundary layer.

$$T_{ad} = T_r = T_{stag} - (1 - r) \frac{u_\infty^2}{2C_p} \quad (2.10)$$

The convective heat transfer coefficient and the adiabatic wall temperature  $T_{ad}$  are the parameters of interest in the current study. The measurements of the heat transfer coefficient is usually performed by setting the wall at a non-equilibrium state compared to the fluid flow and measuring its temperature. Knowing the wall temperature and the heat flux, the heat transfer coefficient can be deduced if the adiabatic wall temperature is known. On the other side the measurement of the adiabatic wall temperature can be directly performed using infrared imaging of a "sufficiently well" insulated wall. Obtaining both quantities often requires two geometrically identical test pieces made out of different material. The need to exchange the setup between tests and the risks of geometrically different setups is a drawback, as steps or gaps will affect the flow behavior and hence the results.

However the linearity of Eq. 2.9 and the fact that the heat transfer coefficient is independent of the boundary conditions have led to the use of two possible wall boundary conditions, isothermal or iso-energetic. In both cases an energy balance given in Eq. 2.11 is used. In fact, the convective heat flux is not measured directly but is calculated based on the known conduction heat flux and estimated radiation contribution.

$$q_{cond} + q_{conv} + q_{rad} = 0 \quad (2.11)$$

When two settings for the boundary conditions are used, two sets of values ( $T_{wall}, q_{conv}$ ) can be used in combination with Eq. 2.9 to solve for  $(h, T_{ad})$ . Two points are a minimum but multiple points can be used, and a linear fit is obtained through a least square method to provide both the heat transfer coefficient and the adiabatic wall temperature. The  $h$  value is the slope and the  $T_{ad}$  is the intercept with the x-axis. The design of an isothermal or iso-energetic setup is a critical part of the process to obtain high resolution data with a high accuracy. A brief description is made in the next paragraphs.

### Experimental setup using an iso-energetic condition

An iso-energetic boundary condition is achieved by a heater that generates an uniform heat flux  $q_{gen}$  using an electrical current circulating in a resistive material. The heater is usually composed of a resistive track made out of Platinum or Nickel based alloy (Inconel) sandwiched between two protective layers of polyimide films (Kapton). The different heat fluxes are then illustrated in Fig. 2.14. A variation of the current circulating in the circuit is then changing the value of  $q_{gen}$ , the surface temperature is changing accordingly, and

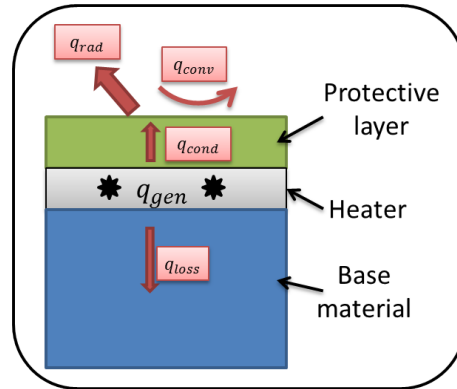


Figure 2.14: Details of the different heat fluxes generated involved a measurement setup with an iso-energetic boundary condition.

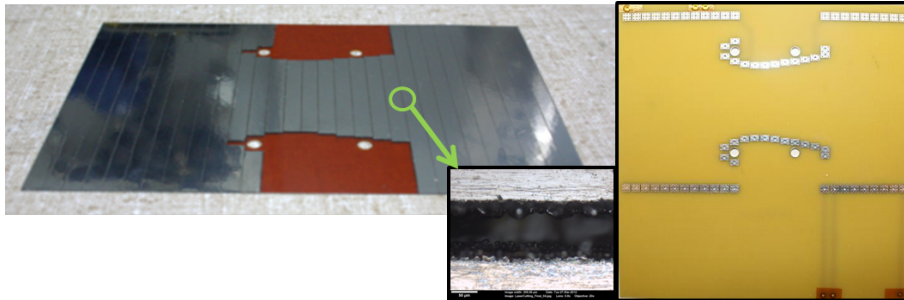


Figure 2.15: The left picture shows the Inconel sheet laminated with the Kapton substrate after the laser cutting process. The middle picture shows micrograph of the  $100\mu m$  cutting line obtained with laser cutting. On the right, the PCB supporting the heater is shown prior to the assembly.

the thermal quantities ( $h, T_{ad}$ ) can be calculated. The conduction losses leaving the heater at the back should be minimized using low thermally conductive materials and accounted for in the calculation process.

In parallel of the work performed using the isothermal setup, described in the next section, the iso-energetic configuration was studied and a setup was developed and manufactured at ETH Zurich by Chen [21]. An example of a heater manufactured during this project is shown in Fig. 2.15 and Fig. 2.16 shows a typical result obtained with this heater. More details on the heater manufacturing and the experiments are available in Chen [21]. The heater made in Inconel was attached to a low conductivity material (POM) followed by a "guard" manufactured in a thermally conductive material (Copper). The low conductive material reduces the conduction losses while the guard is used to make the temperature field uniform and provide a temperature measure to calculate the losses.



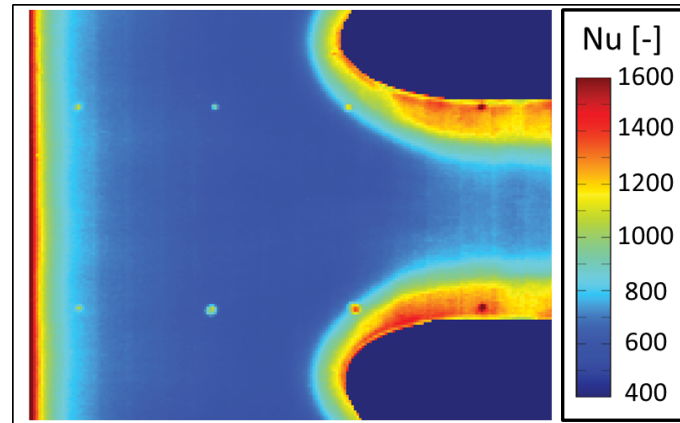


Figure 2.16: Measured Nusselt number distribution obtained using an iso-energetic boundary condition in the linear cascade installed in the Laval facility.

To summarize the pros and cons of this technique:

Pros:

- ease of use: require only a change of current
- short response time to a change in current: fast overall measurement time
- possibility to directly measure the adiabatic wall condition
- high resolution results

Cons/Limitations:

- can only provide wall conditions above mainstream temperature
- quantification of the conduction losses
- uniformity of heat flux requires strong tolerances on the heater track dimensions
- cannot be used to perform in-situ calibration of the infrared camera
- connection to the electrical network is critical (hot spots)

This boundary conditions was developed for future projects in parallel of the work described here but the isothermal setup already known and established in the Laboratory was preferred.

### Experimental setup using a quasi-isothermal condition

**Setup and governing equations** The Fig.2.17 illustrates the concept of the isothermal setup. Practically it is almost impossible to maintain the surface at a uniform temperature and measure the heat flux leaving by conduction, in combination to measurements at a high resolution. Multiple heaters controlled with thermocouples on their surface and with their power monitored were used in previous works but this reduces the resolution that can be achieved for the results.

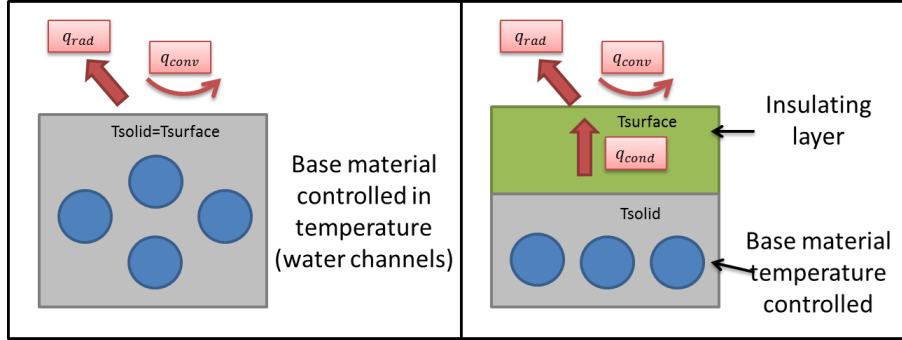


Figure 2.17: Details of the different heat fluxes involved in a measurement setup with an isothermal setup (left) and quasi isothermal boundary condition (right).

Therefore a quasi-isothermal approach described in Fig.2.17 is used in the present work. The isothermal condition is set and maintained below an insulating layer covering the surface. Practically the isothermal conditions is achieved using circulating water through a material with high thermal conductivity, namely copper in Chapter 3 or aluminum in Chapters 5 and 7. Due to the importance of the thermal layer in the calculation, the thermal conductivity and the thickness of this layer should be known accurately. Any uncertainty in the thermal resistance  $R_{th} = \frac{th_i}{k}$  is directly transferred to the accuracy in the heat transfer coefficient. A sheet of  $125\mu m$  polyimide material called Kapton and manufactured by Dupont is used and attached to the surface using 3M adhesive 200MP. The adhesive is used in sheet form to ensure an uniform thickness available. The top of the surface is coated with high emissivity paint 3M Nextel Velvet Coating to provide optimum conditions for infrared imaging.

The complete set of governing equations that is used to derive the heat transfer quantities from the measurements can be summarized as follows:

$$q_{cond} + q_{conv} + q_{rad} = 0 \quad (2.12)$$

$$q_{cond} = \left. \frac{k}{t} \right|_{eq} (T_w - T_{iso}) = \frac{(T_w - T_{iso})}{R_{th}} \quad (2.13)$$

$$q_{conv} = h(T_w - T_{ad}) \quad (2.14)$$

$$q_{rad} = \epsilon\sigma(T_w^4 - T_{amb}^4) \quad (2.15)$$

$$R_{th} = \sum_i \frac{t_i}{k_i} = \frac{t_{adh}}{k_{adh}} + \frac{t_{Kapton}}{k_{Kapton}} + \frac{t_{paint}}{k_{paint}} \quad (2.16)$$

The calculation of the heat transfer quantities is based on an energy balance at the top surface as presented in Eq. 2.12. At every plate temperature,  $T_{iso}$ , the measured surface temperature  $T_w$  is used as an input to a conduction model as illustrated in Eq. 2.13. In this expression, an equivalent term is used to account for the thermal resistance of the multilayer structure. The conduction model (either 1D for the flat endwall or 3D for the contoured endwall) uses the known material properties and thicknesses to calculate the

heat flux leaving the surface by conduction. The radiation term is simply evaluated using Eq. 2.15 and a measured ambient temperature in the wind tunnel. An internal study by Vidakovic [88] using the radiosity method and other similar studies, Baldauf et al. [9], showed that the estimation made with Eq. 2.15 and the calculated values represents less than 1% of the total heat flux on the surface. Multiple sets of data points ( $T_w, q_{conv}$ ) are finally obtained and a linear regression is used to deduce the heat transfer coefficient  $h$  and adiabatic wall temperature  $T_{ad}$  according to Eq. 2.14.

### Summary of measurement procedure

*Step1: Calibration* - The camera is calibrated in the absence of flow in the facility by setting the isothermal plate at different temperature levels and measuring the top surface temperature using the infrared camera.

*Step2: Measurements* - The solid temperature  $T_{iso}$  is set and maintained constant and uniform but modulating the power to the heating system and by monitoring the temperature using embedded sensors. The surface temperature  $T_w$  is then measured using the infrared camera device. When the measurements at one temperature are completed, the temperature is changed and the process is repeated for multiple temperatures.

*Step3: Data reduction* - The surface temperature and the solid temperature are used to obtain the conduction heat flux through the multilayer. The heat flux balance on the top surface provides then the convective heat flux. A linear regression is used at every surface point using the multiple conditions measured to derive the heat transfer quantities.

## 2.2 Image processing techniques

The use of a digital or an infrared camera allows data acquisition with a high resolution rapidly over large regions. But on the contrary to single point measurements where the location of the measurement device is known (hole, groove or any manufactured pocket), the image recorded by the camera does not contain any information on the location of every pixel. A geometrical calibration of the camera then provides then the needed relation between any point on the surface and its pixel coordinates in the image. This mathematical transformation between 3D and 2D euclidian coordinate systems is called a projection and the relationship between a point in the scene  $X = (X, Y, Z, T)$  and a point on the picture  $x = (u, v, w)$  is given by Eq. 2.17 where  $P_{3 \times 4}$  is the projection matrix. The next section describes a common model for a camera and how this is used to map the camera images onto the real surface.

$$\begin{pmatrix} u \\ v \\ w \end{pmatrix} = P_{3 \times 4} \begin{pmatrix} X \\ Y \\ Z \\ T \end{pmatrix} \quad (2.17)$$

It should be noted that homogeneous coordinates are used in this section to allow the representation of projection transformation as matrices. In  $\mathbb{R}^3$  a point is described as  $(X, Y, Z, 1)$  and in  $\mathbb{R}^2$  as  $(X, Y, 1)$

### 2.2.1 General model of a camera

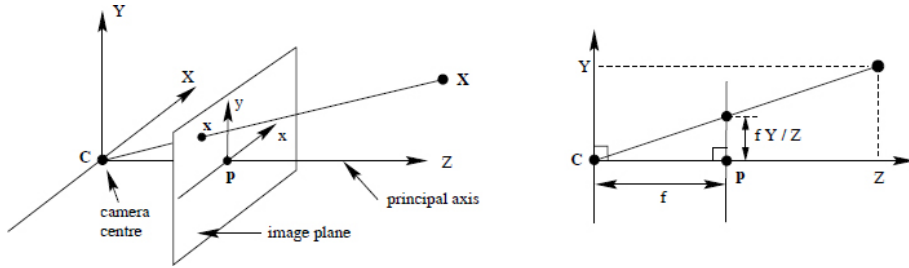


Figure 2.18: Description of the pinhole camera model and the projection principle. On the left isometric view, the projection of a point  $X$  on the image plane of the camera centered in  $C$  is shown. The left view explains the geometrical relationship using a side view of the scene.

The common model used in imaging to describe the behavior of a digital camera is the pin-hole camera model, on which different corrections (distortion) are added. This model describes the mathematical relationship between a 3D point in a scene and its projection onto the sensor of an ideal pin-hole camera. In the ideal camera model, no lens is used to focus the light and the aperture is a single point. Figure 2.18 illustrates the projection of point onto the image plane and shows the basic geometrical relationship associated. When the camera coordinate system and the world coordinate system are identical (same origin and axis aligned), the transformation matrix can be written as shown in Eq. 2.18.

$$\begin{pmatrix} u \\ v \\ w \end{pmatrix} = \begin{pmatrix} fX \\ fY \\ Z \end{pmatrix} = \begin{pmatrix} f & 0 & 0 & 0 \\ 0 & f & 0 & 0 \\ 0 & 0 & 1 & 0 \end{pmatrix} \begin{pmatrix} X \\ Y \\ Z \\ 1 \end{pmatrix} \quad (2.18)$$

The 2D planar coordinates of the projected point on the image plane ( $fX/Z, fY/Z$ ) can be retrieved by dividing the results of the matrix multiplication using the 3rd coordinate as a "scaling factor".

In real situation, the world and camera coordinate systems are not identical and a set of rotation  $R$  and translation  $t$  matrices is required to link them as shown in Eq. 2.19.

$$X_{camera} = R_{cam\_world}X_{world} + t_{cam\_world} \quad (2.19)$$

The final transformation matrix describing the pin-hole camera model is written in Eq. 2.20, where  $f$  is the camera focal distance,  $(p_x, p_y)$  the coordinates of the camera principal point,  $R = (r_{ij})$  the 3x3 rotation matrix and  $t = (t_x, t_y, t_z)$  describing the transformation between the camera and the world coordinates system.

$$x = KR[I | -C]X = \begin{pmatrix} f & 0 & p_x \\ 0 & f & p_y \\ 0 & 0 & 1 \end{pmatrix} R \begin{pmatrix} 1 & 0 & 0 & t_x \\ 0 & 1 & 0 & t_y \\ 0 & 0 & 1 & t_z \end{pmatrix} \quad (2.20)$$

The parameters used in the  $K$  matrix are only dependent of the camera and are called the internal parameters of the camera, whereas the parameters of  $(R, t)$  describes the camera location and attitude and are called the external parameters of the camera.

The formulation introduced in Eq. 2.20 can be completed to describe a real camera by adding skew, scaling factors (if pixels are not squared), distortion effect,... The matrix  $K$  on the left hand side will then become a full 3x3 matrix with 9 unknowns.

### 2.2.2 Calculation of the camera matrix

When a number  $N$  of correspondence  $x_i \mapsto X_i$  between the image point  $x_i$  and the 3D point  $X_i$  are known,  $N$  linear equations can be written according to Eq. 2.20. If all the equations are combined, the linear system of equation can be rewritten as Eq. 2.21 where the 3x4 projection matrix is written as  $P = (p_{ij})$ .

$$AP = \begin{pmatrix} x & y & z & 1 & 0 & 0 & 0 & -ux & -uy & -uz & -u \\ 0 & 0 & 0 & 0 & x & y & z & -vx & -vy & -vz & -v \end{pmatrix} \begin{pmatrix} p_{1,1} \\ \vdots \\ p_{3,4} \end{pmatrix} = 0 \quad (2.21)$$

The minimum number of points required to solve the system is 6 since each point correspondence leads to only 2 equations. This system can then be solved for  $P$  using a Singular Value Decomposition (SVD). The unit vector corresponding to the smallest singular value is the solution of the system. This procedure to obtain the transformation matrix is also called the Direct Linear Transformation algorithm.

A camera transformation matrix must be calculated for every position of the camera or focus settings. However according to the camera model described previously, for a camera with fixed focus the internal parameters remains the same and only the external parameters should be determined. This additional constraint is commonly used when imaging a scene from different locations with identical cameras.

In the present project, the camera was used with constant focus settings to position the robot and camera relative to the measurement facility as explained in section 2.2.5 but during the measurements the focusing was adjusted at every camera position to ensure the quality of the data and a camera transformation was calculated therefore at every location.

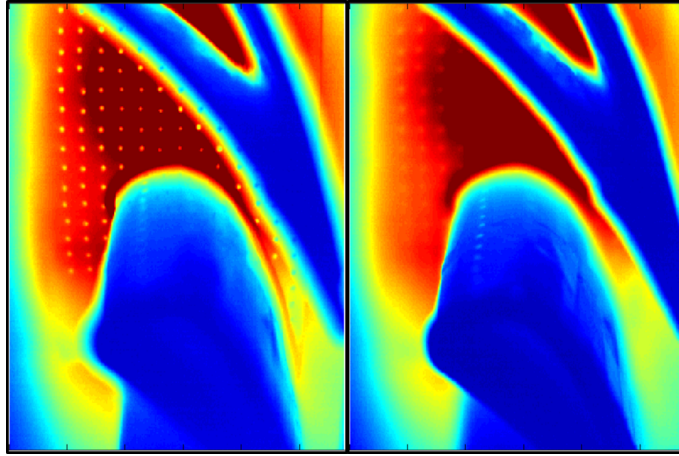


Figure 2.19: Thermograms of a vane (cold - in blue) endwall (hot - in red) scene acquired on a test bench with different focus settings. On the left the endwall is in focus while on the right the focus is made on one of the points on the vane surface.

### 2.2.3 Blurring and focusing of the camera

An infrared imaging system is usually designed to be able to capture a maximum amount of radiation coming from a scene. Therefore the aperture  $N = f/D$  of such a system is important:  $f/1$  for bolometers and  $f/2$  for cooled systems are the most common value used. One disadvantage of such a wide aperture system is the reduced depth of field (DOF), which is the distance between the farthest and closest object that can be considered "in-focus". The in-focus judgment is very subjective and often related to the circle of confusion parameter which is on the order of the sensor pixel size in infrared imaging. The formula used to estimate the depth of field for moderate to large camera to object distances is shown below, Eq. 2.22. This equation shows that when  $N$  is reducing, DOF is also reducing.

$$DOF = \frac{2Nc^2f^2s^2}{f^4 - N^2c^2s^2} \quad (2.22)$$

where:  $f$ : focal distance

$N$ : aperture number

$c$ : circle of confusion diameter

$s$ : distance camera to object

For the current camera, the depth of field determined experimentally is around 10mm for an object at a distance of 200mm and 26mm at 300mm.

A typical example of an object out of focus in thermography is shown in Fig. 2.19. It can be seen that the temperature field is affected by the elements that are out of focus, the temperature gradients are reduced or seen as "blurred". Due to the reduced depth of field of the camera, the field of view is also reduced by edges that are located between the camera and the endwall. In the left image of Fig. 2.19, the endwall close to the top vane is not accessible as the dots closest to the vane are within a temperature gradient, in fact

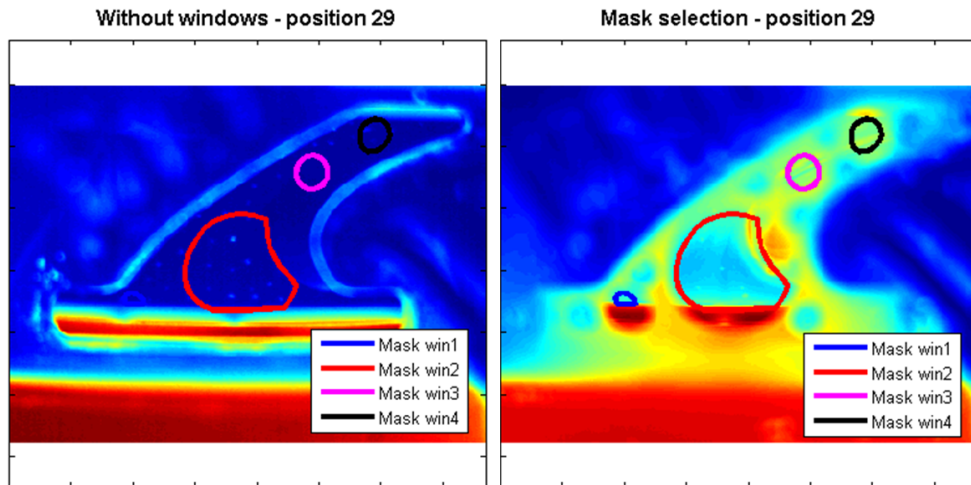


Figure 2.20: Thermograms acquired for the K2 case with cylindrical endwall. The two images are acquired at one camera position before the installation of the window (left) and after (right). The lines delimit the selected area for the data reduction procedure.

the vane tip edge disturbs the view. Therefore in order to focus the camera on the surface, sharp temperature gradients need to be present on the target surface. These gradients could be created by changing locally the temperature by heating the surface with a laser (spot or line) or by modifying the surface emissivity. The infrared markers used in this work are locally changing the emissivity of the surface. This change is achieved by placing little pieces of aluminum tape on the surface (temporary markers), by making dots using silver ink pen (permanent markers), by machining out the paint on an aluminum part coated with high emissivity paint, or finally using a black painted mask with a matrix of holes placed on top of an aluminum part. These four ways of creating emissivity contrasts have been used on calibration targets or on the measurement platform in this project.

The parts of the image out-of-focus are excluded from the final results since the temperature sensed reflects a superposition of the background radiation and the radiation coming from the out-of-focus element. Masks are defined manually to exclude the parts of the image where the holder is and where the edge around the windows create blurring. Figure 2.20 shows on the left the infrared image taken before the windows are installed and on the right hand side after the installation is completed. The limited access to the endwall when windows are used is clearly seen when comparing these two images. The superposed lines delimit the part of the image that is considered acceptable and usable for the data reduction. It is essential to correctly select the masks otherwise data outside of the region of interest can superpose with endwall data and corrupt the averaging from multiple views.

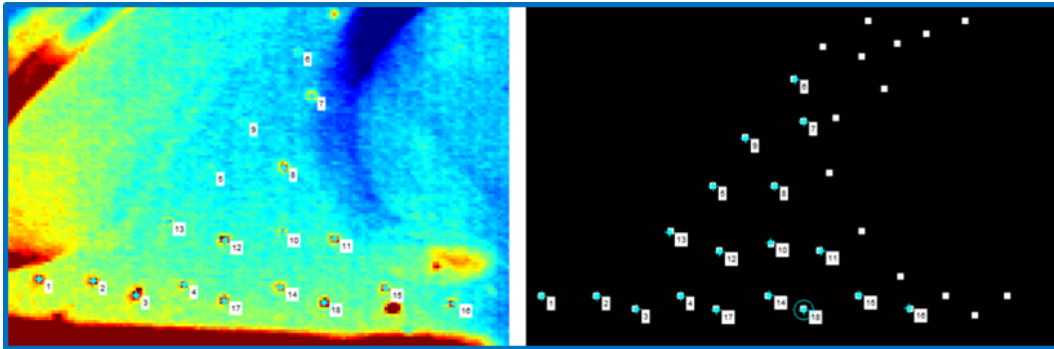


Figure 2.21: Manual selection of the corresponding points: IR picture (left) and reference picture (right)

#### 2.2.4 Complete passage reconstruction.

Due to the geometry of the configuration tested and the different limitations due to the camera (blurring, short depth of focus), multiple camera positions are required to provide a complete map of temperature on the endwall. For every camera position, a succession of operation is performed:

- manual selection of corresponding pair of points between the infrared image and a reference image, Fig. 2.21
- calculation of the geometrical calibration is performed
- interpolation of the measured temperature onto the projection of the fine endwall mesh, Fig. 2.22
- filtering of the image is made using mask(s), Fig. 2.20

When this process is finished, the complete passage can be reconstructed using an averaging of all the images acquired. The endwall mesh is kept the same for all the camera position and serves as a reference for the averaging. At every point on the endwall, data from 2 to X camera positions are available and averaged. The number of points used for averaging in the cylindrical endwall measurements is shown in Fig. 2.23. The number corresponds to the count of camera positions providing data at this location.

The geometrical calibration and reconstruction procedure was developed and validated using a test bench shown in Fig. 2.25. A surface of the same radius as the turbine endwall is covered with a thin steel layer painted in black, creating a dot pattern visible with the infrared camera when the support is heated using an infrared lamp. Infrared pictures were acquired with the camera at different location, and a complete image of the passage could be assembled, as shown in Fig. 2.25. More advanced technique to match pair of points (Shapiro & Brady, Scott and Longuet-Higgins algorithms) have been tested but always failed in associating a certain number of points. A "brute force" method based on the selection of only 4 points (without correspondence) in the image and the iterative calculation of projective transformation and association using closest



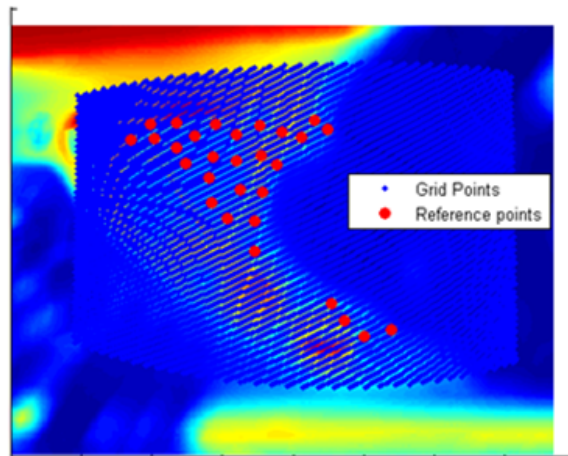


Figure 2.22: Projected endwall mesh (blue dots) onto the infrared picture for data interpolation. The red dots correspond to the infrared marker used to defined the projection matrix.

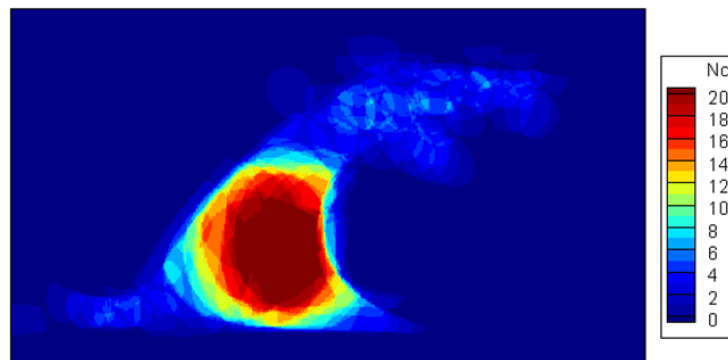


Figure 2.23: Number of points used for the averaging during the passage reconstruction.

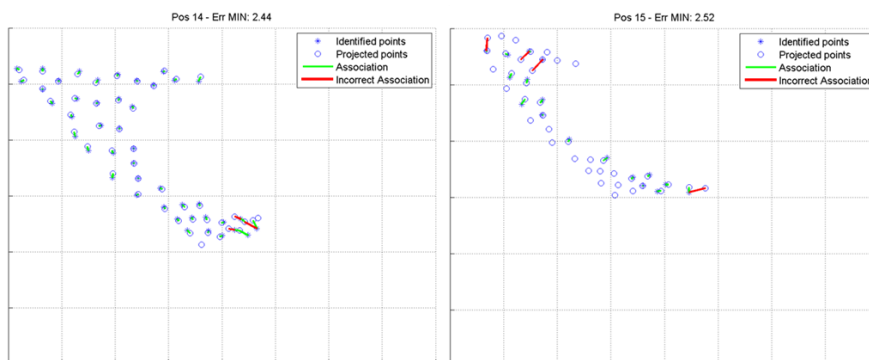


Figure 2.24: Example of points pairing result for two camera positions. The correct pairs are linked with green lines while the red lines show the incorrect ones.

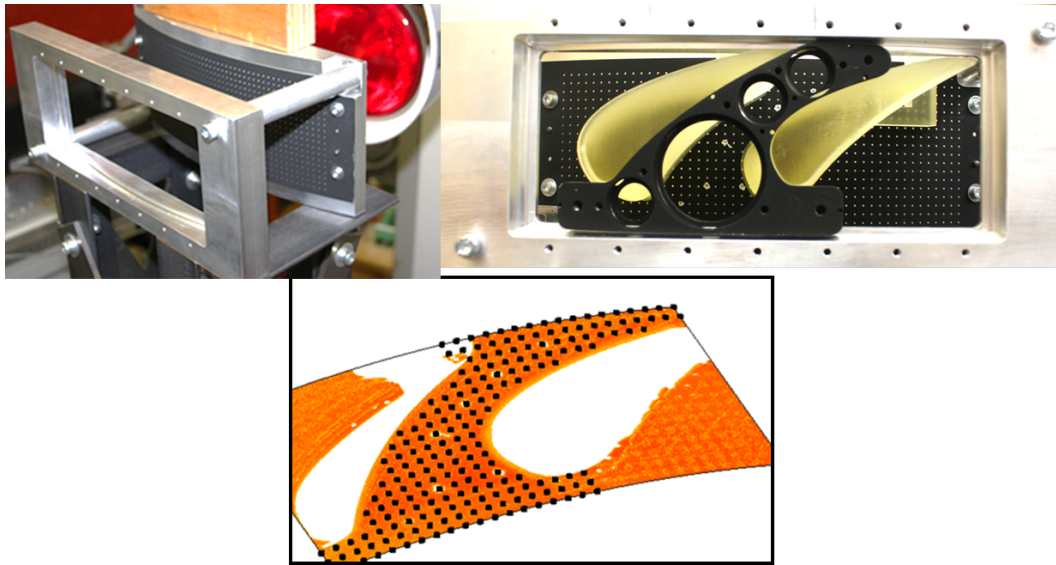


Figure 2.25: Demonstration of the geometrical calibration procedure on a test bench. Test bench composed of a cylindrical surface with infrared markers (left). Results of the passage reconstruction procedure (right).

point methods (ICP algorithm) provided better results. However it still missed certain association (see Fig. 2.24) either close to the edges or because of a configuration close to a singular case (points aligned,...), which required manual re-processing. As the technique is not 100% reliable, the manual selection of the corresponding points was preferred.

### 2.2.5 Use of images as a measurement or a positioning tool

The theory of the camera model explained in the previous sections is used in different ways in the current work. In fact high resolution digital images are used to obtain the position of infrared markers with a high accuracy, while infrared images of a known calibration target are used to obtain the camera and robot positions.

#### Processing of digital pictures to extract precise locations of infrared markers

When aluminum tape or silver ink markers are used, they are positioned manually on the surface and, depending on the accessibility of the surface, their exact location is unknown. The measurement of their location becomes non trivial when those markers are positioned in the middle of a stator passage on a curved surface. A procedure based on image registration technique is developed and used as follows:

- place the marker on the surface
- take high resolution digital pictures of the complete platform, maximizing the presence of reference points in the field of view

- establish the correspondence between known points in the picture and points in reality, for example from CAD model
- calculate the preliminary transformation matrix as described in section 2.2.2
- select points on edges in the picture corresponding to known edges from the CAD
- iteratively refine the transformation by minimizing the re-projection error of the selected points on edges
- extract a fine mesh of the surface of interest (CAD model) where the infrared markers are located
- calculate the 3D coordinates of the infrared markers based on the projection of the fine mesh of the surface in the image

Figure 2.26 shows the superposition of the digital image and points (red) and lines (blue) known from the CAD that are projected using the calculated projection transformation. Multiple pictures are processed to obtain overlapping information on the infrared markers positioned on the endwall.

The result of this procedure is presented in Fig. 2.27. The infrared markers position have been calculated using the pictures shown in Fig. 2.26 and are shown on top of the contoured endwall geometry.

With an appropriate choice of reference points (holes, edges, corners) and by using multiple images, the 3D position of the infrared markers can be recovered with a precision of 0.3mm. The quantification of the error is made by using this method to calculate the position of the dots on the reference target shown in Fig. 2.25.

### **Infrared calibration target and robot positioning**

Another application is the calculation of the camera position relative to the surface of interest. In fact, in order to access the complete endwall, multiple camera position and orientation are selected from ray tracing simulations or from the CAD model of the platform. However these camera positions are known in the target coordinate system only, which is generally not aligned with the world coordinate system where the traversing system is manipulating the camera. The transformation between these two systems is required.

The camera location is this time obtained by imaging a reference target with the camera at multiple locations and orientation while the focus setting is not changed. Again the use of correspondence between points on the target and their infrared image provides the set of linear equations required to obtain the transformation for every image. As multiple images of the same target with the same camera parameters are used, the internal parameters of the camera are calculated and more informations can be extracted. In particular, the camera location is now accessible. These calculations are based on scripts from the camera calibration toolbox developed for Matlab by J-Y Bouquet [18].

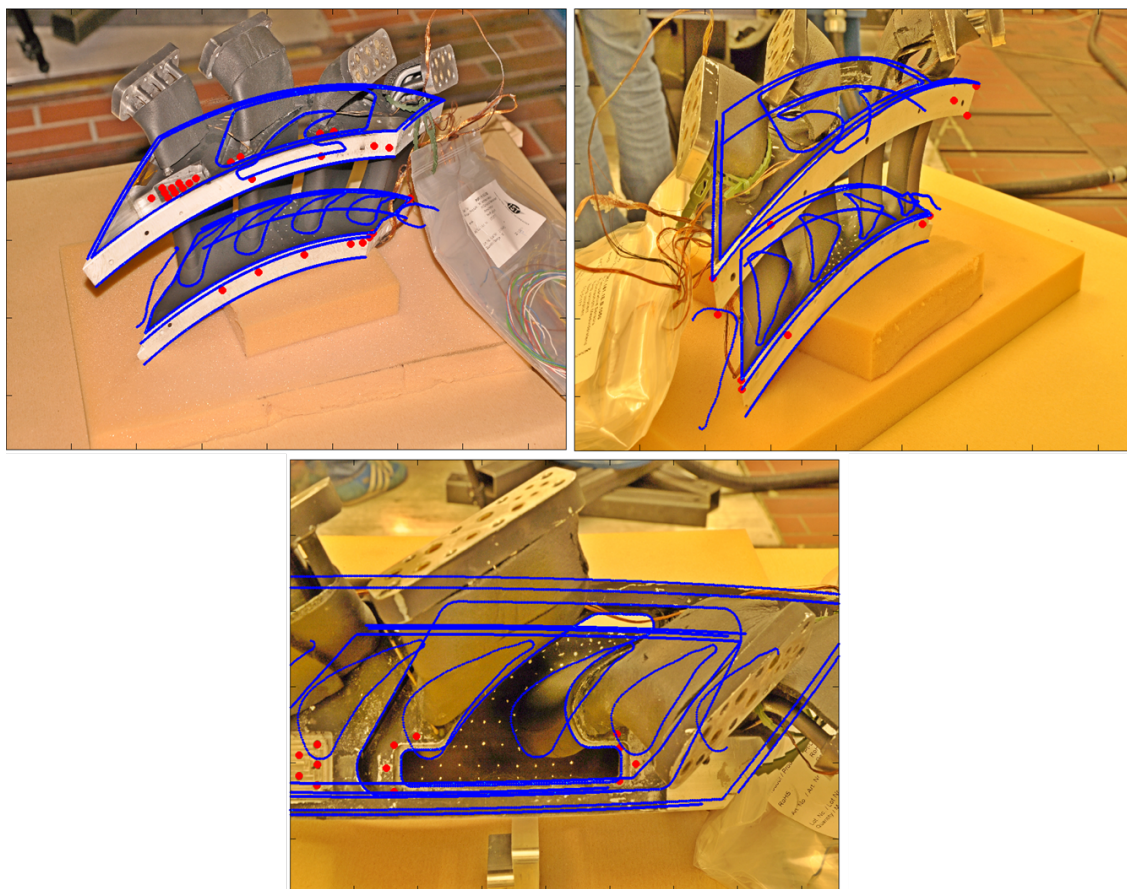


Figure 2.26: Illustration of the infrared markers reconstruction procedure with the calculation of projective transformation for multiple digital pictures focused on the inlet (top left), outlet (top right) parts of the passage or for a top view (bottom).

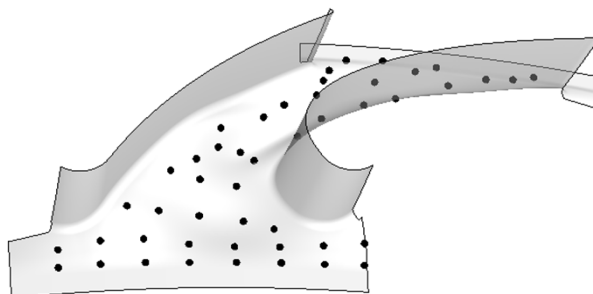


Figure 2.27: Reconstructed infrared markers on top of the contoured endwall geometry.

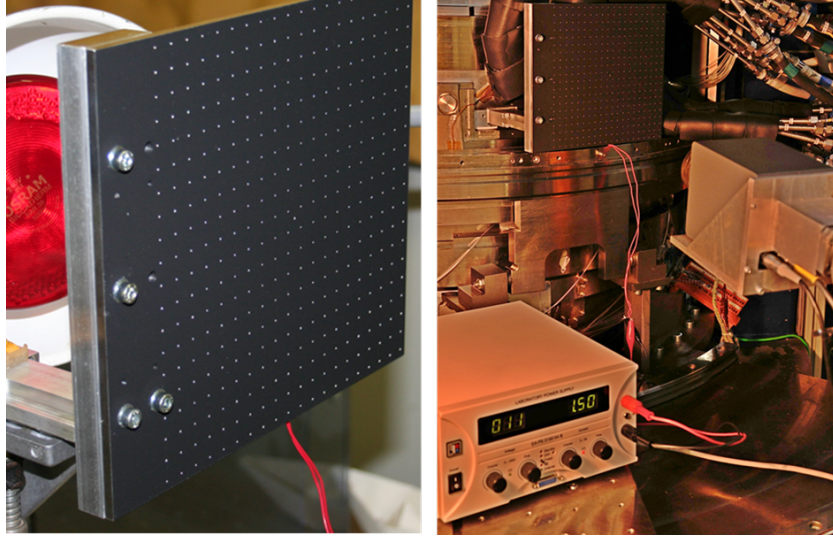


Figure 2.28: Infrared target plate (left) and mounted on the heat transfer platform (right) with the power supply and the infrared camera.

Figure 2.28 shows the infrared target mounted on the heat transfer platform for the positioning of the robot. The target is a plate with a 10x10mm dot patterns covering an 200x200mm area. The dot pattern is created by painting the 5mm thick aluminum plate with high emissivity paint and then machine the dot pattern by removing 0.1mm aluminum and the paint. At the back of the plate a thin film heater (manufactured by Minco) is mounted and powered with a DC power supply to heat the plate and ensure a proper contrast in the infrared pictures.

The procedure is divided in two steps, a first set of pictures captured by manually traversing the robot and camera is used to calculate a preliminary coordinate transformation matrix and define another list of camera position. This step covers a wide range of camera angle (yaw, pitch and roll). The second list of camera position includes incremental variation of pitch and yaw angles of the camera, as well as translations to ensure a more accurate calculation of the coordinate transformation.

Figure 2.29 shows the automated identification of points in the infrared image, corresponding to the markers on the infrared target. The right part of the picture shows the calculated location of the camera relative to the target. Combined with the known camera location  $(x_0, y_0, z_0)$  and orientation  $rot_{03} = f(\alpha, \beta, \gamma)$  in the robot frame of reference, shown in Fig. 2.30, the link between the platform coordinate system  $\mathbb{R}^4 = (x_4, y_4, z_4)$  and the robot coordinate  $\mathbb{R}^0$  system described in Eq. 2.23 is derived.

$$\begin{pmatrix} x_0 \\ y_0 \\ z_0 \end{pmatrix}_{R0} + rot_{03} \begin{pmatrix} OC_x \\ OC_y \\ OC_z \end{pmatrix}_{R3} = rot_{03} \left[ rot_{34} \begin{pmatrix} x_4 \\ y_4 \\ z_4 \end{pmatrix}_{R4} + t_{34} \right] \quad (2.23)$$



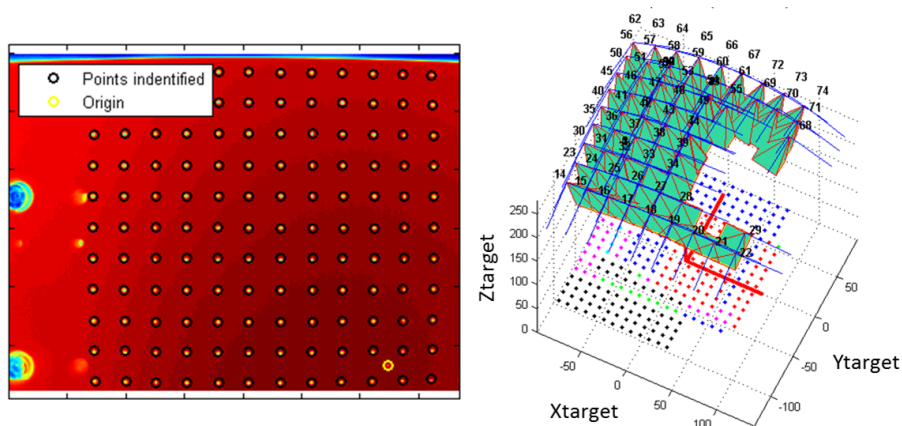


Figure 2.29: Identification of the reference points in the infrared picture of the target (left). Calculated position of the camera relative to the infrared target.

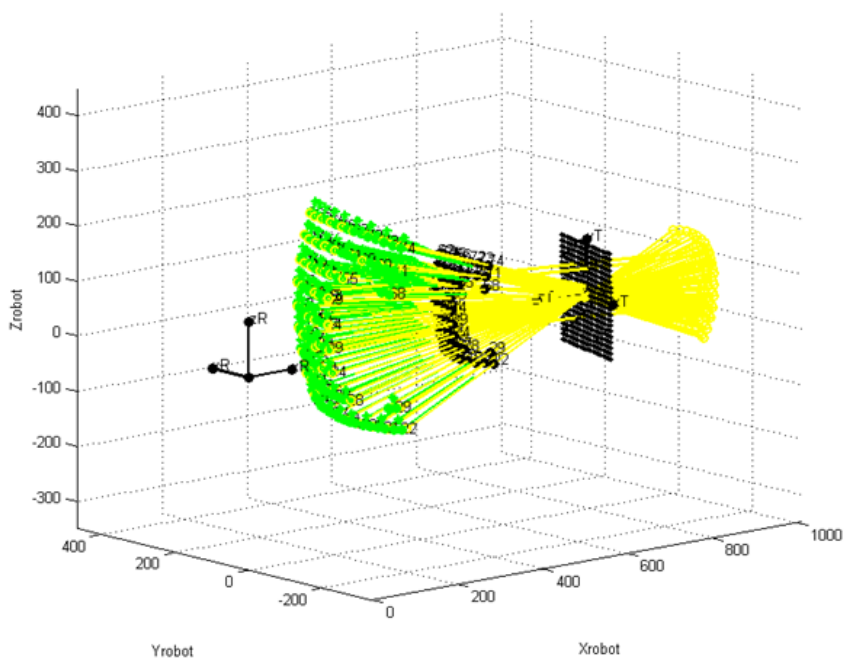


Figure 2.30: Calculated position of the camera relative to the robot world coordinate system.

# Chapter 3

## Experimental investigation of heat transfer on the endwall of a linear cascade with symmetric airfoils.

The heat transfer measurement technique was already established in the Laboratory but mainly applied to film cooling performance measurements [6, 52]. In order to perform similar measurements in the axial turbine facility LISA, multiple improvements had to be gradually introduced to reduce the risks. The first step targets the improvement of the the measurement know-how by installing a similar configuration in the controlled environment of the LAVAL facility and bounds the uncertainty of future measurements in LISA.

This chapter will therefore introduce the wind tunnel and the geometry tested, then describe the specific data acquisition and data reduction technique before presenting the results and a comparison to CFD predictions. The measurements of heat transfer quantities are performed on two different endwall configuration, a flat case and a contoured case. The shaped endwall design is derived from existing turbine design but adapted to a linear cascade.

### 3.1 Experimental facility LAVAL

#### 3.1.1 Description of the wind tunnel

The preliminary work was preformed in a subsonic closed loop wind tunnel named LAVAL and used for heat transfer experiments [13, 5, 52] but also for detailed flow analysis [7]. The main flow is delivered by a 250 kW centrifugal compressor to a water-air heat exchanger that sets the flow temperature and maintains it constant. After a series of piping and flow measuring devices (flow meter, temperature, pressure), the air passes through a steam/air heat exchanger capable of heating the mainstream up to 120degC

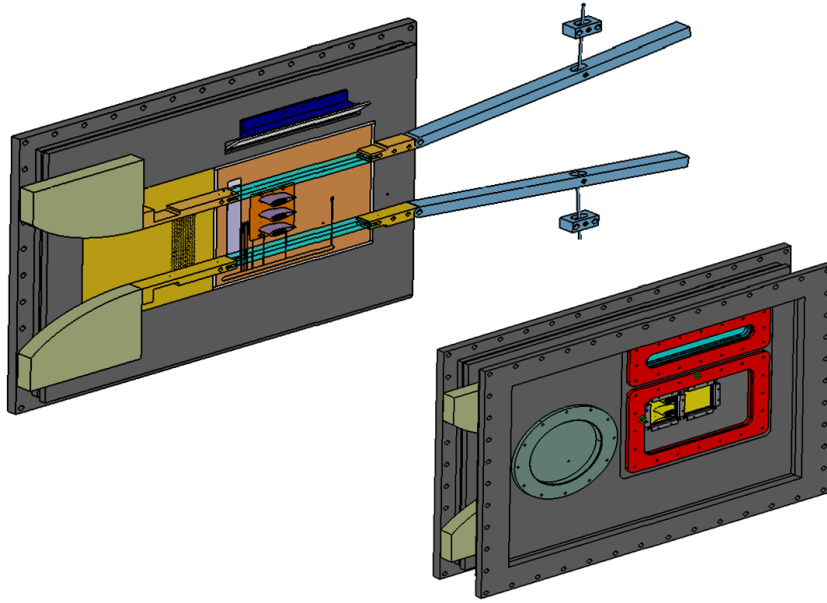


Figure 3.1: CAD view of the inside of the rig (top) with the contraction, the test section and the diffuser. The bottom picture shows the modular front plate on which the infrared windows are shown assembled.

(not used in the present study). The flow continues then through a flow straightener before undergoing an acceleration through a 3D nozzle and then a 2D Laval nozzle ensuring uniform inlet flow conditions. A suction arrangement, installed upstream of the test section plate, controls the thickness of the incoming boundary layer. The suction is driven by a centrifugal blower, extracting air through a dense array of discrete holes stacked over an area of 60x180 mm and feeding it back into the loop downstream of the test section. A schematic of the equipments is shown in Fig. 3.2. The test section is a rectangular flow path with a cross section of 40x181 mm where heat transfer studies or detailed flow analysis using intrusive (aerodynamic probes) or non-intrusive (Particle Image Velocimetry) techniques can be performed. The air then leaves the test section through a 2D diffuser leading to a water-air heat exchanger capable of cooling the fluid back to 30degC and returning it back to the compressor. A CAD view of the inside of the facility is shown in Fig. 3.1

### Flow conditions

The flow pressure and temperature are measured at multiple locations along the flow path which permits real time monitoring of the flow conditions within the rig, as shown in Fig. 3.2. The pressure measurements are performed using a 16 differential channels PSI module and the temperature data are acquired using PT100 probes connected to a PCI6033E National Instrument card. The monitoring and logging of the operating



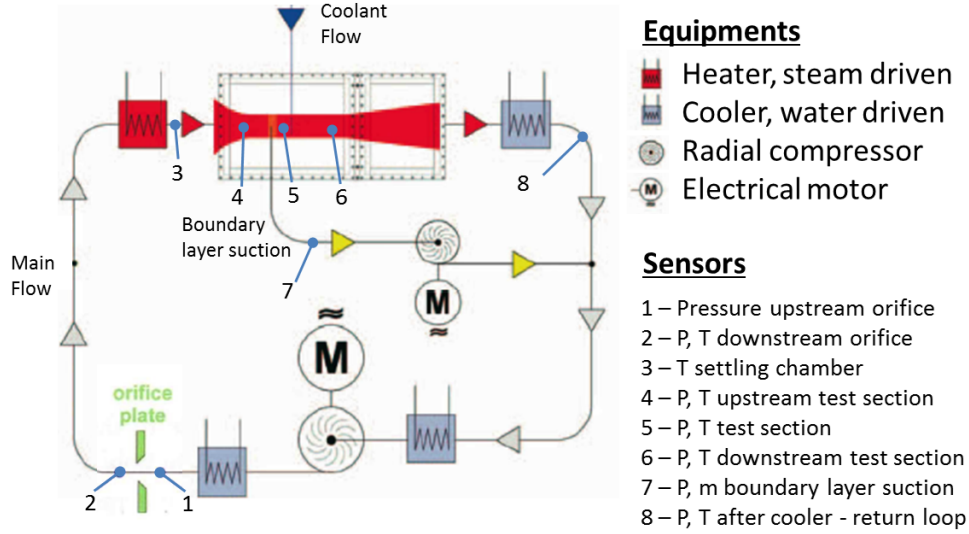


Figure 3.2: Schematic of the different air flows and equipment in the LAVAL facility. The location and type of sensors present along the flow path are also shown with blue dots.

conditions is achieved through a LabView program collecting data from all the sensors within the loop via the acquisition devices.

The main mass flow  $\dot{m}_m$  is measured using temperature and differential pressure measurements across a calibrated orifice plate located in a straight section of the piping allowing fully developed flow conditions. The air mass flow collected through the boundary layer suction arrangement is deduced from the measured flow rate coming from the compressor to obtain the mass flow entering the test section. This secondary mass flow is measured using a thermal mass flow meter (Ecoflow) using convective heat transfer as a measurement principle. The inlet flow velocity is then calculated using Eq. 3.1 in which the density and speed of sound are calculated based on the flow temperature measured by a PT100 and static pressure taps located just upstream of the test section.

$$M = \frac{u_m}{a} = \frac{\dot{m}_m}{A_m \rho_m \sqrt{\gamma RT}} \quad (3.1)$$

### Modular test section

The front wall is composed of a steel frame on which various types of windows can be mounted depending on the measurements:

- a steel frame holding two infrared transparent windows made of Zinc Selenide for infrared thermography
- a Plexiglas window used as an optical access for PIV measurements
- a Plexiglas window with discrete access ports to insert pneumatic or time resolved aerodynamic probes (Frap and FENT)

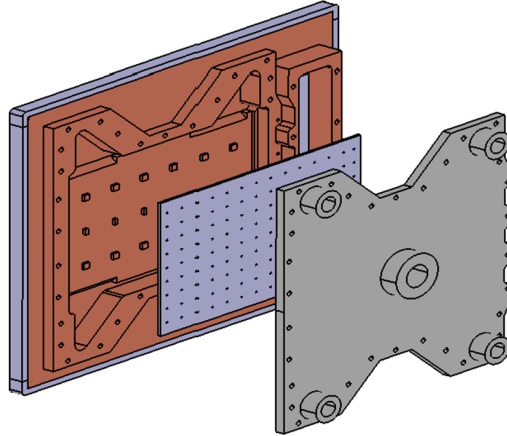


Figure 3.3: Exploded CAD view of the isothermal plate with the thick copper plate (orange), the impingement plate with holes (blue) and a back aluminum plate (grey) with the connections to the water network.

- a circle in circle system allowing high resolution probe measurements over the complete test section (multiple planes can be scanned)

The back surface is also a steel panel that can be equipped with different back plates. The present configuration is composed of a thick copper plate that is thermally managed to provide quasi-isothermal boundary conditions for heat transfer measurements. This condition is created using circulating water impinging at the back of the plate. The water is injected in the center of the plate and a plate composed of 10x15 2mm diameter holes split the flow in multiple jets. The design and manufacturing shown in Fig. 3.3 was handled by Bernsdorf [13].

Multiple miniature PT100 sensors are mounted on the surface of the plate at different downstream location along the flow path. The sensors are fed with a 1mA current provided by a NI PCI 4351 card which is also used to record their signal. The sensors are manufactured by IST AG and have an overall size of 1.6x1.2x0.8 mm. They are embedded in trenches using high thermally conductive glue (Electrolube TBS20S with  $k = 0.9W/m/K$ ). These sensors allow the monitoring of the plate temperature used as a feedback for the water temperature control, but they are also used to account for non-optimum isothermal conditions. In fact the lateral conduction observed close to the edges of the plate affects the accuracy of the heat transfer measurements and can effectively be corrected using the temperature profile measured by the sensors.

**Calibration oven** The calibration of the temperature sensors embedded in the measurement platforms is performed in a well controlled environment using a calibration oven (Binder 115L). The large volume of the oven (60x48x41cm) allows the calibration of large parts such as the copper plate used to provide the thermal boundary condition in

LAVAL. The temperature calibration are performed by setting stabilized known temperature steps in the oven and acquire the output of the sensors The complete measurement chain used for the experiments is used also for the calibration to acquire the data and ensure highly accurate calibration. The oven operation is controlled via a LabView program, therefore the calibration procedure is automated and multiple cycles including many temperature steps are used.

### 3.1.2 Water network

The water network is a closed loop that can circulate water to both the LAVAL and LISA facilities. According to the characteristics of the pump, it can provide up to 10m head at a flow rate of  $2m^3/h$ , or 2m head at  $10m^3/h$ . A 80kW heater is used to heat the water up to 90degC. In order to achieve high stability of the water temperature, the electrical power delivered to the heater is controlled by a semi-conducting relay (Carlo Gavazzi - RZ3A60D75P) commanded by a Pulse Width Modulated (PWM) signal delivered by a counter output of a National Instruments card (NI PCI 6033E). The signal has a constant frequency of 1Hz but its duty cycle is controlled by a software-based PID regulator. The target temperature is set by the operator while the feedback temperature is a water temperature that can be the loop temperature measured using a Jumo PT100, or the solid temperature in the area of interest allowing a faster response time. For the experiments performed in LAVAL the temperature used is an average of the temperature measured on top of the copper plate using the miniature PT100.

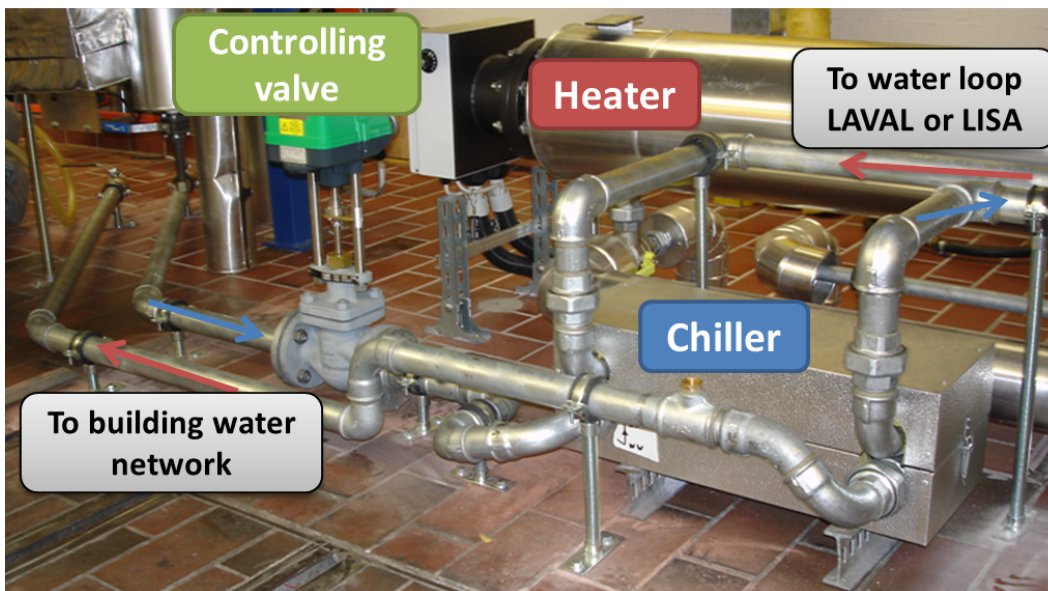


Figure 3.4: Picture of the electrical heater and water chiller installed controlling the water loop temperature circulating in LAVAL or LISA.

Figure 3.4 shows the heater and chiller installed in LAVAL. Downstream of the circulating pump a water-water plate chiller is installed to allow temperatures below the mainstream temperature. The 40kW heat exchanger is connected to the building cooling water loop, supplying a maximum of 20m<sup>3</sup>/h of 14degC water. A regulation valve controlled electronically sets the cold water flow rate through the secondary loop. The control of the valve and monitoring of the temperature in the loop are achieved using a NI USB 6008 card. An analog output is used to generate the voltage controlling the valve position. And the temperatures at the inlet and outlet are measured using Jumo PT100 fed by a 1mA custom made current source and connected to two analog inputs of the card.

Two manual 3-way valves are used to divert the flow and bypass the chiller to reduce the water head loss and ensure higher flow rate through the loop when needed. Another set of manual 3way valves are used to direct the flow to the LAVAL test section or to equipments located in the LISA facility.

### 3.1.3 Traversing system

As described in a previous section, the test section can be accessed using multiple measuring devices such as a camera or aerodynamic probes. The traversing of these devices is performed using two distinct traversing systems:

- a system with 3 linear traversable axis manufactured by ISEL allowing movements in a 800x800x600mm volume
- a probe traversing system composed of a yaw axis and a 300mm linear axis that are assembled in-house

Both systems can be controlled by a LabView program allowing automated traversing following a list of position provided in a task file.

For the measurements performed in this project the 2 systems were combined to offer a 4 axis system (x,y,z and yaw) to manipulate the infrared camera. The camera could therefore acquire data on the surface at different locations and with different view angle to the surface. The two controlling software were also integrated in a single LabView program controlling the complete system and ensuring a complete automation of the traversing tasks.

### 3.1.4 Setup for heat transfer measurements

For the heat transfer measurements the isothermal plate located in the test section is covered with a multilayer composed of a painted Kapton layer (Dupont Kapton 500HN) attached to the surface using an adhesive sheet (3M pressure sensitive acrylic adhesive 200MP). A high emissivity black paint (3M Nextel Velvet Coating 811-21) is used to enhance the surface emissivity for accurate infrared thermography. The thicknesses and thermal properties of the different layers are summarized in the table ....

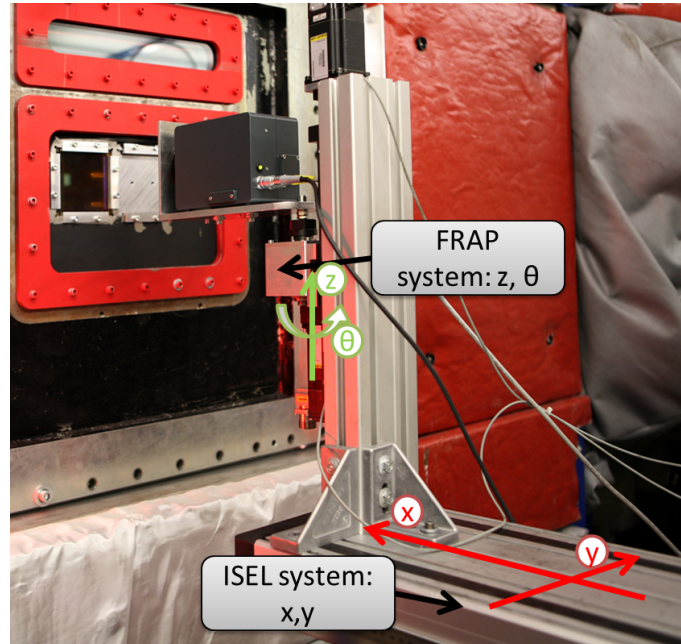


Figure 3.5: Infrared camera mounted on the combination of the traversing systems, allowing movements in  $(x, y, z, \theta)$ .

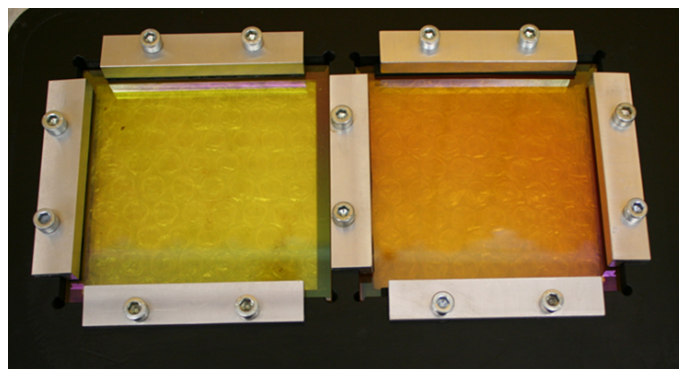


Figure 3.6: Infrared transparent windows mounted on the steel holder before assembly of the rig front panel. The two windows are made out of Zinc Selenide but were manufactured at different time.

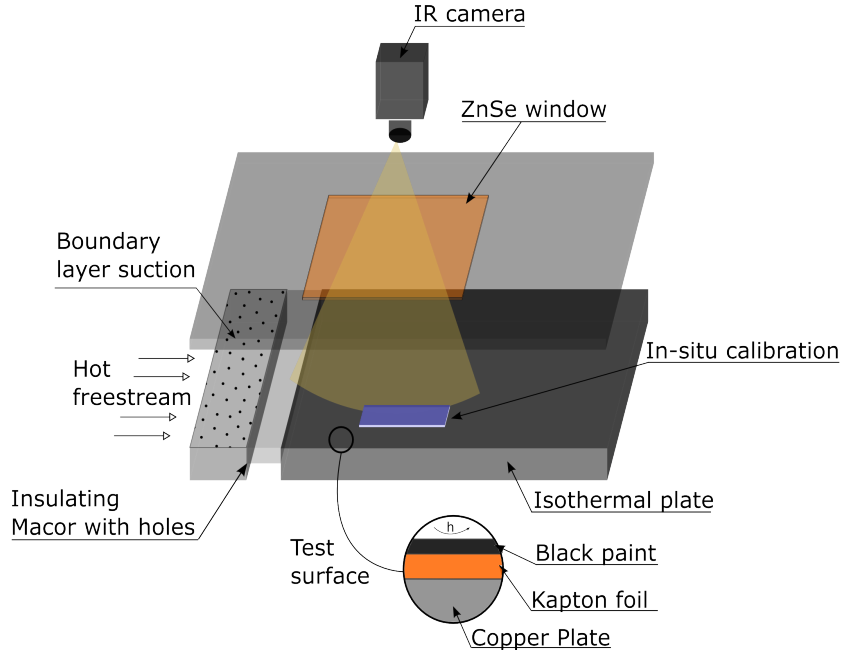


Figure 3.7: Test section configuration for heat transfer measurements.

The front panel is equipped with infrared transparent windows made out of Zinc Selenide (ZnSe) coated with an anti-reflective coating to enhance their transmission capabilities. Figure 3.6 shows the two 100x100mm windows assembled on the steel holder before the assembly on the rig front panel. The color difference is due to a change in the manufacturing process to enhance the transmission properties in the visible, the properties in the infrared remains however the same. The relatively poor mechanical properties and the cost of Zinc Selenide prevent the use of large windows, the test area is therefore observed through two different view ports. The windows are mounted on a steel frame to match the thermal expansion factor, itself assembled on the front panel. Safety guards are installed during the assembly procedure to reduce the risk of dropping or damaging the windows.

## 3.2 Linear cascade geometry

For the current study a linear cascade composed of three symmetric NACA 0025 airfoils is installed in the test section as shown in Fig. 3.10. The airfoils have an axial chord  $C_{ax}$  of 70 mm and the pitch is 45 mm. The side walls are kept straight and therefore only the periodicity of the middle vane is ensured. The airfoils are made out of POM plastic and they are directly mounted on the copper plate (CaseA: flat case) or on a thick copper insert that is either flat (Case B: flat Insert) or shaped (CaseC: contoured) for the contoured endwall. Figure 3.8 illustrates the difference between the cases. The inserts are mounted in a pocket machined into the thick copper plate with a thin layer



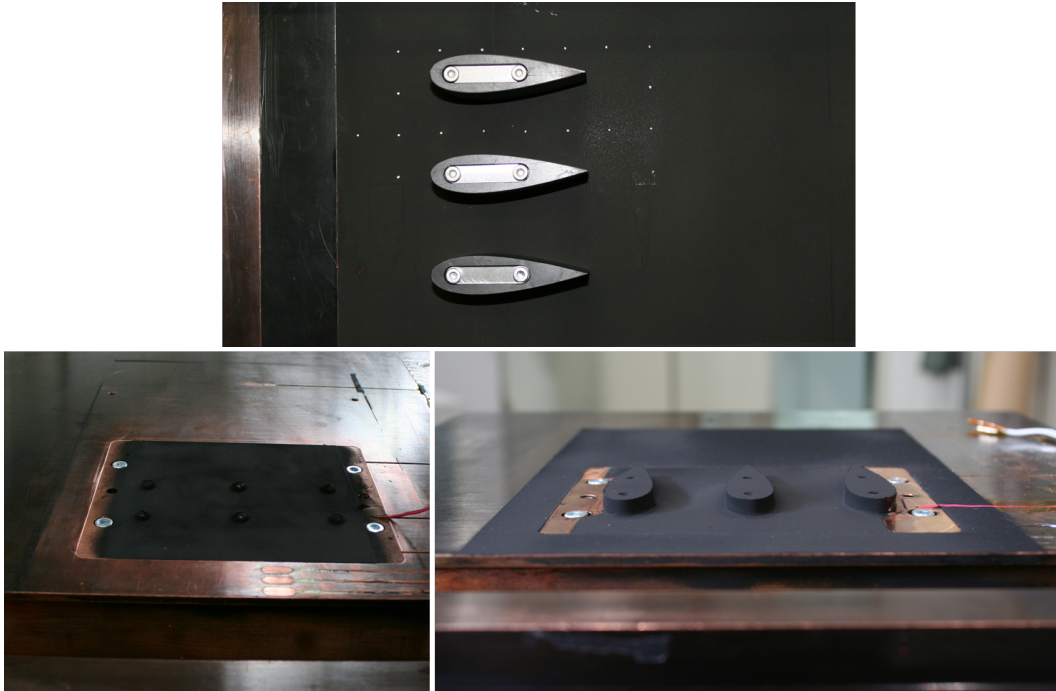


Figure 3.8: Description of the different test cases tested. Top - flat endwall case A. Bottom left - flat endwall with insert. Bottom right - contoured endwall with insert.

of thermally conductive compound to ensure optimal contact between the solids and uniform heating of the insert.

Symmetric NACA profiles were used to obtain a simplified vane-endwall configuration allowing the development of the measurement procedure, without requiring a complete redesign of the test section and diffuser section. In fact, vanes with a turning angle would have been closer to the geometry tested in LISA but the turning of the flow, even small, would have required a second row to redress the flow. The current width and length of the test section are limiting the accommodation of more advanced geometry. The NACA 0025 profile is selected because of the change in flow speed along this profile is similar to what the flow conditions are in the stator 1 in LISA. A peak velocity of  $Mach=0.48$  is achieved in the passage as shown in Fig. 3.9 that is comparable to the expected exit velocity in LISA around  $M=0.5$ .

A set of PT100 temperature sensors is additionally installed under the surface (1 mm depth) to monitor the solid temperature along the flow direction. The measured data are used in the data reduction phase to account for conduction losses in the starting part of the plate. The location of the PT100 is different for case A and case B&C due to the pocket machined to house the inserts. A schematic of the location of the PT100 for both configurations is shown in Fig. 3.11.

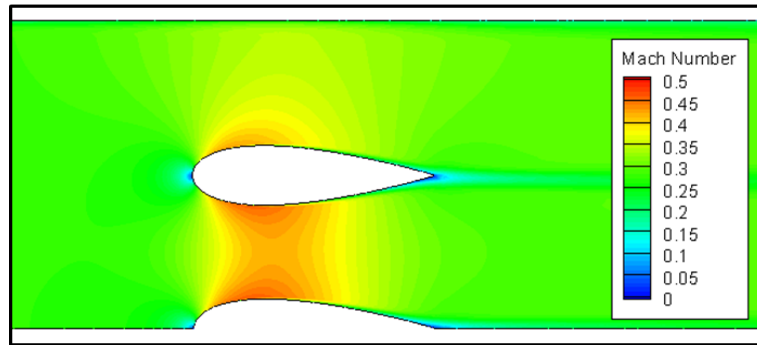


Figure 3.9: Mach number distribution in the three vanes cascade formed by NACA 0025 profiles predicted using a Fluent 2D simulation.



Figure 3.10: Test section (opened) of the facility. Three NACA profiles mounted on the isothermal plate.

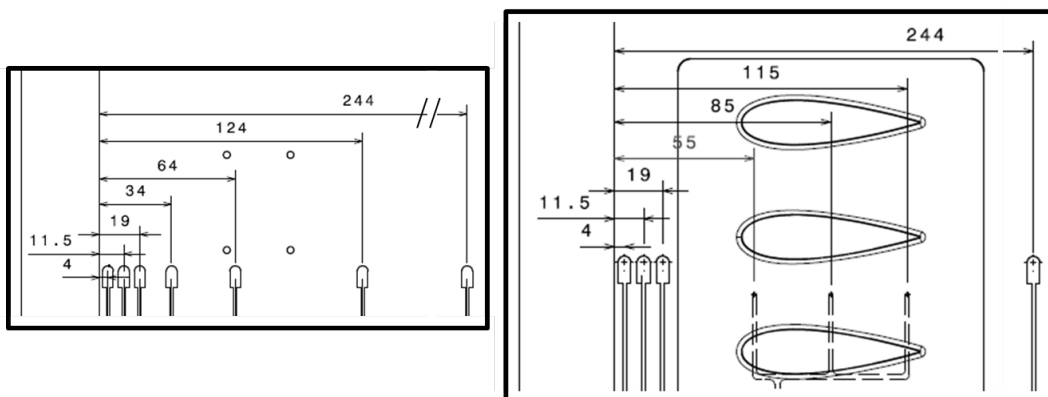


Figure 3.11: Location of the PT100 embedded in the copper plate for the different cases. On the left the flat endwall case A. On the right the cases B&C using an insert to support the vanes.



### Flat endwall

In order to derive the heat transfer quantities, the isothermal plate is covered with a 127 microns thick layer of Kapton, a polyimide film with a low and well-known thermal conductivity of 0.12 W/m/K. This layer is attached on the copper surface using an adhesive directly laminated on the Kapton sheet. This ensures an optimal contact between the layers (no air bubbles trapped) and adhesion onto the solid (preventing peel off). Finally the structure is painted with black paint (Nextel Velvet Coating), which has a high emissivity of 98%.

The thickness of every layer is measured during the assembly process using a thickness gauge traversed by a linear axis. The flatness of the copper insert is measured first and then the measurements are repeated after every layer application, adhesive and Kapton, and after the painting process.

### Contoured endwall

The contoured endwall geometry is derived from typical contoured endwall design approaches. A certain number of operations were used to flatten, redress, enlarge and adapt the endwall shape to the dimensions of the passage with symmetric airfoils. The contouring is therefore not optimized for our configuration, but it exhibits similar levels of curvature. The shape of the surface can be seen in Fig. 3.12 and is quantitatively described in Fig. 3.13.

The generated endwall shape is a non-developable surface and a critical step is the attachment of the Kapton insulating layer to the geometry. A certain number of slits have to be used to shape the sheet and ensure a correct contact and adhesion. The thin cuts are filled with glue to prevent any peel off of the layer and the resulting contoured shape is smooth to the touch.



Figure 3.12: Contoured endwall case. Copper insert covered with the insulating Kapton layer.

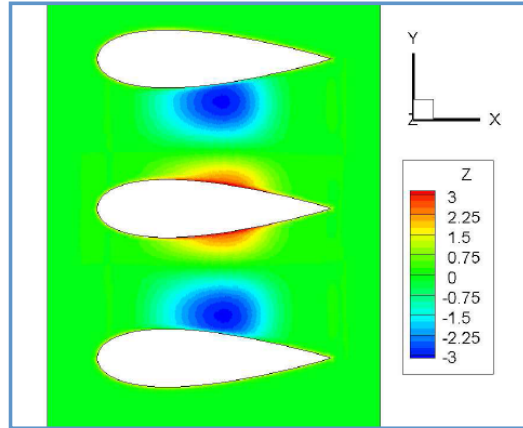


Figure 3.13: Shape of the contoured endwall. Variation of surface height (in mm) along the passage.

### 3.3 Measurement procedure and data reduction

#### 3.3.1 Measurement procedure

The procedure firstly involves the setting of the desired flow conditions (Mach number, stabilized inlet temperature). The isothermal plate is then set and maintained at a constant temperature  $T_{iso}$  by heating the circulating water using the electrical heater. The feedback signal for the PID regulator is the averaged copper plate temperature measured by the embedded PT100 sensors.

Once the plate conditions are held constant, fifty thermograms are acquired for averaging. An automated non-uniformity correction (NUC) of the camera sensor is performed prior to every acquisition. The endwall junction is observed through two separated viewports corresponding to the upstream and the downstream area of the passage. Because of the limited height of the channel, portions of the surface cannot be reached from a single position. Therefore the camera is positioned at different angles relative to the surface in order to obtain a measurement of the whole passage. A total of 24 positions are used to fully describe the passage. The measurements are performed at a distance of 30 cm, providing a measurement resolution of 0.4 mm/px. The maximum angle between the camera axis and the surface normal is set to 15 degrees in order to maintain the entire area observed in the field of focus of the camera. For this angle variation the directional emissivity of the paint remains constant as discussed in [30].

When the measurements for all the positions are completed, the plate temperature  $T_{iso}$  is changed. Seven plate temperatures ranging from 303K to 363K with steps of 10 degrees are successively measured. The total inlet flow temperature is maintained below the plate temperature as shown in Table 5.2. The real time monitoring of the heating process ensure that uniform and stable conditions are reached prior to every measurement.

Note: the chiller described in section 3.1.2 was not installed yet when this measurements were performed, therefore only temperature above the mainstream temperature could be achieved.

### Image Processing

Fifty thermograms are acquired for every camera position (24 in total) and plate temperature (7 in total), resulting in a total of 8400 thermograms acquired for one configuration (geometry and operating condition). For each plate temperature, the thermograms are averaged per camera position and the resulting pictures are combined to obtain the passage temperature field. The image registration procedure uses reference points (silver dots visible in Fig. 3.8) distributed over the observed area to redress and locate the image from one camera position as described in section 2.2. The redressed images are then interpolated onto a fine grid and combined to form a final picture containing the surface temperature of every point of the passage. The temperature  $T_w$  of the whole passage is used to calculate the heat transfer quantities.

### Heat Transfer Calculation

The calculation of the heat transfer quantities is then based on the governing equation introduced in section 2.1.2. Seven sets of data points ( $T_w, q_{conv}$ ) are acquired using seven plate temperatures and a linear regression is used to deduce the heat transfer coefficient  $h$  and adiabatic wall temperature  $T_{ad}$  according to Eq. 2.14. Theoretically two points are sufficient to solve this equation with two unknowns, but in the current study more data points are used and the coefficients are deduced from a linear fit as illustrated in Fig. 5.5.

The in-situ calibration of the camera is performed by traversing the camera at every position for every plate temperature in the absence of airflow. A correction matrix (first order polynomial fit) is then calculated based on the temperature measured with the camera while measuring the surface temperature with the embedded sensors. This accounts for disturbances at every camera position: external reflection, view angle effects, and so forth. The curves obtained in the correction procedure show that an equivalent transmittance of about 90% is obtained for the system.

## 3.4 Numerical setup

Two computational setups were also created for the blade-endwall junction with flat and contoured endwalls. The goal is to provide more insight into the flow structure and its modification due to endwall contouring. Heat transfer data have also been calculated using two simulations with different isothermal plate temperatures in order to derive the heat transfer quantities ( $h, T_{ad}$ ) using a similar method to the experiment. The geometry

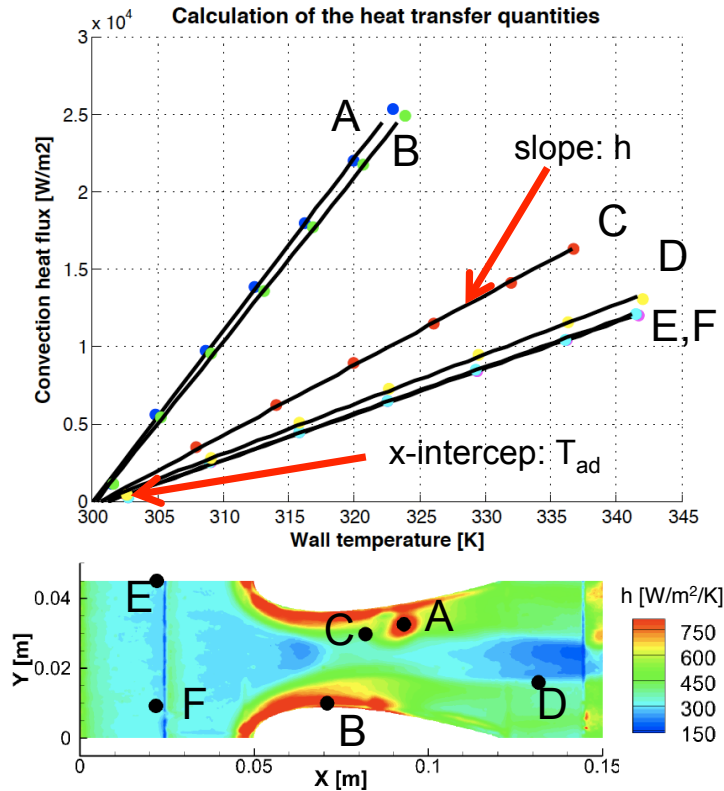


Figure 3.14: a) illustration of the linear fit procedure (top) to deduce the heat transfer coefficient and the adiabatic wall temperature. b) position of the points for the linear fit illustrated in a).

simulated includes half of the test section, i.e. 1.5 NACA profiles with a symmetry condition. The domain starts immediately after the position of the boundary control system in the facility and extends far downstream of the position of the blades. The development of the boundary layer is therefore included in the calculation.

The grids were generated using ICEM CFD with the following specifications: low Re mesh close to the surfaces of interest (airfoils, endwall), higher  $y^+$  (above 10) and use of wall functions set on the other top and side walls. An expansion factor of 1.22 was used for the first cells in the boundary layer. The simulations were performed using ANSYS CFX with the flow boundary conditions taken from the experiments (Table 5.2). The turbulence model used for the calculations was the  $k$ - $\omega$  model, i.e. fully turbulent simulations. A turbulence intensity of 1% and a length scale of 6mm representative of the flow conditions and the geometry of the facility were used as inlet turbulence boundary conditions. The airfoils surfaces are set with adiabatic boundary conditions.

The two similar meshes for the flat and contoured endwall cases were composed of 8.5 Mio nodes. A grid sensitivity study (Fig. 3.15) performed for the flat case showed that this mesh size already provides a grid- independent heat transfer coefficient.

|   | Pt inlet | Tt inlet | M    | $Re_{Cax}$        |
|---|----------|----------|------|-------------------|
| <b>CaseA:</b><br><b>Flat Plate</b>        | 101025   | 300.9    | 0.27 | $4.5 \times 10^5$ |
|   | 105500   | 301.6    | 0.37 | $6.2 \times 10^5$ |
| <b>CaseB:</b><br><b>Flat Insert</b>       | 100950   | 301.6    | 0.27 | $4.5 \times 10^5$ |
|   | 105600   | 300.9    | 0.37 | $6.2 \times 10^5$ |
| <b>CaseC:</b><br><b>Contoured Endwall</b> | 101050   | 301.1    | 0.27 | $4.5 \times 10^5$ |
|   | 105500   | 301.1    | 0.37 | $6.2 \times 10^5$ |

Table 3.1: Experimental operating conditions. The Pt and Tt data are used as boundary condition for the CFD predictions of the M=0.28case.

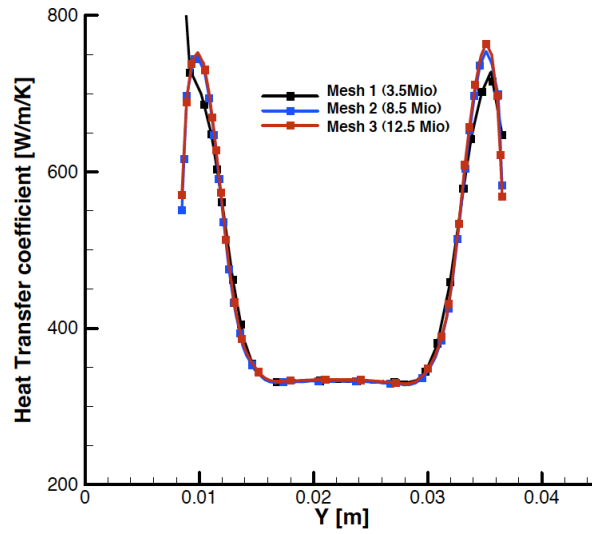


Figure 3.15: Heat transfer coefficient extracted along the line X=0.065 for the different meshes.

### 3.5 Experimental Uncertainty Analysis

The dominant terms for the uncertainty analysis can be derived from the calculation procedure described in Eq. 2.12-2.15 and are listed in Eq. 5.1-5.3.

$$\frac{\partial T_{ad}}{\partial T_w} = 1 + \frac{1}{h \cdot R_{th}} \quad (3.2)$$

$$\frac{\partial T_{ad}}{\partial T_{iso}} = -\frac{1}{h \cdot R_{th}} \quad (3.3)$$

$$\frac{\partial h}{\partial R_{th}} = \frac{-h}{R_{th}} \quad (3.4)$$

These terms highlight the importance of the thermal resistance in the overall uncertainty. As the calculation of heat transfer quantities is computer-based and involves a linear fit, the method described in Moffat [65, 49] with successive perturbation of the inputs, is also used here to calculate the uncertainty based on the measurements. As

already shown in the analytical description of the uncertainty, the heat transfer coefficient is mostly dependent on the uncertainty value from the thermal resistance. An uncertainty level (2 sigma or 95% confidence interval) of 13% is calculated for the heat transfer coefficient both analytically and computationally using the perturbation method. The uncertainty values for the different parameters are summarized in Table 5.1

|                  |               |
|------------------|---------------|
| $\delta T_w$     | 0.5 K         |
| $\delta T_{iso}$ | 0.15 K        |
| $R_{th}$         | 0.0015 +- 13% |

Table 3.2: Uncertainty values.

As observed in Eq. 5.1 and 5.2, the uncertainty in adiabatic wall temperature varies with the local value of the heat transfer coefficient. A contour plot of the absolute uncertainty is shown in Fig. 3.16. An averaged absolute uncertainty of 1.7 K is calculated with maximum values around 3 K where the heat transfer coefficient is the lowest.

In addition to the uncertainty analysis a certain number of studies, not detailed here, were performed to validate different aspects of the method.

1. The uniformity of the thermal boundary condition was validated using a 3D thermal calculation. The thermal load measured on the contoured endwall was used as a boundary condition together with the measured temperature of the circulating water at the back of the plate. The study showed limited spatial variation of the temperature on the surface below the multilayer structure (0.1K). This is included in the uncertainty contribution of  $T_{iso}$ .
2. A comparison between a 1D and a 3D conduction model for the heat flux calculation (Eq. 2.13) was also performed for the measurements on the contoured endwall. Negligible differences (< 1%) were obtained between the two models.

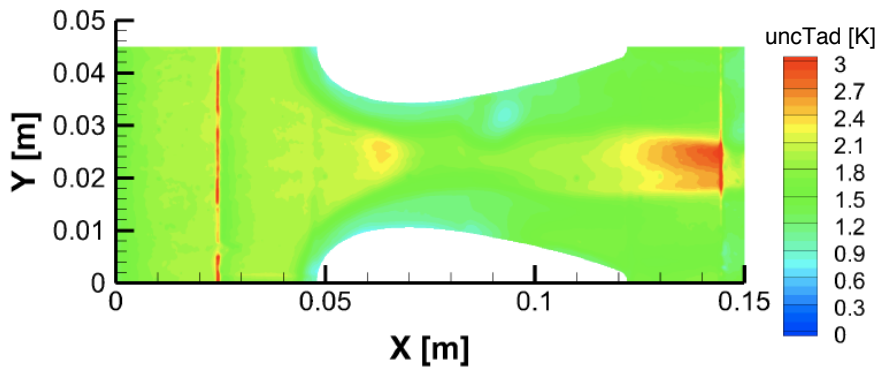


Figure 3.16: Absolute uncertainty in measured adiabatic wall temperature in the case with contoured endwall.

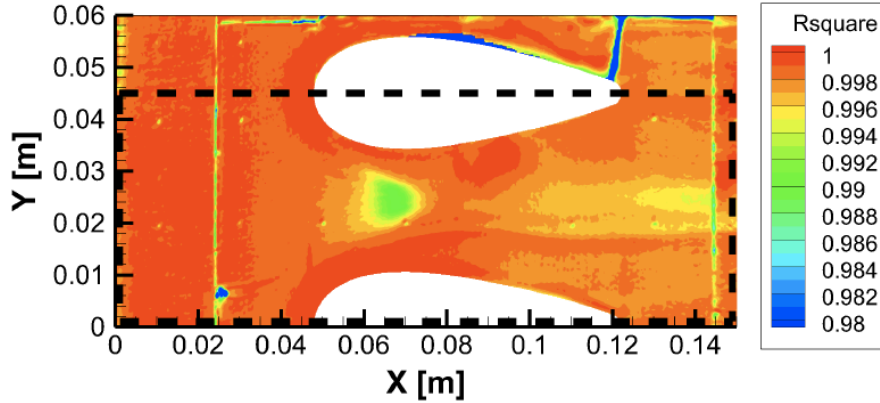


Figure 3.17: Coefficient of determination ( $R^2$ ) from the linear regression (Eq. 2.14) for the contoured endwall case. Area of interest highlighted with dashed line.

3. The coefficient of determination from the linear fit  $q_{conv} = f(h, T_{ad})$  was used as an indicator of the correct attachment of the layer as shown in Fig. 3.17 where the signature of a large slit is noticeable near the top airfoil trailing edge.

## 3.6 Experimental Results and comparison to numerical predictions

### 3.6.1 Flat plate heat transfer

The measurements are first performed on a flat plate without airfoil and compared with a flat plate correlation in order to validate the method and ensure reliable results.

Data from experiments at two different flow velocities were used and plotted in a non-dimensional manner in Fig. 3.18. The correlation used for comparison described in Eq. 3.5 is the expression for the heat transfer coefficient on a flat plate with unheated starting length  $\xi$  expressed in Kays, Crawford and Weigand [48].

$$St.Re_x^{0.2} = 0.0287Pr^{-0.4} \left[ 1 - \left( \frac{\xi}{x} \right)^{9/10} \right]^{-1/9} \quad (3.5)$$

The boundary layer code TEXSTAN [2] was also used for comparison. The calculation was made using a mixing-length turbulence model. The case simulated with TEXSTAN included the region where the boundary layer develops upstream of the heated plate. The velocity inputs were taken from aerodynamic measurements performed in the facility using a four-holes probe.

As expected the curves from the two measurements performed at two distinct flow conditions collapse on each other. The error bars also show that the difference between the measurements and the data from correlation and calculation lie within the measurement uncertainty.

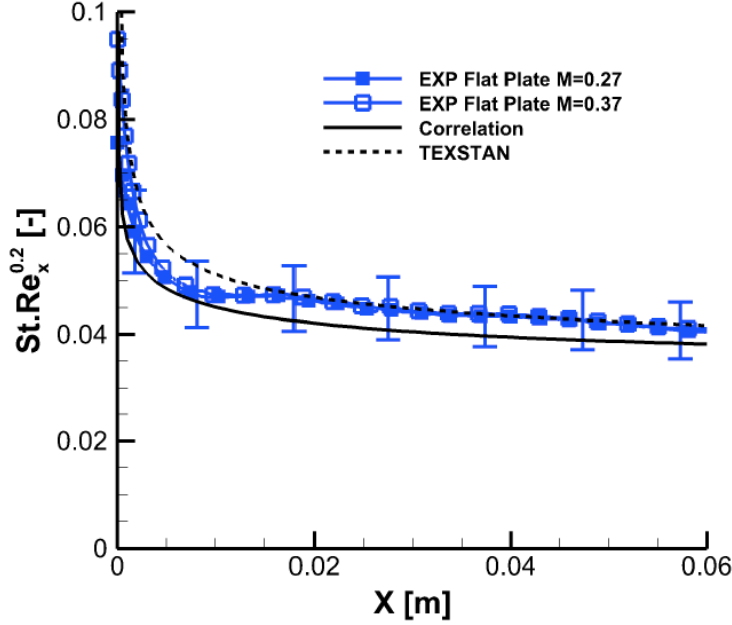


Figure 3.18: Comparison of laterally averaged measured heat transfer in a non-dimensional form with correlation (Eq. 8) and a TEXSTAN calculation.

### 3.6.2 Measurements in the cascade on flat and contoured end-wall

The results for the cascade configuration with flat and contoured endwalls are plotted in Figs. 3.19 and 3.20. Each figure represents both the flat (bottom part  $Y < 0$ ) and the contoured (top part  $Y > 0$ ) results for ease of comparison of the two sets of data. The adiabatic wall temperature is plotted in terms of temperature difference  $T_{delta}$  as expressed in Eq. 3.6, to account for variation of total inlet temperature  $T_{t_{in}}$  (see Table 1) between tests.

$$T_{delta} = T_{t_{in}} - T_{aw} \quad (3.6)$$

The line or discontinuity observed at  $X=0.025$  m is an assembly feature since it corresponds to the location where the copper insert starts. (it ends at  $X=0.145$  m).

The common features for the heat transfer coefficient distribution are noticed in Fig. 3.19. A high heat transfer region is observed near the airfoil leading edge, where the boundary layer rolls up and the horseshoe vortex is created. Another region of high heat transfer is observed on the sides of the blades where the horseshoe vortex extends and develops through the passage, but has yet to lift away from influencing the endwall heat transfer. The wedge area located in the entrance region of the passage and pointing toward the passage is also a typical feature of heat transfer in a linear cascade. As also



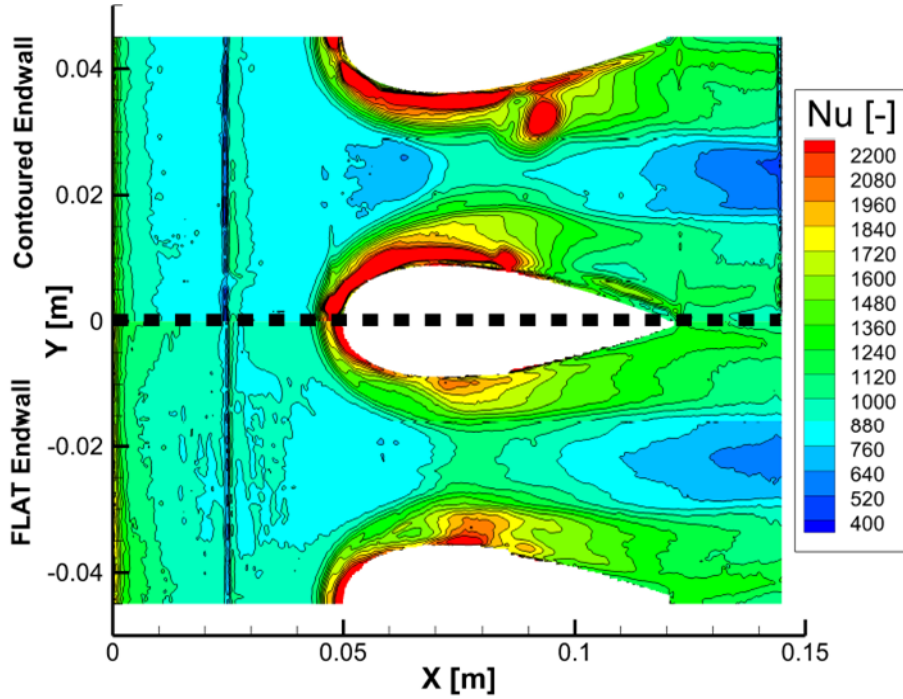


Figure 3.19: Nusselt measured at  $Ma=0.28$  for the flat (bottom - case B) and contoured endwall (top - case C) configurations.

shown in Graziani et al. [34] and Lynch et al. [58], a uniform heat transfer coefficient at a level similar to the incoming boundary layer is measured in this region.

### 3.6.3 Effect of the vanes mounted on a flat endwall.

The measurements performed on the flat endwall with and without vanes highlights the increase in heat transfer coefficient due to the presence of the vane. Figure 3.21 presents the results for the two flow conditions tested in terms of ratio of the Nusselt number in the case with vanes and the one without vanes. The increase in heat transfer close to the leading edge region where the horseshoe vortex forms is visible and the the heat transfer coefficient is multiplied by up to 2.4 in this region. Within the passage, the acceleration of the flow caused by the vane shape increases by approximately 30% the levels found in a flat plate case. Finally around the vanes, the region where the flow is turned, accelerated and where the legs of the horseshoe vortex are present, sees the maximum increase by a factor of 2.5. The bottom part of Fig. 3.21 presents the same type of result the second flow condition. The same patterns of heat transfer coefficient increase are observed. However the location of the peak increase in the middle of the passage is shifted upstream (approx. 5-6%  $C_{ax}$ ) as well as the high heat transfer region (red) along the vanes. The levels remains of the same magnitude.

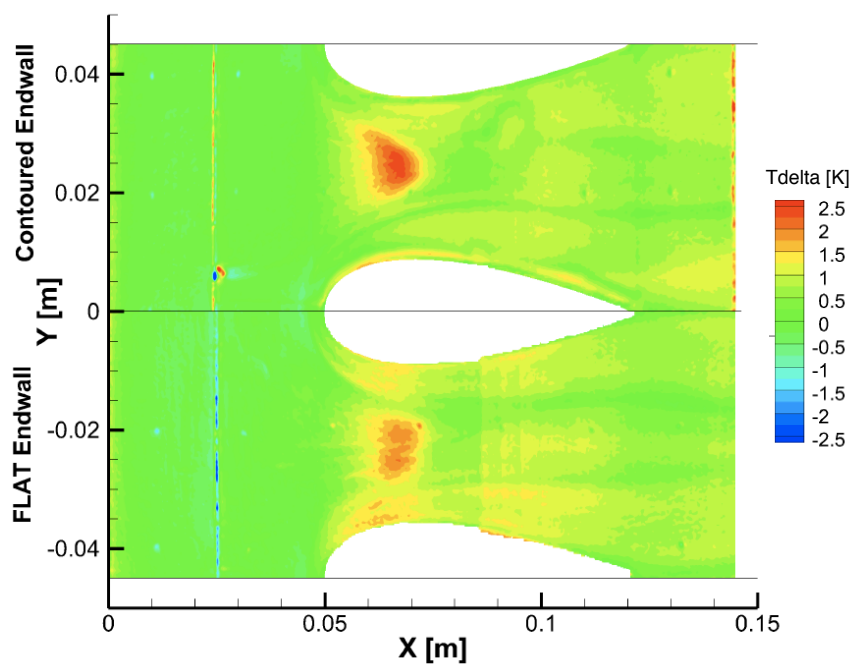


Figure 3.20: Delta temperature between total inlet and adiabatic wall temperature measured at  $Ma=0.28$  for the flat (bottom - case B) and contoured endwall (top - case C) configurations.

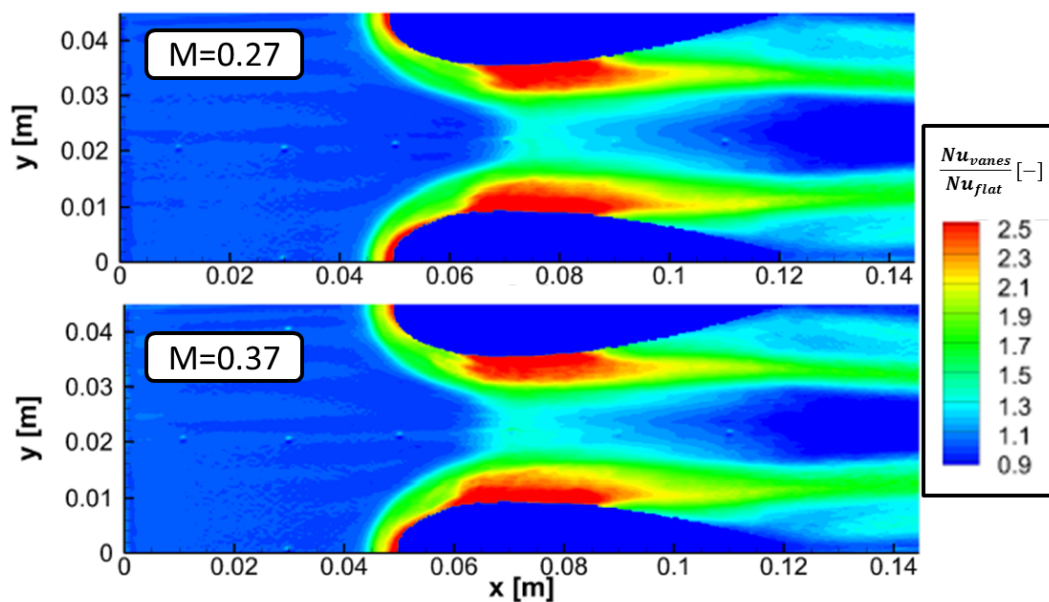


Figure 3.21: Effect of the vane installation on heat transfer coefficient distribution for  $M=0.27$  (top) and  $M=0.37$  (bottom).

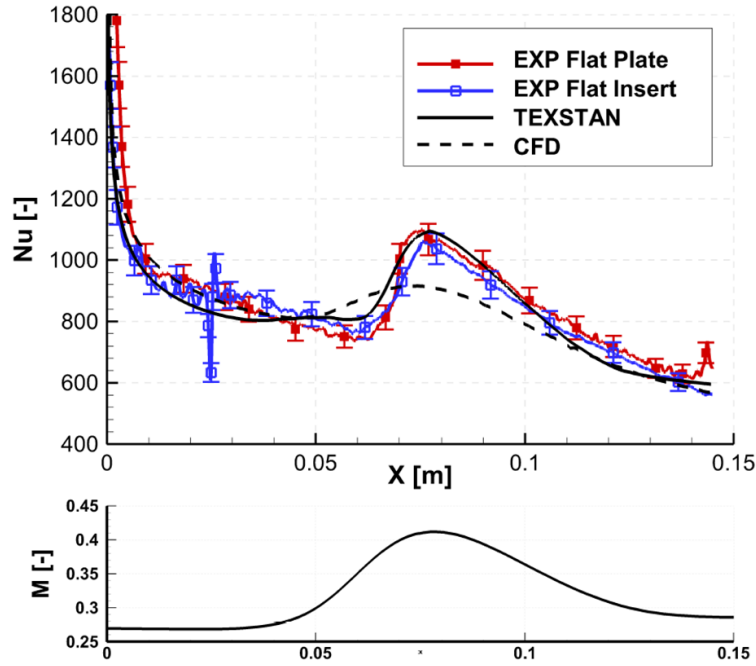


Figure 3.22: **Top** - Nusselt number values in the middle of the passage ( $Y=0.0225$  m) extracted from the measurements of the flat cases A (red) and B (blue), the CFD simulation and a boundary layer calculation performed using TEXSTAN. **Bottom** - Mach number variation in the middle of the passage extracted from the CFD calculation of the flat case.

### 3.6.4 Results from predictions and comparison to the experiments

Due to the limited amount of data available from literature for a similar configuration, the boundary layer code TEXSTAN [2] was used to provide additional heat transfer data for comparison purposes. The calculation was performed using the freestream velocity profile in the middle of the passage ( $Y=0.0225$  m) extracted from the 3D CFD simulation. Comparisons between experimental data for the flat cases and the values predicted by TEXSTAN using a mixing-length turbulence model are presented in Fig. 3.22 for the heat transfer coefficient and Fig. 3.23 for the delta temperature (defined in Eq. 3.6). A strong increase (+30%) in the heat transfer coefficient is measured in the middle of the passage at approximately  $X=0.07$  m, the location corresponds to the peak of the flow velocity in the passage. The heat transfer coefficient plots show a very good agreement between the experimental results and the values predicted by TEXSTAN. The heat transfer coefficient from the CFD calculation exhibits a similar trend with respect to the other data, but the magnitude is somewhat under-predicted.

The data shown in Fig. 3.23 for the adiabatic wall temperature (in the form of a delta temperature), exhibit a similar evolution with a constant value upstream of the blade,

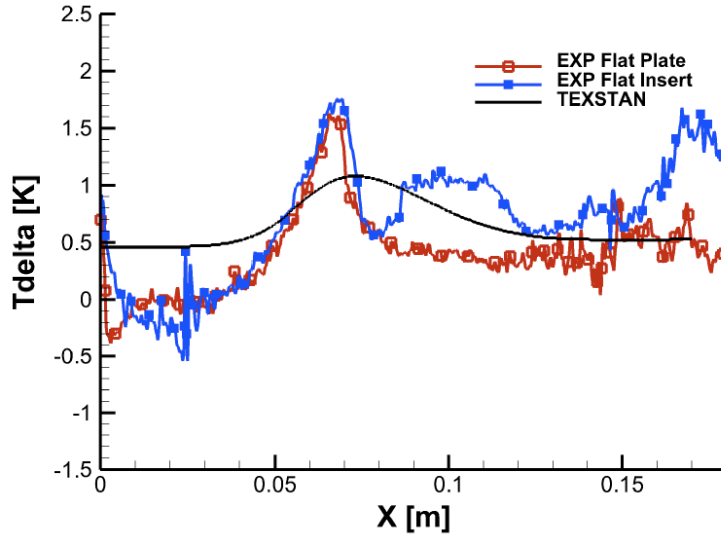


Figure 3.23: Delta temperature (Eq. 3.6) values in the middle of the passage ( $Y=0.0225$  m). The data are extracted from the measurements of the flat cases A (red) and B (blue), and results from a boundary layer calculation performed using TEXSTAN.

an increase where the flow is accelerating and another plateau close to the trailing edge of the airfoil. The magnitude of the temperature measured and predicted are in good agreement when accounting for the uncertainty.

The Figure 3.24 presents the measured heat transfer coefficient for the flat endwall case and data obtained from numerical simulations. Similarities can be observed in terms of the incoming level of heat transfer and in the wedge area, but significant differences also appear in the middle of the passage and in the downstream region. The high heat transfer area upstream of the airfoil leading edge linked to the formation of the horseshoe vortex is observed to extend more upstream in both measurements than in the CFD study. Overall reduced values are predicted which could result from a different inlet boundary condition. The state of the incoming boundary layer and the turbulence intensity may differ between the experiments and the numerical predictions and could help to explain such discrepancies. In his review on junction flows [84], Simpson also highlighted the difficulty of numerical models in correctly predicting the formation and the behavior of the horseshoe vortex when compared to flow measurements. In fact at high Reynolds number, the behavior of the vortical structures created upstream of the leading edge is highly unsteady. After the throat ( $X=0.07$ ) the heat transfer level increases in the middle of the passage and more strongly close to the blades. As shown also in Fig. 3.22, the CFD is not capturing this increase in heat transfer due to the flow acceleration in the passage.

Figure 3.25 presents the relative heat transfer augmentation measured (top part) and predicted (bottom) for the contoured endwall compared to the flat endwall. The

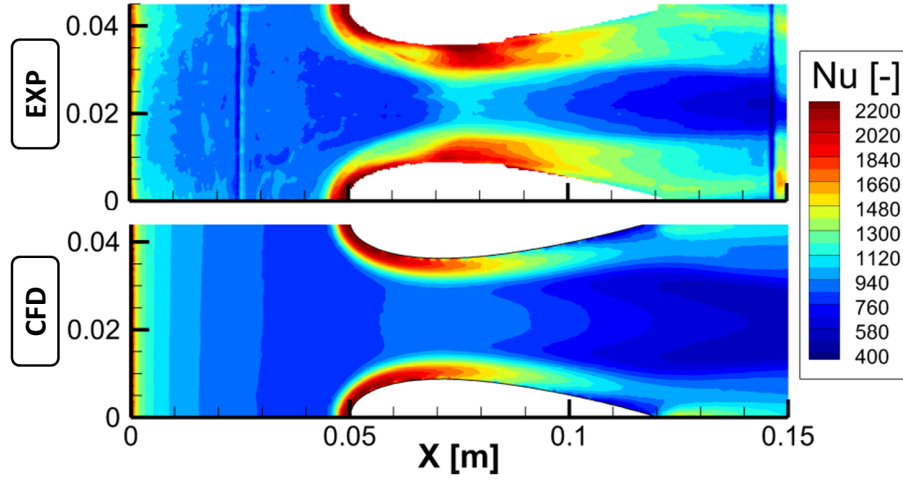


Figure 3.24: Comparison of Nusselt number measurements (top) with CFD predictions (bottom) for the flat endwall case at  $Ma=0.28$  and  $Re_{Cax}=4.5 \times 10^5$ .

protrusion is located near the center chord of the middle blade as shown in Fig. 3.13, while a valley is located near the trailing edge of the outer-most blades. When comparing the heat transfer coefficient for flat and contoured endwalls, different regions can be highlighted. A reduced heat transfer coefficient (-10%) is observed in the approaching boundary layer in the contoured endwall case. A potential explanation is a change in the blockage effect due to the endwall contouring, which could lead to a non-uniform distribution of the flow in the different passages. Higher heat transfer values are generally observed for the contoured case close to the airfoil.

The contouring plays a significant role in the modification of the heat load distribution through the passage. As highlighted with the different arrows in Fig. 3.25, four distinct regions with strong variation of heat transfer are identified. These regions are located upstream and downstream of the protrusion and valleys. The iso-height lines in Fig. 3.25 help to identify these regions and to link the heat transfer features to the endwall shape. Compared to the flat case, the contoured case exhibits:

- a higher heat transfer upstream of the hill,
- a lower heat transfer downstream of the protrusion (28%),

Close to the trough the opposite trend is observed,

- a reduced heat transfer upstream of the valley (30%),
- an increased heat transfer downstream of the trough (70%).

The CFD data presented in the bottom half of Fig. 3.25 show similar behavior to that described for the measurements, as highlighted with the arrows. The magnitudes of the changes are different but the positions of the maximum reduction or augmentation are similar to the experiments.

The CFD results of surface pressure and pressure gradient shown in Fig. 3.26 provides more insight into the flow field and the static pressure modification due to endwall

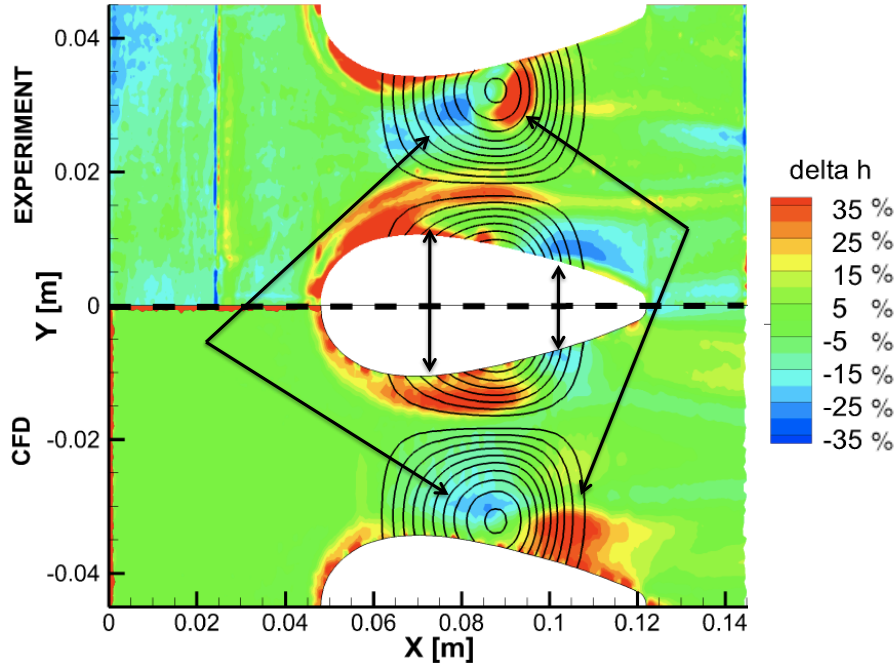


Figure 3.25: Relative heat transfer augmentation  $(h_{\text{contoured}} - h_{\text{flat}}) / h_{\text{flat}}$  in % plotted for both the experiments (top) and the numerical predictions (bottom) at  $Ma=0.28$ . The lines represent the changes in surface altitude.

contouring. Due to the protrusion and the dimple the pressure gradients' orientation in the passage are modified. The trough located close to the outer-most blade locally creates a flow deceleration and a region of high static pressure. The presence of the trough also modifies the position of the minimum pressure which is moved upstream from 26%  $C_{ax}$  in the flat endwall case to 17%  $C_{ax}$  in the contoured case. The orientations of the pressure gradients are consequently modified. Downstream of the throat ( $X=0.07$  m), the adverse pressure gradient aligned along the flow direction in the case of a flat endwall is now inclined along the direction between the trough and the hill. Close to the outer blade, the flow now faces an adverse pressure gradient upstream of the trough and a favorable gradient downstream of it before facing another adverse gradient at the exit of the passage. The succession of stabilizing and destabilizing events will have an impact on the motion of the horseshoe vortex in this region of the passage.

With the help of Figs. 3.27 and 3.28 the position and intensity of the horseshoe vortex legs can be observed. In Fig. 3.27, the  $Q$  value refers to the second invariant of the velocity gradient tensor. It is used as a criterion to identify vortices [46]. The vortex leg developing on the hill side is pushed and stretched toward the middle of the passage where the pressure gradient then prevents further deflection of the vortex core. This results in a high heat transfer level measured upstream of the hill. The low level of heat transfer downstream of the hill can then be attributed either to a boundary layer

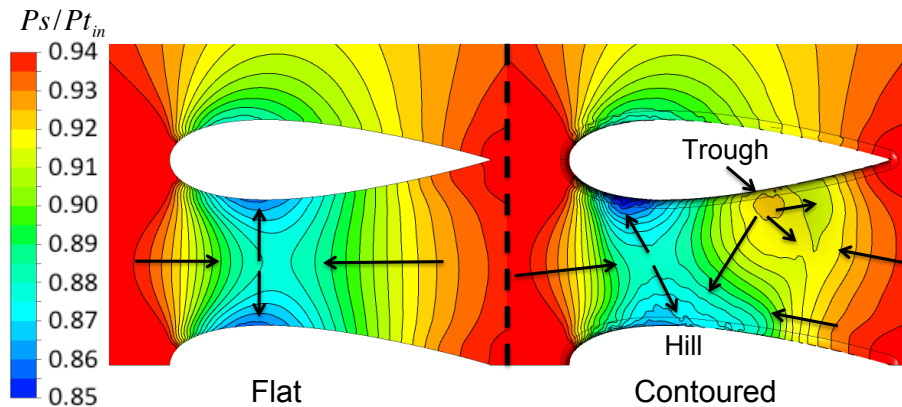


Figure 3.26: Endwall static pressure non-dimensionalized with total inlet pressure and pressure gradient (arrows) from CFD shown for both flat (left) and contoured (right) endwalls.

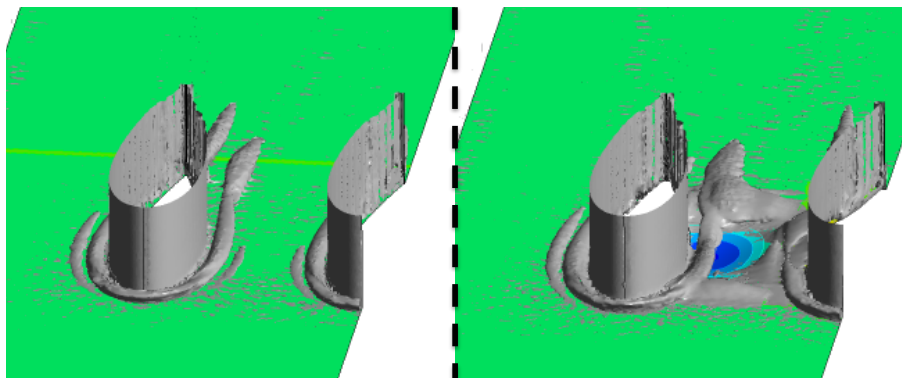


Figure 3.27: Iso-surface of constant  $Q$  value from the CFD predictions of the flat (left) and contoured (right) cases.

separation or to a strong thickening of the boundary layer. On the trough side, the iso-surface of Fig. 3.27 shows first that the horseshoe vortex is stronger (larger core shown) for the contoured endwall case compared to the flat case, which explains the higher heat transfer coefficient predicted and measured for the contoured case in the leading edge region.

The trough region has a double impact on the flow field for two reasons:

1. the flow approaching the trough will decelerate due to the increase of the cross-sectional area and this phenomenon leads to a larger vortex with a reduced strength. An area of lower heat transfer is then observed.
2. in the second part of the trough, the cross-sectional area is decreasing and the flow velocity increases, leading to a smaller vortex with a stronger intensity. In this region a higher heat transfer coefficient is measured.

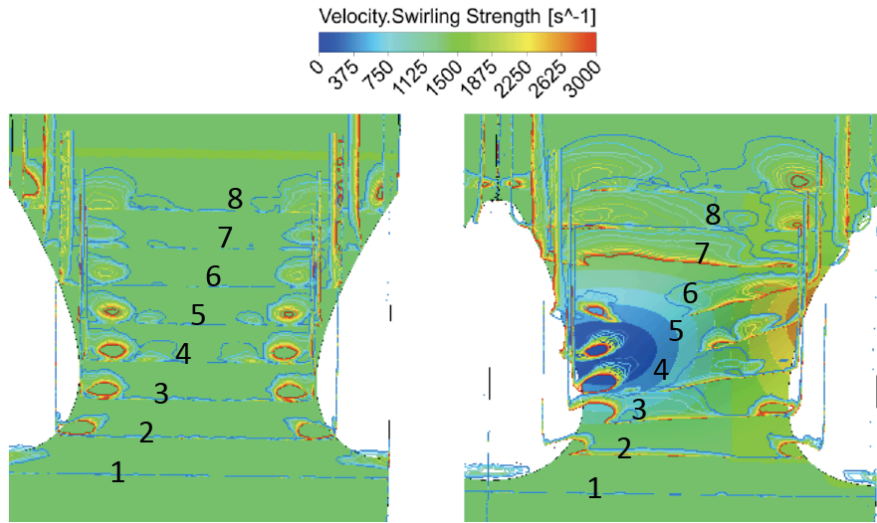


Figure 3.28: Axial slices of the horseshoe vortex from CFD calculations for the flat (left) and contoured (right) endwalls. Lines of iso-swirling strength are displayed in perpendicular slices at the same axial positions for both cases. The endwall surface is colored with the Z coordinate.

The slices along the passage shown in Fig. 3.28, also illustrate the variation of the vortex core shape and intensity when approaching and leaving the trough, as well as its deformation due to the presence of the hill. The decay of the vortex intensity through the passage is clearly observed in the flat case. However the contoured endwall case shows a different evolution:

- On the trough side the vortex remains stronger (slices 5-6) in the case of the contoured endwall. After the trough the vortex seems to be merged into the boundary layer.
- Due to the presence of the hill, the vortex core is pushed toward the center of the passage (slices 4,5,6) and seems to remain very close to the endwall surface, which can explain the higher heat transfer values observed in this area. Downstream of the hill (slice 8), the vortex remains stronger compared to the flat endwall.

### 3.6.5 Overall effect of contouring on heat transfer.

In a real gas turbine stage, one of the primary goals of endwall contouring is to reduce the aerodynamic losses to improve the overall performance. This can be achieved through a reduction of the passage vortex strength during its movement in the passage. Reducing the passage vortex strength will also have a positive impact on the heat transfer distribution on the endwall. This may lead to an overall (area-averaged) reduction of the heat load on the endwall as shown in previous studies [58]. However, locally the heat transfer coefficient can be substantially increased (up to 35% in [58]). As such, a more



tailored and locally adjusted cooling design is needed to appropriately redistribute the cooling flow to achieve the required lifetime and durability of the component. The area-averaged calculation for the present case shows an overall increase in the area-averaged heat transfer coefficient of 3.8%. When the increase of endwall surface area (close to 1%) is taken into account, an overall heat load increase of 4.8% is observed.

$$\frac{h_{contoured}}{h_{flat}} \frac{A_{contoured}}{A_{flat}} = 1.048 \quad (3.7)$$

### 3.6.6 Effect of a variation of Reynolds number for the two end-wall geometry.

The measurements are performed for two operating conditions, detailed in Table 5.2, providing a variation of Reynolds number of 38%. According to turbulent flat plate correlation, the expected increase in heat transfer coefficient is 29% as derived in Eq. 3.8. The changes in HTC distribution are presented in Fig. 3.29 for the two endwall configurations. The measured level of HTC increase matches the correlation approximation, except in regions where the flow is accelerated and where secondary flows are dominating. In fact, the change in incoming flow speed will modify the location where the horseshoe vortex forms and change its intensity. In the flat endwall case, an increase in HTC upstream is observed upstream of the leading and continues along the vanes as the flow is turned. The major changes in HTC are present in the middle of the passage where the flow flow is accelerated. At the throat, the increase reaches up to 70%. In the downstream part of the passage, an increase of 40-45% is measured due to the flow in the region where the vortices mixes out, a difference in the vortex intensity can explain a faster mixing of the HV legs in the lower Reynolds number case. In the case of the contoured endwall, a similar pattern is observed up to the throat. Downstream, the contouring has an impact on the heat transfer distribution, especially downstream of the hill  $x > 0.1m$  (close to the bottom vane). In this region, an increase up to a factor 2 is measured. The behavior of the horseshoe vortex is modified due to the hill and at higher flow speed it appears to be deflected more into the passage leading to a region of higher heat transfer. Close to the upper vane where the trough is located, the HTC levels are similar in the low and high Reynolds number cases.

$$Nu_{ratio} = \frac{Nu_{M=0.37}}{Nu_{M=0.27}} = Re_{ratio}^{0.8} = 1.29 \quad (3.8)$$

## 3.7 Conclusions

This chapter presents and analyzes the measurements of heat transfer quantities on a contoured endwall using an isothermal boundary condition. In order to adapt the heat transfer measurement technique to a vane-endwall configuration, a linear cascade

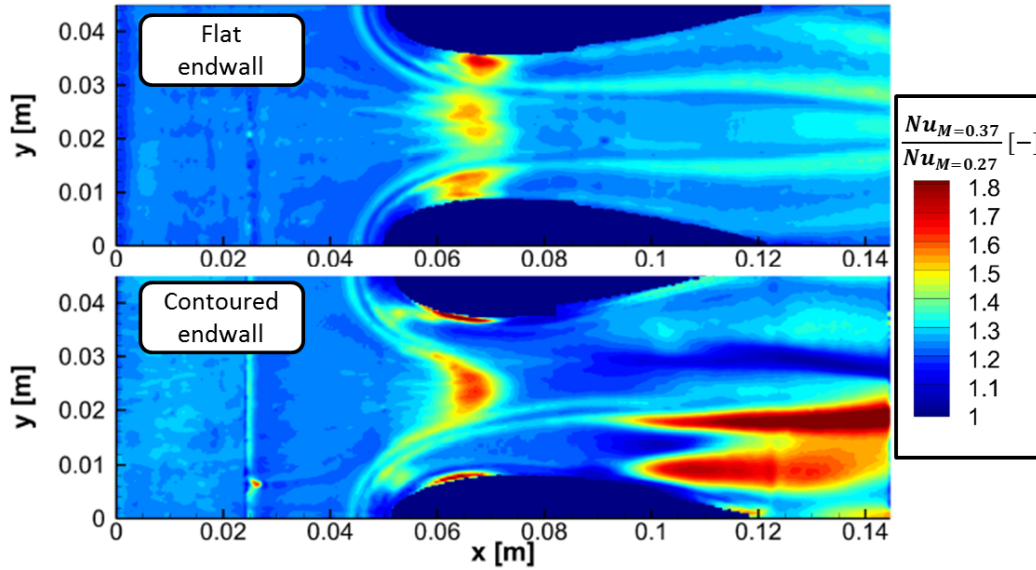


Figure 3.29: Effect of the variation of flow Reynolds number on the heat transfer coefficient for the two endwall configuration, flat (top) and contoured (bottom).

composed of symmetric airfoils was installed and tested with flat and contoured endwall configurations. The shape of the contouring was derived from an existing geometry for a stator passage and adapted to a flat plate study. Successful measurements of heat transfer coefficient and adiabatic wall temperature on a complex three-dimensional endwall shape were presented and compared with a correlation, with predictions from a 2D boundary layer code, and with results from 3D CFD simulations. The insight provided by the CFD simulations helped to highlight the impact of the modification of the flow field due to endwall contouring on the measured variation of heat loads.

The interaction between the horseshoe vortex and the endwall shaping is seen to impact the distribution of thermal loads, especially in a non-optimized configuration. The following points were highlighted in the study concerning the variation of heat transfer coefficient:

1. increase of up to 25% for the contoured case compared to the flat case in the LE region,
2. increase up to 70% downstream of a valley,
3. modification of the horseshoe vortex upstream of a hill leading to an increase of the heat transfer coefficient up to 30%, and
4. a local reduction (20%) downstream of a bump and upstream of a trough.

Because of the endwall shape, the impact on the heat transfer coefficient due to a change in flow conditions is more important in the contoured case than for the flat geometry. Downstream of a hill, especially, the change in flow conditions has a dramatic impact and increase in HTC values up to a factor 2 are measured.

Despite a limited overall increase of area-averaged thermal loads of only 4.8%, local variations of up to 70% were measured. These local variations have a large magnitude and should be accounted for during the cooling design of a turbine. As the average heat load is not significantly higher, the aerodynamic benefits of endwall contouring could be maintained without any significant additional cooling flow provided the cooling design system is locally adapted to account for the spatial variations in the heat load. As such, future design systems incorporating endwall contouring need to adapt their design system to carefully map the endwall heat load and design an appropriate cooling system.



# Chapter 4

## Integration of a heat transfer measurement platform into the turbine axial facility LISA.

The heat transfer measurement technique was already established in the Laboratory and Chapter 3 showed the improvement of the measurement know-how by performing measurements in a cascade with a vane-endwall configuration. The previous measurements are performed on a thermally controlled flat plate which has to be transposed to a measurement platform that can be installed on a stator segment and that can be housed in the LISA axial turbine facility. This chapter starts with an introduction to the LISA facility and after a description of the rig and its operation, explanations on the redesign of the test section and the design of the heat transfer platform are provided. A description of requirements and the bounding box for the design of the platform is made and the chosen technical solutions are presented as well as their design procedures. Finally the newly designed water distribution system and the traversing system for the camera that are required to allow the heat transfer measurements are described.

### 4.1 Axial turbine facility LISA

#### 4.1.1 Description of the wind tunnel

The final set of experiments are performed using the research axial turbine facility LISA. A schematic view of the experimental facility extending over three floors is given in Fig. 4.1. The facility is designed to accommodate 1.5 or 2 stages turbine configurations. The facility operates at a low inlet temperature between 45 and 55degC and at a moderate rotational speed between 1900 and 3000rpm.

The air loop of the facility is quasi-closed and includes a radial compressor, a two-stage water to air heat exchanger and a calibrated venturi nozzle for mass flow measurements.

At the exit of the compressor, the air is directed through a set of heat exchangers that control the turbine inlet total temperature  $T_{t,in}$  to an accuracy of  $\pm 0.3\%$ . A 3m long flow conditioning stretch ensures a homogeneous flow field at the turbine inlet. Additionally the flow undergoes acceleration ahead of the turbine section in order to reduce the significance of remaining flow non-uniformities from upstream. At the exit of the test section, two successive rows of de-swirl vanes help recovering the static pressure before going through the venturi nozzle and back to the compressor. Downstream of the de-swirl vanes, the air loop is open to atmosphere making the facility sensitive to daily variation of atmospheric conditions. The power available on the shaft is then transmitted to a DC generator via a gearbox. The generator absorbs the turbine power and controls the rotational speed with an accuracy of  $\pm 0.02\%$  ( $\pm 0.5\text{rpm}$ ). Part of the power used to drive the compressor is therefore recovered and fed back to the grid via the gearbox, DC generator and a converter unit. A torque meter installed on the vertical shaft between the turbine and the gearbox measures the torque on the rotor shaft. Two safety coupling ensure a decoupling of the DC generator, the gearbox and the rotor shaft in case of a failure. The facility is controlled via multiple computers to ensure independent operation of the compressor, the generator and monitoring of the rig. The safety devices are automatically actioned by the software to ensure immediate reaction to a failure and prevent further damages to the facility.

The description of the rig in this section and the following sub-section is restricted to the information that helps to understand the current work. More technical details about the rig, the assembly or other features are accessible in the work of Behr [12], Schuepbach [80] and Jenny [45].

### Rig operation

The turbine is operated by keeping the 1.5 stage total to static pressure ratio as well as the total inlet temperature constant. The total to static pressure ratio refers to the total inlet pressure measured by pitot tubes located on struts positioned upstream of the test section divided by the averaged static pressure measured at the exit of the second stator using pressure taps located on the endwalls. The compressor pressure ratio  $\pi_{comp}$  is adjusted to account for the daily variations of atmospheric pressure and maintain the total to static pressure ratio of the stage constant. Due to the maximum compressor pressure ratio of  $\pi_{comp} = 1.5$  and the sensitivity of the rig to atmospheric conditions, a safety margin is kept when selecting the operating conditions to make sure the conditions can be reached every day and therefore maximize the facility running time.

Two flow operating conditions are used in the current study to achieve a variation of Reynolds number in the first stator row. The variation is achieved by changing the mass flow delivered by the compressor. The rotor dynamics and its coupling with the gearbox and the generator are limiting the operating range of the rig. In fact, multiple

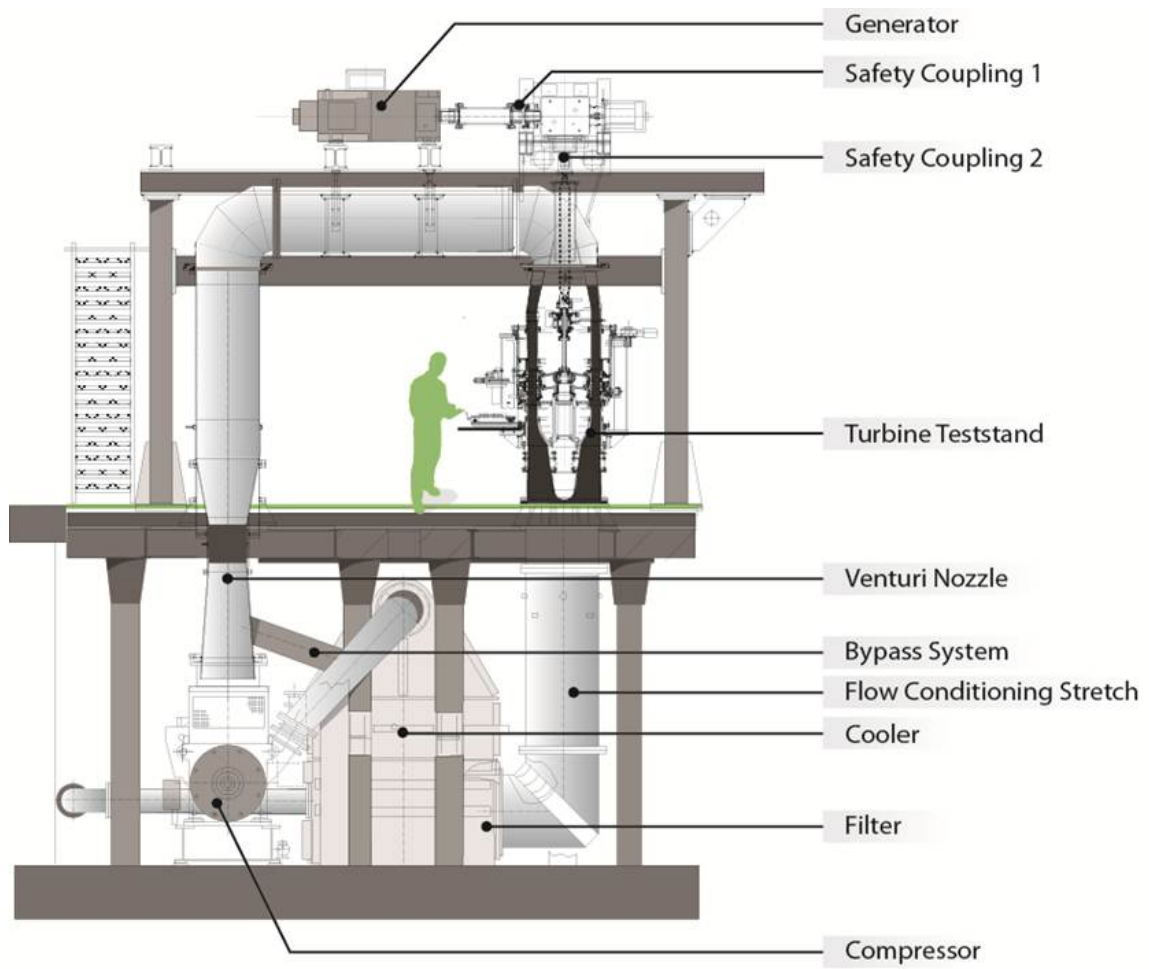


Figure 4.1: Schematic view of the LISA research turbine test rig.

resonance frequencies are present in the system and they delimit operating windows within acceptable vibration levels and therefore available for a safe operation.

### **Description of the test section and the aerodynamic measurement setup.**

A drawing of the test section is shown in Fig. 4.2. The configuration shown is the D-case designed and integrated by Behr [12] which is the starting point of the current work. As it can be seen the three rows (NGV, Rotor and Stator2) are assembled vertically and a set of support parts visible on the left side sets the relative positioning and clearance of the row to ensure the operation of the rig. The vane and blade counts are 36 vanes for the NGV, 54 blades on the rotor, 36 vanes for the second stator. A purge air flow can be injected between the NGV and the rotor row. This air flow is picked downstream of the heat exchanger and is injected through the airfoils of the first row into a cavity before entering the main flow. Different labyrinth seals ensure the sealing between the rotating and stationary parts. The cavity below the first row is sealed with a radial labyrinth seal highlighted in red at the bottom of Fig. 4.2, whereas an axial seal provides the necessary sealing below the second stator (top of Fig. 4.2).

The assembly of the facility is made in a bottom to top approach with groups of parts pre-assembled outside of the facility and then inserted into the rig. The sub-assembly of interest for the current work is the NGV group which is shown in Fig. 4.3. The sub-assembly is composed of a "clocking ring" part that is housing all the NGV airfoils (as a full 360 ring or multiple segments) and the connection to the purge air supply. Upstream of the NGV row a traversable ring allows the measurements of the flow conditions at the turbine inlet (A-plane). A groove through the support ring and probe access holes through the traversable ring grant the access to the flow for the aerodynamic probes.

The rig is mainly used for aerodynamic measurements to provide 2D map of the flow field at different plane in the test section, basically the ABCD planes located upstream and downstream of every airfoil row. The different measurements are shown in Fig. 4.4. The probe is accessing the flow through holes located on traversable rings. The core part of the turbine is contained in a traversable casing that is shown in the CAD view in Fig. 4.5. During the aerodynamic measurements the external casing is circumferentially traversed and entrained the ring through which the probe is inserted using the traversing bar and clamp arrangement shown in Fig. 4.5. A table is also attached to the traversable casing and serves as a support for the probe dedicated traversing system. More details on the traversing system installed in the facility can be found in Schlienger [79].



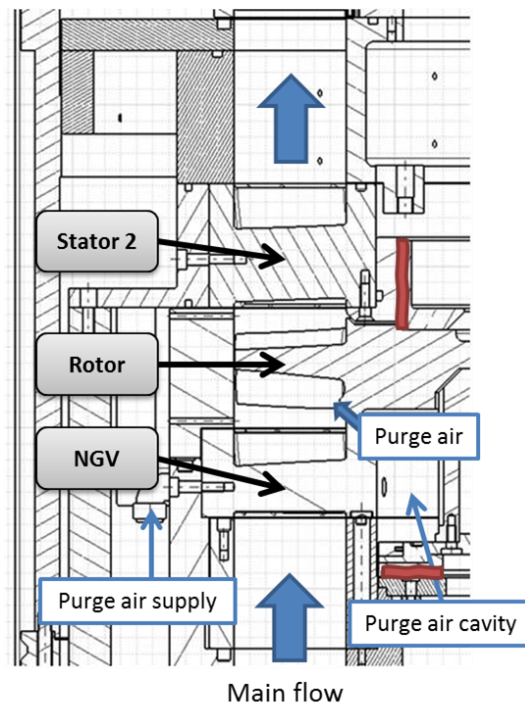


Figure 4.2: Technical drawing of the test section. The three rows and the purge air system are included. The red patches shows the location of the labyrinths seals that ensure the sealing between the stationary and rotating parts.

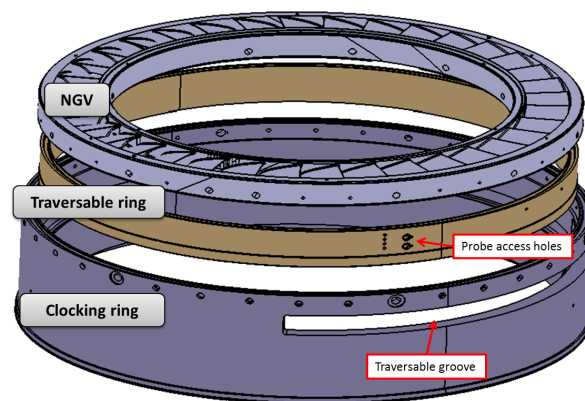


Figure 4.3: CAD view of the NGV sub-assembly with the support ring, the traversable ring and the D-case NGV.

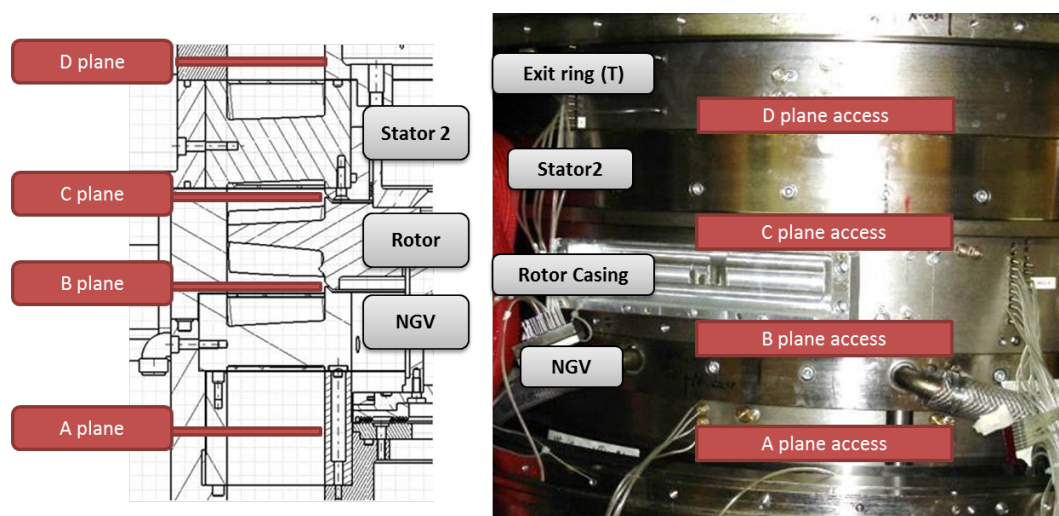


Figure 4.4: Location of the different planes traversed by the probes during aerodynamic measurements. On the left the planes are shown on top of a drawing of the test section. On the right, the different planes are shown on an actual picture of the facility. The exit ring can be traversed as well as the rotor casing.

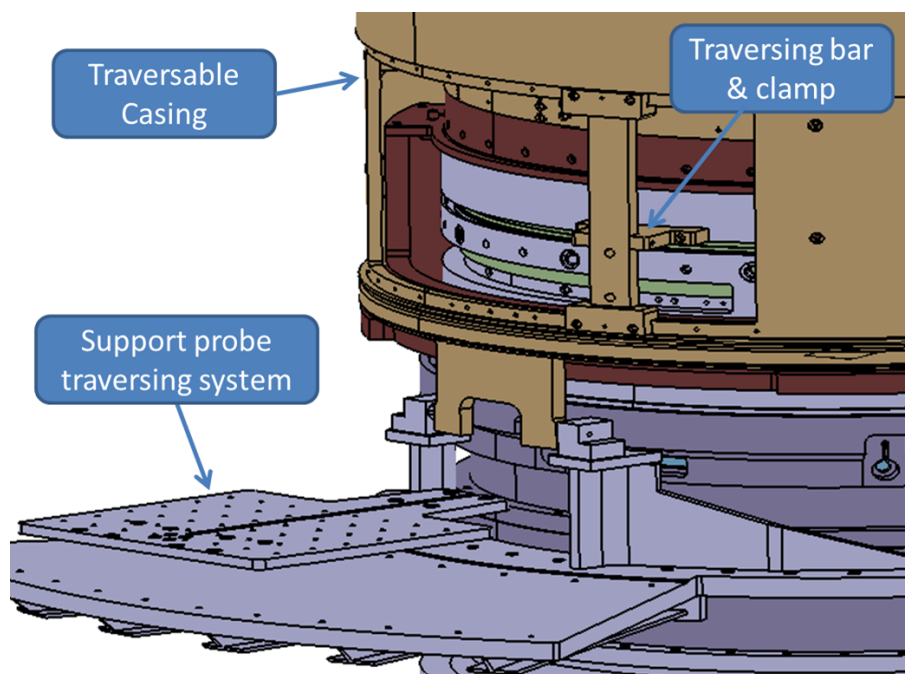


Figure 4.5: CAD view explaining the location of the different traversable rings and how the coupling to the traversable casing is made.

## 4.2 Redesign of the test section to house a heat transfer measurement platform.

This projects aims at increasing the measurement capabilities in the axial turbine facility and therefore no impact on the aerodynamic measurement is acceptable. The design of the heat transfer platform should then meet the following requirements for the two types of measurements.

### Aerodynamic measurements:

- allow access to the different planes A,B,C,D
- ensure traversing the probe for more than one passage at every plane
- allow clocking of the NGV row relative to the fixed stator2

### Heat transfer measurements:

- provide access to the hub endwall using infrared transparent windows
- provide isothermal boundary condition using circulating water and ensure safe operation - no leakage
- minimize the thermal losses to the neighboring mechanical parts
- can connect/disconnect the connection to the water network
- minimize the impact of the platform on the aerodynamic

Because of the vertical assembly of the rig and the presence of the rotor assembly close to the NGV hub platform (shown in Fig. 4.2), the link to the water network could only be established from the outer casing directly through the opening of the traversable casing shown in Figures 4.5 and 4.4.

In order to release the constraints on the heat transfer platform design, the NGV airfoils were shifted upstream by 8mm compared to the D-case and the hub platform is extended upstream of the leading edge by 50% of the NGV axial chord. Also the ring supporting the NGV ring/segments is re-designed to accommodate the modified parts and provide a direct access to the heat transfer segment.

Figure 4.6 shows how the limitations are translated into an available volume around a 4 vanes NGV segment. Radially the volume is limited on the right hand side (blue part) by the clocking possibility and the stator2 support. On the left (yellow) the constraints are released because a 40deg clocking is not realistic and the radial extent is then limited by the radius of the traversing bar and casing. Circumferentially the extent of the box is limited by the connections to the purge air supply. The minimum inner radius is reduced to R310mm, very close to other aerodynamic segments (R311.5mm) to maintain an acceptable safety distance to the rotating parts, especially upstream of the platform.

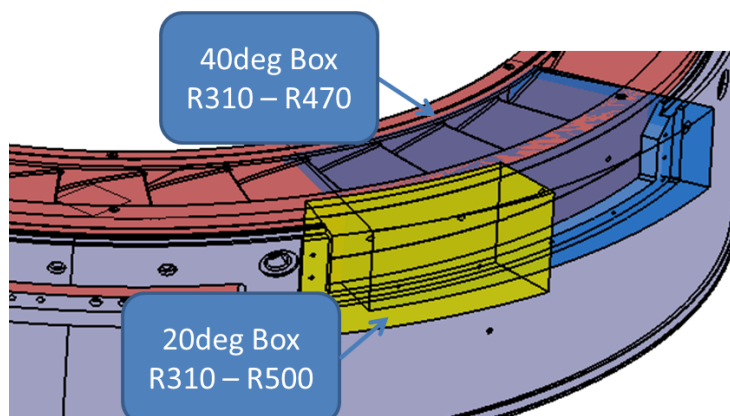


Figure 4.6: CAD view describing the bounding box around the NGV segment that is available for the design of the heat transfer platform.

Two different 1.5 high work turbine stages are tested in the present work. The first generation named K2 is composed of 3 rows equipped with 3D airfoil geometries. The optimized 3D shape is an evolution of the LISA D-case optimized for minimizing the aerodynamic losses. For the second measurement campaign, the airfoils geometries are kept identical but the hub endwall of the three rows are shaped to further enhance the performance of the turbine 1.5 stage. The endwall contouring is restricted to the hub endwalls to keep the tip casing cylindrical and allow access for infrared imaging technique.

The three rows of airfoils are provided after optimization by our industry partner Siemens and are integrated then in the mechanical design of the test section. In order to accommodate the heat transfer platform, the NGV row is split in multiple 40 to 60deg "aero" segments that are then assembled together to form a complete ring. After the redesign of the test section, the integration of the "aero" segments is straightforward but the heat transfer measurement platform requires further attention.

### 4.3 Design of the heat transfer platform.

In the previous section, the limitations inherent to the safe operation of the rig and ability to perform aerodynamic measurements were introduced. This section describes the procedure used to design the heat transfer platform as well as the mechanical realization of the platform. First the thermal design procedure is explained. The design of the optical access to the hub endwall is then explained and finally the complete heat transfer platform assembly is described.

The NGV row is equipped with 36 airfoils with a complex 3D shape. The shape shown in Fig. 4.7 includes lean in the axial direction and a compound lean in the circumferential direction.

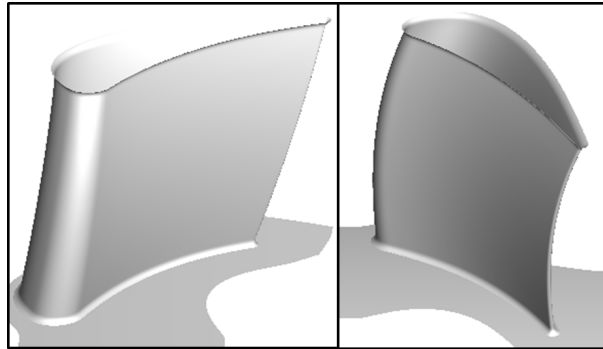


Figure 4.7: CAD views of the NGV airfoil geometry with the axial lean and circumferential compound lean.

### 4.3.1 Thermal design of the platform using 3D thermal analysis.

The heat transfer platform is composed of a four vanes segment that is controlled in temperature using circulating water. In addition thermally insulating parts are attached on the sides of the platform to reduce the thermal losses to the adjacent part. The segment includes four vanes and therefore three complete passages, ensuring the periodicity of the middle endwall. The design is optimized to provide uniform temperature boundary condition to the middle endwall.

The connection to the water network is only possible through the outer casing, and channels through the vanes are then used to bring the water to the hub platform. The water is conveyed from one side of the platform to the other in channels machined into the hub platform. The dimensions of the hub endwall, the calculation of the water network (flow velocity, head loss) and preliminary thermal simulation performed on 2D sections of the hub endwall showed that six 5mm diameter channels could be used in the hub and would provide an acceptable temperature uniformity. The necessity to control the middle vane temperature using circulating water was also highlighted in a preliminary study performed using the D case geometry. In particular, the control of the trailing edge of the middle vanes is critical to the endwall temperature uniformity. The configuration of the platform is then described in Fig. 4.8. The hub channels are connected to the water network via the two extreme blades of the segment. The middle vanes are equipped with six 5mm diameter channels identical to the ones feeding the hub and four additional channels of smaller 2mm diameter to better control the temperature field close to the trailing edge. The channels through the middle vanes are paired and closed at the bottom to form a U shape.

The thermal design of the heat transfer platform is performed using 2D and, at a later stage, 3D thermal analysis. A heat transfer base load was predicted using CFD capabilities and is used in the design process. The heat transfer loads shown in Fig. 4.9, namely heat transfer coefficient and adiabatic wall temperature, are used as a boundary condition for the thermal analysis. The CFD predictions used a low-Re mesh with y-plus

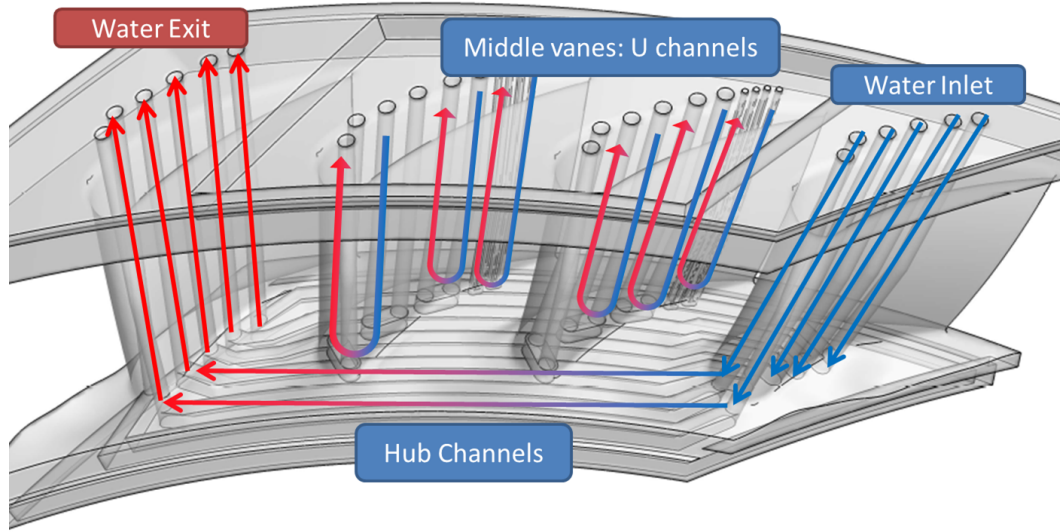


Figure 4.8: Water channel strategy for hub platform and middle vanes.

values 1 on endwall and an expansion rate of 1.17. The turbulence model used is the SST version of the  $k$ - $\omega$  closure model. The simulations are performed using ANSYS CFX. Two calculations, an adiabatic one and a diabatic with isothermal walls, are used to derive a heat transfer coefficient based on the adiabatic wall temperature according to  $q = h(T_w - T_{ad})$

The positions of the tubes are optimized first using 2D thermal simulation of vane sections at the hub, mid-span and close to the tip. The procedure is illustrated in Fig. 4.10. The external boundary conditions are taken from section of the CFD results. The boundary condition in the tube is set using the correlation of Sleicher and Rouse shown in Eq. 4.1 for forced internal convection in pipes. The goal is to reduce the temperature non-uniformity on the sides of the vanes difference between the suction side and pressure side of the vane by allowing a degree of freedom for the pipes perpendicular to the camber line. A set of constraints in the minimum tube spacing, minimum wall thickness is used to ensure the manufacturability of the parts.

$$Nu = 5 + 0.015Re^a Pr^b$$

$$\text{where } a = 0.88 - \frac{0.24}{4 + Pr}, \text{ and } b = 0.333 + 0.5e^{-0.6Pr} \quad (4.1)$$

From the position of the tubes obtained at three span locations (hub casing, mid-span, tip casing) the 3D CAD model of the segment can be elaborated. The hub channels are then designed to ensure the water circulation from one side of the segment to the other. The channels are equally spaced below the passage where the measurements will be performed. In order to validate the 3D design and assess the temperature uniformity on the hub surface a 3D thermal FEM model was used and simulations performed with ANSYS.

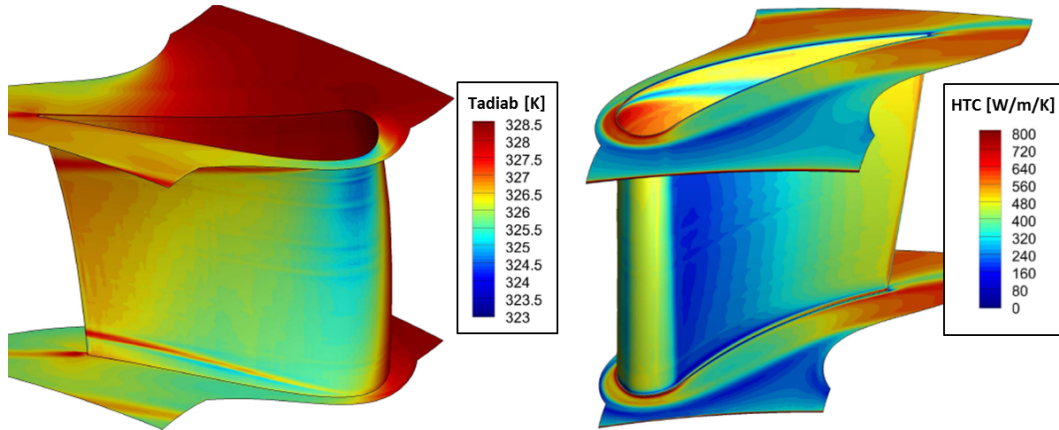


Figure 4.9: Predicted heat load used as boundary conditions for the thermal design of the platform. Left - Adiabatic wall temperature and Right - Heat transfer Coefficient.

The model shown in Fig. 4.11 includes adjacent parts to account for lateral conduction effects to both the other vane segments of the NGV assembly but also to the other parts positioned axially upstream and downstream of the row.

Multiple iterations between the 3D CAD and the thermal simulations were needed in order to obtain a satisfying temperature distribution on the endwall. As part of the improvements, the control of the temperature for the two “central” vanes is added as it is essential to limit the temperature gradient in the middle passage and smaller tubes close to the trailing edge of the two central vanes are added to minimize the temperature gradient in the aft part of the passage

The temperature non-uniformity achieved at the end of the design phase is for the “worst” case, corresponding to an adiabatic wall temperature close to  $T_{ad} = 328K$  and a water temperature equal to  $T_{water} = 293K$ , equal to  $\pm 0.3K$  on the hub endwall and on one vane (trailing edge excluded)  $\pm 1K$ .

## 4.4 Design of the optical access to the endwall for the infrared camera

The optimum shape of the transparent windows shown in Fig. 4.12 covers the complete space between the two middle vanes on top of the endwall of interest and has the two faces cylindrical to fit in the casing. Steps are also used for the window positioning and preventing leakages of air around the window. However the complexity of this part coupled with the mechanical properties and the costs of the Zinc Selenide crystal are reducing the design possibilities to multiple round windows. Other materials were tested in the LAVAL test bench, such as an infrared transparent polymer manufactured by IRISS [1] but the mechanical properties would not allow a safe operation. Sodium



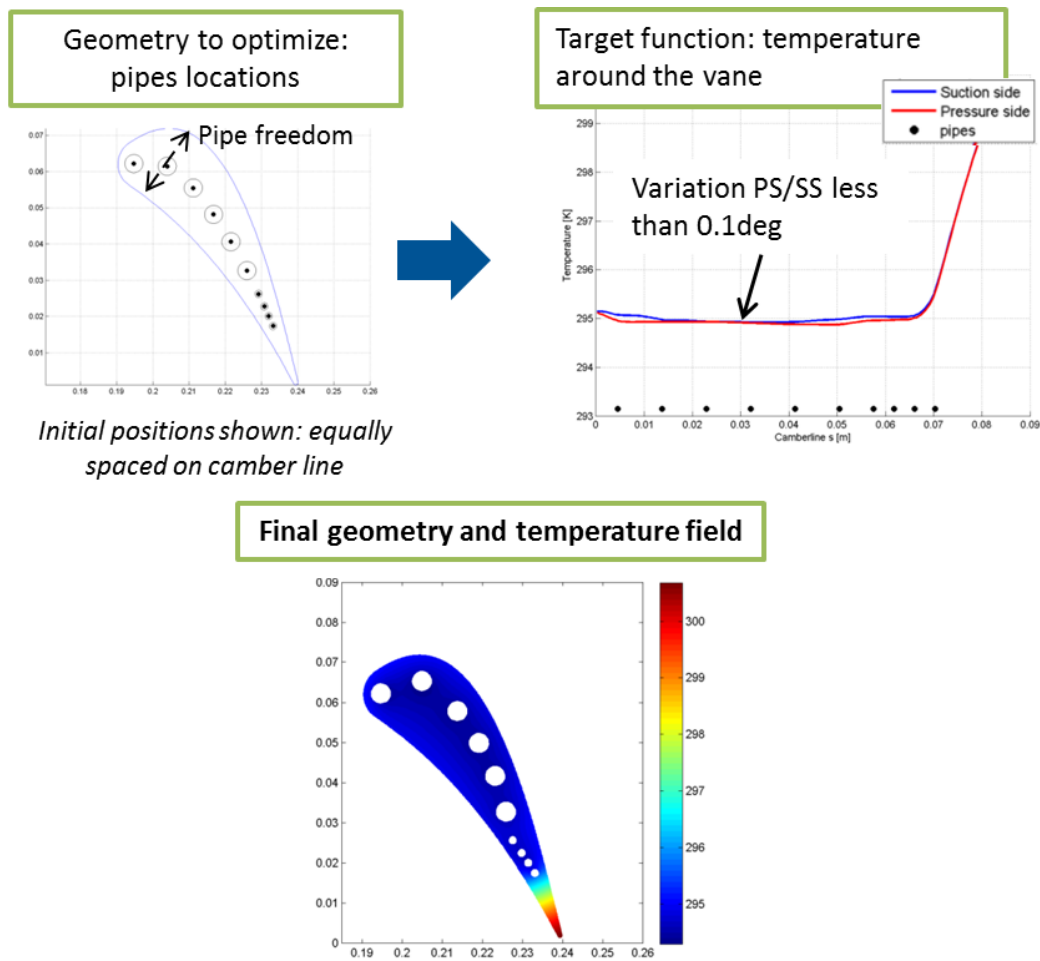


Figure 4.10: Description of the design procedure used to optimize the position of the tubes going through the vanes by minimizing the temperature non-uniformity on the suction and pressure sides.

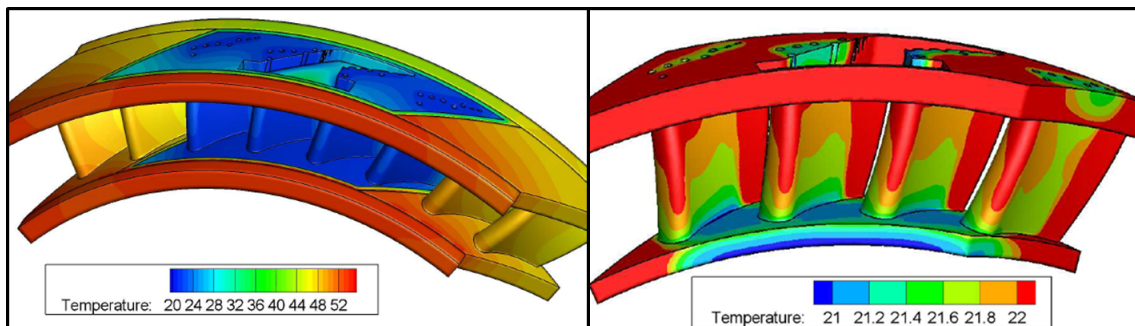


Figure 4.11: Results from the 3D thermal simulation. On the left, view of the complete model including neighbouring parts. On the right, focus on the test segment controlled in temperature.



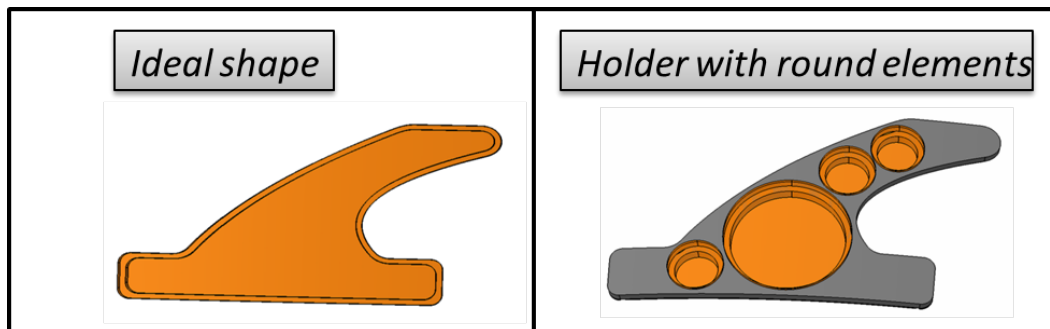


Figure 4.12: Ideal shape of the infrared transparent window (left) and the feasible solution with a holder and multiple round elements (right).

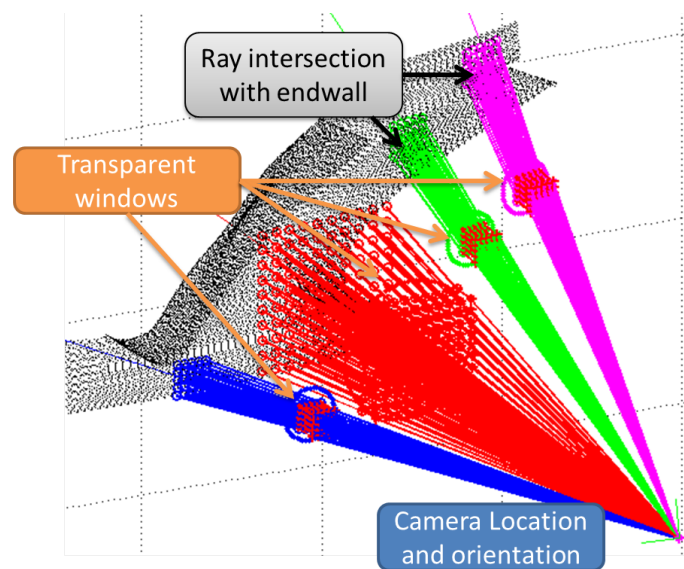


Figure 4.13: Result of a ray tracing calculation performed in Matlab. The trajectory of rays leaving the camera is computed through the windows until they reach the endwall.

Chloride already mentioned in section 2.1.1 is another cheap alternative material but this material is soluble and the proximity to the network water is another unacceptable risk.

A preliminary estimation of the accessibility of the endwall through small windows was made using a ray tracing script developed in Matlab. A typical calculation is shown in Fig. 4.13 and illustrates the possibility to access area such as the right vane trailing edge using the smaller windows. The calculation shown uses a matrix of  $5 \times 5$  rays for the small windows and  $10 \times 10$  for the larger one, leaving the camera in the direction of the small windows. The intersection of the ray and the window is calculated as well as its refraction through the transparent material, and finally the intersection of the ray with the endwall is computed. The rays intersecting with the vane surfaces are filtered later to ensure a correct assessment.

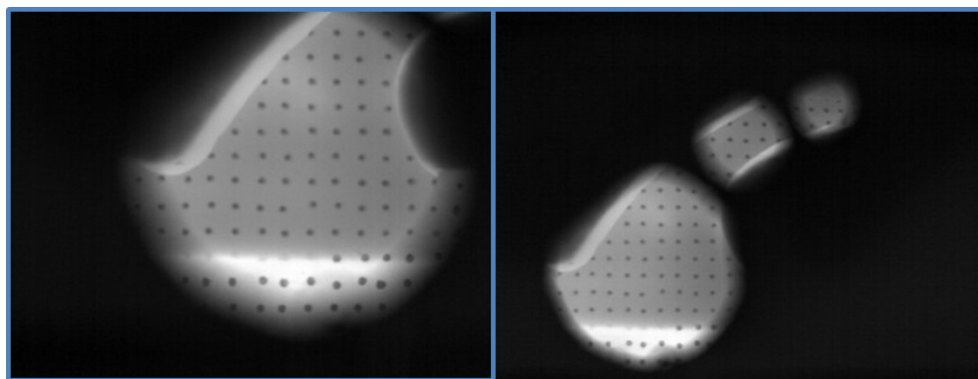


Figure 4.14: Pictures of the 3D printed endwall acquired with the infrared camera viewing through a cardboard mask. Left - camera focused on the leading edge region. Right - complete view through three windows (preliminary configuration).

The calculations performed in Matlab however do not provide a final assessment on the accessibility of the complete endwall, in fact the out of focus window edges are creating a blurred region around the windows (refer to section 2.2.3) which reduces the effective field of view. The blurring due to the bowed airfoil surface is reducing the field of view as well. A final assessment is made using a 3D printed vane passage and cardboard masks to simulate the different windows as shown in Fig. 4.14.

The final design is composed of a steel holder, to match the thermal expansion of Zinc Selenide, and four windows with cylindrical faces and steps manufactured by Spectrovision Ltd (Russia). A sealing made of NBR material is cut to the shape of the window step. The windows are finally maintained in place using a laser cut steel sheet forming a mask overlapping the sides of the windows and tightened with screws. For the measurements the steel parts are painted using the high emissivity black paint to avoid any background reflection affected the data. The two types of windows and their assembly on the holder is shown in Fig. 4.15.

The cost and fragility of the Zinc Selenide windows required them to be mounted in the facility only when the heat transfer measurements are performed. A blank insert with the same shape as the holder is manufactured out of steel to close the rig during aerodynamic measurements.

## 4.5 Mechanical design, manufacturing and assembly of the heat transfer platform.

After the validation of the thermal design, the parts composing the platform are designed and prepared for manufacturing. As a requirement the heat transfer platform should not change the characteristics of the flow inside of the passage, and because of the insulating layer of Kapton, the passage is recessed by 0.2mm to accommodate the layers



Figure 4.15: Top - pictures of the smallest D18mm windows (left) and largest piece of D42mm. The bottom part shows the assembly of the windows into the steel holder.

without changing the throat area and capacity of the row. In this section, pictures from the cylindrical endwall K2-case are used to illustrate the different steps. A particular attention is put on the manufacturability of the parts, minimum wall thicknesses of 1mm on the airfoil and 0.5mm in the hub region are limiting the design. The core part of the platform is the four vanes segment manufactured in aluminum (EN AW 7075) by SM Weber and can be seen in Fig. 4.16.

### 4.5.1 Hub platform.

The hub is machined with preliminary channels linking the leftmost and rightmost vanes as shown in Fig. 4.17. The channel separations are added in the middle part of the segment only after small plugs closing the U channels from the middle vanes are welded. In fact due to the bowed vane shape, the holes through the vanes are made in two steps and drilled from both sides, one hole through the hub up to 50% span and the other through the tip casing down to 50% span. The separations are laser welded on top of the plugs and on the core segment to ensure individual separation of the channels. Figure 4.18 shows the platform after laser welding. The welds are manually polished using sand paper to obtain an acceptable surface for the seal that is laid on top. The hub platform is then closed by an aluminum cover machined with the negative shape of the channels to control the channels dimensions and provide a better control of the seal positioned between the segment and the cover. The cover and seal are shown in Fig. 4.18. The seal is cut from a 1mm thick NBR sheet using a water jet. The platform extends inside the cavity where the purge air is injected, a additional cover made out of insulating plastic POM is manufactured and attached on the aluminum cover. The assembly is completed by screwing the different covers onto the core aluminum segment, Fig. 4.18. On the sides, the segment is thermally separated to the neighboring parts using 6mm thick parts manufactured out of low conductive plastic PET-C.

**Installation of temperature sensors and attachment of the Kapton layer.** In order to monitor the temperature field in the solid, multiple temperature sensors are embedded in the core aluminum part of the platform. The sensors are used to monitor the solid temperature below the passage endwall and along the vanes at around 20% span and 80% span. The temperature data acquired from the hub sensors are used as a reference temperature for the PID regulator controlling the water temperature and as inputs for the conduction model described in section 2.1.2. The sensors are miniature PT100 (1.6x1.2x0.8mm) manufactured by IST AG and are glued 1mm below the surface, using thermally conductive glue (WLK from Fischer Electronick). Figure 4.19 illustrates the location of the PT 100 installed with black symbols. The sensors are fed by a 1mA current and the signal is acquired using the electronic system described in section 4.6.

The Kapton layer is attached onto the segment using adhesive 200MP from 3M, available in sheet forms and laminated on the Kapton using a lamination machine. The

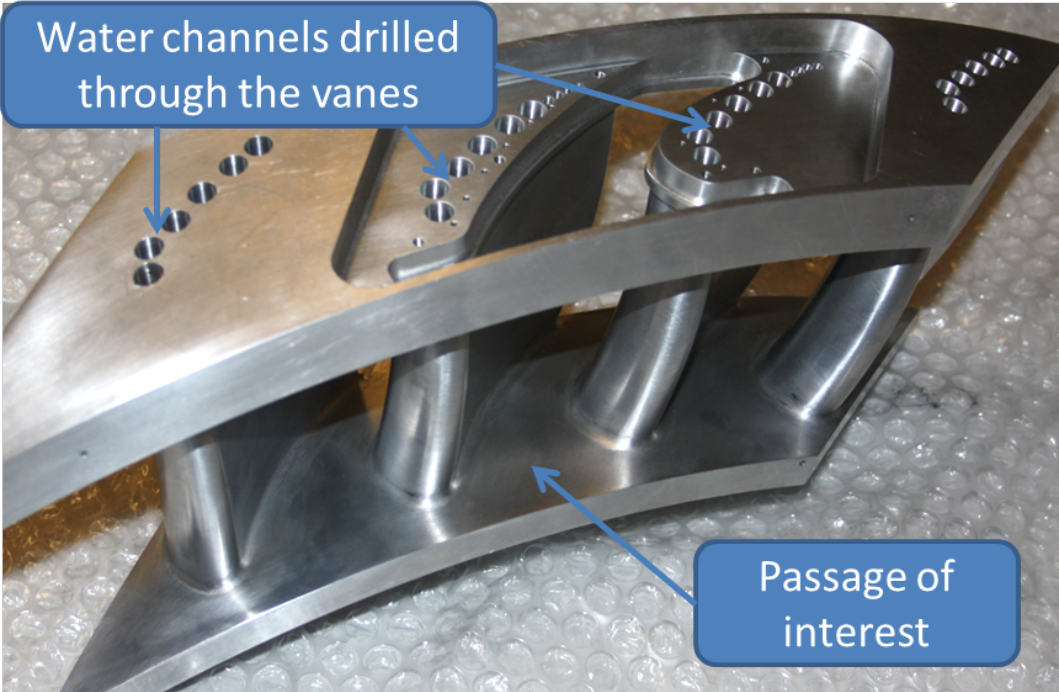


Figure 4.16: Picture of the core part of the platform manufactured in aluminum.

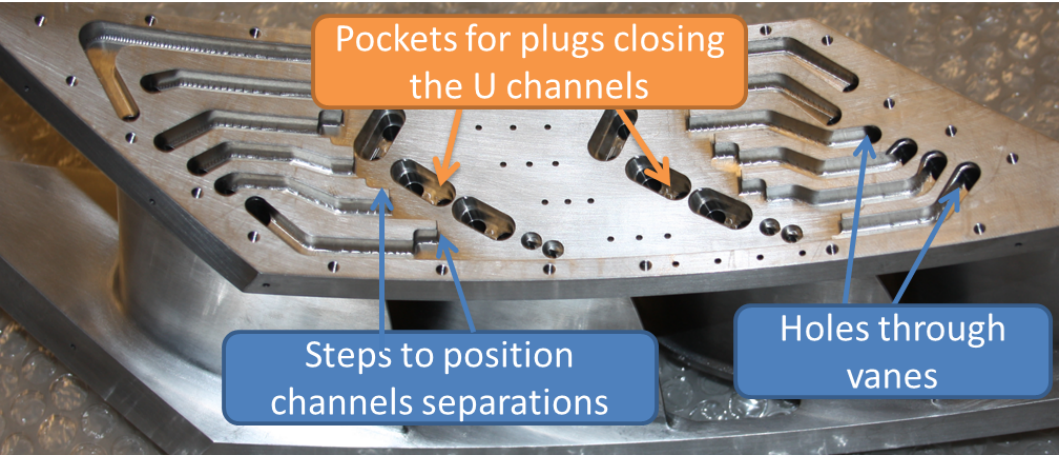


Figure 4.17: Picture of the channels through the hub platform before plugs and separations are assembled.



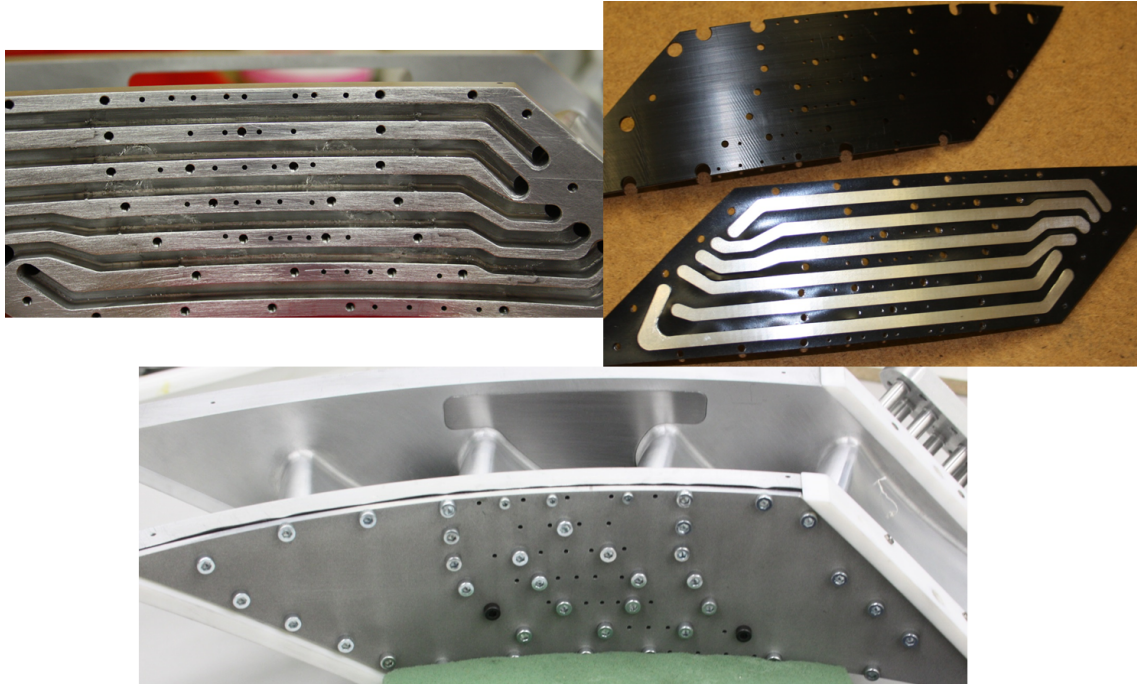


Figure 4.18: Top left - Hub channels after assembly, laser welding of the plugs and separations. Top right - Cover and NBR seal assembled. The top black part is the POM insulation cover. Bottom - Hub platform closed with the different covers

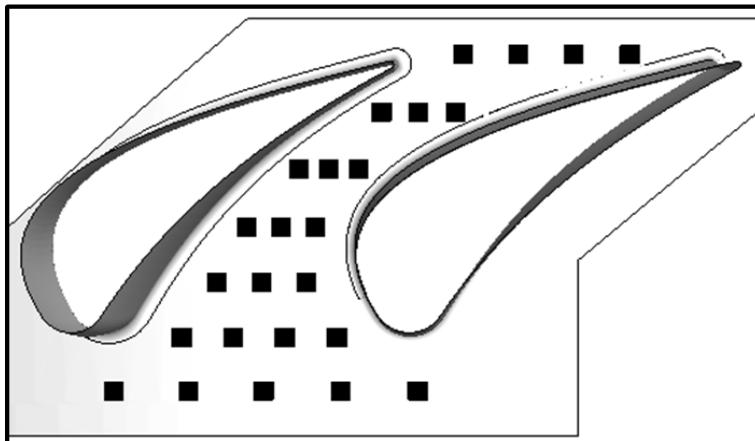


Figure 4.19: Location of the PT100 installed in the hub platform.

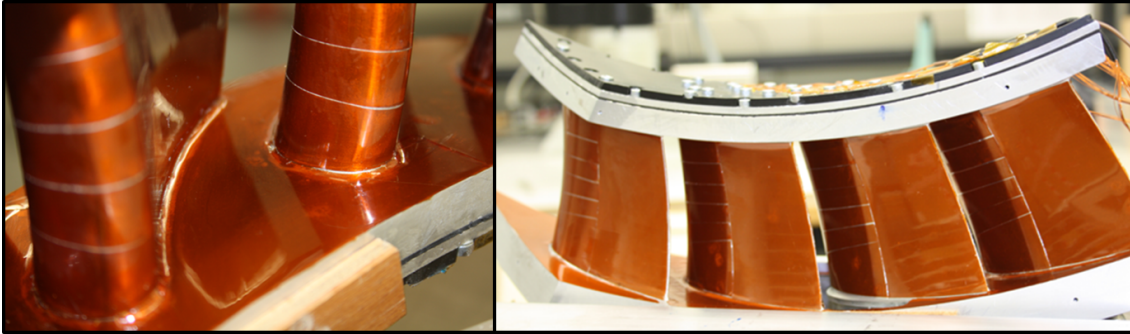


Figure 4.20: Close view of the Kapton layer attached on the measurement passage (left). Right - view of the large patch on the suction side for the four vanes.

complete segment, four vanes and three full passages plus two half passage, has to be covered with the Kapton layer. The procedure divides the segment in three parts, the cylindrical hub and shroud endwall and the vanes. The hub and shroud endwall are covered with large patches of Kapton covering the endwall and part of the filets. The layer is pressed firmly while the paper coating is removed to prevent any air bubble from being trapped underneath. The Kapton patch covering the middle hub endwall is extended at the leading and trailing edges and covers part of the adjacent passages, preventing any disturbance of the flow or measurements due to the presence of an edge. The attachment of the layer on the vane is more complex since the airfoil have a non-developable shape, especially due to the bowed shape at the leading and trailing edges. The airfoil is divided in three zones as shown in Fig. 4.20, the leading edge region is covered with narrow pieces (1cm width) of Kapton to better follow the shape of the airfoil; the downstream regions on the pressure and suction sides are covered with large patches of Kapton. For all the surfaces, the gaps between the patches are filled with epoxy glue (Vishay AE-10) and then polished using a micro-turbine tool. The finishing glue lines are used to prevent any peel off of the layers and ensure an aerodynamically smooth surface.

A trip step is installed afterwards on the suction side of the airfoil to force the flow transition at a specific location. The 0.2mm step is made using epoxy glue shape using a mask and polished to ensure a constant height. The description of the installation of the trip steps is made in the work of Regina. [74]. Before installation in the facility, the segment is painted with the high emissivity black paint mentioned in section 2.1.1 and infrared markers are spread on the endwall surface using a silver ink pen.

#### 4.5.2 Connection to the water network.

The dimensions of the bounding box (Fig. 4.6) and the endwall accessibility (camera extreme angles to access trailing edge) require the connectors to the water network to extend "outside" of the optical access. The connection to the water network is split

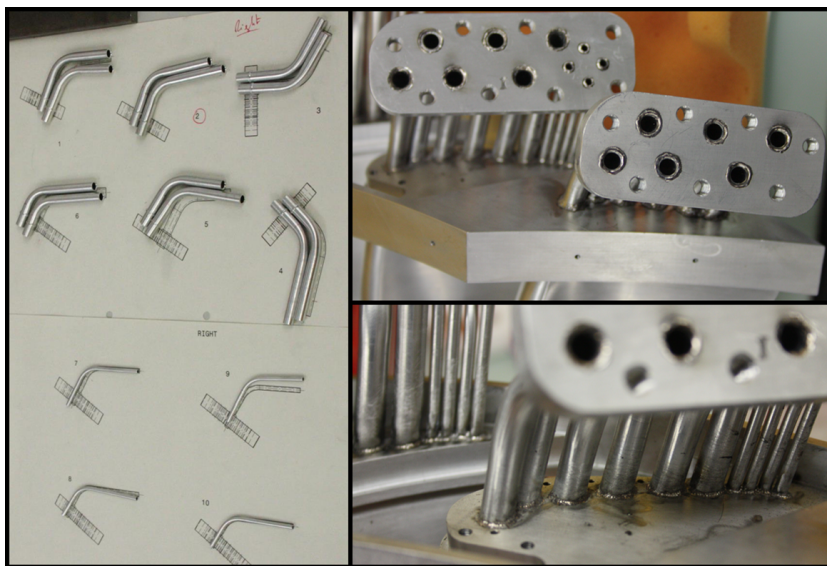


Figure 4.21: Left - Bended tubes on superposed on top of printed reference shapes. Right top - Welding of the tubes tip to the connector. Right bottom - Laser welding of the tubes to the segment.

in two elements, one part attached to the segment feeding the individual vanes with water and another part that can be dismantled when only aerodynamic measurements are performed. The lines feeding the channels have to be individually controlled and monitored and therefore all the connection ensure adequate sealing between the channels. Bended tubes are used to link the individual channels through the segment vanes and the connectors. To simplify the manufacturing of the individual tubes, only one bend per tube has to be made. Therefore a real scale pattern could be printed to adjust the shape of the tubes during the bending operation. The tubes are inserted in the segment for about 8-10mm and through the flat connector manufactured in aluminum. The tubes are laser welded manually to the segment and the tip of the tubes is welded to the connectors. The minimum spacing between tubes close to the trailing edge is 0.25mm which requires precise laser welding skills. Figure 4.21 shows the individual bended tubes (24x5mm diameter tubes and 8x2mm, plus spare parts), the assembly of the tubes and connectors to the segment, and the parts welded together. A manual grinding of the weld lines using sand paper ensure a flat surface of the connector.

The second part of the connection is composed of a flat steel connector matching the aluminum one and ensuring the sealing using O-rings, then standard Swagelok tubes and connectors are used to complete the link to the water network. The Swagelok steel tubes are bent and "routed" along the outer casing of the test section to maintain the accessibility for the aerodynamic holes. The tube bending was performed on a test bench with a mock-up of the facility due to the restricted access to the turbine rig. Figure 4.22 shows the connection of the platform to the water network. Standard Swagelok tubes of



3/8in and 1/4in diameter are assembled (glued with GA61 or metal paste) to the flat steel connectors. The shape of the connectors is defined by the location of the different tubes in the segment and the minimum spacing between tubes to accommodate O-rings and tightening screws.



Figure 4.22: Heat transfer platform installed in LISA and connected to the water network.

## 4.6 Water network

The water network used in the LAVAL facility and described in section 3.1.2 also includes piping to provide temperature controlled water in the LISA facility. A water distribution and monitoring system is developed to provide the water to every channel of the heat transfer platform and control the flow quantities. The schematic of the complete network is shown in Fig. 4.23. The new part located in the LISA facility includes a measurement of the water flow rate using a flow meter ProcessMaster (FEP311) manufactured by ABB, then the flow enters a loop that can be bypassed for safety reason. Three fast acting membrane valves from Norgren are controlled electronically and divert the flow to a bypass pipe in case of emergency. The flow enters a distributor which splits the incoming flow rate to the six hub channels and five tubes further divided in two providing the water to the two middle vanes. The water is brought to the segment using flexible tubes, to isolate the water network from the rig vibration, and enters the segment through the connection described in the previous section.

At the exit of the segment, the individual channels are connected to a measuring section composed of a pressure sensor (0-6bar relative Jumo Midas), a temperature sensor (PT 100 Jumo), a flow meter (REWAG) and a manual valve. The manual valve is used to control the balance the flow rate between the different channels and ensure an acceptable level of temperature uniformity in the test section. The ten U-channels

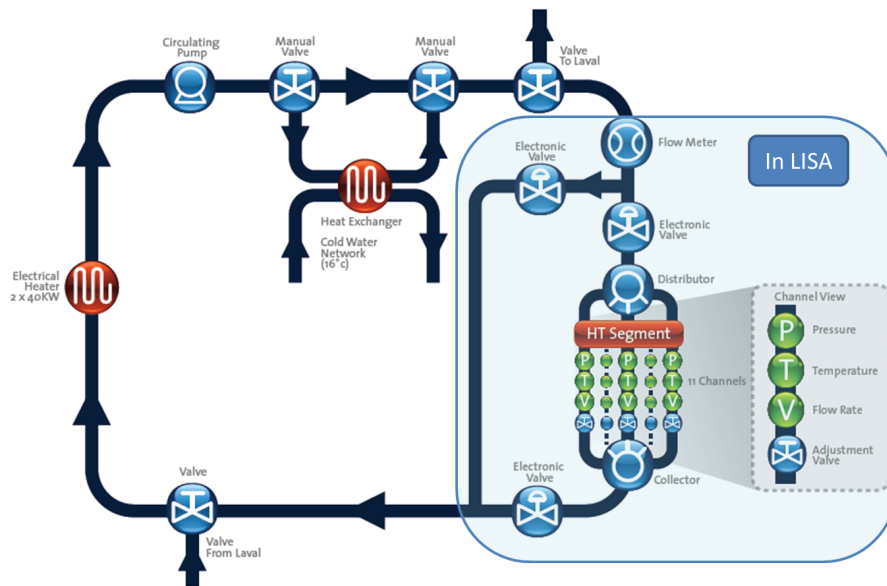


Figure 4.23: Schematic of the complete water network including the newly assembled distribution system in LISA.

of the middle vane are grouped by two, one from the left vane and one from the right vane to reduce the complexity of the network. Finally, the channels are connected to a collector connected to the return channel to the heater. All the equipments are attached to a support made using aluminum profiles which can be moved easily in and out of the facility. Figure 4.24 describes the different component of the water network and Fig. 4.25 shows the installation of the distribution system in the LISA facility. All the equipments were assembled on a test bench to ensure the correct performance of every component as well as the complete network and acquisition chain. The leaktest is a critical milestone in the development of the platform and is performed prior to the installation in the facility.

A volume is created around the distribution system to isolate it from the environment and reduce the variation of temperature, due ventilation. Transparent PVC panels are used to make a containment around the system while granting the access to the manual valves through the top. The tubing connecting the distribution system to the segment are also insulated especially close to the test section, shown in Fig. 4.26.

**Electronic equipments and acquisition system controlling and monitoring the water network.** Multiple sensors are located along the water network and require specific conditions to operate and provide a signal that can be acquired with acquisition cards. PCB boards are designed and manufactured to provide the required current for temperature sensors, or voltage for pressure sensors. The electronic boards are assembled using SMD components and provide external flat DIN connectors to connect to terminal

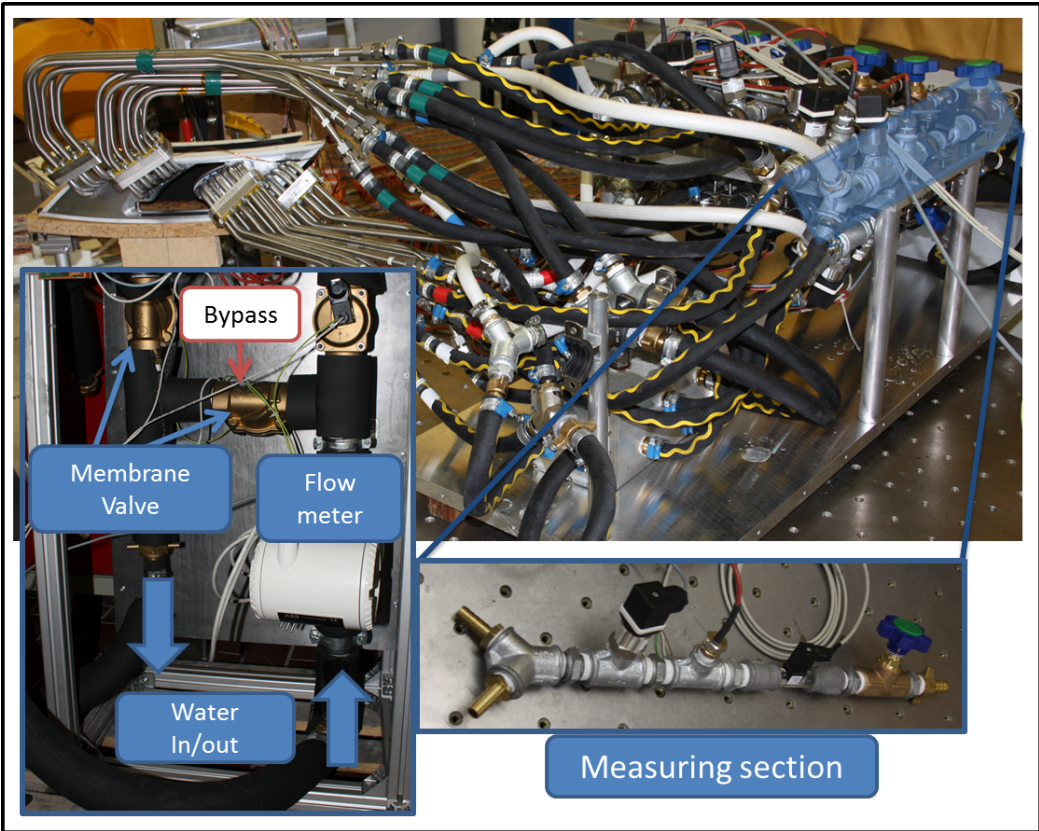


Figure 4.24: Water distribution system on the left the bypass loop, and the zoom on the measuring section with the different sensors.



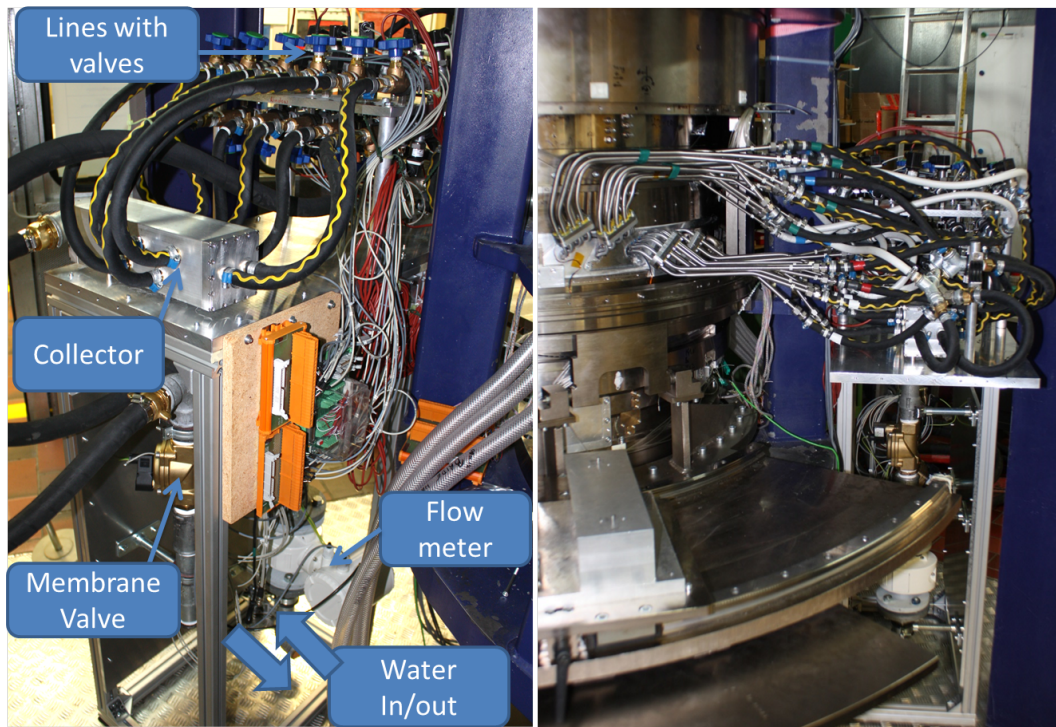


Figure 4.25: Water distribution system installed in the LISA facility. Left - support and connection to the network. Right - Connection to the test section.

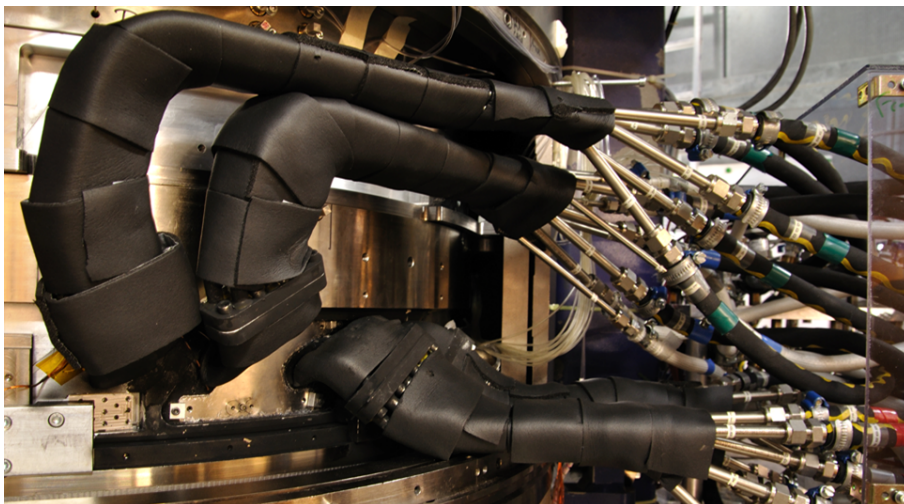


Figure 4.26: Heat transfer platform connected to the distribution system. Black insulating material is taped around the tubing to reduce the heat losses to the environment.

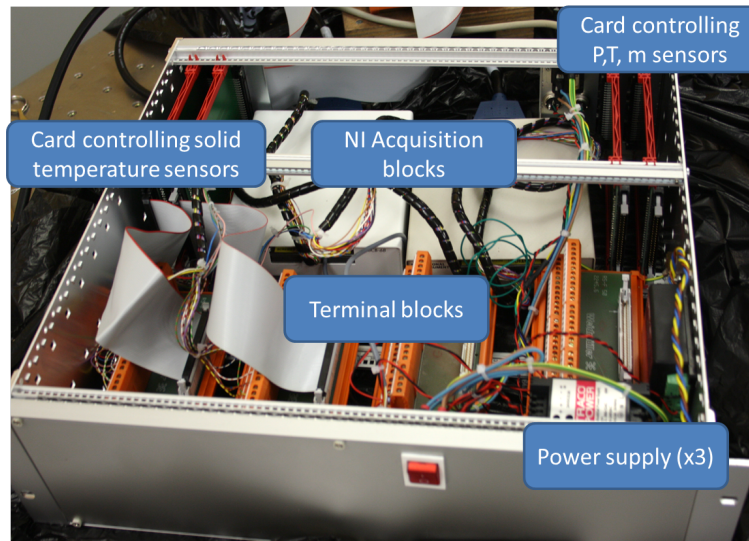


Figure 4.27: Electronic system packaged in a rack monitoring the sensors and controlling the valves.

blocks and the different sensors and the acquisition boards. The electronic system is packaged in a rack shown in Fig. 4.27. Two computers are used to control the water network. One system located in LAVAL monitors and controls the heater and chiller as described in section 3.1.2. The other system is linked to the electronic system of Fig. 4.27, acquires the sensor data from the distribution system, that are the pressure, temperature and flow rate of the main supply and every line. In addition the system controls the operation of the fast acting membrane valves. The data acquisition is spread on two cards, one National Instrument PCI 6225 and one NI PCI4351. The two computers exchange information such as the solid temperature used as an input for the PID regulation of the water temperature.

The live acquisition of the data and the monitoring of the parameter evolution is performed using a program written in LabView. The interface shown in Fig. 4.28 shows the parameters acquired for every line and their evolution in time. This ensures that thermal steady state of the system is established prior to the measurements.

## 4.7 Design of a traversing system to manipulate the infrared camera

The use of multiple view ports to access the endwall with the infrared camera requires a multi axis traversing system allowing the positioning of the camera at a specific location and orientation. The degrees of freedom needed are three translations and three rotation to be able to orient the camera in every position. Also the volume in which the camera should be traversed is as large as 50cm in height to access the two hub platforms, 60cm

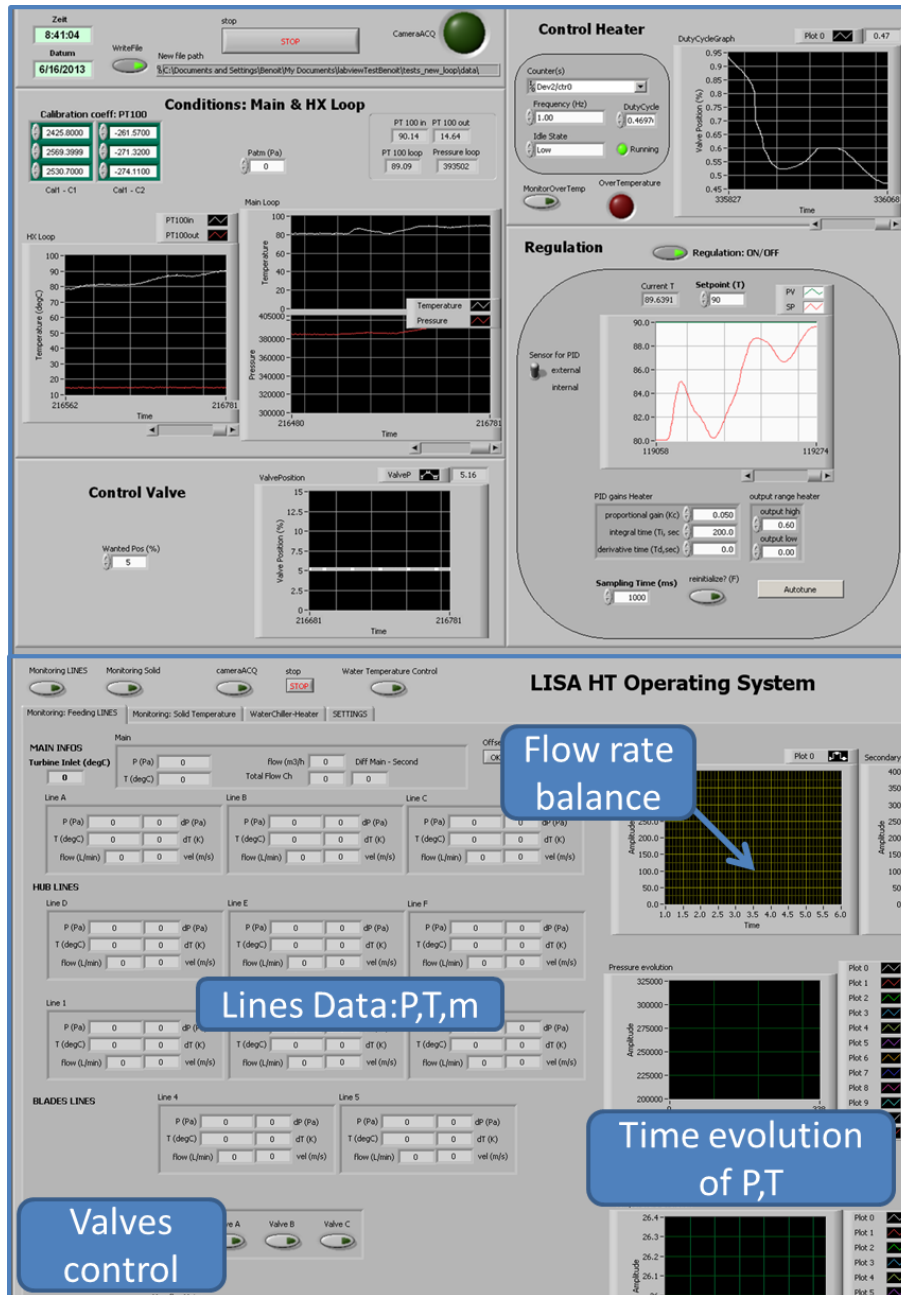


Figure 4.28: Interface of the LabView programs controlling the heater/chiller (top) and the distribution system (bottom).

|                           |        |
|---------------------------|--------|
| Robot weight              | 45kg   |
| Nominal load              | 2.5kg  |
| Max operating temperature | 40degC |
| Max speed                 |        |
| Minimum robot range: Rmin | 230mm  |
| Maximum robot range: Rmax | 600mm  |

Table 4.1: Properties of the robot

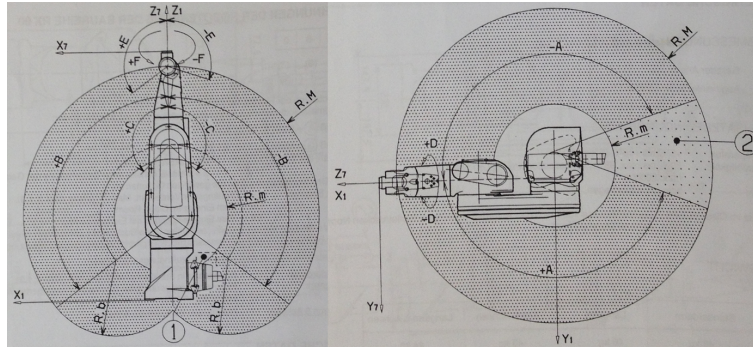


Figure 4.29: Volume traversable by the robot.

in width and 30 in depth. These requirements can only be fulfilled with a 6 axis robot arm. The robot used is a Staubli Rx60, controlled by a CS7 command unit. A pendant allows manual manipulation axis-by-axis in the world or tool coordinate systems, whereas automated tasks can be performed via scripts written in V+ language and loaded on the command system. A few properties of the robot are summarized in Table 4.1 and the volume accessible by the robot is shown in Fig. 4.29. In order to access both platform and stabilize the robot when the arm is extended, a steel support mounted on rails is manufactured. The assembly is visible in Fig. 4.30.

The location and orientation of the robot in the world coordinate system is defined by its position  $(X, Y, Z)$  and a set of Euler angles  $(yaw, pitch, roll) = (\alpha, \beta, \gamma)$  defined by successive rotation around  $Z_0, Y_1$  and  $Z_2$ . The geometrical transformation between the axis system attached to the robot base ( $\mathbb{R}_0$ ) and to the tool ( $\mathbb{R}_3$ ) is described in eq. 4.2 where  $V_3$  is a vector in the tool reference system and  $V_0$  its equivalent in the world system.

$$\begin{aligned}
 X_3 &= R_{30}X_0 = R_{roll}R_{pitch}R_{yaw}X_0 \\
 &= \begin{pmatrix} \cos\gamma & \sin\gamma & 0 \\ -\sin\gamma & \cos\gamma & 0 \\ 0 & 0 & 1 \end{pmatrix} \begin{pmatrix} \cos\beta & 0 & \sin\beta \\ 0 & 1 & 0 \\ -\sin\beta & 0 & \cos\beta \end{pmatrix} \begin{pmatrix} \cos\alpha & \sin\alpha & 0 \\ -\sin\alpha & \cos\alpha & 0 \\ 0 & 0 & 1 \end{pmatrix} \quad (4.2)
 \end{aligned}$$

**LabView program controlling the robot** The robot control unit is rather old and there is direct communication channel (Ethernet or Profibus or any other standard)



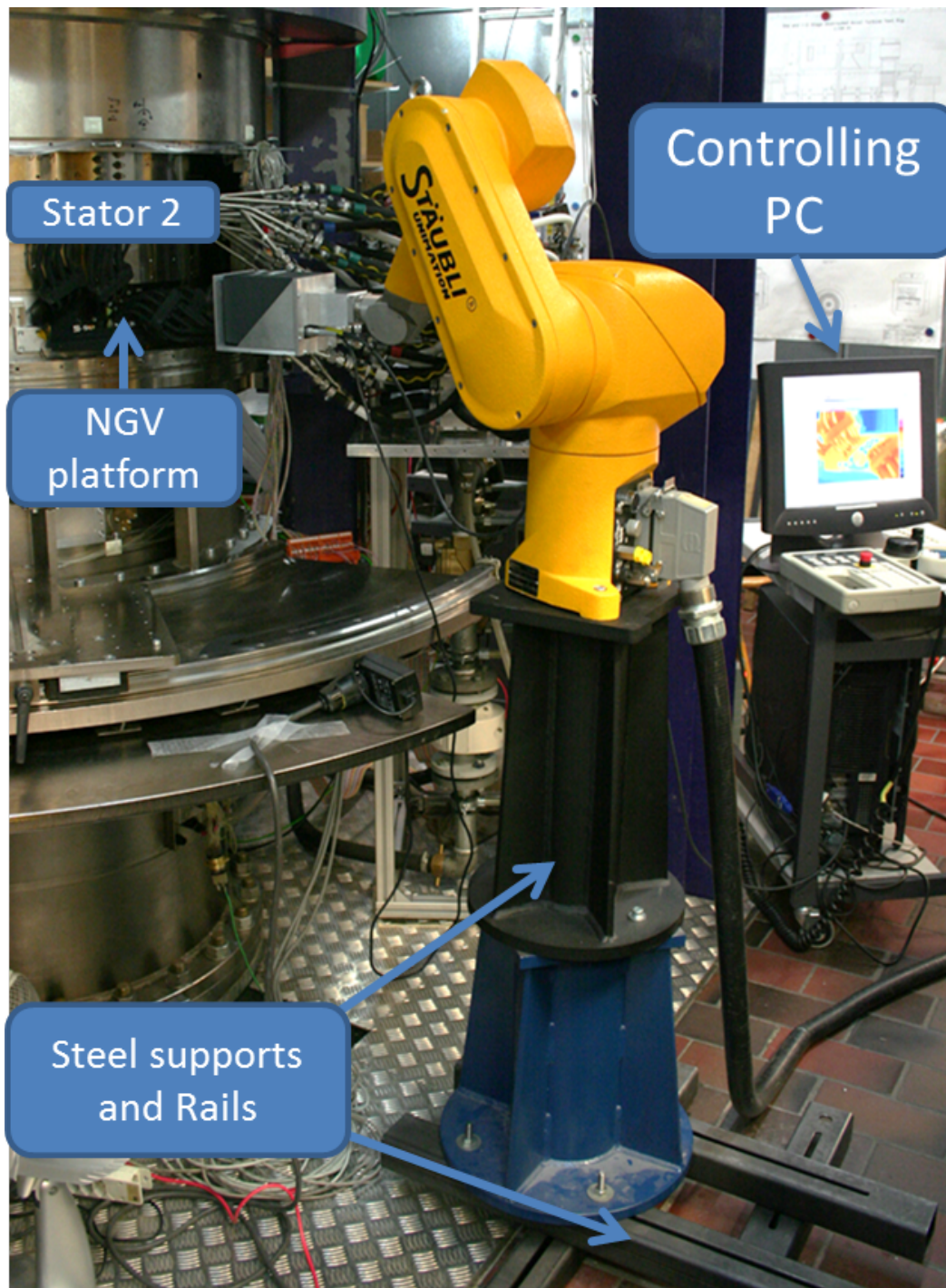


Figure 4.30: Installation of the robot on a steel stabilizing support moving on rails in the facility LISA.



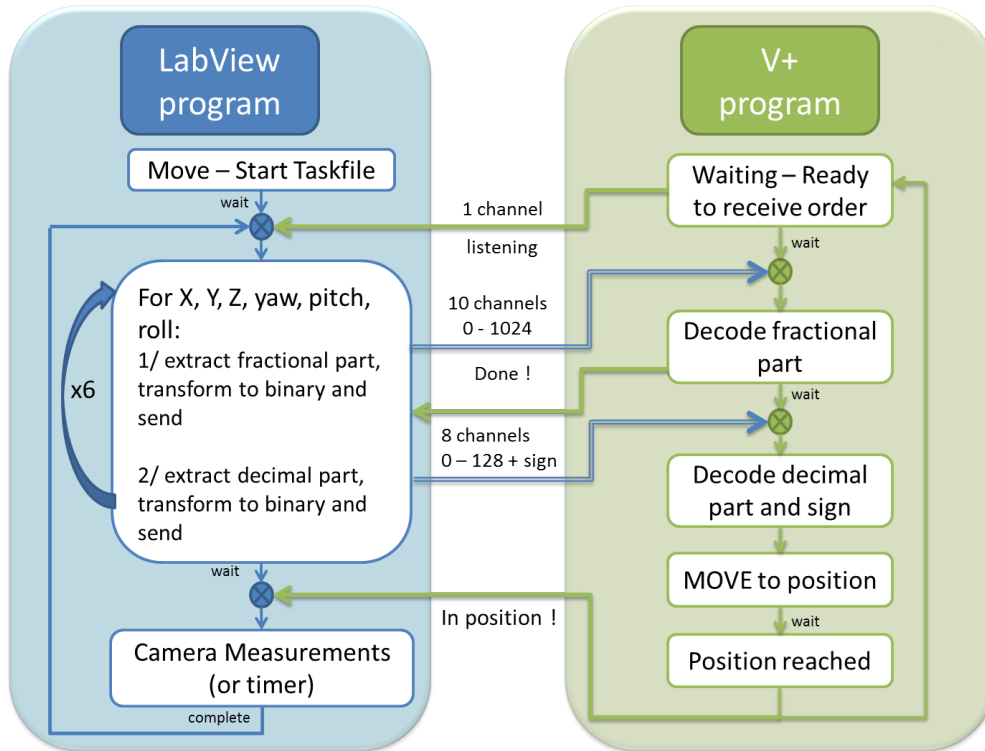


Figure 4.31: Installation of the robot on a steel stabilizing support moving on rails in the facility LISA.

between the robot and an external computer. However the robot is equipped with an interface card providing 12 digital bidirectional channels (inputs or outputs). A LabView program running on a desktop PC controlling a USB 6051 with 12 digital inputs/outputs and a V+ script running on the robot control unit are then used to exchange signals describing commands (move) or status (in position) and binary numbers representing the desired location. The communication process is described in Fig. 4.31 and was initially developed by Lucchini [57]. The key part of the program is the transcription of every position (X,Y,Z) and orientation ( $\alpha, \beta, \gamma$ ) information into three signals: a 10bits binary word for the fractional part, a 7bits words for the decimal part and one bit for the sign. In addition the robot and the PC exchange status information to synchronize their actions. This procedure allows a flexible way to send orders to the robot and position it at any desired location using a single LabView program. The automation of the traversing using task files and its integration with the camera acquisition in a complete LabView program is then done in a similar way as the test bench program. The final interface created for the LabView program is shown in Fig.4.32.

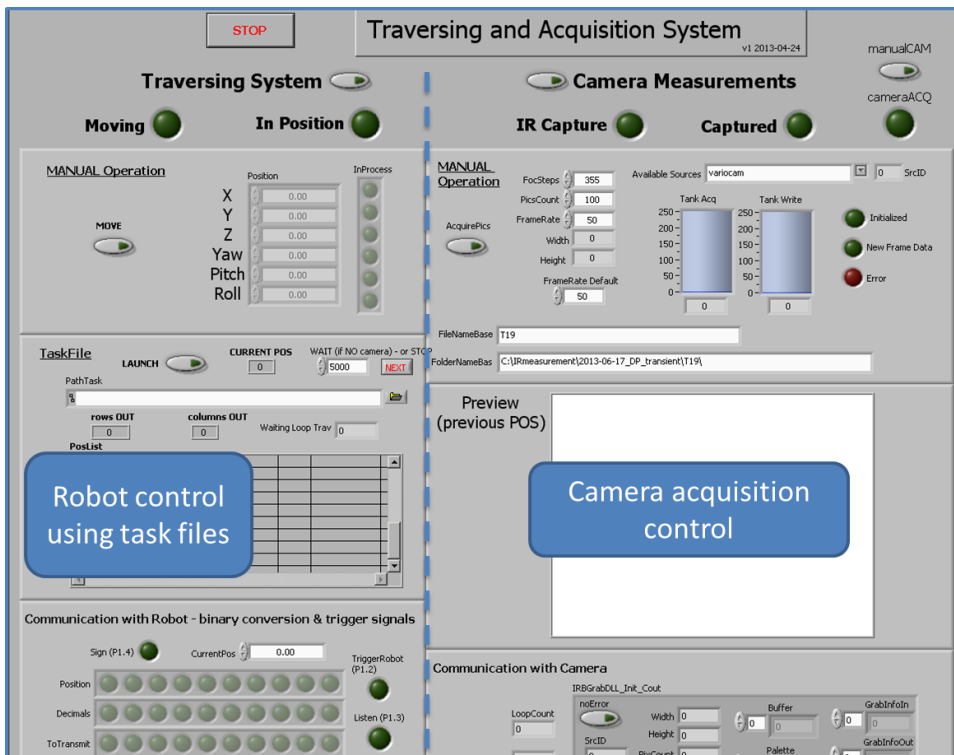


Figure 4.32: Installation of the robot on a steel stabilizing support moving on rails in the facility LISA.

# Chapter 5

## Measurements of heat transfer on the cylindrical hub endwall of an axial turbine.

In this chapter, the measurements of heat transfer on the the NGV hub endwall are presented. The design and integration of the setup is presented in chapter 4. A quick summary of the measurement procedure is made first and then the results are presented for two operating conditions, design points and reduced mass flow. The change in mass flow allows a variation of Reynolds number around 30% which leads to a variation of measured heat transfer coefficient on the endwall. The measurements are compared to numerical predictions performed using the in-house code Multi3. The current chapter also focuses on the uncertainty analysis and the verification of the different assumptions made during the design phase, quasi-isothermal boundary condition, effect of the temperature non-uniformity on heat transfer coefficient. Finally the results obtained raised the question of a change in surface roughness due to the paint laer applied to the segment. A complete characterization of the surface is presented and

### 5.1 Measurement procedure

The heat transfer platform is assembled in the facility together with the rest of the NGV row to form a ring composed of 36 vanes. Fig. 5.1 illustrates the complex 3D shape of the NGV and the Mach number distribution at mid-span predicted using the computational model. The flow experiences a strong acceleration through the passage and switches from an incompressible flow regime at the inlet ( $Ma=0.145$  at design point) to a compressible regime with an averaged exit Mach number of 0.55 (at design point).

The operation of the rig involves first the setting of the desired turbine flow conditions (stage pressure ratio, inlet temperature) and the establishment of a steady state regime (inlet and cavity temperatures mainly). The heat transfer platform is then set and

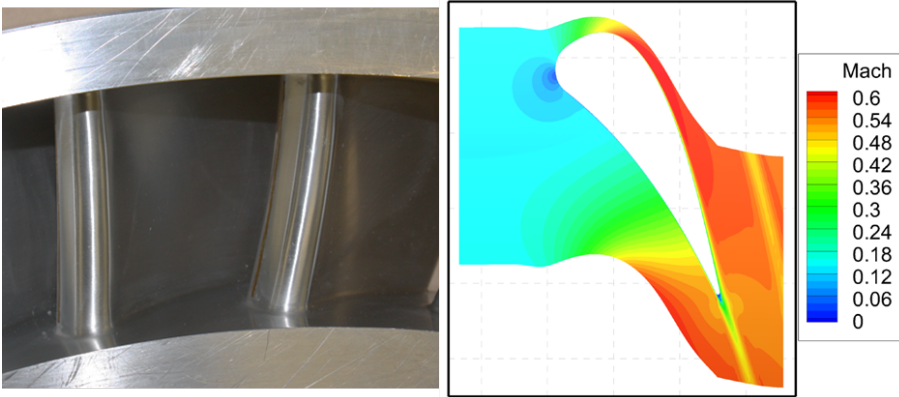


Figure 5.1: 3D geometry of the NGV (left) and predicted Mach number distribution at mid-span.

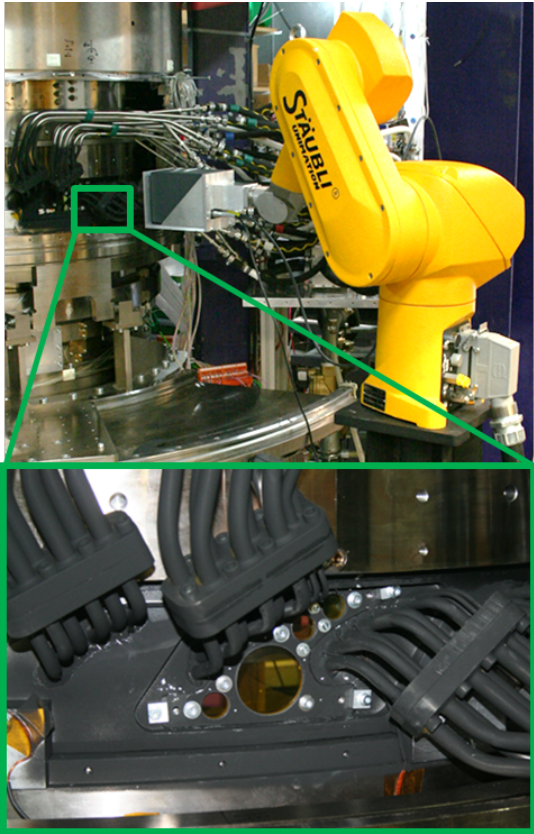


Figure 5.2: Test area in the turbine test rig. The camera is being traversed in front of the infrared transparent windows (highlighted) using the robot-arm.



Figure 5.3: View of the hub endwall covered with Kapton through the opening between vanes.

maintained at a constant temperature  $T_{iso}$  by acting on the circulating water temperature. The embedded sensors provide live information to the user and allow a judgment of the temperature stability, approximately 35-40min were needed to obtain a steady state condition.

Once the conditions are held constant, the surface temperature measurements are performed. An automated non-uniformity correction (NUC) of the camera sensor is performed prior to every acquisition. Because of the limited solid angle provided by each window the infrared camera is traversed in order to map the complete passage. A total of 38 positions determined by a ray-tracing tool developed in Matlab are used to successfully access all the passage points. Each camera position is defined using six parameters (x,y,z,yaw,pitch,roll) to ensure correct positioning using a 6axis robot-arm Staubli RX60. The measurements are performed at a distance of 30 cm, providing a surface resolution of  $0.4mm/px$ . This results in a total of approximately 16000 pixels used to describe the passage. The traversing of the camera and the acquisition of the thermograms are fully automated and performed using a second LabView script.

When the measurements for all the camera positions are completed, the solid temperature  $T_{iso}$  is changed. Multiple solid temperatures ranging from 20 to 90 degC are successively measured. The water chiller coupled with the regulated heater allows fine control of the water temperature below and above the mainstream air temperature (Tab.5.2) . The real time monitoring of the heating process ensures that uniform and stable conditions are reached prior to every measurement.

Fourteen sets of data points ( $T_w, q_{conv}$ ) are acquired using fourteen circulating water temperatures. The linear regression used to deduce the heat transfer coefficient  $h$  and adiabatic wall temperature  $T_{ad}$  is shown in Fig. 5.5. In this graph and as described in section 2.1.2, the intersection of the best fit line and the x axis provides the adiabatic wall temperature as illustrated in the zoom in the same figure. The slope of the line gives

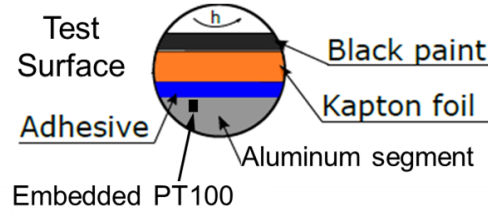


Figure 5.4: Cross section of the multilayer attached to the aluminum segment.

the heat transfer coefficient. The linearity of the fit is also highlighted in Fig. 5.5. Over the complete passage the minimum coefficient of determination  $R^2$  obtained is better than 99.6%.

The solid temperature used as an input for the conduction heat flux calculation is taken as an average of the temperatures measured using the PT100 sensors over the whole passage. This averaging procedure neglects the temperature non-uniformity in the solid which is studied in the uncertainty analysis section. This procedure is preferred since few temperature sensors were lost during the measurements due to thermal cycling or proximity to the rotating parts.

Prior to the measurements, an in-situ calibration of the camera is performed using the temperature sensors embedded in the solid as reference. Measurements with the camera at every position for every plate temperature are performed in the absence of airflow. A correction matrix (first order polynomial fit) is then calculated based on the temperature measured with the camera while measuring the surface temperature with the embedded sensors. This accounts for disturbances at every camera position: external reflection, view angle effects, and so forth. The curves obtained in the correction procedure show that an equivalent transmittance of about 90% is obtained for the system.

## 5.2 Experimental Uncertainty Analysis

The dominant terms for the random uncertainty can be derived analytically from the calculation procedure described in Eq. 2.12-2.15 and are listed in Eq. 5.1-5.3.

$$\frac{\partial T_{ad}}{\partial T_w} = 1 + \frac{1}{h \cdot R_{th}} \quad (5.1)$$

$$\frac{\partial T_{ad}}{\partial T_{iso}} = -\frac{1}{h \cdot R_{th}} \quad (5.2)$$

$$\frac{\partial h}{\partial R_{th}} = \frac{-h}{R_{th}} \quad (5.3)$$

These terms highlight the importance of the multilayer thermal resistance in the overall uncertainty.

In addition to these contributions, a systematic uncertainty has to be taken into account due to the assumption of uniform solid temperature over the passage. In order

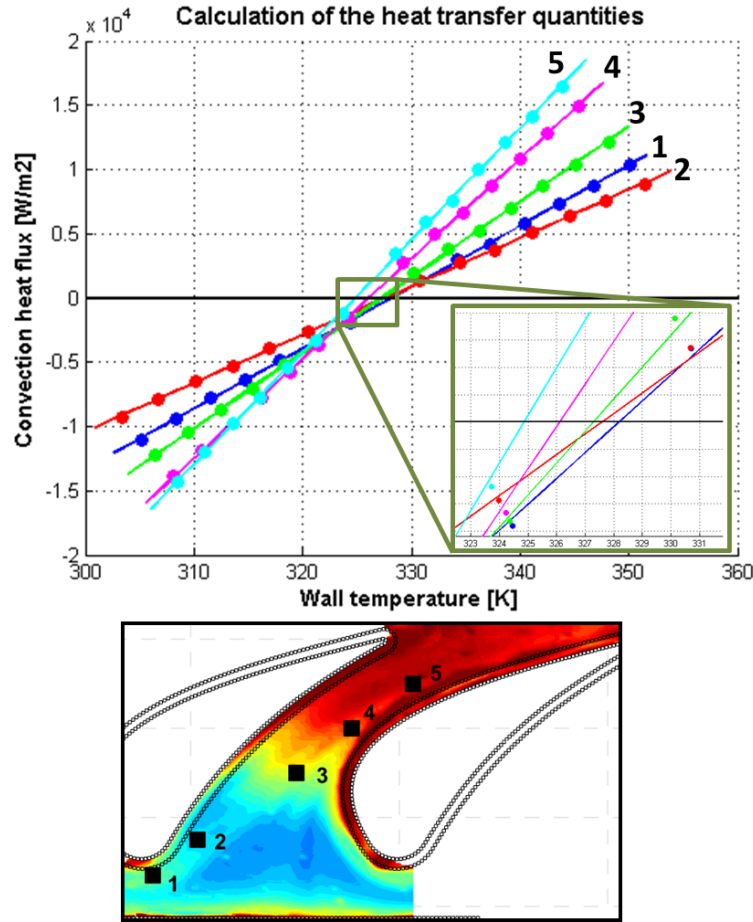


Figure 5.5: Illustration of the linear fit procedure to deduce the heat transfer coefficient and the adiabatic wall temperature. Each best-fit line represents a different location in the passage shown in the bottom contour plot.

to quantify the temperature non-uniformity in the solid, a thermal analysis using a Finite Element Model was performed. The measurement platform as well as adjacent parts (upstream and downstream insulations and parts) were modeled to simulate a realistic configuration accounting for lateral conduction effects. The model is composed of 2.8Mio elements. The boundary conditions are taken from the experiments and are set as follows:

- forced convection in every channel using an estimated heat transfer coefficient based on measured flow rate (correlation of Sleicher and Rouse in [48]) and the water temperature is taken as an average of the inlet and outlet measured temperature on every line
- convection ( $h, T_{ad}$ ) from the measurements is imposed on the passage hub endwall
- convection on the vanes and tip endwall are taken from CFD predictions

Calculations were performed for every circulating water temperature and the solid temperature values were extracted at the position of the PT100 sensors embedded in the solid. Figure 5.6 illustrates the positioning of the PT100 sensors and the temperature non-uniformity quantified as a difference between the maximum and the minimum calculated value at these locations.

The uncertainty in the temperature measurement is calculated using the GUM Workbench software according to the uncertainty analysis guide [44]. Using this tool and its description of the uncertainty with statistical distribution, the propagation of the error from the calibration of the solid sensors to the in-situ calibration of the infrared camera can be assessed. The uncertainty (2 sigma) in the solid temperature measured using the PT100 is calculated to be  $\pm 0.15K$  based on the accuracy of the acquisition devices and the standard deviation of the recorded signal. This leads to an uncertainty (2 sigma) in the measured surface temperature of  $\pm 0.4K$ .

As the calculation of heat transfer quantities is computer-based and involves a linear fit, the method described in Moffat [65, 49] with successive perturbation of the inputs is also used here to calculate the uncertainty based on the measurements as illustrated in Eq.5.4-5.5. As already shown in the analytical description of the uncertainty, the heat transfer coefficient is mostly dependent on the uncertainty value for the thermal resistance. An uncertainty level (2 sigma or 95% confidence interval) of  $\pm 9.8\%$  is calculated for the heat transfer coefficient for nominal  $h = 500W/m^2/K$  and  $\pm 1.1K$  for the adiabatic wall temperature. The uncertainty values for the different parameters are summarized in Table 5.1.

$$\partial h = \sqrt{\left(\frac{\partial h}{\partial T_w}\right)^2 \delta T_w^2 + \left(\frac{\partial h}{\partial T_{iso}}\right)^2 \delta T_{iso}^2 + \left(\frac{\partial h}{\partial R_{th}}\right)^2 \delta R_{th}^2 + \dots} \quad (5.4)$$

$$\partial T_{ad} = \sqrt{\left(\frac{\partial T_{ad}}{\partial T_w}\right)^2 \delta T_w^2 + \left(\frac{\partial T_{ad}}{\partial T_{iso}}\right)^2 \delta T_{iso}^2 + \left(\frac{\partial T_{ad}}{\partial R_{th}}\right)^2 \delta R_{th}^2 + \dots} \quad (5.5)$$

The calculation of the uncertainty for every point on the surface is performed using the successive perturbation of the inputs and the routines used for post-processing. The uncertainty distribution for the heat transfer coefficient is shown in Fig. 5.7.

The uncertainty related to the mapping of the results on the endwall was estimated by re-projecting the infrared markers using the calculated geometrical transformation and comparing the values with their known position. It is estimated to be within  $\pm 0.4mm$  in the portion of the passage that has good coverage of infrared markers.

|                  |                  |
|------------------|------------------|
| $\delta T_w$     | $\pm 0.4K$       |
| $\delta T_{iso}$ | 0.4 - 1 K        |
| $R_{th}$         | $0.0010 \pm 9\%$ |

Table 5.1: Uncertainty values.



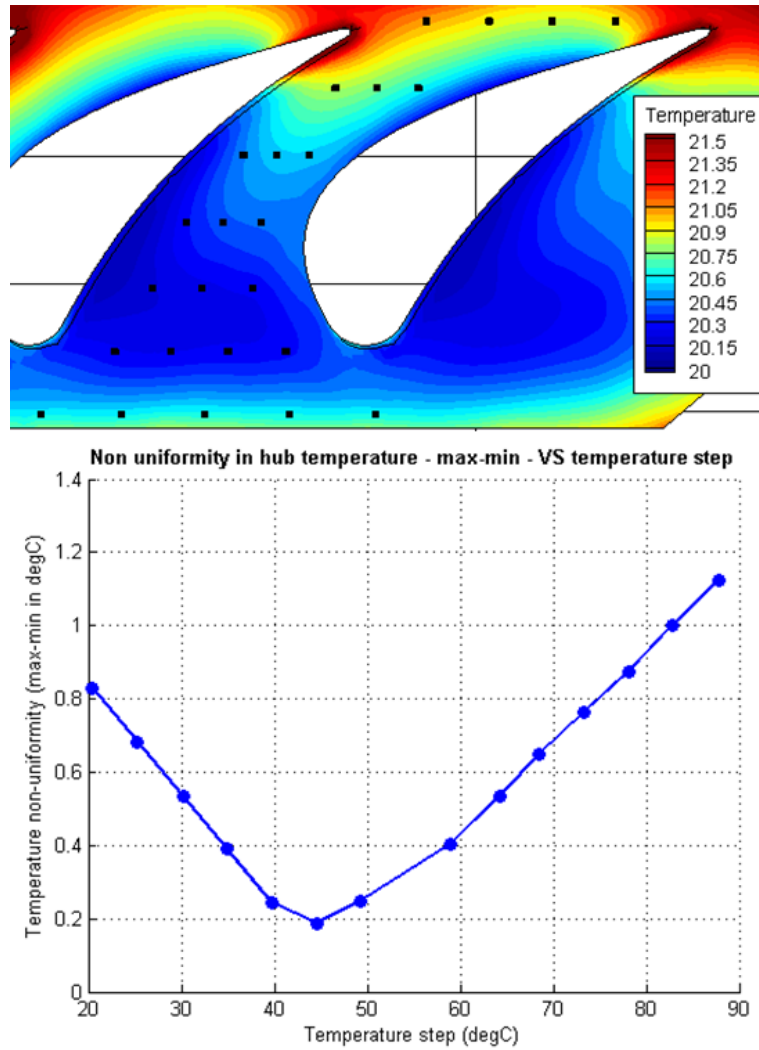


Figure 5.6: Top - thermal predictions of the temperature distribution below the multi-layer. The dots highlight the positions of the temperature sensors embedded in the solid. Bottom - maximum temperature non-uniformity predicted across the passage.

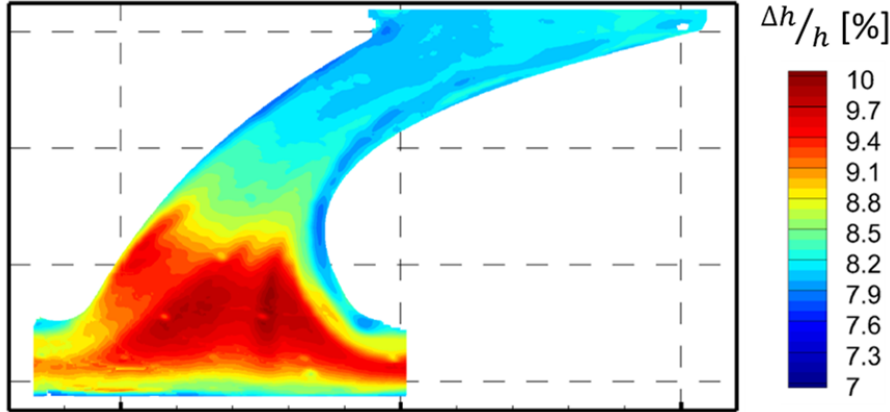


Figure 5.7: Heat transfer coefficient relative uncertainty map.

### 5.3 Computational Setup

The measurements are complemented by a flow simulation in order to obtain a detailed flow field description and help the understanding of the heat transfer physics involved.

#### Solver

The in-house computational fluid dynamics (CFD) code MULTI3 used in this study is an unsteady compressible Reynolds Averaged Navier Stokes (RANS) solver. The solution method is based on an explicit, finite-volume, node-based time-marching algorithm developed by Ni. The discretization is second order both in time and space. To prevent high frequency oscillations and capture shock waves, an anisotropic artificial dissipation algorithm is implemented, which is based on a blending of the second- and fourth differences. The adaptive scaling of the smoothing coefficients accounts for the discrepancy in local CFL numbers in different cell dimensions in the high aspect ratio cells used at the wall. The modeled eddy viscosity is also taken into account in the scaling of the smoothing coefficients. For closure of the RANS equations, a two equation Wilcox  $k-\omega$  turbulence model is implemented in its low Reynolds number form. To speed up the convergence, a local time-stepping approach is used for steady simulations, and dual time-stepping for time-resolved simulations. The latest version of the code running on GPUs is used in the present work. More information can be found in [20, 11].

#### Mesh

A low Reynolds number mesh with approximated file containing 2.2Mio nodes was used ensuring a maximum  $y$ -plus value of 1.2 at design point conditions. The inlet boundary conditions are taken from measured values during the experiments, or from previous measurement campaigns. Inlet total pressure and turbulence intensity levels profile are imposed at the inlet [12]. The inlet total temperature is taken constant across the span

|   | <b>Case1:<br/>Design Point</b> | <b>Case 2:<br/>Low massflow</b> |
|---|--------------------------------|---------------------------------|
| <b>Inlet total temperature</b> $T_{t,in}$           | 328.3 $\pm$ 0.3 K              | 328.0 K                         |
| <b>Stage Pressure ratio</b>                         | 1.65 $\pm$ 0.4%                | 1.32                            |
| <b>Inlet Mach number</b>                            | 0.145                          | 0.12                            |
| <b>Reynolds number</b><br>NGV1 exit - $Re_{C_{ax}}$ | 720k                           | 520k                            |
| <b>Massflow</b>                                     | 11.7 kg/s                      | 8.3 kg/s                        |

Table 5.2: Experimental operating conditions.

and equal to the value reported in Table 5.2. The turbulent length scale is estimated to be 5mm. At the exit of the passage, a radial equilibrium condition is used.

## 5.4 Experimental results

The measurements of heat transfer quantities are performed at two different operating points as detailed in the Table 5.2. The incoming flow conditions were measured in a previous work [12] using pneumatic probes and fast response aerodynamic probe (FRAP).

The results for the heat transfer quantities in the design point case are plotted in Fig. 5.8 and 5.9. Each figure represents the distribution of the measured Nusselt number or the adiabatic wall temperature in the passage. The results are typically reconstructed on a mesh of the passage including the endwall, the upstream and downstream insulations, as well as a portion of the vanes. This allows a more precise assessment of the reconstruction procedure by direct comparison of features from the reconstruction and the geometry (edges, interfaces, etc.). For clarity, the figures shown here present the data on the endwall, and symbols illustrates the location of key geometrical elements. On the sides, the black symbols represent the start of the fillet and the junction fillet-vane. The open black squares located upstream and downstream of the passage highlight the limits of the thermally managed part. Figure 5.10 presents the Nusselt number distribution measured for the low Reynolds number case.

The common features of the heat transfer distribution are noticed in Fig. 5.8 and 5.10. A high heat transfer region is observed near the airfoil leading edge where the boundary layer rolls up and the horseshoe vortex is created.

The migration of the pressure side leg of the horseshoe vortex towards the suction side can be tracked by the high heat transfer line observed on the contour plot. Two zones are then defined:

- the wedge area located in the entrance region of the passage and pointing toward the passage is a typical feature of heat transfer in a cascade. As also shown in

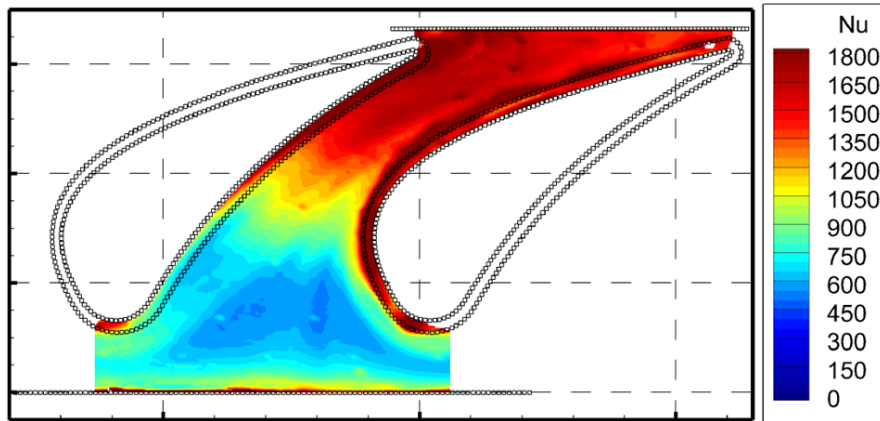


Figure 5.8: Nusselt number distribution in the passage in case1: design point.

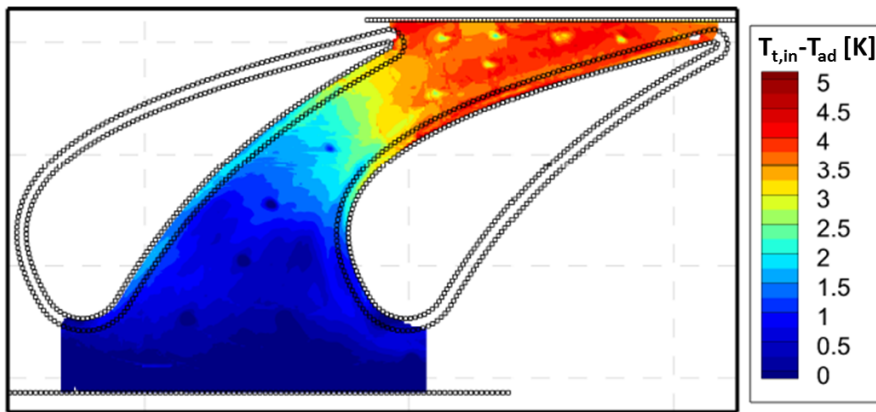


Figure 5.9: Delta temperature between the total inlet temperature and the measured adiabatic wall temperature for case 1 - design point.

Graziani et al. [34] and Lynch et al. [58], a uniform heat transfer coefficient at a level similar to the incoming boundary layer is measured in this region.

- a region of high heat transfer is observed where the horseshoe vortex is seen to migrate from the pressure side to the suction side of the passage. This is a result of the sweep of low momentum fluid contained in the incoming boundary layer by the horseshoe or passage vortex. Downstream of this "separation" line, a new boundary layer develops, leading to high heat transfer rates. The heat transfer coefficient value is then seen to decay from this line in the direction of the pressure side of the passage.

On the other side of the passage, the suction side leg of the horseshoe vortex is also seen to have a significant impact on the heat transfer coefficient distribution when being convected in the passage.

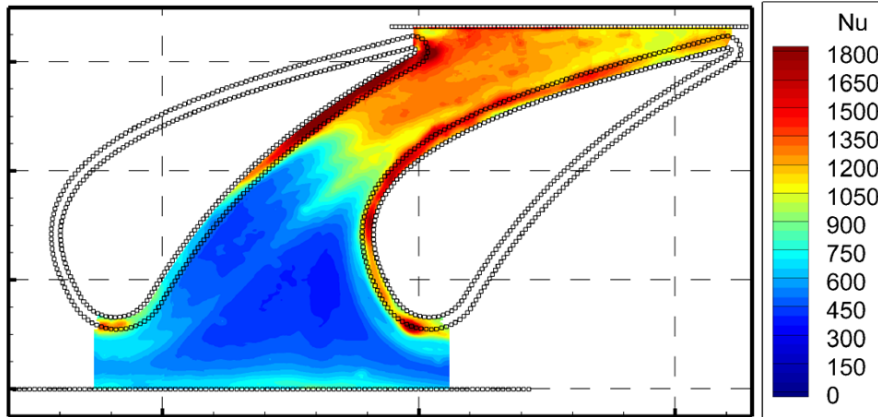


Figure 5.10: Nusselt number distribution in the passage in case2: low mass flow.

A region of very high heat transfer coefficient is observed in the throat area and at the exit of the passage where the flow is accelerated and maintained at elevated velocity (Mach 0.6 in throat at design point). At the exit of the passage the distribution appears uniform across the pitch.

In the second case shown in Fig. 5.10, the heat transfer coefficient levels are generally seen to be lower but a similar distribution is observed. In the upstream part of the passage, a reduction of Nusselt number close to 30% is observed in the wedge area. The location of the high heat transfer pattern caused by the migration of the pressure side leg of the horseshoe vortex is clearly identifiable and seems to be pushed more into the middle of the passage in the second case. The increase in heat transfer close to the throat is observed at a more downstream location compared to the design point case (case 1). In the exit portion of the passage, the Nusselt number remains higher and appears more uniform across the pitch. A variation of 28% of the Reynolds number was achieved by varying the mass flow passing through the turbine stage. According to common correlation for Nusselt number, a change of 30% in the heat transfer coefficient is expected:  $(\frac{Re_{DP}}{Re_{lowM}})^{0.8} = 1.3$ . The area-averaged heat transfer coefficient ratio  $\frac{h_{DP}}{h_{lowM}} = 1.373$  gives a measured increase of 37.3% over the passage in the measurements.

Figure 5.9 shows a contour plot of the measured adiabatic wall temperature on the endwall. The dots that can be seen on the contour are the signature of the permanent infrared markers that are used for the image reconstruction procedure. These marks are not seen in the heat transfer coefficient contours since this other parameter is linked to the slope of the linear fit in the calculation procedure and not the absolute level. As mentioned in Table 5.2, the inlet total temperature is 328.3K. At the inlet of the passage the adiabatic wall temperature is close to the total inlet temperature and then decreases with the effect of the flow acceleration. The decrease is mainly concentrated at the throat where the velocity increase is highest. Downstream of the throat, the adiabatic wall temperature appears to remain constant.

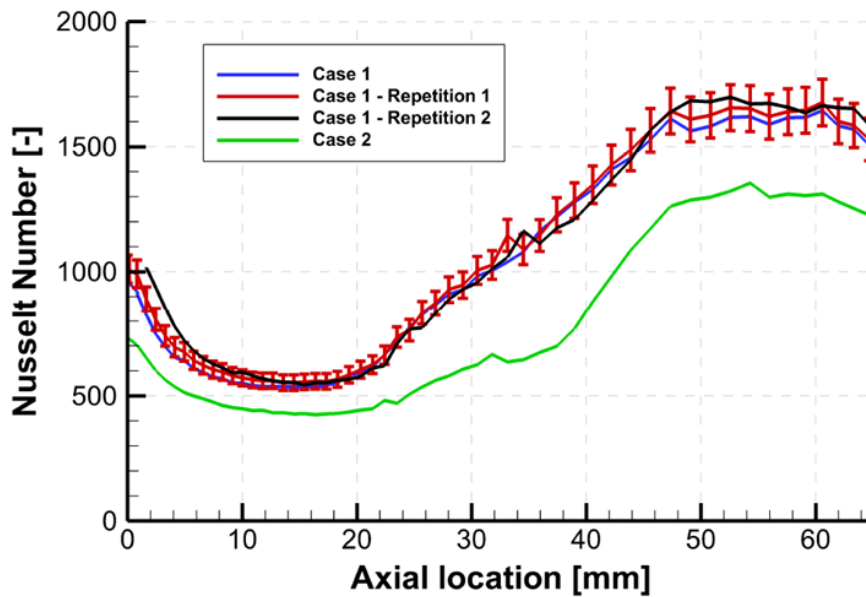


Figure 5.11: Data extracted along a streamline showing the repeatability of the measurement procedure. The error bar shows the  $\pm 10\%$  uncertainty.

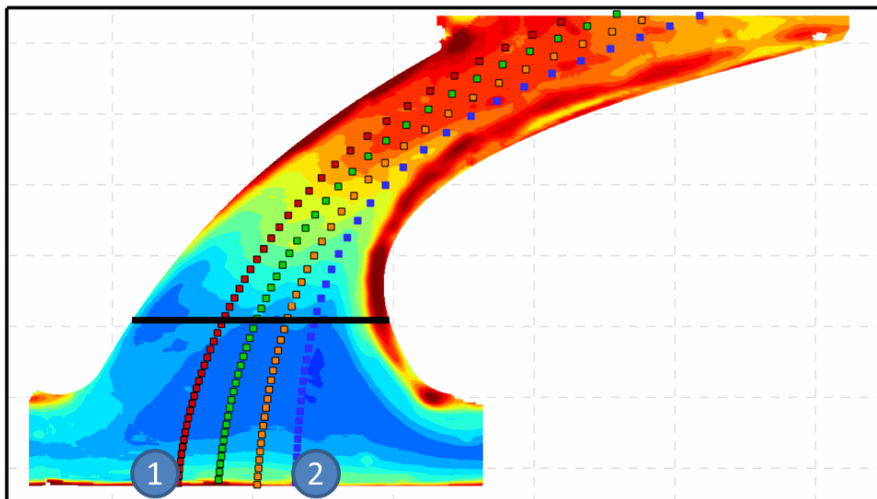


Figure 5.12: Location of the streamlines used to extract the data for quantitative comparison. The black line shows the extent of the streamlines used in Fig. 3.18 and their color code. The line labeled 1 is used in Fig. 5.11. Lines labeled 1 and 2 are used in Fig. 5.15 and 5.17.

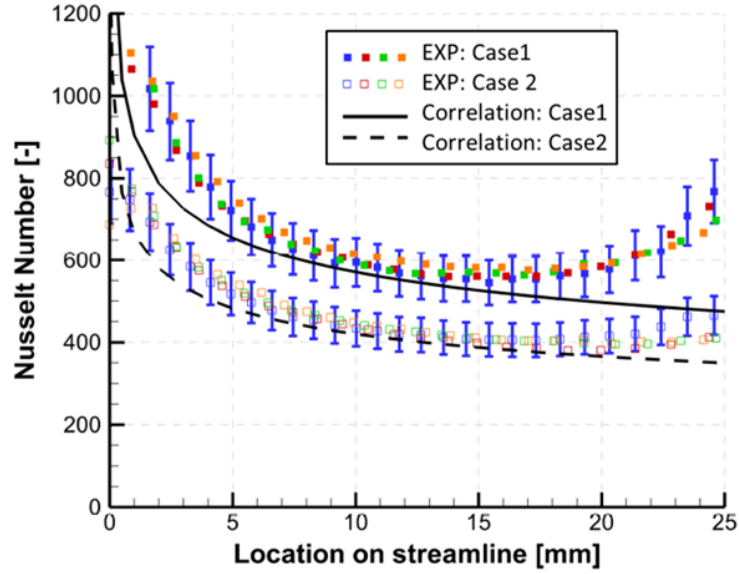


Figure 5.13: Comparison of the measured Nusselt number with established correlation for the corresponding incoming flow velocities. The error bars ( $\pm 10\%$ ) are plotted for only one streamline per case. Fig. 5.12 provides the streamline locations.

An estimation of the adiabatic wall temperature using a turbulent recovery factor equal to  $r = Pr^{1/3}$  is shown in Eq. 5.6, using  $M = 0.65$ . The calculated value is in the same order of magnitude as the measured temperature for case1.

$$T_{t,in} - T_{ad} = (1 - r) \frac{u_{\infty}^2}{2C_p} = 2.9K \quad (5.6)$$

The repeatability of the measurement technique is shown in Fig. 5.11 using data extracted along streamlines. Three measurements of the design point case were performed on non-consecutive days and for two camera and robot installations. The data shown here therefore includes the effect of the camera positioning and the data reconstruction procedure. During the measurement campaign, the reconstruction procedure was improved and mainly the number of markers used on the surface was increased. This explains the apparent shift between the black curve and the other two lines for case1 in the inlet part of the passage. The comparison between measured datasets shows a difference below the uncertainty level quoted previously and appear to be around  $\pm 5\%$ . The data from case 2 also provide a comparison between repeated measurements and the variation due to a change in Reynolds number.

Figure 5.13 shows a comparison of the measured data for the two operating conditions with correlation published in the literature (heat transfer on a turbulent flat plate with unheated starting length). The data from the measurements are extracted along inviscid streamlines as depicted in the top part of Fig. 5.13. The comparison is made only in the region where the acceleration is limited and where no 3D flow features impact the

heat transfer. The comparison of the heat transfer coefficient decrease with downstream distance and the absolute level measured shows a good agreement with values from the correlation for both cases. The increase in Nusselt number due to the flow acceleration in the passage is already noticeable on the rightmost part of the curve.

## 5.5 Comparison with numerical predictions.

The numerical model is also used to provide heat transfer quantities to compare with the measurements. A similar approach to the experiment is used to calculate the heat transfer coefficient. Three simulations are run, one with adiabatic walls and two with isothermal walls at different temperatures. The adiabatic wall temperature is extracted from the adiabatic simulation and a linear fit using data points from the three predictions is then used to obtain the heat transfer coefficient.

Figures 5.14 and 5.16 show the results from the numerical predictions in terms of temperature difference between the total inlet temperature and the adiabatic wall temperature and Nusselt number. The predicted adiabatic wall temperature shows a strong agreement with the measurements shown in Fig. 5.9. In particular the location and magnitude of the sharp decrease in adiabatic wall temperature is observed at the same location in both CFD and experiments, it occurs close to the throat where the strongest acceleration takes place. These observations are confirmed quantitatively when looking at Fig. 5.15 which shows the data extracted along two streamlines for the experiments and the predictions. In Fig. 5.15, the difference between experimental data (symbols) and numerical prediction (lines) is within the experimental uncertainty levels.

The Nusselt number distribution shown in Fig. 5.16, on the other hand, seems to be over-predicted by the numerical model at the entrance of the passage but appears closer to the experimental data shown in Fig. 5.8 at the exit. Fig. 5.17 complements this observation quantitatively with a comparison of data extracted along two streamlines, one close to the pressure side and one closer to the suction side. Overall the Nusselt number extracted along streamlines from the predictions is relatively far from the measurements for certain reasons, especially close to the pressure side of the vane where a difference up to 50% can be observed.

Figure 5.18 represents the location of the horseshoe vortex (HV) from its formation close to the leading edge of the vane to its migration through the passage. Two sets of streamlines highlight the trajectory of the pressure side leg of the HV across the passage from the pressure side to the suction side. The first set is injected close to the leading edge where the vortex forms and another set is injected at a different circumferential location to show how the flow is entrained and swept in the passage. The superposition with the Nusselt number contours confirms the link between the increased heat transfer coefficient values and the down wash side of the vortical structure. Downstream of the leading edge, between the HV and the vane pressure side, the pattern of heat transfer coefficient comes



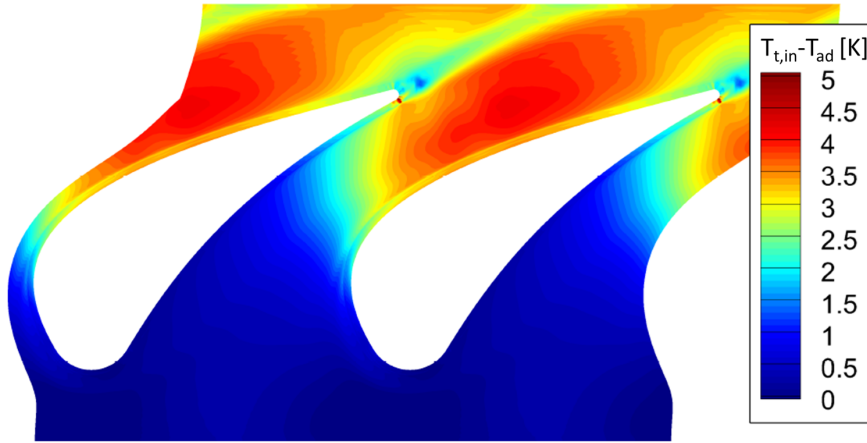


Figure 5.14: Difference between total inlet temperature and adiabatic wall temperature predicted for case 1.

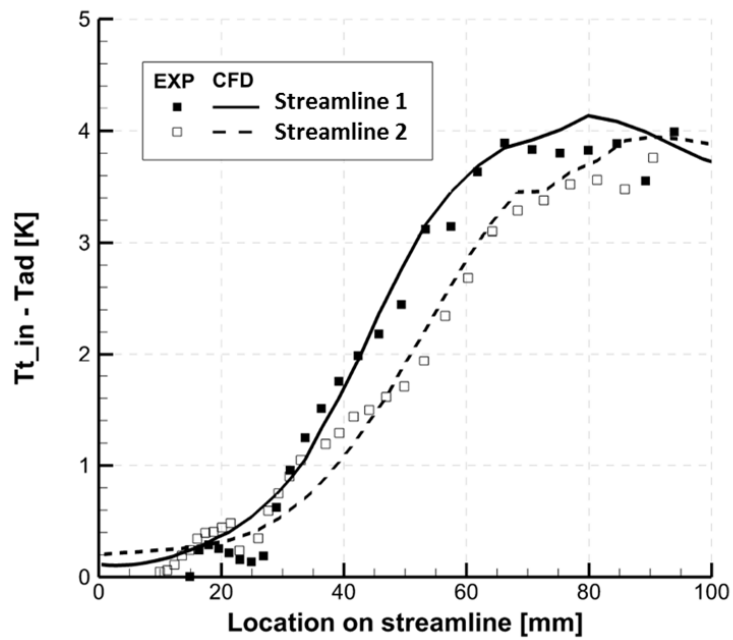


Figure 5.15: Comparison of measured and predicted temperature difference  $T_{t,in} - T_{ad}$  along two streamlines for case1. Fig. 5.12 provides the streamlines locations.

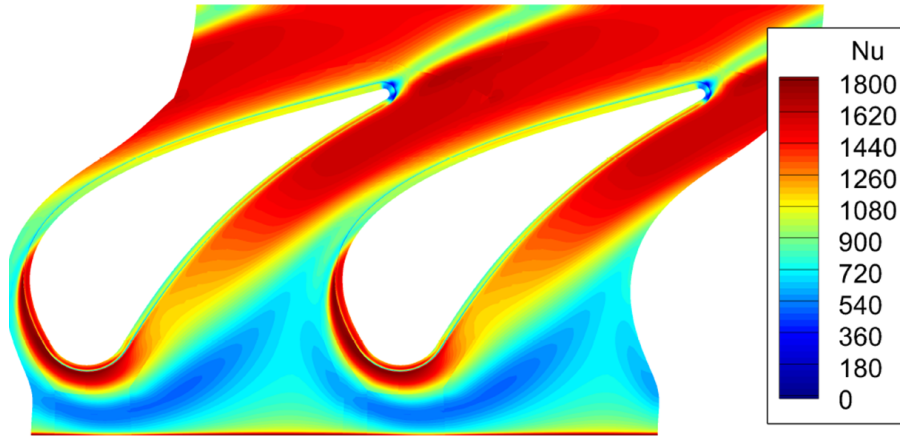


Figure 5.16: Nusselt number distribution predicted for case 1.

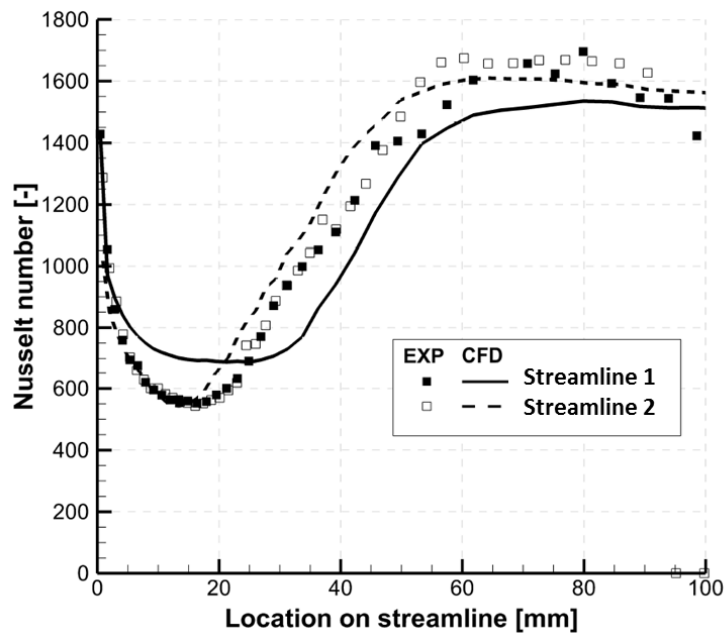


Figure 5.17: Comparison of measured and predicted Nusselt number along two streamlines for case 1. Fig. 5.12 provides the streamlines locations.

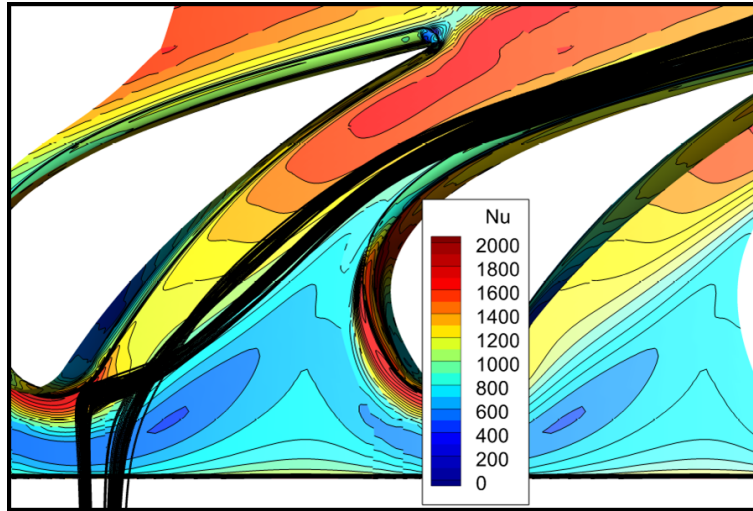


Figure 5.18: Superposition of streamlines highlighting the formation and the trajectory of the horseshoe vortex, and the Nusselt number contours.

from the creation of a new boundary layer immediately downstream of the leading edge and its development along the passage. The effect of the flow acceleration is visible in the continuous increase in heat transfer coefficient when approaching the throat.

The location of the horseshoe vortex and its migration through the passage seems to differ between the predictions and the experiment. In the first half of the passage, in particular, the predicted region of high heat transfer downstream of the horseshoe vortex is almost absent in the measurements while the increase in heat transfer coefficient due to flow acceleration is better predicted.

## 5.6 Effect of temperature non-uniformity on heat transfer coefficient

As highlighted in the uncertainty analysis section, the measurements are performed over a quasi-isothermal surface. The temperature non-uniformity observed in the thermal analysis can also have an impact on the measured heat transfer coefficient data. An analytical analysis of the impact of non-uniform surface temperature on the heat transfer coefficient is carried out. The approach chosen is to extract the surface temperature variation along a streamline, model it using a power series and derive analytically the heat flux and heat transfer coefficient for a turbulent flat plate case with varying surface temperature. The analytical solution is extracted from Kays, Crawford and Weigand [48].

The surface temperature decomposition in power series is done according to Eq. 5.7 where  $T_\infty = 328.35K$ , and the corresponding wall heat flux is calculated using Eq. 5.8. Finally the heat transfer coefficient is calculated using Eq. 5.9.

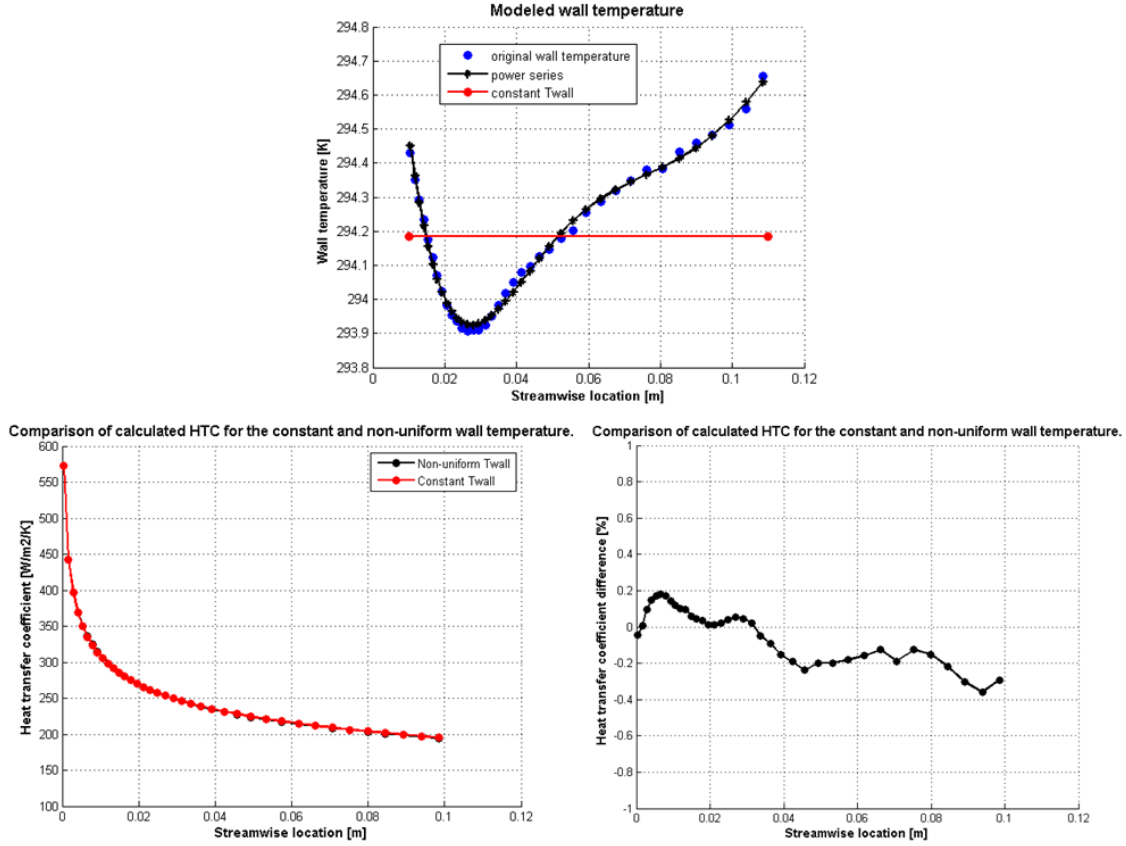


Figure 5.19: Top - Modeling of the surface temperature using 7th order polynomial fit. Goodness of fit: R-square: 0.9986. Bottom left - Heat transfer coefficient obtained using Eq. 5.9 for uniform and non-uniform wall temperature. Bottom right - difference between the two cases: maximum change of HTC expected  $\pm 0.5\%$ .

$$T_s(x) = T_\infty + A + \sum_{n=1}^{\infty} B_n x^n \quad (5.7)$$

$$q_s''(x) = 0.0287 \frac{k}{s} P_r^{0.6} Re_x^{0.8} \left( A + \sum_{n=1}^{\infty} n B_n x^n \right) \frac{10}{9} \beta_n \quad (5.8)$$

$$\text{with } \beta_n = \frac{\Gamma(\frac{8}{9})\Gamma(\frac{10}{9}n)}{\Gamma(\frac{8}{9} + \frac{10}{9}n)}$$

$$HTC(x) = \frac{q_s''(x)}{T_s(x) - T_{infty}} \quad (5.9)$$

The results of the analytical study show that the variation of heat transfer coefficient is confined to  $\pm 0.5\%$  with the current temperature variation along the passage. The impact of the non uniformity in wall temperature on the heat transfer coefficient is therefore negligible.

## 5.7 Conclusions

This paper presents and analyzes the measurement of heat transfer quantities on a cylindrical endwall in the first vane passage of a rotating turbine facility using a quasi-isothermal boundary condition. A four-vane segment dedicated to heat transfer measurements was developed to ensure the correct set-up of the isothermal boundary condition, provide optical access to the surface and allow the calculation of heat flux through an insulating layer. High resolution measurements ( 20k points every 0.4mm in the passage) were performed using infrared imaging through multiple view ports and reconstructed using projective geometry to obtain a full passage map.

Heat transfer quantities in terms of heat transfer coefficient and adiabatic wall temperature were successfully derived from a set of hub endwall temperature measurements using a quasi isothermal boundary condition. The tests were performed under two different sets of operating conditions with a variation in exit Reynolds number of 28%. The overall increase in heat transfer coefficient is 37% close to the 30% expected using a turbulent flat plate correlation. The repeatability of the measurements was seen to be  $\pm 5\%$  for the design point case. A comparison of the data to a correlation published in literature confirmed the evolution and magnitude of measured Nusselt number at the inlet of the passage.

The insight provided by the CFD simulations helps to highlight the impact of the secondary flow features on the measured variation of heat loads. The high resolution of the measurement helps to identify the impact of the pressure leg of the horseshoe vortex during its migration through the passage. The comparison between the two cases highlights the strong relationship between the secondary flow structure and their migration through the passage and the thermal loads on the endwall. Overall the difference between measurements and predictions is especially important when looking at data along streamlines. The contour plots show that the impact of the flow acceleration and 3D flow features can be captured in the predictions, but their location remains an issue.

While the level of uncertainty would not yet allow accurate component lifetime predictions, the present work is a first milestone in providing high resolution experimental data for real turbine geometry operating under realistic conditions that can be directly compared to numerical predictions.



# Chapter 6

## Numerical predictions of heat transfer on rough surfaces.

### 6.1 Surface roughness measurements

The paint used to coat the Kapton layer and ensure a high emissivity is manually sprayed on the surface using a professional air gun. However this process generates a relatively rough surface compare to the bulk material used as a support (aluminum or copper). This surface property has an impact on aerodynamic performances as well as on heat transfer. The surface roughness was therefore quantified after applying the paint, before and after the measurements in the rig. A first set of measurements of integral roughness quantities is provided using a line scan performed with a profilometer. In order to obtain more information on the roughness type and statistics, a more detailed 3D scan of the surface is performed using an optical system. The equivalent sand grain roughness is derived from the later measurement technique.

#### 6.1.1 Measurement of integral roughness quantities

The integral quantities are measured using a profilometer, shown in Fig. 6.1 which measure the oscillation of the surface from which integral quantities are deduced. The major quantities of interest are the arithmetic roughness  $R_a$ , the peak to peak roughness  $R_z$ , the root-mean-square value  $R_q$ , the skewness  $R_{sk}$  and kurtosis  $R_{ku}$ . Some of these parameters from measurements on the painted platform are shown in Table 6.1.1.

The measurement system Talysurf 800 is composed of a  $2\mu m$  diamond tip that is mechanically touching the surface and traversed along lines on the surface. The deflection of this tip is measured using an optical sensor providing a vertical resolution of  $0.8nm$ . Horizontally the resolution is on the order of  $1\mu m$ . From the raw measurements, the primary profile of the surface is determined using a filter according to ISO norms (ISO4287:1997),

| Case           | Inlet K2 | Exit K2 | Inlet K3 | Exit K3 |
|----------------|----------|---------|----------|---------|
| Ra [ $\mu m$ ] | 11.7     | 11      | 11.3     | 19.6    |
| Rz [ $\mu m$ ] | 91.3     | 72.6    | 72.9     | 121.2   |
| Rq [ $\mu m$ ] | -        | -       | 14.5     | 24.8    |
| Rsk [-]        | -        | -       | 0.28     | 0.37    |
| Rku [-]        | -        | -       | 3.1      | 3.4     |

Table 6.1: Measured integral values of roughness.

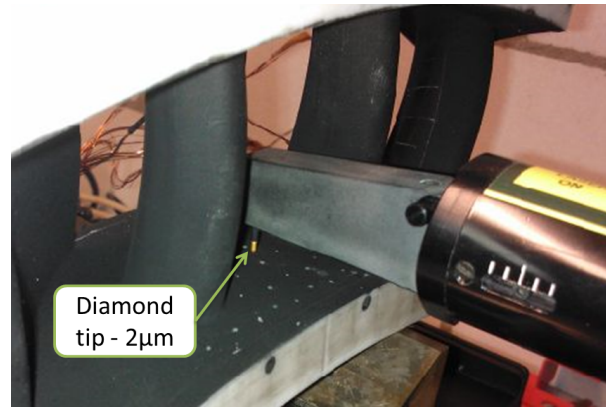


Figure 6.1: Measurement of roughness quantities on the inlet portion of the NGV endwall using a profilometer.

and the roughness quantities are derived after subtraction of the primary profile from the data.

However for a modeling purpose, a variety of correlations can be used based on these values to obtain an equivalent sand grain roughness and lead to a wide range for the results. The surface roughness needs more detailed measurement of its distribution, shape, spacing, etc. to be better characterized.

### 6.1.2 Determination of an equivalent sand grain roughness using a 3D scan of the surface.

The 3D measurements of the surface are performed on a flat test piece composed of an identical structure as the measurement platform, an aluminum support covered with a Kapton sheet attached with adhesive and finally painted using the same mixture and spray gun. The use of a test piece is motivated by the limitations from the measurement system, which can mainly scan flat surfaces and require a short working distance. The hub endwall is not accessible with these requirements. The system is an Alicona Infinite focus system which uses different focus settings and identify the in-focus part of the image to reconstruct the 3D picture of a scanned surface. Every scan covers roughly a 1x1mm square and the test part can be traversed to cover larger area. A 15x15mm region



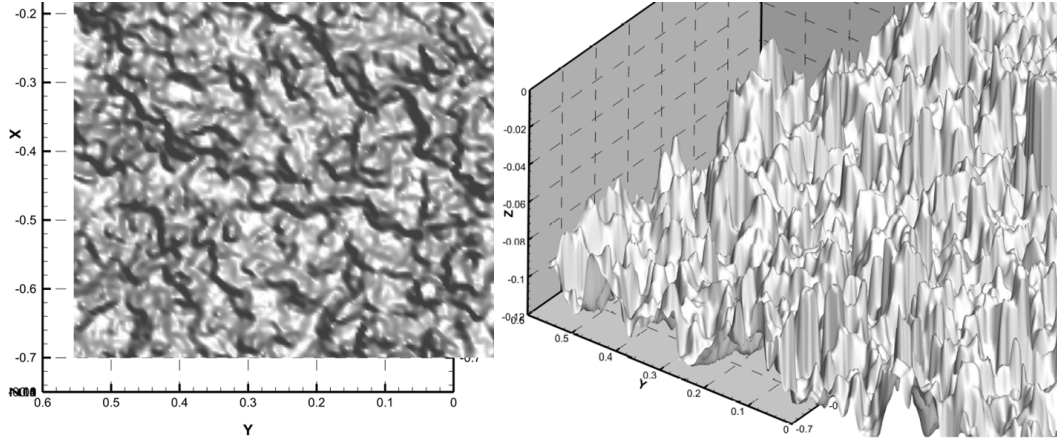


Figure 6.2: Top view (left) and 3D view (right) of the surface roughness obtained from the 3D scan.

is scanned in the current test. The outcome of the procedure is a 3D mesh describing the surface shape at a microscopic scale. The vertical resolution of the tool is around 10nm. Figure 6.2 shows the shape of the roughness elements and their distribution. The roughness is very "peaky" and has a very stochastic distribution. The 3D triangular mesh obtained is composed of 31.5Mio elements.

The concept of shape factor is used to obtain the equivalent sand grain roughness parameter. As described first in Sigal and Danberg [23], a roughness density parameter is calculated for every roughness elements. It is decomposed in a wetted area and a projected frontal area to calculate the shape factor  $\Lambda_s$  as described in Fig. 6.3. The definition used in the present work follows the recommendation of van Rij et al. [87], who defined the shape factor as a integral value over the complete surface and not for a single element, as defined in Eq. 6.1.

$$\Lambda_s = \frac{S}{S_f} \left( \frac{S_f}{S_w} \right)^{-1.6} \quad (6.1)$$

$S$  : Area of the Reference Area

$S_f$  : Area of the Frontal Wetted Surface of all Roughness Elements

$S_w$  : Sum of all Wetted Surfaces of each Roughness Element

The random type of roughness distribution corresponds to the deposition of particles, as also shown in Bons [17]. The calculation of the sand grain roughness is then based on a correlation developed by van Rij [87] defined by Eq. 6.2, which better suits this type of roughness. The use of the correlation provides then a value for the ratio  $\frac{k_s}{k}$ , where  $k_s$  is the equivalent sand grain roughness and  $k$  is the physical roughness height, taken equal to  $R_z$  in the current work.

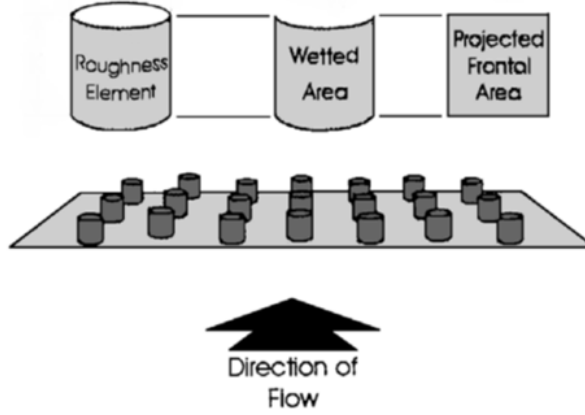


Figure 6.3: Decomposition of a roughness elements according to Sigal and Danberg [23].

$$\frac{k_s}{k} = \begin{cases} 1.583 \cdot 10^{-5} \Lambda_S^{5.683} & , \Lambda_S \leq 7.842 \\ 1.802 \cdot \Lambda_S^{0.03038} & , 7.842 < \Lambda_S < 28.12 \\ 151.71 \cdot \Lambda_S^{-1.1379} & , 28.12 \leq \Lambda_S \end{cases} \quad (6.2)$$

More details of the numerical procedure to obtain the value of  $k_s$  is detailed in Dauch [24]. The calculation considered multiple flow direction as the measurements were performed on a flat plate and provided a value for  $k_s = 120 \mu m$ . This value is then used in the numerical model as the equivalent sand grain roughness characterizing all the painted walls of the segment.

## 6.2 Numerical model

The Multi3 solver used in this chapter is described in section 5.3. A roughness model was implemented in the solver by Dauch [24] by modifying the wall omega boundary condition. A new meshing strategy is developed to better discretize the passage with the aim of obtaining high fidelity heat transfer predictions.

### 6.2.1 Modeling of rough walls

The implementation of the roughness model in the solver is done through the adaptation of the calculation of the omega boundary condition on rough walls, as proposed by Wilcox [91] to extend his k-omega turbulence closure model. The smooth omega value imposed at the wall nodes given in Eq. 6.3, which is only dependant on the flow viscosity  $\nu$  and the first cell height  $y$ , is changed to the expression given in Eq. 6.4, where the friction velocity  $u_\tau$  is used.

$$\omega(y) = \frac{6\nu_W}{\beta y^2} \quad (6.3)$$

$$\omega_W = \frac{u_\tau^2}{\nu_W} \cdot S_R \quad (6.4)$$

The parameter  $S_R$  depends on the roughness regime according to Eq. 6.5 with  $k_s^+ = Re_k = \frac{k_s u_\tau}{\nu_W}$ .

$$S_R = \begin{cases} \left(\frac{200}{k_s^+}\right)^2 & , k_s^+ \leq 5 \\ \frac{100}{k_s^+} + \left[\left(\frac{200}{k_s^+}\right)^2 - \frac{100}{k_s^+}\right] \cdot e^{5-k_s^+} & , k_s^+ > 5 \end{cases} \quad (6.5)$$

### 6.2.2 Mesh of the vane passage

The mesh used on the previous section 5.3 extends axially only immediately downstream of the vane. As aerodynamic measurements have been performed downstream of the painted segment, the mesh is extended axially to the measurement plane. Also the previous mesh does not have an O-grid around the endwall and uses approximate fillet. A new methodology to generate the mesh for Multi3 based on the ICEM CFD software developed by Chiron [22] is used in this section. The blocking topology shown in Fig. 6.4 is used for the stationary rows. The topology features a classical J-shaped block around the rightmost vane and classical H grids in the rest of the passage. An O-grid around the endwall and airfoils is then generated as a "skin" offset from the surface. This procedure can be conformed to any geometry and is especially usable for contoured endwalls.

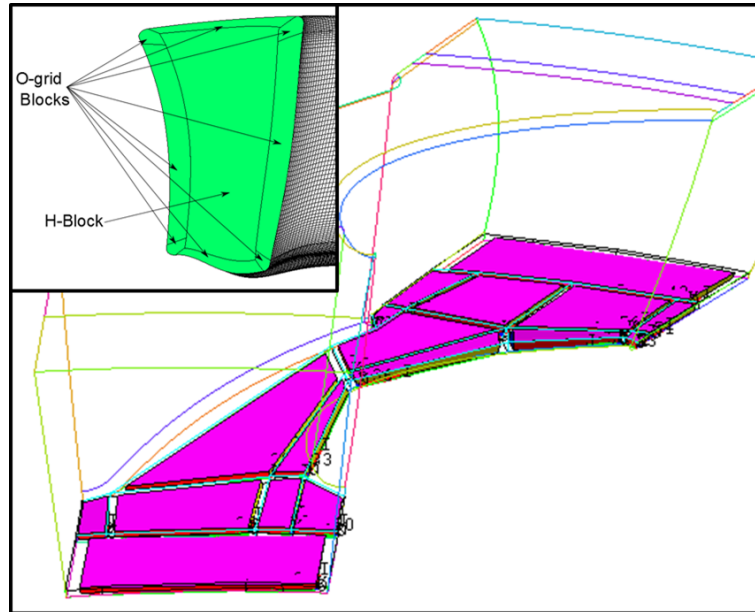


Figure 6.4: Illustration of the blocking strategy developed and fitted to the NGV geometry.

**Mesh sensitivity analysis** Three mesh wall resolutions are tested to obtain the sensitivity of the results to the mesh. The only parameter varied is the first cell height of

|        | Setting 1st cell height | Grid size | Achieved $y^+$ |
|--------|-------------------------|-----------|----------------|
| Mesh 1 | $1\mu m$                | 2.25Mio   | 1              |
| Mesh 2 | $0.5\mu m$              | 2.45Mio   | 0.5-0.6        |
| Mesh 3 | $0.25\mu m$             | 2.55Mio   | 0.3-0.4        |

Table 6.2: Size of the different mesh used in the mesh sensitivity analysis.

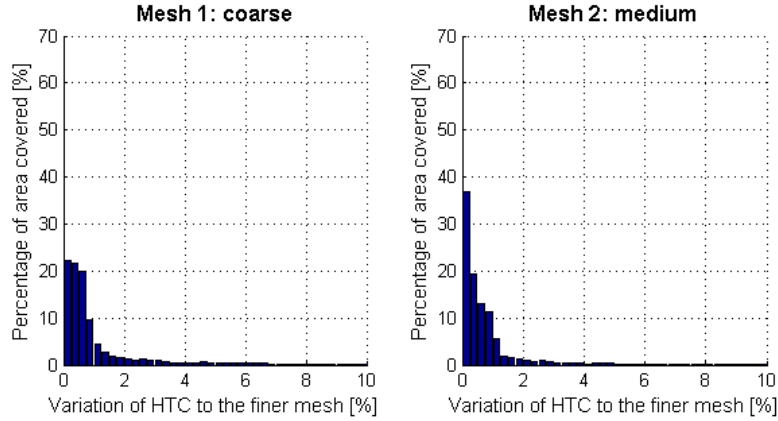


Figure 6.5: Results of the mesh sensitivity analysis in terms of distribution of the variation of HTC obtained for the coarse and medium mesh relative to the fine mesh result.

the O-grid covering the endwall and the vanes. The three mesh sizes and achieved  $y^+$  are shown in Tab. 6.2.

The quantity of interest is the heat transfer coefficient and is compared for the different meshes. Two simulations with isothermal walls are performed for every mesh to derive the heat transfer coefficient in the same manner as the experimental procedure described in section 2.1.2. The results of the mesh sensitivity are shown in the form of variation of HTC relative to the fine mesh. It shows a reduction of the error with the reduced  $y^+$  value. The cumulative distributions show that 75% of the endwall area for the coarse mesh has an HTC value within  $\pm 1\%$  of the HTC value calculated on the fine mesh, in the case of the medium mesh 95% of the endwall surface agrees within  $\pm 1\%$  with the fine solution. The medium mesh is considered sufficient and the  $y^+$  values obtained are used as a recommendation for other heat transfer studies.

### 6.2.3 Judgment of convergence of a calculation

The residuals are commonly considered to judge the convergence of the solution. In the current case, the mesh resolution is very fine close to the wall and the adaptive smoothing makes the simulation running at the limit of stability, and oscillations of the residuals are commonly observed. Therefore a criterion based on the quantity of interest is used. A variation of the adiabatic wall temperature within  $\pm 0.02K$  is considered converged for the adiabatic simulations and a variation of  $\pm 0.5\%$  is accepted for the wall heat

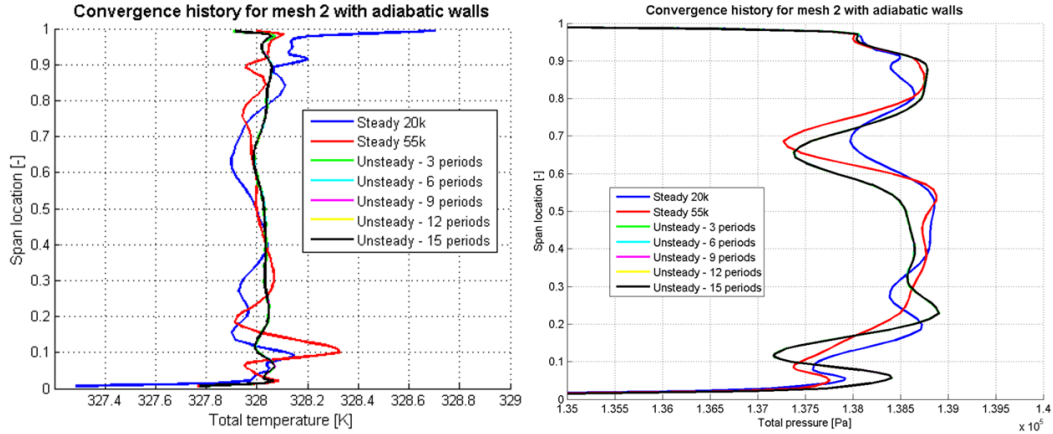


Figure 6.6: Convergence history of the laterally averaged total pressure (left) and total temperature (right) of the flow field for the medium sized mesh.

flux. Due to the fine mesh used, flow oscillation are observed in the wake and therefore the simulation are performed using the unsteady solver with parameters forcing the solution to be steady. The convergence is obtained for the wall quantities after between 9 and 12 unsteady periods, with a period representing a physical time around 1ms. The convergence of the flow field is obtained earlier, after 6 periods as shown in Fig. 6.6.

The simulations are run therefore for 20000 iterations in a steady manner to convect the inlet boundary condition across the domain and then in an unsteady manner for a minimum of 12 periods to obtain converged wall data.

## 6.3 Results from numerical predictions

The boundary conditions used in this section are based on measured data at the inlet of the turbine and are identical to the ones described in section 5.3. For the reduced mass flow case, the inlet profile of total pressure is scaled by the lower inlet total pressure at mid span. The rest of the inlet profiles are kept identical. The static pressure at the exit of the row is also adjusted based on the static pressure at the NGV hub exit measured during the heat transfer measurements.

### 6.3.1 Effect of roughness on aerodynamic losses

The multilayer attached to the heat transfer platform is modifying the shape of the airfoil, due to the multiple cuts, and shows an increase in roughness level compared to the aerodynamic segment made out of polished aluminum with a measured  $Ra \approx 0.4\mu m$ . The difference in roughness has then an impact on the pressure losses measured downstream of the row. Aerodynamic measurements are performed with a 4-hole probe downstream of the heat transfer platform and are compared to the measurements behind an aerodynamic

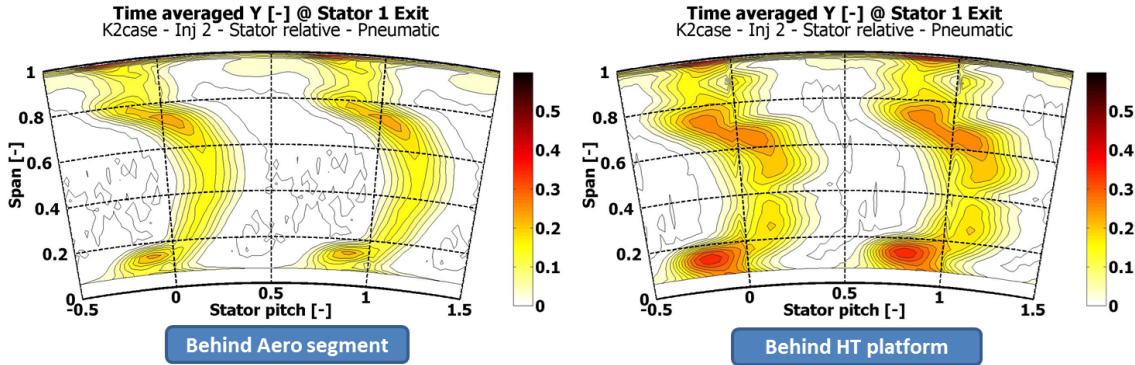


Figure 6.7: Pressure loss coefficient  $Y$  measured downstream of the NGV row, behind an aero segment (left) and the painted segment (right).

segment. The measurement plane is located downstream of the NGV row, just upstream of the rotor row. More details on the probe technology can be found in Mansour[62] and Jenny[45].

The comparison of the two flow field is shown in Fig. 6.7. The quantity shown is the pressure loss coefficient defined by  $Y = 1 - \frac{P_{t,in} - P_t}{0.5\rho U_\infty^2}$ . Overall the losses are increased downstream of the coated passage. The loss cores corresponding to the hub passage vortex at 15% span and the tip passage vortex at 70% span are larger and show a higher magnitude. The wake is generally enlarged due to the rough surface. The wake appears with a cut at around 40% span, which could be the resulting effect of a gap present on the Kapton layer applied to the airfoil surface.

The measurements are compared then to the predictions obtained with Multi3 for a smooth case and a rough case using the  $k_s$  value obtained from the 3D measurements. The 2D contour plot shown in Fig. 6.8 shows the CFD data extracted from the simulation at the same location as the measurements and processed using the same data reduction tool. The losses predicted by the numerical model are generally higher than the measurement, especially in the wake region. The hub and tip loss cores are over predicted by the CFD. In the middle of the passage, the predicted losses appear lower than the measured one. The location of the hub passage vortex is identical to the measured one, while the tip core is predicted at a lower span position. The migration of this secondary flow structure is then not correctly captured by the CFD tool. When comparing the smooth and rough predictions, the increase of losses is again clearly visible and concentrated in the wake and the vortices.

The data predicted and measured on the B plane are then laterally averaged to compare the agreement quantitatively. The curves are shown in Fig. 6.9. The color code helps separating the rough and smooth conditions while the symbols and lines refers to the measured versus predicted data. The quantity of interest is the non-dimensional total pressure. Similar conclusions can be made from this plot in terms of the rough configuration showing greater losses. Overall the agreement between the CFD and the

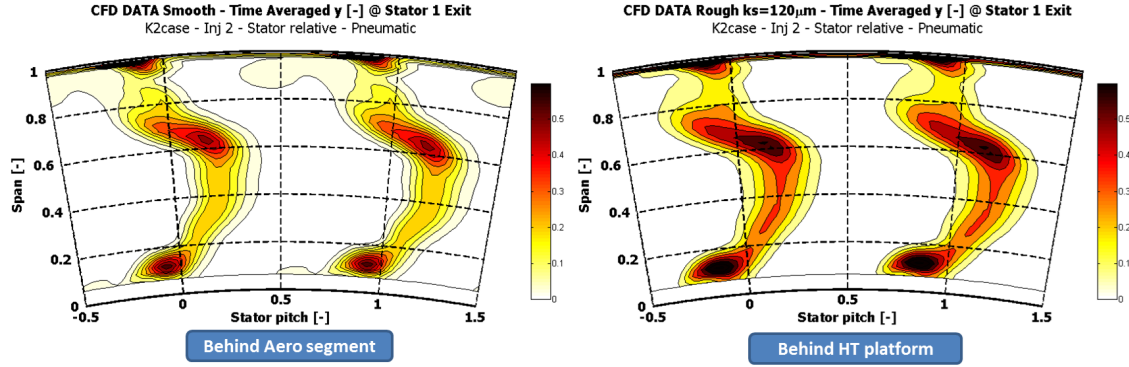


Figure 6.8: Pressure loss coefficient  $Y$  predicted downstream of the NGV row, behind an smooth segment (left) and a rough segment (right).

measurements is surprisingly good. The magnitude of the change in total pressure is correctly predicted as well as the change at the span position where the hub and tip loss core are. In the smooth case, the difference between the predicted and measured tip passage vortex can be identified, while this difference is reduced for the rough case. In the rough, the difference between the prediction and measurement at 40% span corresponds to the wake being split in two observed in the measurements of Fig. 6.7.

Some of the differences between the predictions and measurements can be attributed to the missing rotor downstream of the stator row. In fact, the predictions are performed on a single row with radial equilibrium condition at the outlet. The measurement plane is located upstream and the potential field of the rotor is visible in time resolved data acquired for this configuration. However the impact is estimated to be limited and should not change the conclusion of this comparative study.

Overall the predictions are very close to the measured aerodynamic losses performed for both the smooth and rough cases. The effect of roughness seems particularly well captured when using the calculated value for  $k_s$  obtained with the 3D scan of the surface.

### 6.3.2 Effect of roughness on heat transfer quantities

The effect of four different roughness levels ranging from a smooth surface  $k_s = 0.01\mu m$ ,  $k_s = 30\mu m$ ,  $k_s = 60\mu m$  and the measured  $k_s = 120\mu m$  are shown in this section. The heat transfer coefficient is calculated using the adiabatic wall simulation and one isothermal simulation with  $T_w = 363K$ , according to Eq. 6.6.

$$h = \frac{q_w}{T_w - T_{ad}} \quad (6.6)$$

The Nusselt number distribution predicted for the smooth case is shown in Fig. 6.10 together with the predicted increase in Nusselt number ratio for the three rough cases. It can be observed that the roughness has mainly an impact in the downstream part of

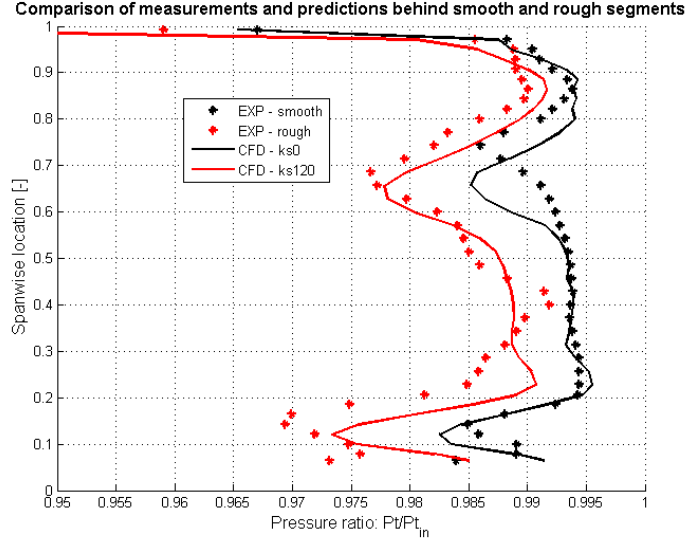


Figure 6.9: Comparison of laterally averaged non-dimensional total pressure measured (symbols) and predicted (solid line) behind a smooth (black) and rough (red) segment.

the passage. The increase is around 30-35% for  $k_s = 30\mu m$ , 50-55% for  $k_s = 60\mu m$  and maximum 65-70% for the largest roughness size. The effect is maximum at the exit of the passage since it is the region where the velocity is highest and the wall shear stress is also maximum. In this region and for the different roughness levels used, the flow regime will evolve from aerodynamically smooth to the fully rough case. The distribution of roughness Reynolds number  $Re_k$  for the largest level of roughness is shown in Fig. 6.11. At the inlet the roughness effect is less pronounced due to the reduced flow velocity and the limited wall shear stress. The increase of the roughness level will change the surface flow regime from smooth to transitionally rough but will not enter a fully rough state.

**Comparison of Reynolds number effect between measurements and predictions** The numerical model is also used to obtain flow data for the low Reynolds number case. In this case the inlet and outlet boundary conditions are adapted to the reduced total inlet pressure measured in the facility for this case. The comparison between the two operating conditions is made in terms of Nusselt number ratio. According to the flat plate theory, this ratio is a function of the Reynolds number as described in Eq. 6.7.

$$\frac{Nu_{DP}}{Nu_{lowM}} = \left( \frac{Re_{DP}}{Re_{lowM}} \right)^x = \begin{cases} 1.3 & \text{with } x = 0.8 - \text{turbulent case} \\ 1.17 & \text{with } x = 0.5 - \text{laminar case} \end{cases} \quad (6.7)$$

The Nusselt number ratio is shown in Fig. 6.12, where the measured and predicted data are compared. This ratio can be used to assess the state of the flow as it evolves through the passage, in fact the variation of the ratio according to Eq. 6.7 can delimit regions covered with laminar or turbulent flows. In the experimental data, the area



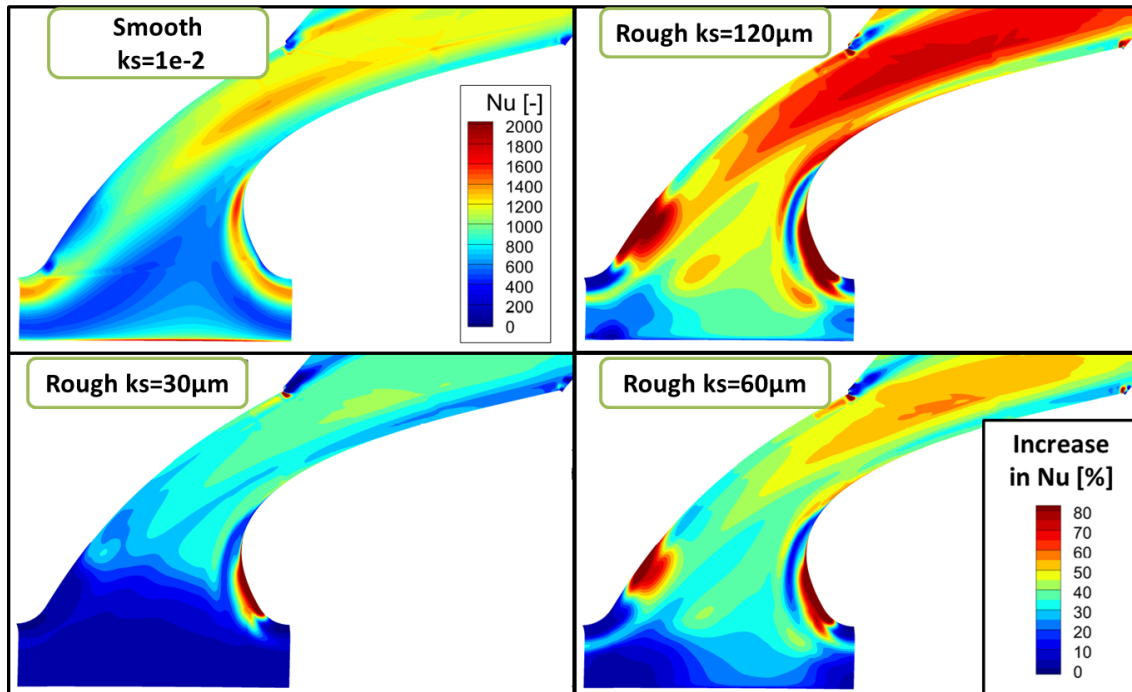


Figure 6.10: Nusselt number distribution predicted in the smooth case (top - left) and increase of the Nusselt number predicted for the rough cases, relative to the smooth cases.

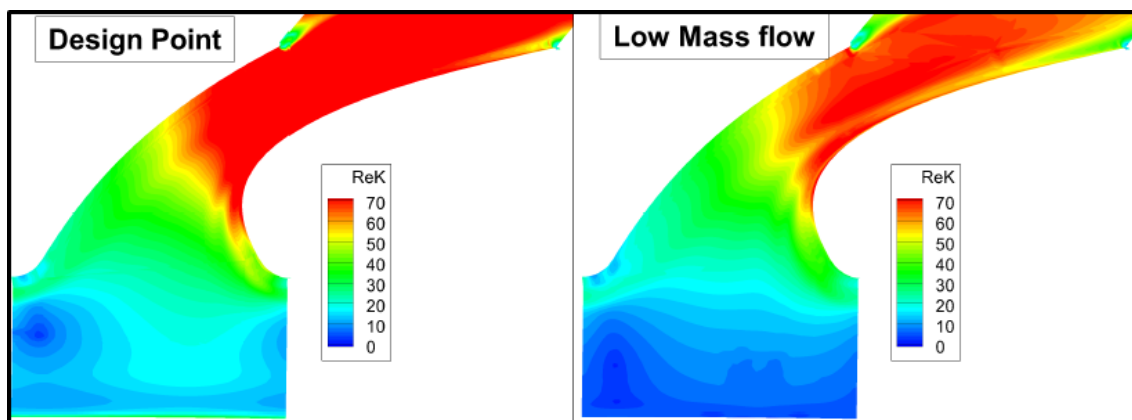


Figure 6.11: Distribution of Reynolds number based on the roughness height and friction velocity  $Re_k$  for the two cases design point and low mass flow.

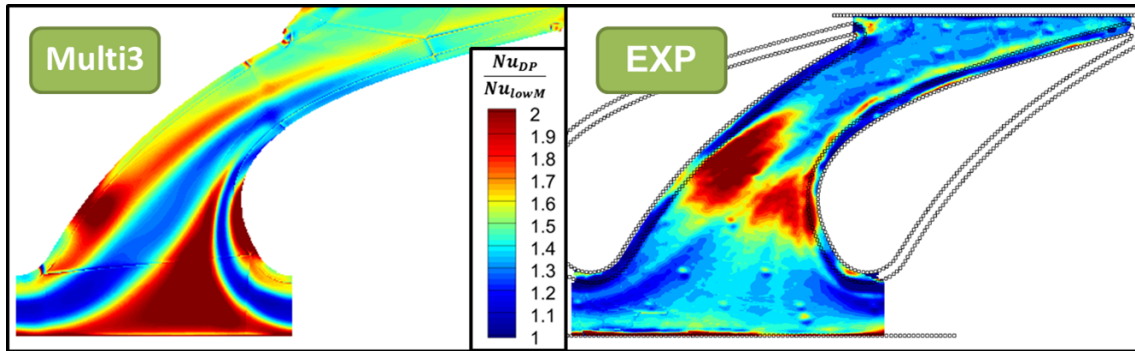


Figure 6.12: Comparison of the Nusselt number ratio measured (right) and predicted (left).

averaged ratio is equal to 37.3%, close to the turbulent correlation data for the 28% variation achieved in Reynolds number. The inlet and exit portion of the passage appear close to the expected value for a turbulent flow. There are a few regions close to the leading edge where the horseshoe vortex forms that shows levels closer to a laminar boundary layer. However, the levels measured in the middle of the passage are very different from the flat plate correlation. The region covered with higher Nusselt number ratio is located upstream of the throat, where the flow acceleration is maximum.

On the side of the predicted quantities, the patterns are very different and highlights strong modification in the flow behavior predicted between the two cases. Few elements are similar, the region covered by the horseshoe vortex and its migration extending from the pressure side to the suction side shows lower levels in both cases. The levels predicted in the upstream region are however very different with a ratio close to 2 in the inlet portion close to the rightmost vane while in the experiments the level is limited to 1.3-1.4. The transition from laminar to turbulent in the simulation may be an explanation. In fact, in the experiments, the insulation located upstream of the platform creates a step that is forcing the transition. In the simulation, the transition is made naturally. The very different levels of Nusselt number present in these two regimes would lead to similar ratios.

The high levels of Nusselt number ratio measured in the middle of the passage are located slightly upstream of the peak flow acceleration. In this region the pressure side leg of the horseshoe vortex is migrating towards the suction side and entrains the low momentum fluid from the boundary layer. High level of turbulence can then be found at this location. The change in Reynolds number affects the behavior of the flow and the strength of the flow structure. The variation of Nusselt number could then be the result of the flow change in a critical region. This behavior also observed where the flow is accelerated in the flat plate cases of Fig. 3.29.

Interestingly, the simulation performed for the two operating points using the roughness model adds a parameter to the equation. In fact, the distribution of the roughness

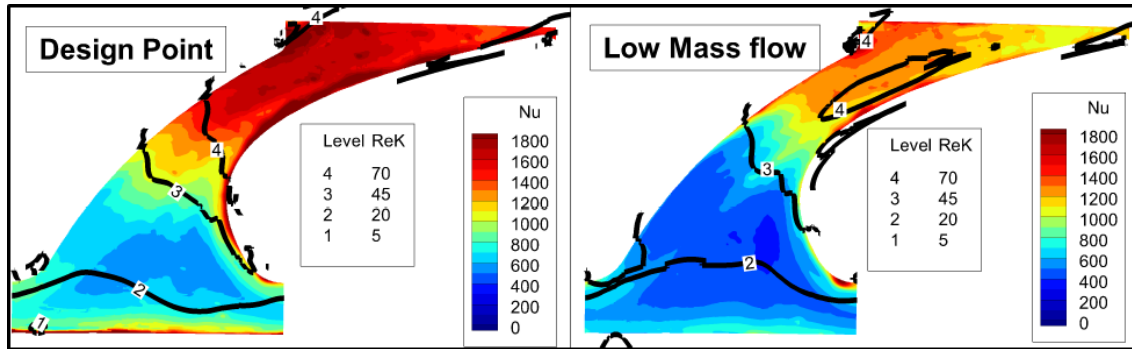


Figure 6.13: Superposition of measured Nusselt number contours and lines of predicted roughness Reynolds number based on  $k_s = 120\mu m$  for the two operating conditions.

based Reynolds number  $Re_k = \frac{k_s u_\tau}{\nu}$  calculated based on the predicted levels of wall shear stress is shown in Fig. 6.11. In this figure, it can be observed that the location of the transitionally rough regime ( $Re_k = 5 - 70$  or  $5-45$  depending on the source) is extending exactly into the region where the high Nusselt number ratio are measured. In Figure 6.13, the lines dividing the different roughness regime are superposed onto the Nusselt number distribution measured experimentally. The regions of high Nusselt ratio is approximately located between the lines 3 and 4 in the design point graph (left). The level observed in the same region for the other operating condition are reduced and shows that the limit of the fully rough zone starts more downstream of the throat. This comparison suggests that potentially the surface roughness can also have an impact in this zone in addition to the flow itself. In fact, the switch from transitionally rough to fully rough is potentially not occurring at the same location for both cases leading to very different wall shear and heat transfer coefficient.

## 6.4 Summary

In this chapter, the roughness data measured on the actual measurement platform are presented. A measurement technique providing 3D surface data is used to provide an equivalent sand grain roughness usable as an input to a numerical model. The roughness model implemented in Multi3 using the modification of the omega boundary condition at the wall is introduced and the impact of the roughness on aerodynamic losses and heat transfer is shown. In particular, predictions of the flow field downstream of smooth and rough segments are compared to the experimentally measured data. The measured increase in losses is globally well captured in the predictions. The effect of roughness on the thermal loads shows an increase of heat transfer coefficient up to 70% predicted in the downstream part of the passage. Finally, the comparison of the roughness based Reynolds number between the two operating conditions measured, highlight the variation of roughness regime especially in regions where large Nusselt number ratio are measured.



# Chapter 7

## Measurements of heat transfer on contoured endwall

In the last phase of the program, the hub endwall of the three turbine rows are modified to further enhance the performance of the turbine 1.5 stage. The three hub endwall shapes have been optimized to increase the 1.5 stage aerodynamic total-to-total efficiency. In particular, the endwall shape is modified upstream and downstream of the vane passages. The endwall of the NGV is shaped from 25% of the vane axial chord  $C_{ax}$  upstream of the vane leading edge until 8% of  $C_{ax}$  downstream of the trailing edge. The contouring is limited to the hub endwall to allow the access for imaging techniques through the shroud casing. In fact, a Zinc Selenide window could not be manufactured with such a complex contouring shape. This chapter presents the adaptation made on the heat transfer platform to integrate the geometry into the facility. The technique used to wrap the Kapton on the endwall with cuts and patches did not prevent micro-air bubbles from being trapped underneath the layer. The location and size of the mis-attachment are obtained using a thermal response test. The newly developed procedure allows the measurements of the air layer thickness. The non-uniformity in the thermal resistance is then accounted for in the data reduction procedure of the measurements. Finally, flow predictions using a numerical model of the passage with the contoured endwall are performed. The comparison of the flow field to the cylindrical endwall is performed in the last section of this chapter.

### 7.1 Adaptation of the platform design to a contoured endwall configuration.

#### 7.1.1 Changes in the mechanical design.

The radial extent of the contoured endwall is comprised between -5.6% span to +7.8% span compared to the nominal platform radius. The heat transfer platform design is

modified accordingly to accommodate this change in the surface shape and maintain a satisfactory control of the solid temperature. Because of the rather extreme depth of the trough, the radial location of the channels had to be modified. In order to provide a better control of the surface temperature below the insulating layers, the channels are re-designed to follow the surface leaving an approximately constant wall thickness. A three dimensional view of the new endwall and channel configuration (limited to the middle passage and side vanes) is shown in Fig. 7.1. The aluminum segment is therefore machined with contoured channels as it is shown in Fig. 7.2. Due to the shape of the channel and the location of the holes drilled through the vanes, the distance between the surface and the water channel could not always be maintained uniform and equal to 5mm. Fig. 7.1 highlights the distance from the surface to the closes water channel and show that close to the trailing edge on the suction side, the channel could not be shaped to follow the surface as close as 5mm. This region is subjected to greater temperature gradients and is analyzed using a thermal analysis after the measurements. In order to maintain a constant flow velocity in the channel, the aluminum cover closing the channels is shaped and maintains the channel hydraulic diameter constant throughout the hub. The manufactured cover is presented in Fig. 7.3. Because of the repositioning of the channels, the plastic cover insulating the segment from convection with the air flow in the cavity is suppressed. On the outer casing, the configuration of the tubes and connectors is kept identical and allow the connection to the water network. The axial and circumferential location of the embedded PT100 is kept identical to the cylindrical endwall case but the sensors are mounted radially 1mm below the endwall surface. In general, minor improvements are made on the mechanical design to facilitate the assembly and further improve the accuracy of the measurements. The sides of the platform are extended radially to offer a “containment” for the cover. The temperature sensors are mounted on short steel shaft to reduce the risk of damaging their wires during assembly and operation. Finally an additional flat surface is added on the outer casing to mount the calibration target used to position the robot and the camera relative to the segment.

### 7.1.2 Attachment of the Kapton layer on the contoured endwall.

The key element in the setup is the Kapton layer that is allowing the calculation of the conduction heat flux. However with the use of endwall contouring, wrapping a Kapton sheet on a non-developable surface becomes non-trivial. On the vanes, the same procedure as in K2 case is used. Large patches are used to cover the downstream part of the passage on both the pressure and suction sides while stripes of 1cm width are used to follow the vane shape close to the leading edge (Fig. 7.5). On the endwall the curvature, shown in terms of Gaussian curvature in Fig. 7.4 is more pronounced, especially the succession of hills and trough leads to zones with high curvature levels in two directions. The task is accomplished by trials and errors and a number of cuts positioned in the regions with high curvature values are used. The top view of Fig. 7.5 highlights the position of the

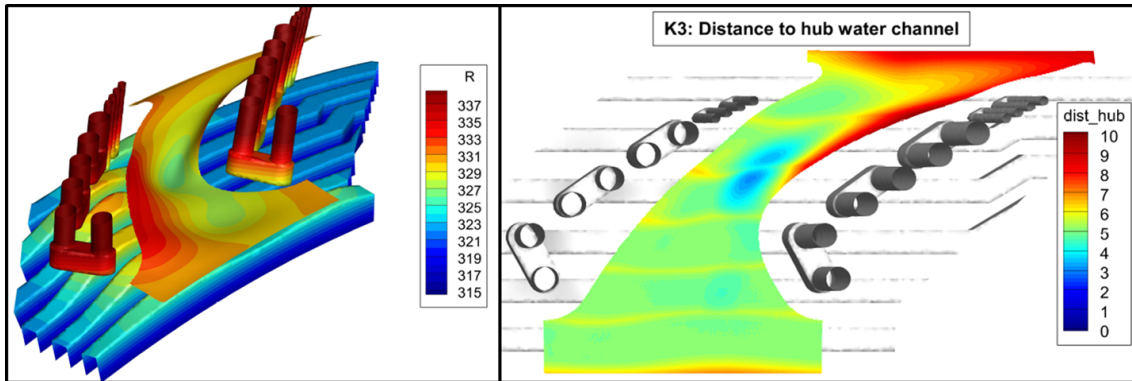


Figure 7.1: Left - 3D view of the endwall and channels configuration and shape below the middle passage. Right - Distance between the contoured endwall surface and the closest water channel. It represents the thickness of the aluminum wall.

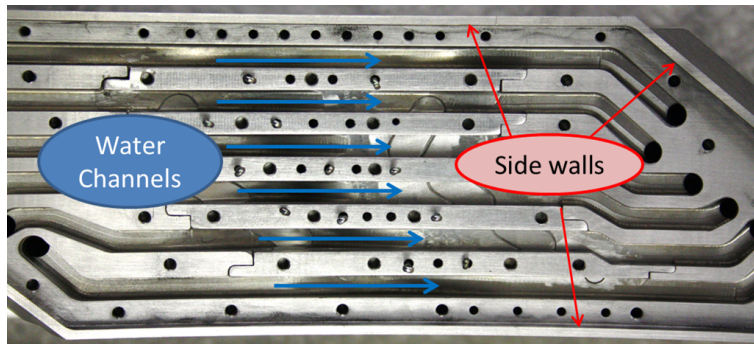


Figure 7.2: View of the channels through the hub platform, with the new side walls highlighted.



Figure 7.3: Cover with contoured negative element ensuring constant channel cross sectional area.

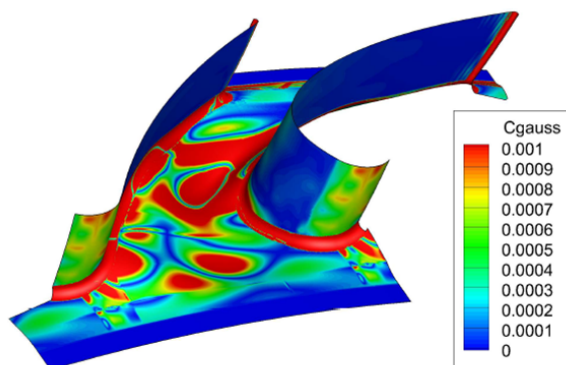


Figure 7.4: Map of Gaussian curvature on the hub endwall. High values mean that the surface is highly curved in two directions.

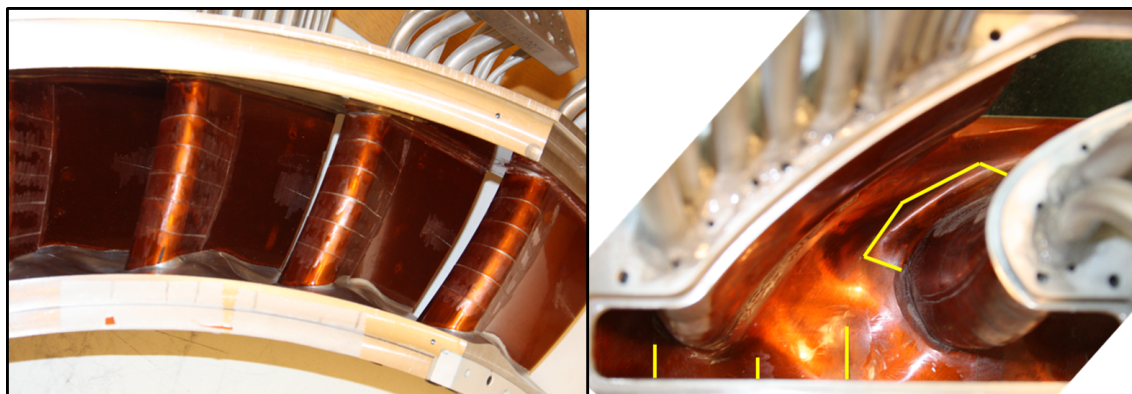


Figure 7.5: Left - Kapton layer wrapped on the vane surfaces. Right - Top view of the endwall equipped with a Kapton layer. The yellow lines superimposed show the locations of the cuts used to better follow the endwall shape.

cut on the hub endwall. The grooves or cut present between two patches of Kapton are filled with epoxy glue, cured and then polished manually to ensure an aerodynamically smooth surface.

As in K2 case, the surface is then painted using a high emissivity black paint to provide an optimum signal for the infrared camera. The endwall surface is scanned along lines after the paint application. A profilometer (Taylor Hubson Talysurf 800) is used to measure the surface shape and ensure that the glue lines or interfaces between Kapton patches are not visible. Figure 7.6 provides the results of two line scans performed at the inlet and exit of the vane passage. The curve represents the endwall shape, measured optically using the deflection of a diamond tip touching the surface. The location of the glue lines or steps could hardly be noticed at the passage inlet or is in the same order of magnitude as the surface roughness for the line scanned at the exit of the passage. In addition infrared markers made using silver ink are positioned over the whole passage.



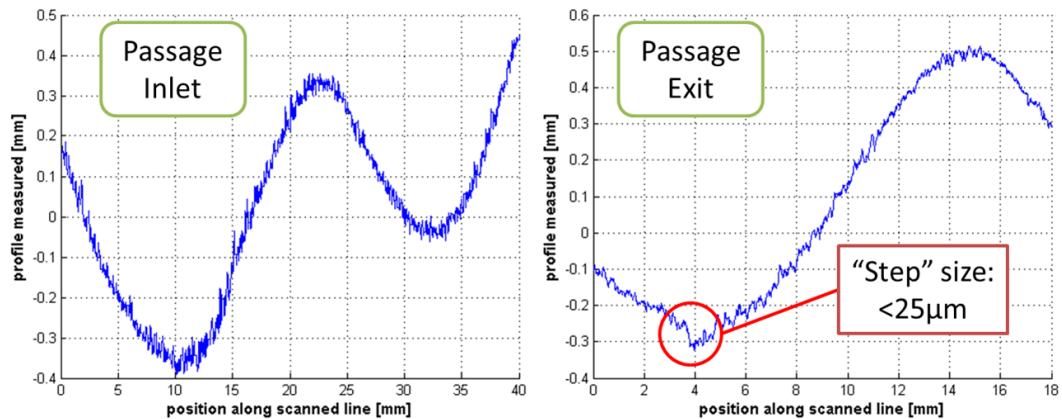


Figure 7.6: Results of the surface profile scan performed along two lines at the inlet (left) and exit (right) of the passage. The curve represents the shape of the endwall.



Figure 7.7: Heat transfer platform painted with high emissivity paint and with infrared markers on the endwall surface.

These markers are used to perform the geometrical reconstruction of the data on the passage. A picture of the segment prior final assembly in the rig is shown in Fig. 7.7.

### 7.1.3 Measurements of roughness levels through the passage.

The measurement system used to quantify the roughness levels through the passage is identical to the profilometer used for the K2 geometry. The measurements were performed before and after the tests the turbine facility. The measurements are performed at the inlet and at the outlet only, because of the limited accessibility. Figure. 7.8 highlights the approximate location of the scanned lines and provide the integral value of arithmetic and peak to peak roughness. The roughness at the exit of the passage is higher than the inlet portion due to the re-painting of this region while installed in the facility. In fact, due to the limited accessibility, a smaller spray gun was used with a different nozzle diameter.

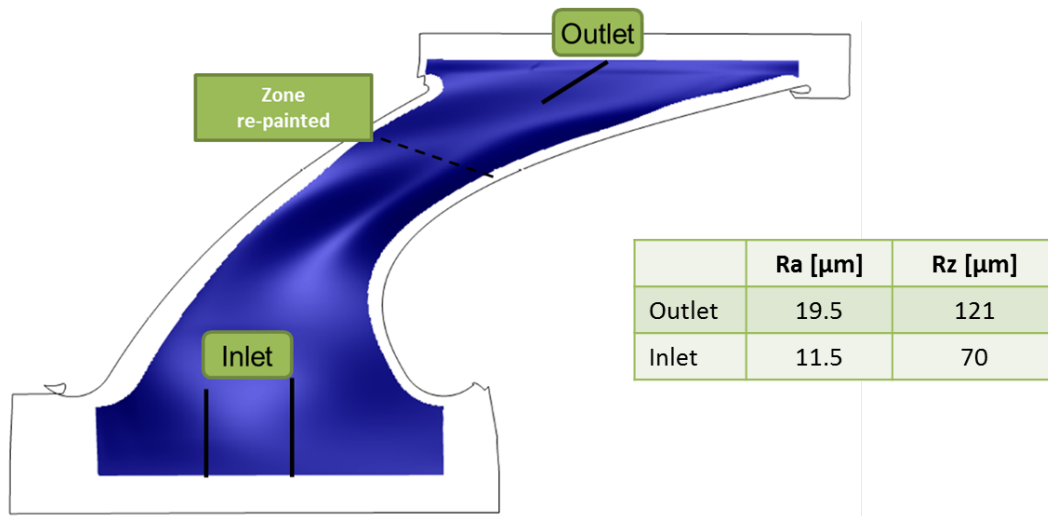


Figure 7.8: Location of the roughness line scan and measured integral values.

## 7.2 Calibration for thermal resistance non-uniformity of the multilayer attached to the platform.

The preliminary results obtained during the measurement campaign showed regions covered with very high heat transfer coefficient values, which are considered non-physical. In fact, the regions affected correspond to portions of the passage where the surface curvature is important. A specific attention is placed on these zones since there may be micro bubbles of air trapped underneath the Kapton layer. In fact due to the pronounced surface deformation, the Kapton layer may not be attached correctly to the surface and air is trapped underneath. This would increase the local thermal resistance compared to the common value and therefore show very high heat transfer data. Multiple paths to investigate this issue were followed:

1. Transient tests performed during the measurement campaign LISA
2. Surface thermal response to laser pulse
3. 3D measurements to obtain a thickness using difference before/after Kapton wrapping

The first option is performed during the measurement campaign while the segment is installed in the facility, while the two other options require the segment to be taken out of the facility. The last two steps are then performed after the measurement campaign. Despite the uncertainty in the success of the second method, the order of the tests is determined by the respective surface property requirements. In fact, the 3D measurements require the surface to be reflecting incident light and therefore require another paint layer. On the other hand, the thermal response tests are based on infrared imaging and require the high emissivity paint as for any other heat transfer measurement test.

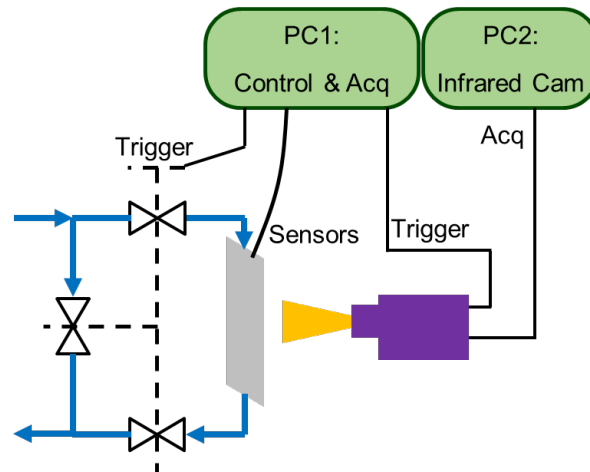


Figure 7.9: Schematic of the water network and trigger signals used to acquire transient data.

### 7.2.1 Transient heat transfer measurements in LISA

First during the measurement campaign, transient tests are performed to obtain data in these zones with a different procedure compared to the classical steady state measurement approach. While the rig is running, a change of the solid thermal boundary condition is achieved by bypassing the circulating water and the transient endwall surface temperature is recorded. In fact, the set of fast acting membrane valves is used to divert the flow and prevent it from entering the segment (Fig. 7.9). The transient acquisition of the images with the camera is started shortly before the step as well as the high speed acquisition of the temperature sensors. A delay in the surface temperature response to the change of boundary conditions should be observed between a sound zone and a mis-attached layer. However, due to the thermal time constant of the system, this delay is not identifiable. All signals are superposed when looking at the graph in Fig. 7.10. The technique is proven to be unsuccessful with this configuration and acquisition system.

### 7.2.2 Surface thermal response measurements using a laser pulse and the infrared camera

The second technique used to get additional information in the zones where the layer is potentially detached, is the thermal response of the surface to a laser pulse or a laser step. Due to the high energy delivered during a laser pulse, abrasion of the paint layer on the surface can occur. In addition, the rather low frame rate of the infrared camera (50Hz) reduces the number of points acquired during the thermal transient. It was shown in the preliminary phase of the project that the signal acquired led to high uncertainty values and therefore was not suitable for a thermal resistance calibration procedure. However with a technique based on a longer laser pulse, ie. a “step”, the camera signal

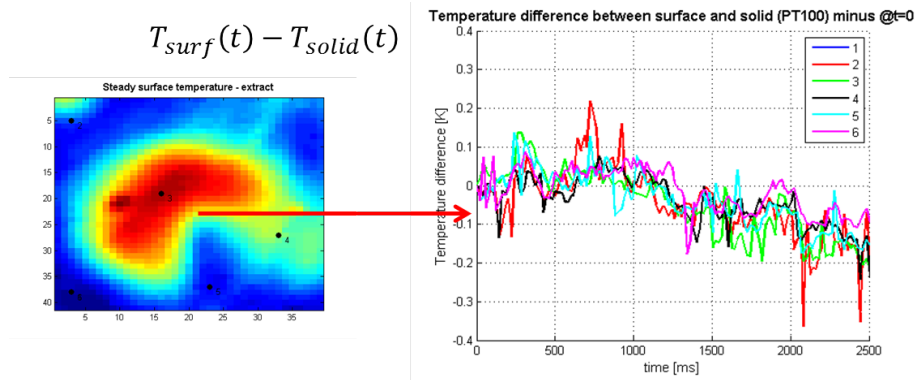


Figure 7.10: Extracted temperature time series at different locations on top and around the zone with suspected detached layer

becomes usable. Used as a proof of concept, a calibration plate (Fig. 7.13) machined with flat bottom holes of different depth and covered with the same multilayer Adhesive-Kapton-Paint is showing a sensitivity of the surface temperature response to the hole depth.

**Theoretical basis for step thermal response tests.** The thermal response tests are based on the local heating of the surface of a solid and the monitoring of the temperature evolution in time. When the surface is heated, waves are generated in the material as discovered by Fourier and Angström in the 19th century. The dispersion and attenuation of these waves are based on the material properties and affects the surface temperature evolution. Time-Resolved Infrared Radiometry (TRIR), also known as Stepped Heating (SH) thermography, is commonly used in Non-Destructive inspection Technique (NDT) to identify delamination of composite structure or inclusion of dirt in metallic alloys, a more complete review is provided in Osiander et al.[70]. The advantages being the short inspection time, the relatively easy and quick setup and mainly the absence of damage on the surface of the tested part. The temperature of the surface is monitored during the heating and cool-down time of the inspection process. The procedure can be used to measure coating thickness, as in Maclachlan et al. [59]. In a two layer system (shown in Fig. 7.11), typically a coating on a substrate, the thickness of the coating can be obtained when the temperature response curve deviates from the theoretical curve for a semi-infinite material. The evolution of the top surface temperature is given by Eq. 7.1 (from Murphy et al. [67]), where  $\alpha$  is the thermal diffusivity of the material.

$$T(t) - T_{t=0} = C_c \sqrt{t} \left\{ 1 + \sum_{n=1}^{\infty} 2(-\Gamma)^n \left[ \exp\left(-\frac{n^2 L^2}{\alpha_0 t}\right) - \frac{nL\sqrt{\pi}}{\sqrt{\alpha_0 t}} \operatorname{erfc}\left(\frac{nL}{\sqrt{\alpha_0 t}}\right) \right] \right\} \quad (7.1)$$

For laser heating, the term  $C_c$  is defined by Eq. 7.2 according to Osiander [70], where  $e = \sqrt{\rho C k}$  is the thermal effusivity,  $\epsilon$  the surface emissivity,  $R$  the reflectivity and  $I$  the

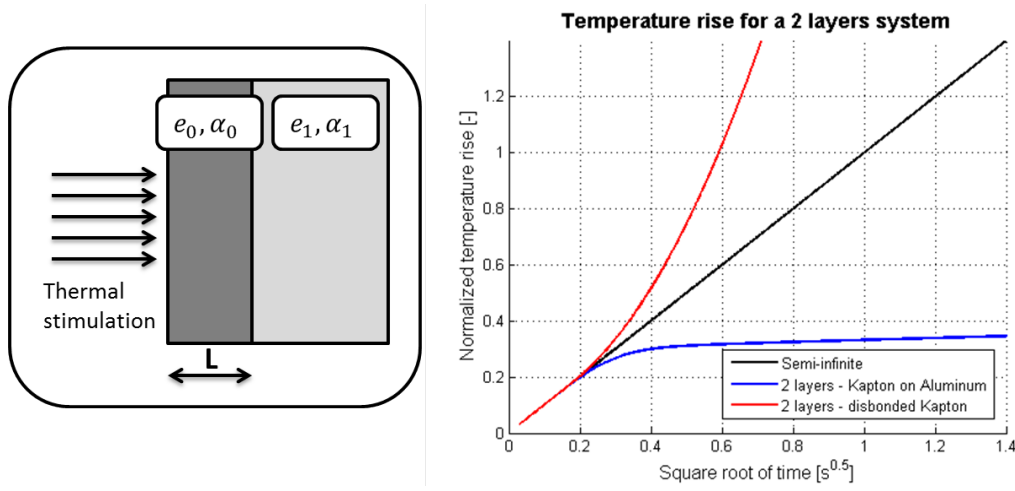


Figure 7.11: Left - Diagram of a 2-layer specimen. Right - Normalized temperature rise for a two layer system similar to the current configuration.

laser intensity. Finally  $\Gamma$  is the thermal mismatch factor between the two layers and is defined as in Eq. 7.3. For a dis-bonded layer,  $\Gamma = -1$  since air has generally much lower thermal diffusivity than the coating. Figure 7.11 shows the temperature rise, normalized by the incident laser power  $C_c$ , for a semi-infinite Kapton layer, a Kapton layer attached on aluminum and a Kapton layer dis-bonded, ie the substrate is air. The Kapton layer used as a coating is equivalent to the one used as an insulating layer on the heat transfer platform and has a thickness of  $127\mu m$ . Until a time corresponding to the thermal time constant of the coating, the semi-infinite, the 2-layers system and the dis-bonded case show an identical behavior, but separates when the thermal wave reaches the interface between the Kapton layer and the substrate. In aluminum the wave propagates faster which leads to a faster decrease of the surface temperature, while the propagation is practically stopped in air and the surface temperature then increases. In the particular case of our multilayer coating on the aluminum segment, no theoretical formula expresses the surface temperature rise that would be measured using a laser, but as the thermal properties of the different layer are very similar, a behavior resembling the graph shown in Fig. 7.11 is expected.

$$C_c = \frac{\epsilon(1 - R)I}{4\pi^{3/2}e_0} \quad (7.2)$$

$$\Gamma = \frac{e_1 - e_0}{e_1 + e_0} \quad (7.3)$$

For more details on the use of infrared thermometry in material inspection, the reader is referred to Maldague [61].

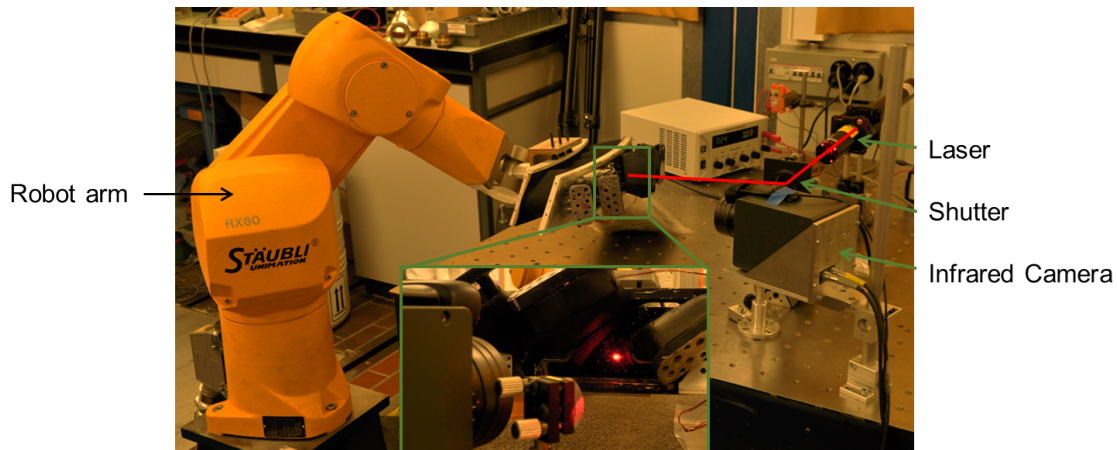


Figure 7.12: Experimental setup used for surface thermal response to a laser step. The zoom highlight the difficulty to access the passage with both the laser beam and the camera.

**Experimental setup and measurement procedure** The setup used to characterize the surface thermal response is composed of a 30mW Helium-Neon continuous laser expanded using a diverging lens and deflected towards the specimen using a flat mirror. Aligned with the laser a shutter, commanded electronically using a digital output of an acquisition card, controls the laser step duration by opening and closing. The calibration plate or the test segment to be scanned is attached to the 6 axis robot arm using a specifically designed clamping tool. In fact, the measurements are performed by scanning the surface with the laser and recording the temperature evolution with the infrared camera. The camera and the laser are kept stationary, attached to an optical table, and the robot is moving the target to scan the complete surface. Every point on the surface is therefore brought to a “focal point” where the laser beam and the camera focusing plane are intersecting at a known location in the infrared picture. The use of the robot arm is motivated by the need to orient the segment in complex positions to grant the access for both the camera and the laser beam. The setup is shown in Fig. 7.12. The camera acquisition is triggered 100ms before the shutter opens and the laser starts heating the surface. After 1sec, the shutter is closed and the cool-down phase starts. The camera acquisition covers the heating and cool-down phases and lasts 3seconds. The maximum frame rate of the camera, equal to 50Hz, is used. After a short waiting time to store the data, another acquisition is started. Five laser steps are acquired for every robot position. Only one point in the center of the laser beam is extracted for one robot position. At every point scanned, the curves obtained for the multiple laser steps are filtered and averaged to eliminate any data recorded during abnormal opening or closing of the shutter.

The results from a scan of the calibration plate are shown in Fig. 7.13. The plate is moved by 0.5mm step along the middle line of the flat bottom holes and the data in the center of the laser beam is extracted from the infrared image. The graph shows the

Temperature response to laser step – Time–space diagram

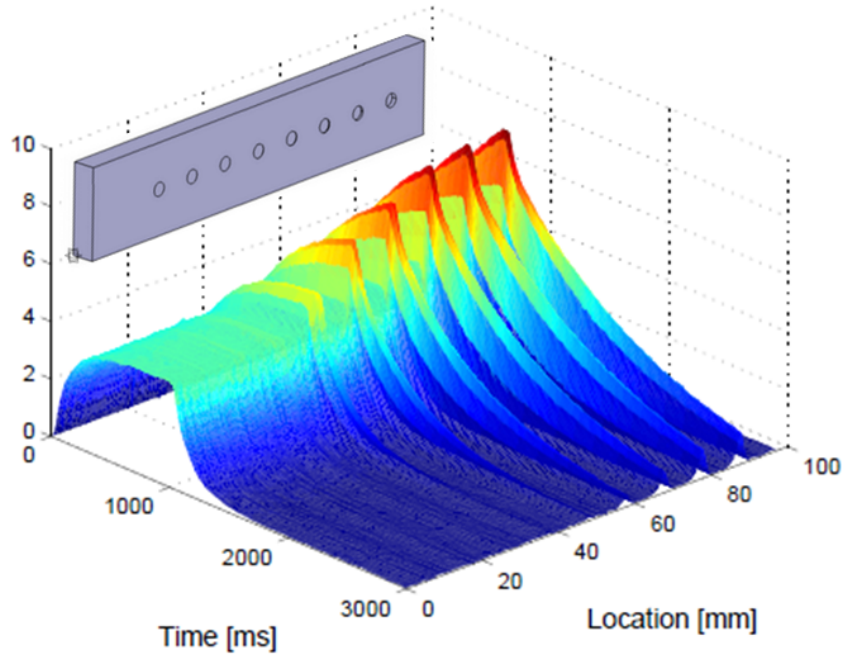


Figure 7.13: Calibration target with holes ranging from  $5\mu\text{m}$  to 1mm depth and the measured transient temperature response.

surface temperature response along the line going through all the holes: it is an assembly of all the images recorded. When looking at the magnitude of the peak in temperature, a trend with higher temperature reached on top of deeper holes can be noticed. Also the temperature increase and the temperature peaks location are exactly matching the position of the holes on the plate.

The NGV segment is also scanned using this technique. First the segment is scanned using a coarse distribution of points on the endwall. After a first post-processing, the point density is refined close in the regions where the layer is not correctly attached. A total of 2000 points is used to cover the passage. 750 images are acquired at every position leading to a total of 1.5 millions picture to process. The thermal contrast parameter is used to identify the regions where the attachment is not correct. The map of thermal contrast is shown in Fig. 7.14. The thermal contrast defined in Eq. 7.4 is a parameter describing how far is the surface response at one point compared to the response at a reference point which is chosen to be a “sound” point. The poor quality of the mesh obtained using Delaunay triangulation in the downstream part of the passage does not affect the final results as no measurements are available in this region. In fact, a position of the segment to provide access to both the camera and laser could not be found.

$$C_{\text{delta}}(t) = T(t) - T_{\text{ref}}(t) \quad (7.4)$$

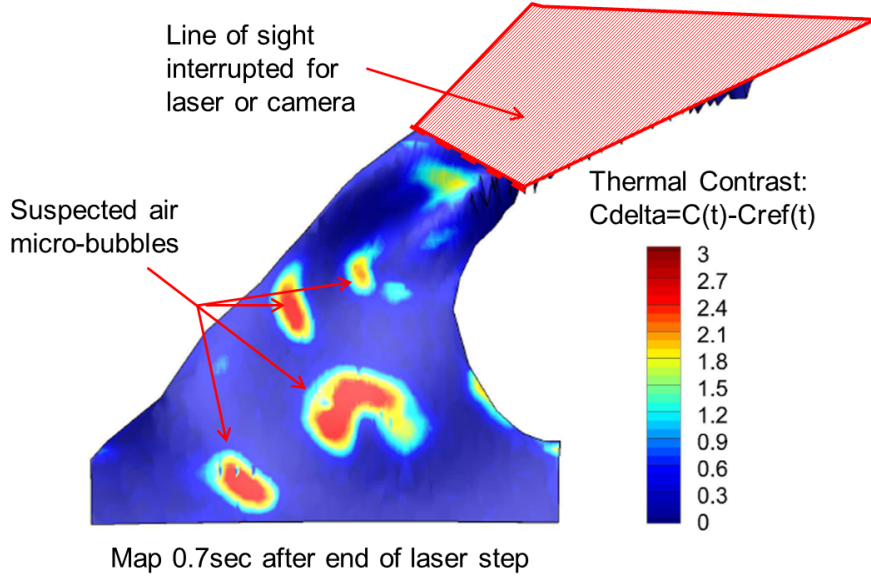


Figure 7.14: Map of thermal contrast  $C_{delta}$  at 0.7sec after the end of the laser step.

Figure 7.14 highlights the location of the zones with higher thermal resistance and therefore the potentially mis-attached layer. When comparing this figure with the preliminary results shown in Fig. 7.25, it is clear that the zones with high HTC are matching with the zones with higher contrast. No results are available in the aft part of the passage due to the difficulty to access the surface with both the camera and the laser. In order to assess the attachment of the layer in this region, data from the third approach using 3D geometrical measurements are used.

The surface response tests allowed the identification of the regions where the multi-layer is mis-attached. Using the measurements performed on the calibration plate, a model providing a relation between the thermal contrast  $C_{ratio}$  and the thickness of the air thickness trapped underneath the layer is defined. As shown in Eq. 7.1, the temperature rise is directly proportional to the incident laser power. A thermal contrast defined in the form of a ratio, as defined in Eq. 7.5, has then a limited dependence to the incident power.

$$C_{ratio} = \frac{T(t) - T_{t=0}(t)}{T_{ref}(t) - T_{ref}(t=0)} \quad (7.5)$$

As the surface of the calibration plate and the segment are coated with the same paint, the other parameters involved in Eq. 7.2 are identical between the two specimen.

The thermal contrast evolution measured above the hole on the calibration plate is extracted at different time during the temperature rise and plotted with respect to the air depth underneath the Kapton layer, as shown in Fig. 7.15. Multiple curves  $thi_{air} = f(C_{ratio})$  are obtained and models are fit through these values for every time step. The thermal contrast  $C_{ratio}$  is calculated for the measurements of the passage endwall and the



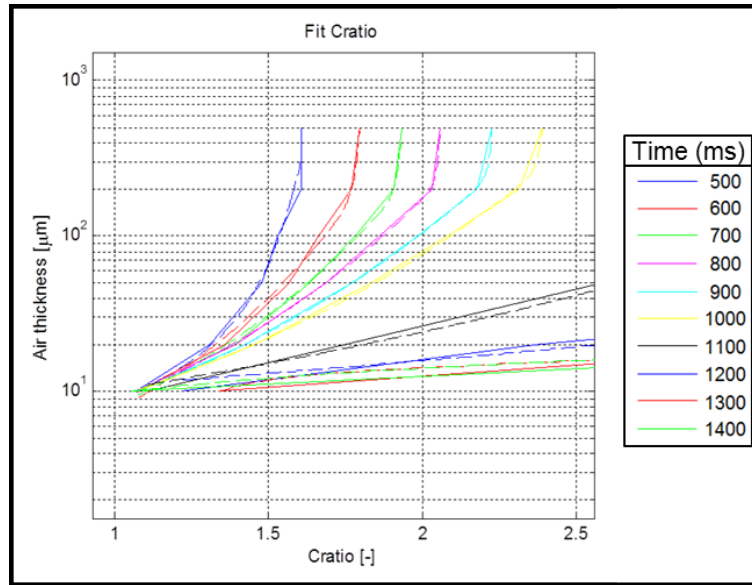


Figure 7.15: Model (dashed lines) fit through the thermal contrast values measured (solid lines) at different times on the calibration plate on top of the holes.

models are applied at multiple time steps. The time difference between images is around 20ms. The use of data at multiple time steps help improving the results obtained for the air layer thickness shown in Fig. 7.16. Discrete points are visible where the thickness is non zero which correspond to infrared markers. To complete the passage map and further refine the spatial resolution of air thermal thickness, the results are combined with the geometrical scan of the segment.

**3D scan of the HT segment** Finally the third approach is the 3D measurement of the geometry. This procedure has to be performed after the thermal response tests since it requires a reflective surface and therefore the black surface has to be covered with silver paint. The 3D measurements are performed using a 3D scanner which allows high resolution measurement of parts with an accuracy up to 20micrometers. The goal is to perform 3D measurement before and after the application of the multilayer and deduce the layer dimension. The measurements are used to first compare the manufactured segment with the CAD geometry (Fig. 7.17) and then the segment equipped with the layers is also compared to an ideal layer of Kapton uniformly attached (Fig. 7.17). The data obtained from the 3D scanner are processed using the GOM Workbench software which allows alignment of the measurements with respect to the CAD and the direct computation of the deviation between a measurement and the CAD. The data for the passage of interest are shown in Fig. 7.18.

The zones with high heat transfer coefficient and already identified with the thermal response tests are again clearly seen in the inlet portion of the passage. However in the middle part of the passage and in the aft part of the passage the additional thickness of

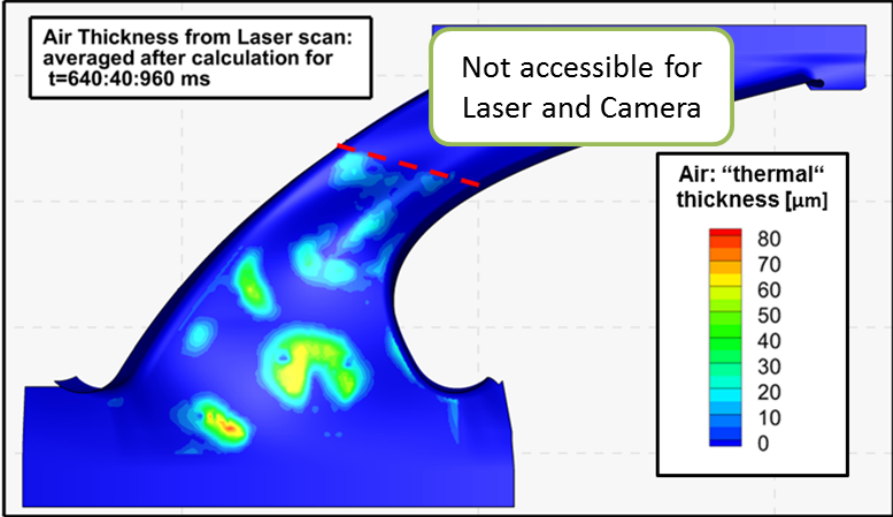


Figure 7.16: Map of air thermal thickness obtained from the thermal response tests.

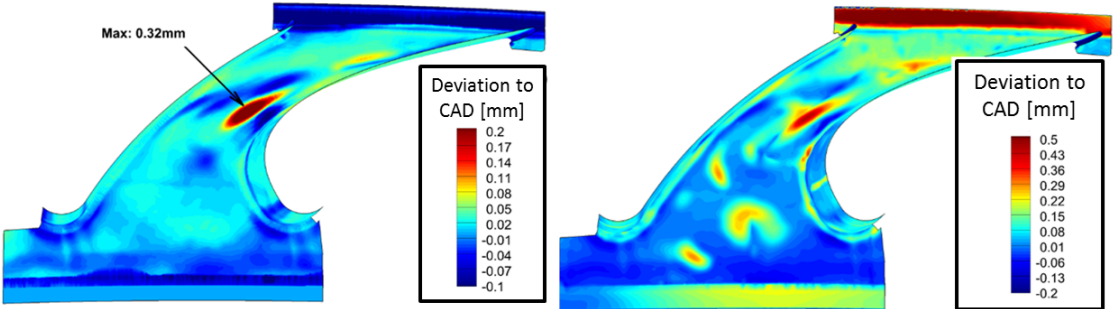


Figure 7.17: Measured geometrical deviation to the CAD model. Left - before Kapton layer application. Right - After Kapton layer attachment and paint coating.

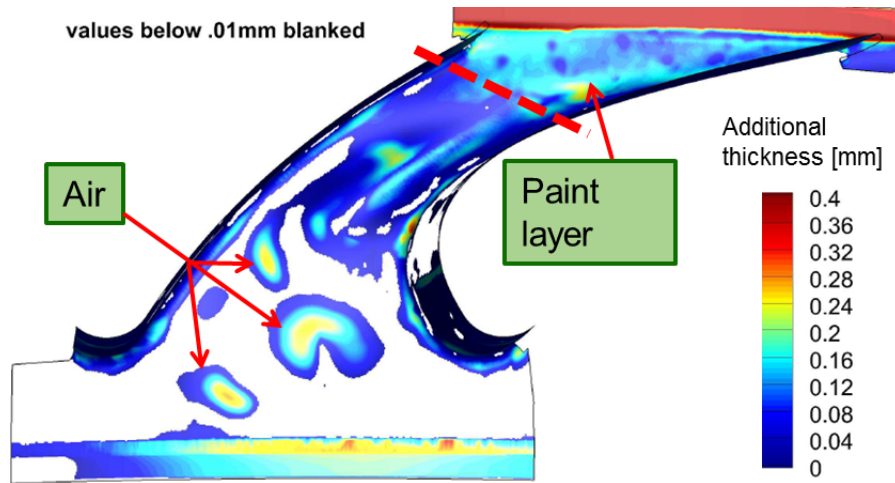


Figure 7.18: Measured additional layer thickness over the passage: difference between the deviation shown in Fig. 7.17.

the layer is attributed to the paint layer. In fact, after the shakedown and the aerodynamic performance mapping, an additional layer of paint was applied to cover infrared markers located at the exit of the passage which were degraded and contaminated a large area.

To conclude, the thermal response tests and the results from the 3D scan of the platform geometry were combined to obtain a complete map of the air thickness covering the complete passage, shown in Fig. 7.20. The map of air thickness and the one of paint thickness (at the passage exit) are used to alter the thermal resistance of the multi-layer structure.

## 7.3 Experimental results

### 7.3.1 Operating conditions

As in the K2 case, the measurements are performed for two operating conditions by changing the mass flow going through the turbine. This corresponds to a reduction of Reynolds number of 28%. More information on the conditions are summarized in Fig. 7.21.

The measurements of heat transfer are performed using 12 to 14 temperature steps in order to obtain accurate heat transfer coefficient and adiabatic wall temperature data. A total of 36 camera positions are used, which leads to a total of 25000 pictures that averaged and processed to obtain a complete map of the passage.

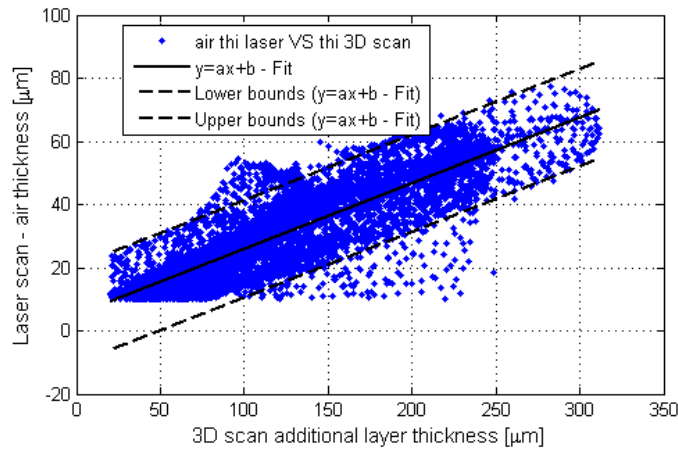


Figure 7.19: Model linking the data from the air thickness from the thermal response test and the measured additional thickness from the 3D scan of the geometry.

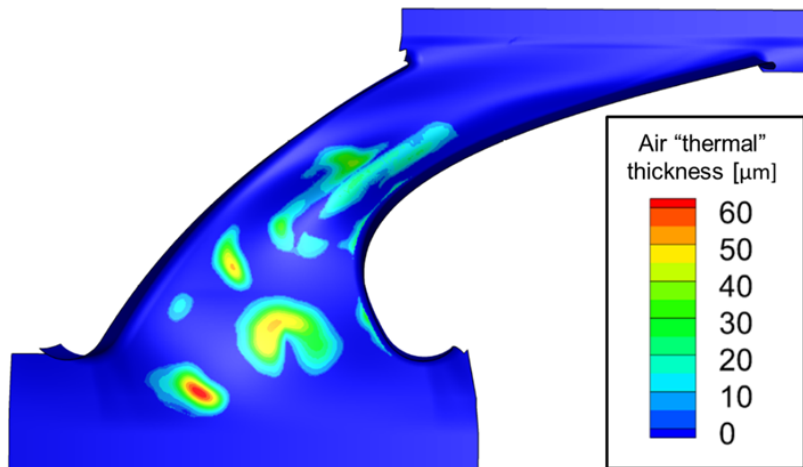


Figure 7.20: Thermal air thickness obtained by combining the laser thermal response and the scan of the geometry.

|                   | Design Pt | LowM   | Design Pt2 |
|-------------------|-----------|--------|------------|
| RPM [-]           | 2700.0    | 2700.0 | 2700.0     |
| m_venturi [kg/s]  | 11.75     | 8.36   | 11.73      |
| m_S1 [kg/s]       | 11.58     | 8.26   | 11.66      |
| IR[%]             | 0.81      | 0.80   | -0.01      |
| PR [-]            | 1.65      | 1.33   | 1.65       |
| T_in [degC]       | 54.53     | 54.60  | 54.48      |
| Number Tsteps [-] | 12        | 14     | 14         |

Figure 7.21: Experimental turbine operating conditions.

### 7.3.2 Heat transfer data calculation

In order to account for the non-uniformity of the thermal resistance measured in the passage, the equation used to calculate the multi-layer thermal resistance Eq. 2.16 becomes Eq. 7.6. A map of the paint thickness is used to account for the additional layer applied at the passage exit.

$$R_{th} = \sum_i \frac{t_i}{k_i} = \frac{t_{adh}}{k_{adh}} + \frac{t_{Kapton}}{k_{Kapton}} + \frac{t_{paint}}{k_{paint}} + \frac{t_{air}}{k_{air}} \quad (7.6)$$

**3D thermal modeling of the test platform** A 3D thermal model of the heat transfer platform is used to quantify the temperature non-uniformity in the solid. The model is shown in Fig. 7.22 and includes the core segment covered with the multilayer composed of adhesive, Kapton and paint, and few neighboring parts. The solid mesh is unstructured but features one layer of prism to limit the first cell height and its orthogonality to the surface. The multilayer mesh is generated by extruding the surface mesh from the segment and features a minimum of 3 layers per body. The thermal simulation are performed using ANSYS Workbench. The boundary conditions are taken from the measurements as follow:

- endwall surface temperature from the measurements with the infrared camera
- forced convection in the channels: the temperature is directly taken from the measurements while the flowrate is used to estimate the heat transfer coefficient in the tubes according to Sleicher and Rouse (in [48])
- convection on the vanes surface from CFD predictions
- convection in the cavity below the platform based on estimated flow velocity and cavity temperature
- convection in the flow path (upstream and downstream) the measurement platform is estimated using the flow velocity and the measured temperature

The sensitivity to the unknown boundary conditions was tested to ensure the accuracy of the selected model. The convection coefficients, on the vanes, in the cavity and on the downstream part are varied. The temperature extracted at the location of the embedded PT100 is used as a criterion to check the dependence of the solution to the boundary conditions. Maximum variation of  $\pm 0.15K$  below the uncertainty from the PT100 are obtained during this analysis. The results are considered therefore unaffected by the uncertainty on the boundary conditions. A typical result from the extracted PT100 is shown in the rightmost graph of Fig. 7.22. In this graph, the green elements represent experimentally measured solid temperature and black the predicted ones. The symbols represent the individual value at the PT100 location while the curves represent laterally averaged data or the overall average. The case shown correspond to the worst case scenario since it corresponds to a solid temperature around 20degC and the mainstream is at 55degC. The predicted and measured data agreed within 0.5K except close to the

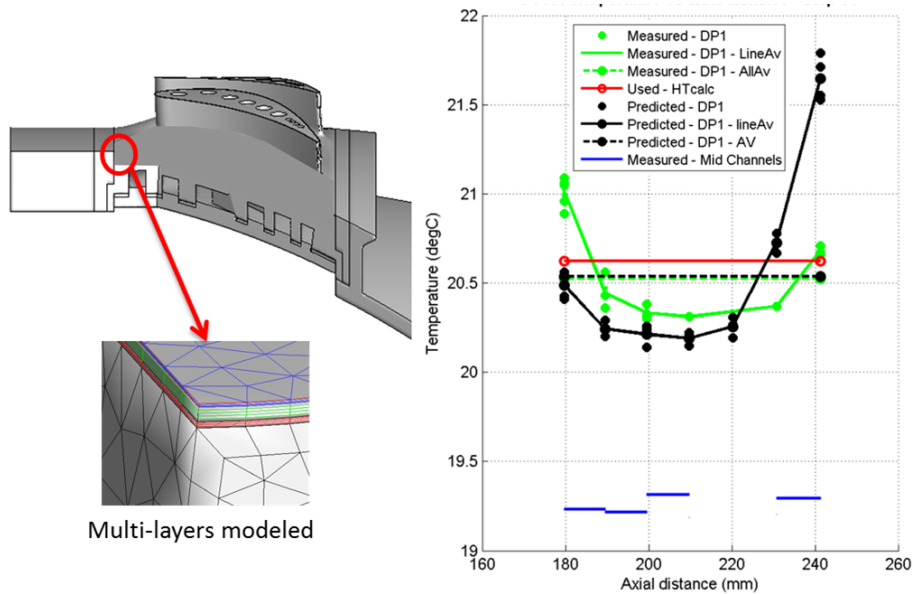


Figure 7.22: Overview of the model used for the thermal analysis (left) to estimate the solid temperature non-uniformity and typical data obtained at the location of the PT100 installed in the segment (right). The results and measurements corresponds to the design point operating condition.

trailing edge where a difference close to 1.2K is shown. The laterally averaged data predicted are used then as input for the solid temperature in the post-processing. In fact the simulation performed for all the temperature steps confirmed the trends shown in Fig. 7.22. Contrary to K2, the uncertainty in solid temperature is only the random error from the PT100 measurements. In K2, the systematic error from the non-uniformity is used.

### 7.3.3 Uncertainty analysis

The uncertainty analysis is performed using the method of successive perturbation of inputs as presented in section 5.2 for the cylindrical endwall case. The difference to the K2 case lies in the solid temperature uncertainty, as an axial variation of the solid temperature is used in the data reduction procedure, and in the uncertainty coming from the non-uniformity in the layer thermal resistance. The values of uncertainty taken into account for the different elements are summarized in Table 7.1. The uncertainty for the air layer thickness measured using the laser is limited to few micrometers but the major source of uncertainty comes from the 3D scan technique, whose accuracy is estimated to  $\pm 10\mu m$ . The uncertainty in the air thickness is therefore driven by the model fit to the data shown in Fig. 7.19.

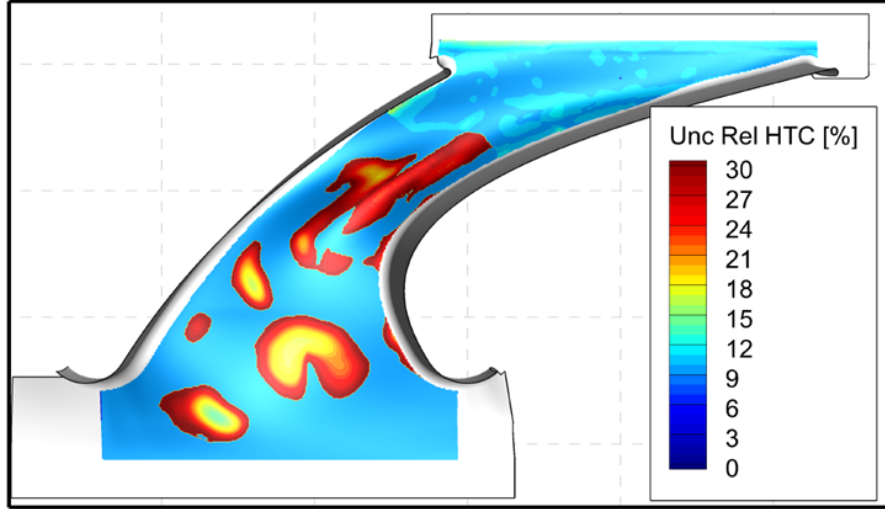


Figure 7.23: Uncertainty in Nusselt number calculated for the design point case ( $Re=720k$ ).

The calculation of the uncertainty is performed for both heat transfer quantities and operating conditions using the tools developed for the data reduction. The distributions of the uncertainty in heat transfer coefficient and adiabatic wall temperature are shown in Fig. 7.23 and 7.24. The effect of the thermal resistance correction is visible in the heat transfer coefficient uncertainty. In region with attached layers, the level is maintained around  $\pm 9.5\%$ , in the downstream part of the passage the level increase close to  $\pm 10.5\%$  due to the extra layer of paint. In the regions covered with detached layer, the uncertainty ranges from  $\pm 15\%$  in the center of the elements to close to  $\pm 30\%$  on the edges where the air layer is very thin. The effect of the micro-air bubbles is opposite on the adiabatic wall temperature, as shown in Fig. 7.24, since it is actually increasing the insulation below the surface. In fact, the adiabatic wall temperature uncertainty is mainly driven by the uncertainty in solid and surface temperatures, but as shown in Eq. 5.1 and 5.2 the increase in thermal resistance will reduce the uncertainty for a given heat transfer coefficient. The levels calculated for the uncertainty ranges from 0.6K in the downstream part of the passage and over the micro-air bubbles up to 1.1K in the inlet portion of the passage.

|                  |                  |
|------------------|------------------|
| $\delta T_w$     | $\pm 0.3K$       |
| $\delta T_{iso}$ | $\pm 0.3K$       |
| $R_{th}$         | $0.0010 \pm 9\%$ |
| $thi_{air}$      | $\pm 15\mu m$    |

Table 7.1: Uncertainty values for the contoured endwall configuration.

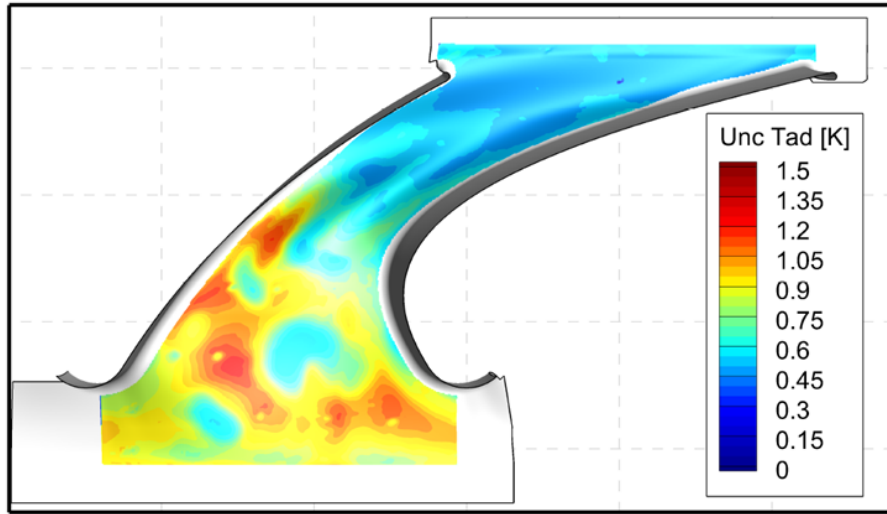


Figure 7.24: Uncertainty in adiabatic wall temperature calculated for the design point case ( $Re=720k$ ).

### 7.3.4 Results

The results obtained from the data reduction procedure including the different corrections applied are shown in Fig. 7.25 & 7.26 for the design point case and Fig. 7.27 & 7.28 for the reduced mass flow case. The correction of the micro-bubbles is visible especially on the edges of the micro-bubbles, but the heat transfer coefficient is recovered and reduced to similar levels as surrounding points. The Nusselt number distributions for both cases are showing similar patterns with an increase of heat transfer after the peak acceleration on the suction side and downstream of the throat. The distribution of adiabatic wall temperature are matching the flow velocity change through the passage. Between the low and high Reynolds number case, the exit Mach number changes from  $M=0.44$  to  $M=0.55$  as measured using 4-hole pneumatic probe. The drop of adiabatic wall temperature is limited to 2K in the lower mass flow case, while a drop around 3.5K is measured for the design point. These values are of the same magnitude as the expected drop in recovery temperature of 2.9K (design point) and 1.5K (low mass flow) for a flat plate calculated using Eq. 5.6.

The increase of the heat transfer coefficient levels of 37% due to the variation of Reynolds number is calculated between Fig. 7.25 and 7.27, and its distribution across the passage is shown in terms of Nusselt number ratio in Fig. 7.29. The Reynolds number reduction achieved between the two operating conditions is equal to 28% and according to the dependence of Nusselt number to the Reynolds number for a flat plate given in Eq. 6.7, the measured variation is close to expected. A region of high Nusselt number ratio shaped as a Z is measured in the middle of the passage and follows the change of the endwall shape around the trough close to the suction side. This zone is also located



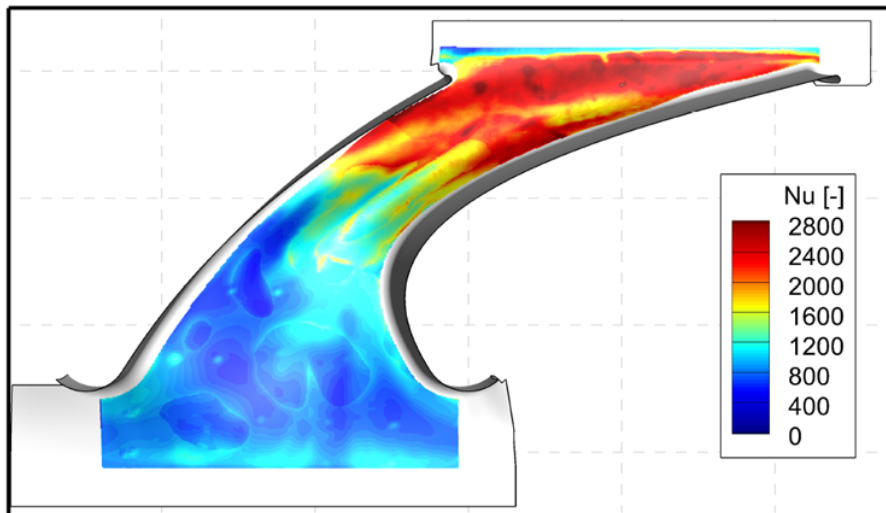


Figure 7.25: Nusselt number measured in the design point case ( $Re=720k$ ).

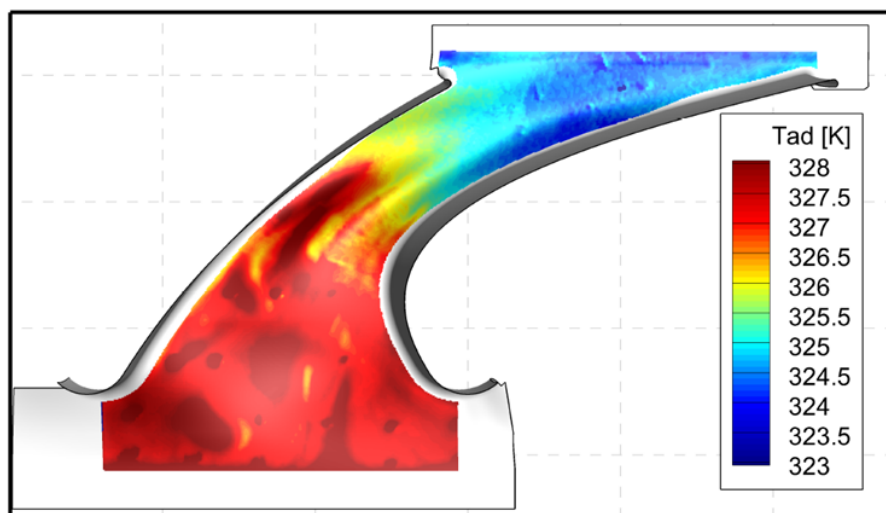


Figure 7.26: Adiabatic wall temperature measured in the design point case ( $Re=720k$ ).

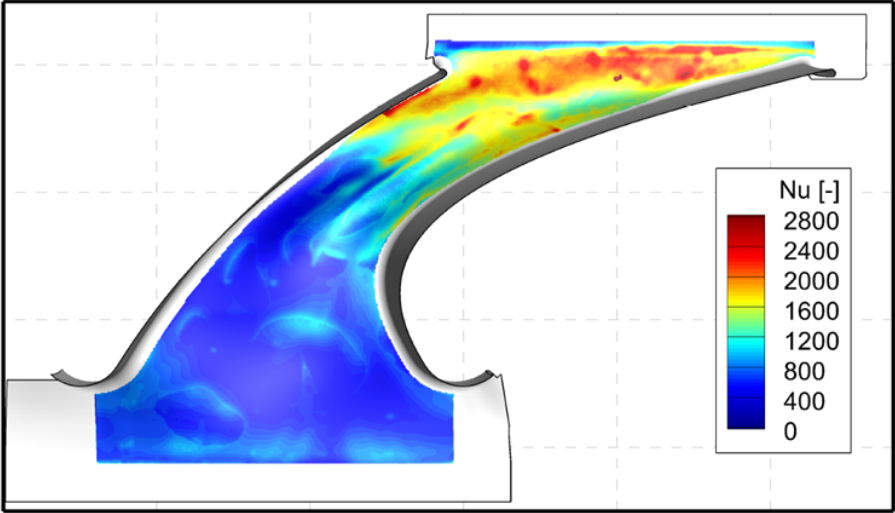


Figure 7.27: Nusselt number measured in the reduced mass flow case (Re=520k).

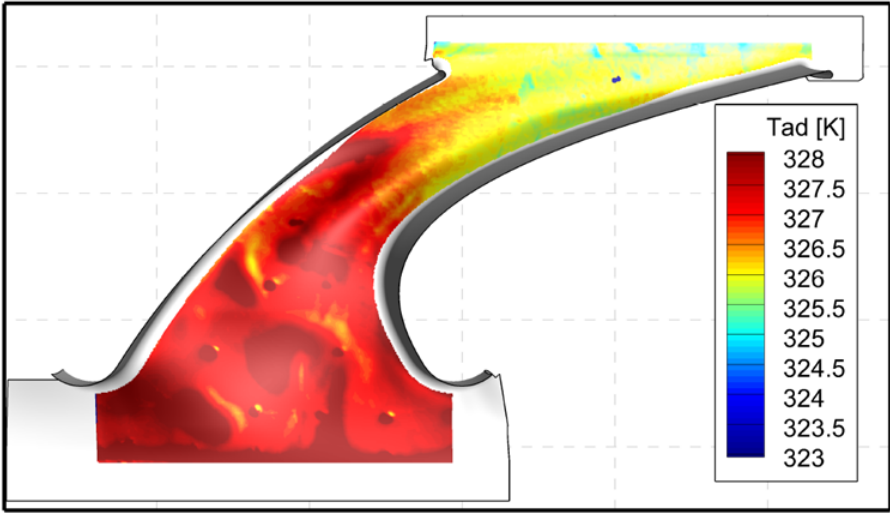


Figure 7.28: Adiabatic wall temperature measured in the reduced mass flow case (Re=520k).

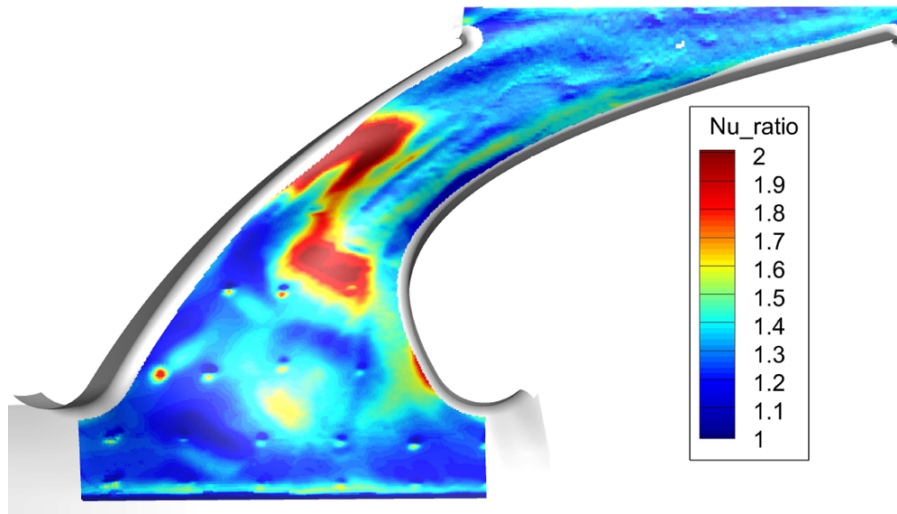


Figure 7.29: Nusselt number ratio highlighting the effect of Reynolds number on heat transfer.

close to the peak acceleration of the flow. At the exit of the passage, the level of the ratio measured is close to a the turbulent estimation and suggests that the high values of heat transfer coefficient measured in this region, compared to the cylindrical case, are due to flow features present at both operating conditions.

### 7.3.5 Effect of the contouring on the thermal loads.

The comparison of the adiabatic wall temperature distributions, shown in Fig. 5.9 for the cylindrical endwall and Fig. 7.26 for the contoured case, does not lead to any conclusion on the effect of the contouring. In fact, the two distribution are very similar and the differences are within the uncertainty band. It should be noted that the area of the endwall, excluding the filet, is increased by 11% in the contoured case compared to the cylindrical endwall. To be beneficial, the effect of the contouring on the thermal loads should compensate also for the wet area increase.

The comparison of the Nusselt number distribution for the cylindrical (Fig. 5.8) and contoured (Fig. 7.25) highlights the high level of heat transfer coefficient measured at the exit of the passage in the contoured case. In the inlet portion, the levels measured are of similar magnitude. The higher HTC trace resulting of the horseshoe vortex which is visible in the contour plot for the cylindrical case, is not present in more diffuse in the contoured case and seems to be directed more towards the suction side of the passage. The laterally area averaged data shown in Fig. 7.30 confirms the trends of the contour plots. The error bar show the impact of the corrected thermal resistance on the results with an increased uncertainty in those regions. In the inlet portion of the passage, the two curves lies within the uncertainty while at the exit of the passage, the contoured case features a level of Nusselt number 45-50% higher than the cylindrical case. Two

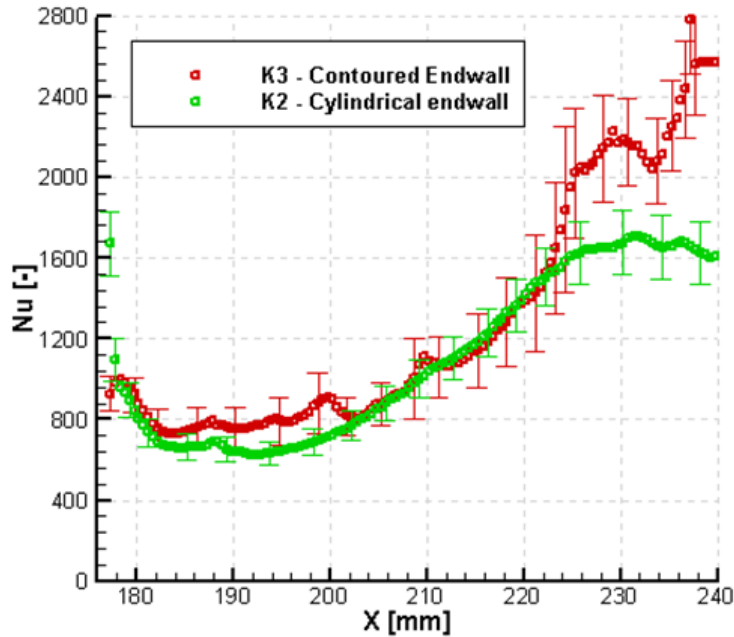


Figure 7.30: Laterally area-averaged Nusselt number distribution for the two endwall configurations at design point. The error bars show the laterally averaged uncertainty.

aspects have to be considered to explain this increase at the passage exit, the change in the flow field introduced by the contouring, especially the wall shear stress, and the level of roughness measured at the exit of the passage due to the additional paint coating deposited using a different air spray system for accessibility reason.

## 7.4 Effect of the endwall contouring on the flow structure.

A numerical model is developed according to the studies performed for the cylindrical case and presented in section 6.2. The simulation are performed with Multi3 on a single passage of the NGV row. The flow predictions are used to investigate the effect of endwall contouring on the flow field.

The effect of the endwall contouring on the static pressure field is presented in Fig. 7.31. The contouring is changing the shape of the pressure distribution especially close to the throat. In general, a convex curvature will increase the static pressure field and thereby reduce the local flow velocity, while a concave curvature will reduce the static pressure and increase the flow velocity. The hill located on the pressure side has a limited impact on the static pressure field. On the other hand, the valley positioned closer to the suction side illustrates the effect of concave curvature. The pressure field appears stretched in the direction of the trough compared to the cylindrical case. While

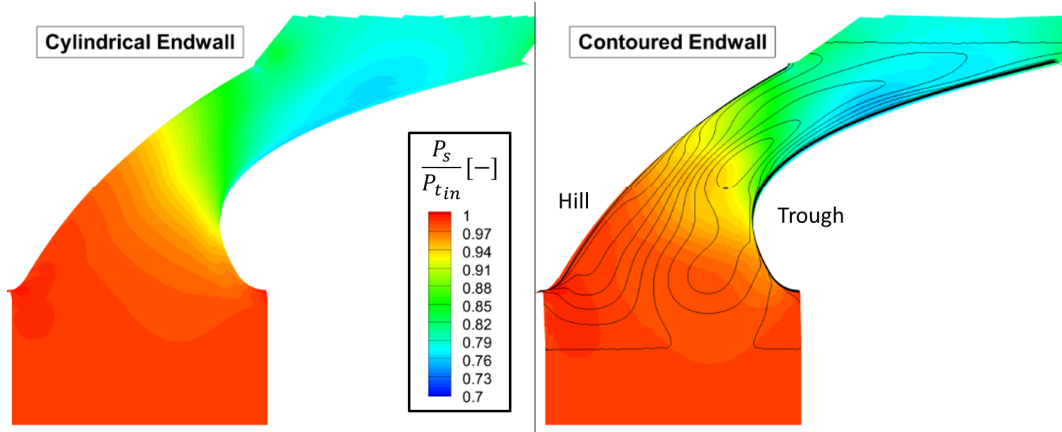


Figure 7.31: Static pressure field predicted on the hub endwall for the cylindrical (left) and contoured (right) cases. The lines illustrates the variation of the platform radius.

this effect could be used to limit the cross-passage pressure gradient as in Schuepbach et al. [81], the current design intent is more affected in accelerating the migration of the horseshoe vortex pressure side leg toward the suction side and limiting its radial migration. The comparison of streamlines issues of identical points for both cylindrical and contoured cases will help in identifying these behavior. After the throat, a hill is present close to the suction side and its effect is visible as the static pressure field is going to a minimum in this region.

As discussed in the introduction, the control of pressure side leg of the horseshoe vortex is critical to reduce the secondary flow losses. To compare the migration pattern of the HV between the two endwall configuration, streamlines releases at the same location are studied. The streamlines are issues from points of constant radius located at the inlet of the fluid domain, as shown in Fig. 7.32. The figures 7.33, 7.34 and 7.35 shows the lines coming from three different radial location 1.5%, 5.7% and 10% span, and the lines are colored based on the radial migration  $dR$  of the "particle", which is the variation in radius compared to the original radius of "injection" ( $dR = R_{particle} - R_{injection}$ ). The first figure Fig. 7.33 considers streamlines injected very close to the wall and illustrates how the flow is swept by the horseshoe vortex when entering the passage. The two views at the exit of the passage (top) and the top view (bottom) shows the difference in the particles trajectories between between the two geometries. In fact, at the inlet of the passage, the presence of the hill extending upstream of the leading edge on the pressure side deviates the flow in a region more upstream of the leading compared to the cylindrical case. The combined effect of the hill on the pressure side and the trough on the suction side creates an early migration of the flow towards the suction side. The presence of the trough results in a negative migration of the flow, ie. the flow follows the shape of the platform below the nominal radius. While following the suction side the flow remains closer to the endwall as illustrated by the color code and the view of the

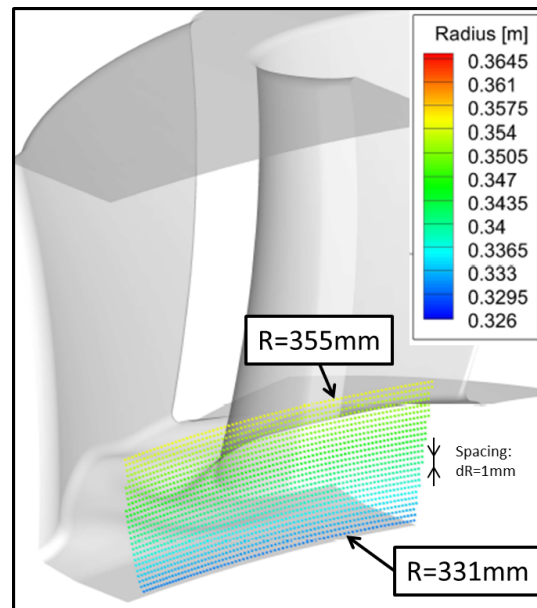


Figure 7.32: Location of the injection points to obtain the streamlines presented in Fig. 7.337.34 and 7.35.

passage exit. At the exit of the passage, the passage vortex appears to cover a wider area but remains closer to the endwall and vanes surfaces. The impact of the early migration on the heat transfer patterns could explain why the pattern following the pressure side leg of the HV in the K2 case is not clearly seen in K3.

Considering the particles released at a higher span-wise position shown in Fig. 7.34, the particles are pushed closer to the suction side in K3 compared to K2. The radial migration of the particles close to the suction side is also reduced. The last figure 7.35 shows that the endwall contouring has a very limited impact at higher span-wise position. For both configurations, the color of the streamlines shows that close to the suction side the particles are migrating towards the tip while on the pressure side, the particles are pushed towards the hub platform.

The figure. 7.36 illustrates the difference on the wall shear stress induced by the geometrical changes of the endwall. Some of the discontinuities of the contour are due to the calculation of the velocity gradient at the wall and should be ignored. The levels of shear predicted on both endwall are overall of similar magnitude but their distribution differs. Levels at the exit of the passage are 10% higher in the K3 case compared to K2. Also close to the left vane leading edge, the increase in wall shear stress corresponding to the down wash side of the HV which is visible for K2, is not present in the K3 case. The location of the HV formation and its migration described using the streamlines explains the difference. Two noticeable high shear regions are noticeable in the case with endwall contouring, one region close to the trailing edge of the leftmost vane which extends circumferentially towards the suction side and one downstream of the trough before

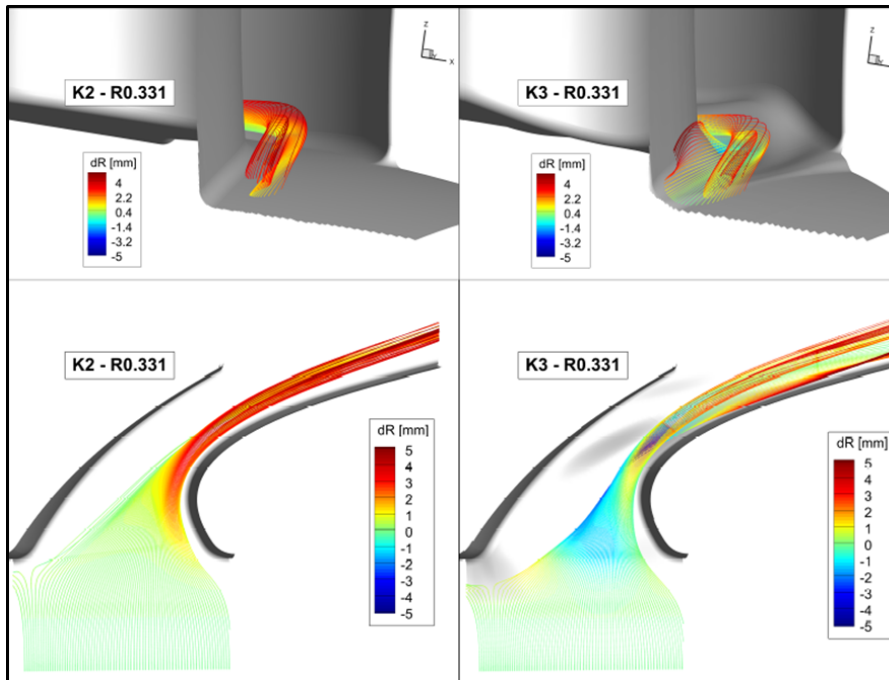


Figure 7.33: Streamlines obtained from CFD predictions for cylindrical (left) and contoured (right) endwalls. The injection points are located at a constant radius of 331mm (1.5% span) as shown in Fig. 7.32.

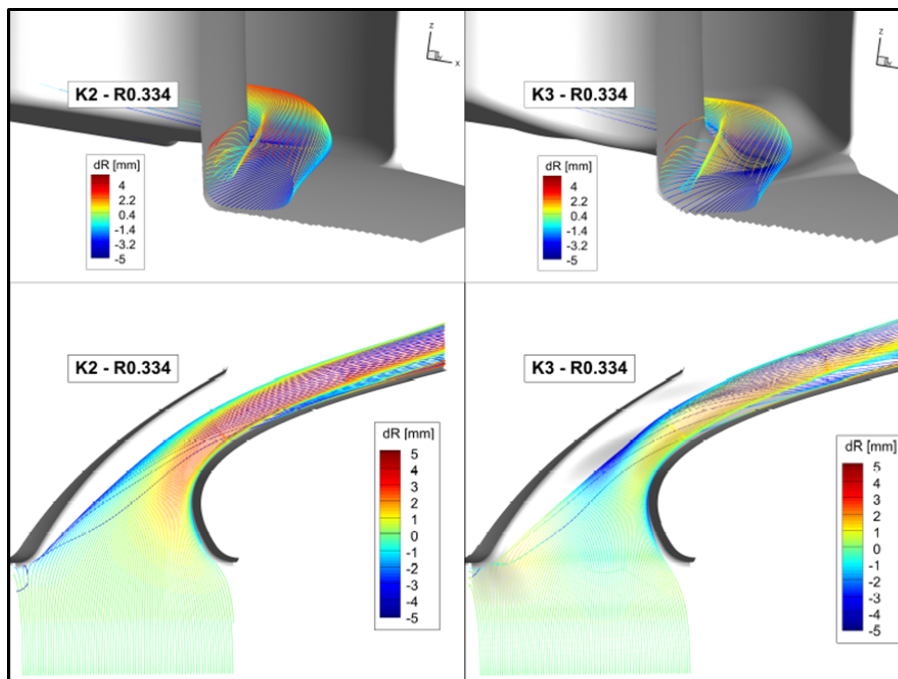


Figure 7.34: Streamlines obtained from CFD predictions for cylindrical (left) and contoured (right) endwalls. The injection points are located at a constant radius of 334mm (5.7% span) as shown in Fig. 7.32.

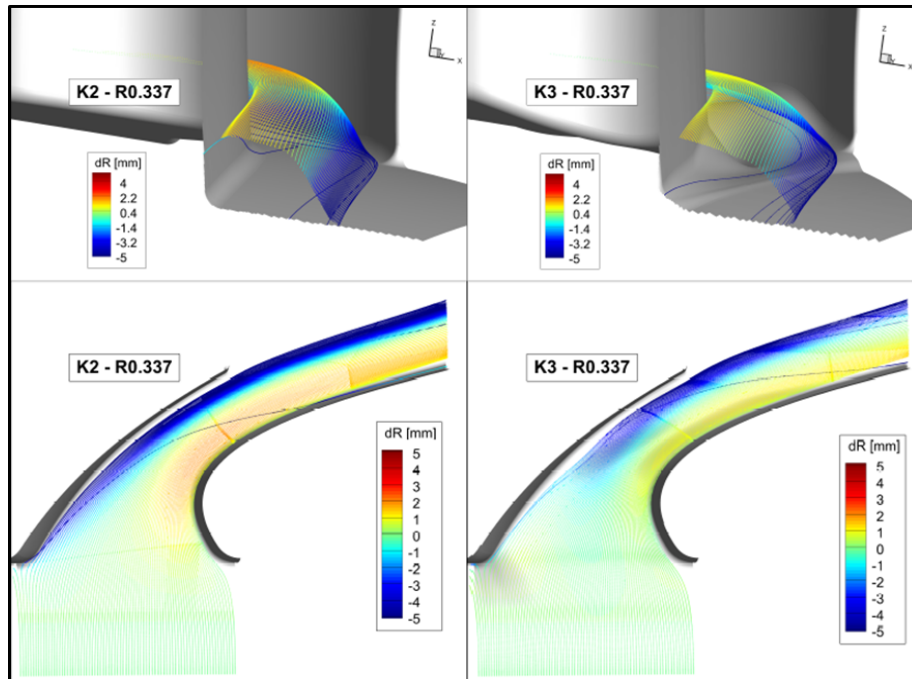


Figure 7.35: Streamlines obtained from CFD predictions for cylindrical (left) and contoured (right) endwalls. The injection points are located at a constant radius of 337mm (10% span) as shown in Fig. 7.32.

the hill close to the suction side. A region of low shear crossing the passage separates the two described regions. This pattern also appears in the Nusselt number distribution (Fig. 7.25 but more noticeable on Fig. 7.27) where a trail with reduced Nusselt value cuts the downstream part of the passage in two. The wall shear stress appears more uniform distributed on the cylindrical endwall, whereas in K3 the high levels are concentrated in smaller regions. This has to be put in perspective with the heat transfer coefficient distribution previously described in Fig. 5.8 and 7.25, where the magnitude of the Nusselt number measured differs but also the distribution appears close to the patterns from the wall shear stress.

The combined effect of the change in predicted wall shear stress levels due to the endwall contouring for smooth endwall, and the increased roughness levels measured at the exit of the stator passage compared to the cylindrical case, can explain the difference of 45-50% in Nusselt number measured in the K3 case compared to K2.

## 7.5 Summary

The current chapter dealt with the measurements of heat transfer quantities on contoured endwall. The heat transfer measurements are performed on the hub endwall of the NGV row using an adapted platform compared to K2. The attachment of the Kapton layer



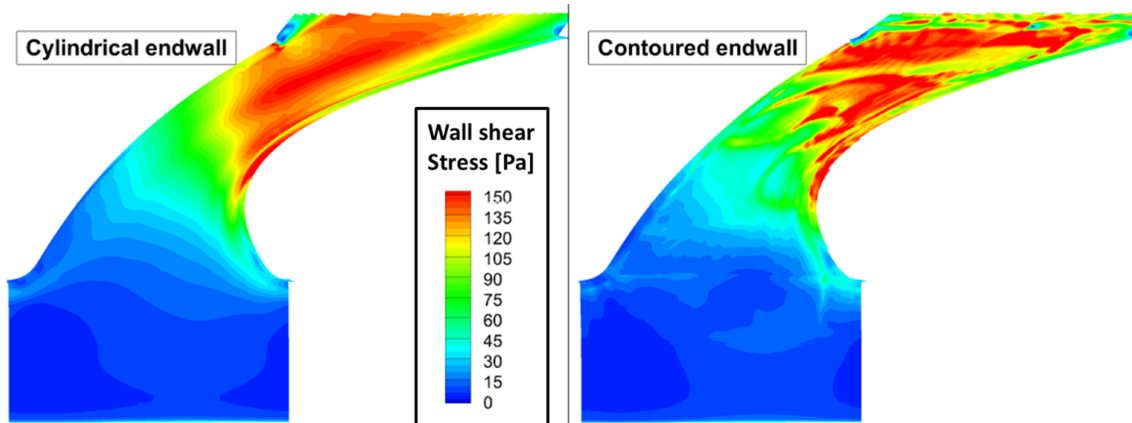


Figure 7.36: Contour plot of wall shear stress for the cylindrical (left) and contoured (right) endwall.

on the contoured surface lead to mis-attachment affecting the results in specific regions covering about 20% of the endwall. A specific methodology is developed to recover the data in the missing regions. The recovery procedure uses surface thermal response tests to quantify the thickness of the air layer trapped underneath the Kapton layer. The results are then successfully corrected in those regions. The adiabatic wall temperature measured for both operating conditions follows the expected trends with decreasing values across the passage corresponding to the increase in Mach number. The magnitude of the reduction is close to the expected value from theoretical correlation. The distribution of heat transfer coefficient is modified by the contouring and the impact of the pressure side leg of the horseshoe vortex is not clearly visible compared to the K2 case. The levels of heat transfer downstream of the throat at the exit of the passage show an increase of 40-45% compared to the K2 case. The combination of the higher predicted shear stress level in those regions and the increased roughness present at the exit of the passage, can explain the large variation to the cylindrical endwall. The laterally averaged data obtained on the contoured endwall highlight the difference to the cylindrical endwall, especially in the downstream part of the passage. A variation of Nusselt number close to 37% between the high and low Reynolds number cases is measured. In particular high ratios are measured where the three deformation of the endwall is maximum. Finally, numerical predictions provided an idea of the modification of the flow field resulting from the endwall shaping. In particular the change in the horseshoe vortex formation and migration pattern is visible.



# Chapter 8

## Detailed analysis of the results and discussions

The heat transfer coefficient measured for the different configurations is shown in Fig. 8.1 and 8.2 in terms of local Stanton number  $St_s$  (Eq. 8.1) divided by the local Stanton number from a turbulent flat plate correlation  $St_{s,0}$  (Eq. 8.2). Different CFD predictions obtained during this project, have highlighted the sensitivity of the horseshoe vortex location and strength to the incoming flow conditions and especially the turbulence length scale. Despite the use of a of distribution length scale for the predictions, coming from inlet simulation or annulus correlation, the predicted streamline location and associated velocity cannot be fully trusted. In this section, the analysis is therefore based on the predicted endwall pressure distribution, which is commonly well predicted with numerical tools. The isentropic Mach number is then obtained from Eq. 8.3 as well as the necessary local density and velocity. The inviscid streamlines have been used to define a coordinate system accounting for the flow turning along the passage.

$$St_s = \frac{h}{\rho(s)C_p U(s)} \quad (8.1)$$

$$St_{s,0} = 0.0287 Pr^{-0.4} Re_s^{-0.2} \quad (8.2)$$

$$M_{is} = \left( \left( \frac{P_{t,in}}{P_s} \right)^{\frac{\gamma-1}{\gamma}} \right)^{0.5} \quad (8.3)$$

The data are non-dimensionalized with the correlation for the Stanton number on a flat plate, defined in Eq. 8.2. While this equation was established based on measurements performed at constant free stream velocity, it remains a tool of choice for the thermal designer when dealing with more advanced flows with favorable and adverse pressure gradient. In fact, the correlations obtained for these cases are often relying on more complex non-dimensional number such as Reynolds numbers based on the boundary layer momentum thickness or enthalpy thickness.

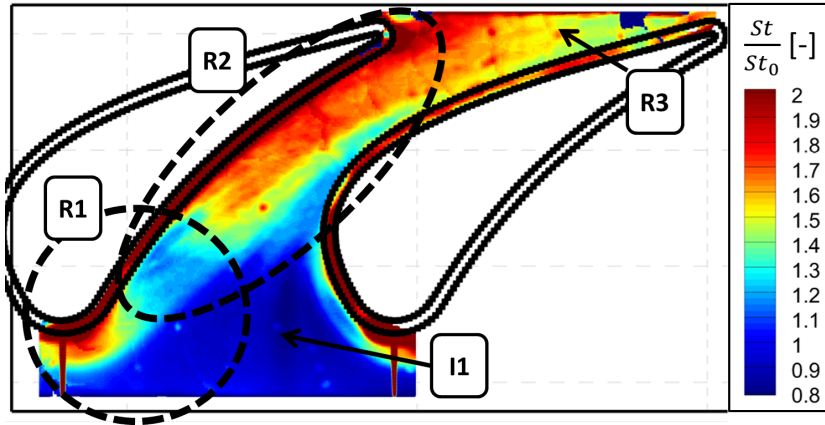


Figure 8.1: Stanton number ratio in the cylindrical endwall case at design point.

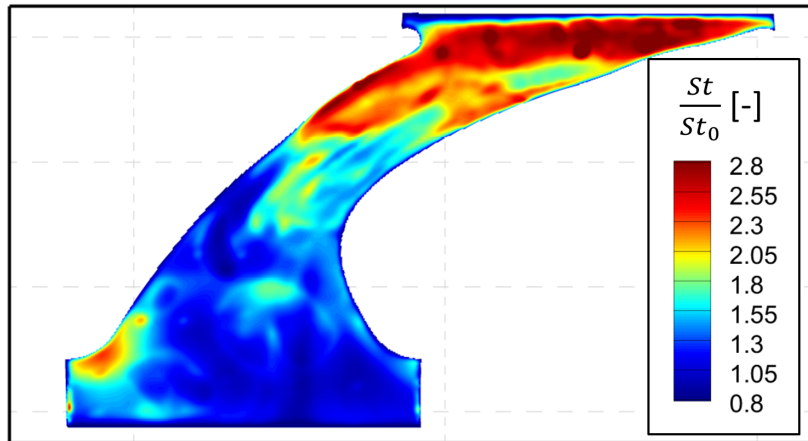


Figure 8.2: Stanton number ratio in the contoured endwall case at design point. Scale different from Fig. 8.1.

The Stanton number ratio  $St_s/St_{s,0}$  highlights the regions where the measured data spread from the classical flat plate values, because of the variation of main flow quantities through the passage (acceleration,...) and the resulting effect on the boundary layer (thickness, turbulence intensity), the impact of three dimensional flow structures on the boundary layer shape and inner layers, the change of surface properties affecting the inner layer of the boundary layer (roughness).

Figure 8.1 shows the Stanton number ratio obtained for the cylindrical endwall case and divides the passage in different regions. In inlet portion I1 of the passage the ratio is close to unity, while accounting for the 10% uncertainty in heat transfer coefficient. Close to the suction side, a region with a ratio lower than 0.9 is observed (at the tip of the arrow I1). This low value stripe actually extends from the start of the thermally managed section until the passage, similar to a wake or a streak from a local variation of incoming flow conditions. A similar streak is noticeable in the contoured endwall case

shown in Fig. 8.2, which points also in the direction of a modified incoming boundary layer. Upstream of the leading edge, the Stanton number is almost doubled compared to the flat plate case. The formation of a complex vortical structure is responsible for this local increase. This region and the beginning of the pressure and suction side of the passage will be further detailed in the next section. Further downstream a region R2 of Stanton number ratio close to 2 is observed. This region close to the pressure side of the vane appears limited circumferentially by the pressure side and a line linking the leading edge and the peak of the suction side. While the ratio is first seen to increase, it then stabilizes close to the throat of the passage. Finally at the exit of the passage (R3), a decrease of the St ratio is visible close to the suction side. The contour of the Stanton ratio are shown in Fig. 8.2 for the contoured endwall case. In order to reduce the visual impact of the corrected area, the contour has been smoothed. In this case, a doubling of the Stanton number is visible also at the leading edge (R1). However, the high value region (R2) observed in the cylindrical case extending close to the pressure side is different. Despite the non-matching scale, a comparison of the two figures 8.1 and 8.2, a difference in the pattern observed close to the pressure side is visible. The ratio reaches a higher value around 2.8 close to the passage throat in the contoured case while the value on the cylindrical endwall is limited to 2. At the exit of the passage (R3), the ratio remains constant close to the suction side on the contrary to the cylindrical case.

Despite the lack of flow field measurements within the vane passage, the high resolution of the measurements provides clearly defined heat transfer coefficient patterns, which help in making hypothesis on the secondary flow structure. Based on existing work related to horseshoe vortex formation, impact of longitudinal vortices on heat transfer and heat transfer on rough surfaces, a more detailed analysis can be performed. Also based on known effects of endwall contouring and an analysis of endwall pressure distribution as well as predicted surface streaklines, additional information are obtained to further explain the patterns.

## 8.1 Impact of the formation of vortices in the leading edge region

The first region of interest is the leading edge of the vane, shown as R1 in Fig. 8.1. This region is essential for the understanding of the flow behavior and thermal loads patterns present in the passage. In fact, in this region the vorticity contained in the incoming boundary layer in the form of a radial velocity gradient is transformed into secondary flow structures due to the presence of the vane leading edge. The secondary flow model of Langston et al. [51] described the roll up of the incoming boundary layer, the stretching of the forming vortex and its separation into a pressure and a suction side leg. The later model of Fig. 8.3 developed in Wang et al. [90], shows a more complex structure forming at the leading edge with two vortex forming and rotating in the same direction. In their

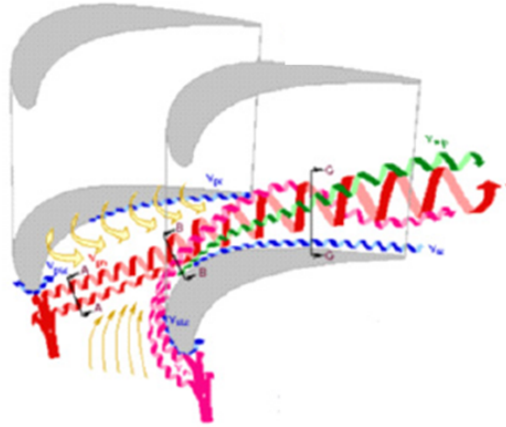


Figure 8.3: Secondary flow model developed by Wang et al. [90].

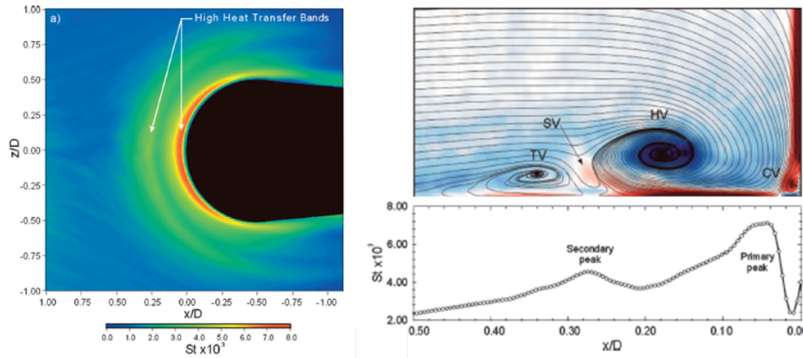


Figure 8.4: Left - time averaged endwall heat transfer distribution in the form of Stanton number ( $St = \frac{h}{\rho C_p U_{in}}$ ). Right - Spatially aligned flow field and endwall heat transfer data on the symmetry plane. From [73].

work, Praisner and Smith [72, 73] focus on the leading area upstream of a symmetric airfoil with a cylindrical leading edge, without fillet, and detail the time resolved [72] and time averaged [73] flow physics and heat transfer patterns measured in this area. The formation of four distinct vortices is highlighted in their work, the horseshoe, secondary, tertiary and corner vortices. Interestingly the tertiary and the horseshoe vortices are rotating in the same direction defined by the incoming vorticity. Two major results are shown in Fig. 8.4 to help the reader in identifying the similarity with the current study. These observations corroborate the flow model of Wang et al. [90]. The signature of the vortices is present in the Stanton number distribution by the presence of two peaks located on the downward side of the horseshoe and tertiary vortices. The maximum value is observed close to the vane, while the secondary peak is observed at a distance approximately 0.3 leading diameter upstream.

The results of the current study are shown in Fig. 8.5, where the contours of heat transfer coefficient are shown and set to emphasize the local variation of the heat transfer

coefficient. Upstream of the leading edge, the extracted profiles highlight a rather peaky distribution of heat transfer coefficient. The initial decrease is linked to the start of the thermal boundary layer, while a maximum value is measured close to the fillet and a peak is observed more upstream. The location of the secondary peak is varying with the operating conditions, the distance from the leading edge changes from 6mm at design point to 7mm at low Reynolds number. The peak closer to the leading edge also appears to move away from the vane for the lower Reynolds number case. The reduction in incoming flow momentum can explain the location of the vortices further away from the leading edge. The comparison of the contour from Fig. 8.4 with Fig. 8.5 also highlight the similarity in the pattern observed on the sides of the leading edge with alternate bands of high and low heat transfer.

The work of Eibeck and Eaton [28] on a single longitudinal vortex embedded in a turbulent boundary layer provides an explanation for the alternate bands of low and high heat transfer close to a vortex. Three reasons are reported for the change in heat transfer coefficient, the change in the mean velocity and temperature fields, the variation of turbulence quantities, and the effect on the near wall layer of the boundary layer. The combined measurements of flow and heat transfer, highlighted an increase of 25% on the downwash side of the vortex, while a decrease close to 15% is measured on the upwash side. The variation is explained by a change in the boundary layer thickness on both side of the vortex. The variation of the heat transfer coefficient with the circulation of the vortex is seen to be non-symmetric, with a larger increase on the downwash side, while the decrease remains around 15%. For the current study, upstream of the leading edge, the difference between the upwash and downwash sides of the tertiary vortex is between 18% at design point and 23%. For the primary peak closer to the leading edge, the heat transfer coefficient is almost doubled with an increase of 88% for the low Reynolds number case. The design point value is not representative since the profile of heat transfer coefficient keeps rising closer to the fillet. Close to the pressure side, a difference is observed between the two operating conditions. In the design point case, a uniform increase of heat transfer coefficient is visible between 5 and 12mm from the vane. An increase of 15% is measured between the lower region and the uniform zone. In the low Reynolds number case, a major increase of 16% is measured 11mm from the vane while a weak secondary peak 5% is visible around 5mm from the vane. Downstream of the leading edge, the two vortical structures are convected along the pressure side of the vane but their intensity is decreasing. In the case of the design point, the two structures remain close to each other and seems to interact and keep a significant effect, which lead to a region with uniform increase. In the second case, the two vortices appears spread further apart. The vortex further apart seems to maintain a high activity and has a impact on the heat transfer coefficient distribution, while the vortex closer to the vane appears weaker, with a limited influence on the distribution. Similar increase of heat transfer coefficient are observed close to the suction side.

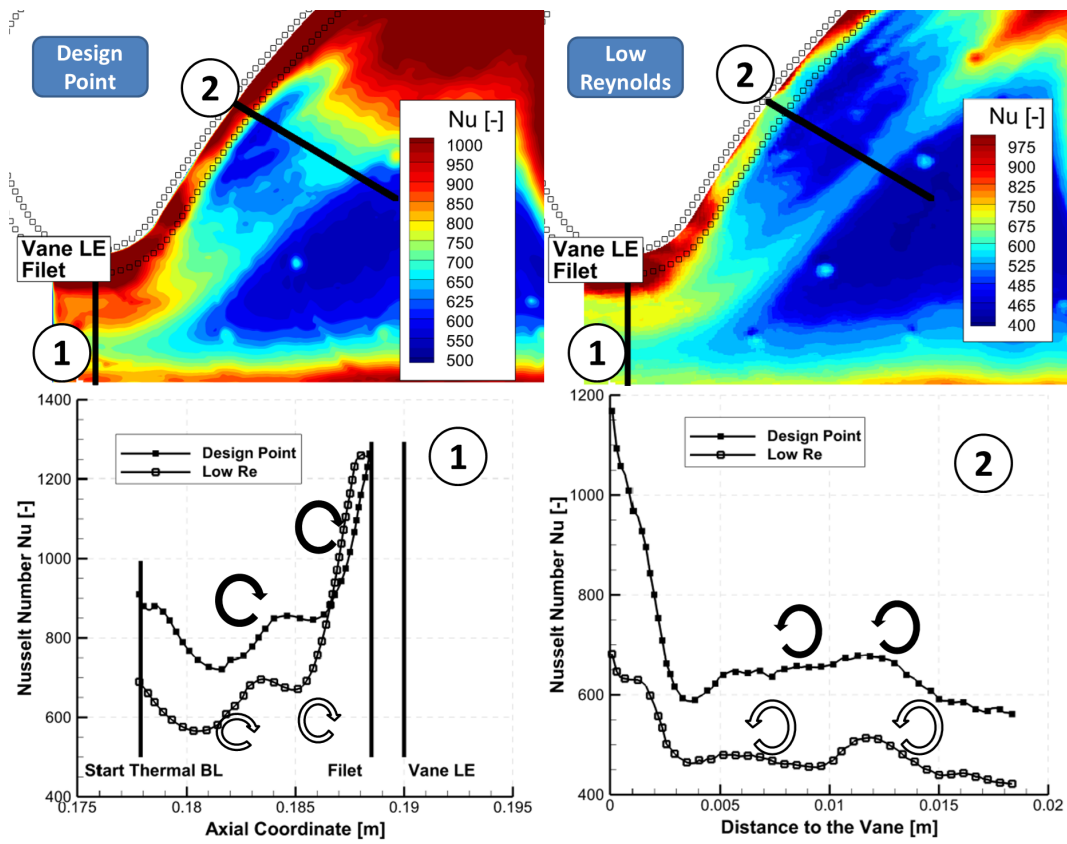


Figure 8.5: Contour of Nusselt number for the cylindrical endwall case for the two operating conditions, design point (top left) and the reduced Reynolds number (top right). Bottom - profiles of Nusselt number extracted along the lines 1 and 2.



To summarize, a complex vortical structure, shown in Fig. 8.6, composed of two primary vortices rotating in the same direction appears to form upstream of the leading edge and influence the heat transfer patterns close to the leading edge as well as along the pressure and suction sides. While the Stanton number values are almost doubled at the leading edge when compared to a flat plate, increase close to 25-30% are observed on both sides of the leading edge. The upwash-downwash effect is visible in the measurements but the amplitude of this effect remains around 20%, lower compared to previously reported data [28].

### 8.1.1 Influence of the endwall contouring on the flow structure close to the leading edge.

Close to the leading edge, the contoured endwall case features an elevation on the pressure side shown in Fig. 8.8, while a trough is further downstream on the suction side. Immediately upstream of the leading edge, the endwall shape is rising in a linear fashion. A profile of heat transfer coefficient extracted upstream of the leading edge is shown in Fig. 8.7. Compared to the cylindrical case, the magnitude is similar but the pattern of heat transfer coefficient is different. Because of the rise of the endwall, the incoming flow is facing a concave curvature close to the start of the thermal boundary layer, leading to a higher blockage and a rise in static pressure rise and a decrease in flow velocity. Because of the vorticity contained in the incoming flow, facing the adverse pressure gradient can lead to a separation, the formation of a vortex and re-circulation zone. An increase-decrease region (+12% in HTC for the low Reynolds number and +29% for the design point case) corresponding to a vortex upwash-downwash is visible close to  $x = 0.18m$  for the design point measurements and slightly downstream for the low Reynolds number case. Closer to the leading edge another local peak in heat transfer coefficient (+29% at design point, +22% in the low Reynolds number case) is visible and should correspond to the formation of the horseshoe vortex. In the immediate vicinity of the fillet and the leading edge, the rise in heat transfer coefficient can be explained by the formation of another vortex, but the data are not sufficient to draw a conclusion. Contrary to the

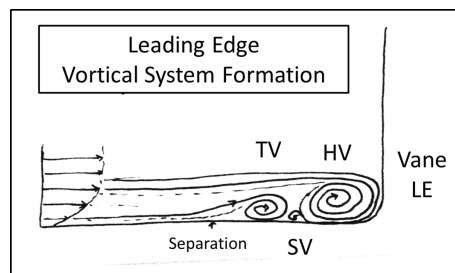


Figure 8.6: Schematic of the complex vortical structures forming at the leading edge of the vane. Adpated from Praisner and Smith [72].

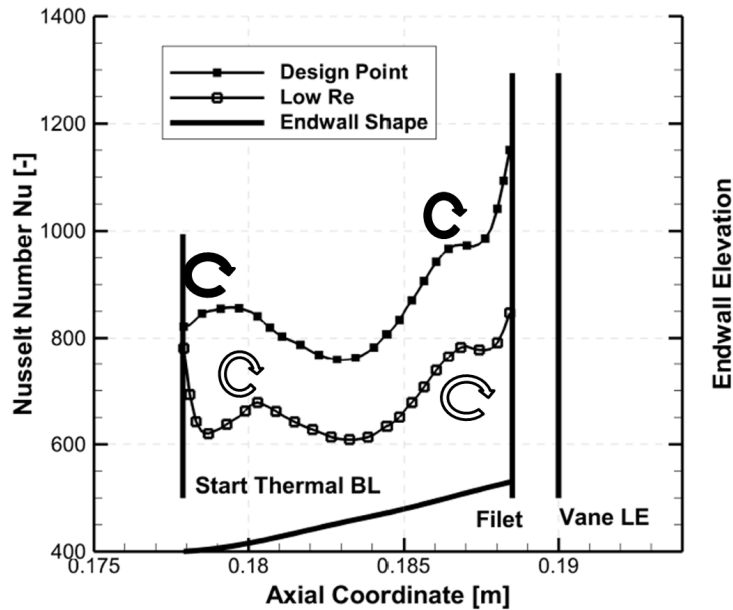


Figure 8.7: Profile of Nusselt number extracted upstream of the leading edge for the contoured case. The profile of the endwall is shown at the bottom of the graph (scale on the right).

cylindrical endwall, the vortices appear to form closer to the vane leading edge for the flow conditions with the lower inlet momentum. The presence of the concave curvature and a re-circulation region immediately at the start of the thermally managed region appear to also affect the decrease of the heat transfer coefficient generally observed at the start of a thermal boundary layer.

The leading edge modifications using a bulb in Sauer et al. [77], and a fillet in Zess and Thole [92] have shown promising results in reducing the aerodynamic losses, and concluded that the fillet should have the a height equal to one boundary layer thickness and an axial extension equal to two boundary layer thicknesses. In the current study, the incoming boundary layer thickness is close to 10mm and the dimensions of the fillet and endwall modifications at the leading edge are not so extreme, but appear to have a significant impact on the heat transfer patterns.

Compared to the cylindrical case, the effect of the vortical structures convected along the vane pressure side are almost non-existing in Fig. 8.2. The extension of the pressure side leg of the vortex or vortices appears to vanish quickly downstream of the leading edge. As seen in Fig. 8.8, the endwall contouring features an elevation on the pressure side of the leading edge, extending well upstream of the passage. The combined presence of the hill and the leading edge will lead to a local increase in static pressure and a reduction of flow velocity. The shape of the hill is altering the inlet flow conditions to the vane, by altering slightly the location of the stagnation point and increasing the flow incidence close to the the root of the vane. The blockage induced by the profiling

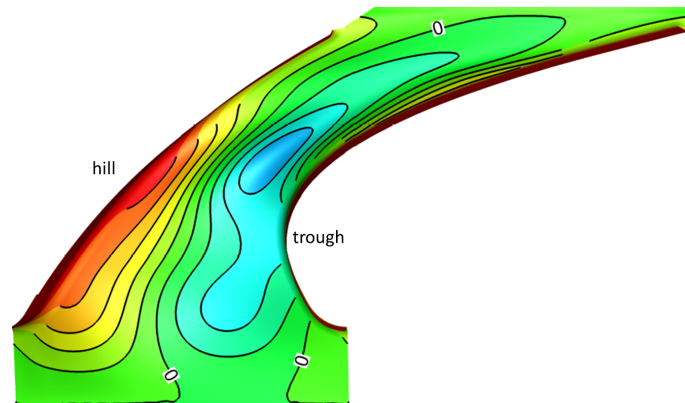


Figure 8.8: Contoured endwall shape, shown in terms of radius difference to the cylindrical case.

will then push the flow toward the suction side and limit the development of structures towards the suction side. This effect was used in Hartland et al. [40] for the design of their non-axisymmetric endwall and validated experimentally by Hartley et al. [41]. Ingram et al. [43] have also used the same principle for the optimization of the inlet portion of the Durham cascade.

The incoming flow conditions are identical for both endwall configurations and therefore the boundary layer contains a similar integrated amount of vorticity. The airfoil shape is identical in both cases. The change in flow behavior close to the leading edge is therefore only attributed to the endwall contouring. The presence of the hill on the pressure side will push the flow toward the suction side of the vane and promote this side of the vortical structure. Immediately downstream of the leading edge, a hill is located on the pressure side up to the middle of the passage, reducing the passage cross-sectional area leading to a flow acceleration and a decrease of the static pressure. Because of the flow acceleration, the pressure side extension of the vortical structures will be stretched and their zone of influence reduced. On the other hand, the suction side leg of the vortical flows will be stronger compared to the cylindrical case. On this side, the contouring features a valley which leads to a reduction of the flow velocity and a rise of the static pressure, thereby reducing the cross passage pressure gradient. Because of the non-linear scaling of aerodynamic losses with flow velocity, the reduction in velocity of the suction side secondary flow can lead to lower losses even though the vortex is stronger. The CFD predictions shown in Fig. 8.9 present slices of vorticity magnitude around the vane and iso-surfaces of streamwise vorticity for the two configurations. The previously described phenomenon can be visualized in the slices, where the vorticity magnitude appears stronger for the contoured case upstream of the leading edge but then rapidly decrease both along the pressure and suction sides. Close to the pressure side in the contoured case, the pressure side legs of the vortical structures seems to weaken quickly and disappear as suggested by the iso-surface. The predictions are considered here as an

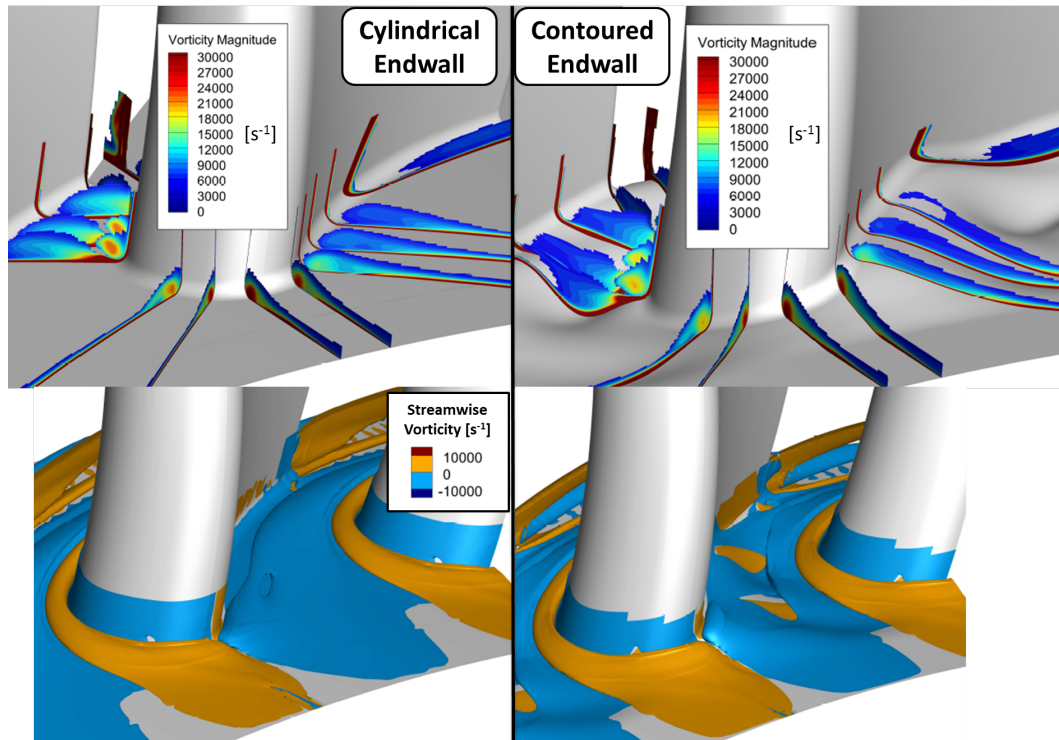


Figure 8.9: Top - Slices around the vane showing predicted contours of vorticity. Bottom - Iso-surfaces of streamwise vorticity  $\omega_s = \pm 7500[s^{-1}]$ .

illustration and are not believed to be an exact replica of the reality. In particular, the multi-vortices, whose influence have been seen for the cylindrical endwall, are not present in the CFD predictions. While the precise development of flow and vortices cannot be trusted, the predictions provide useful trends allowing a deeper understanding of the measurements and their link to the flow physics.

Figure 8.10 presents the measured heat transfer coefficient distribution on which the shape of the endwall is super-imposed. The lines correspond to the change in endwall elevation as a percentage of the span, a positive value refers to an addition of material and a reduction of the passage cross-sectional area. Based on the description of the vortical structure of Fig. 8.9, a couple of new comments can be added to the description of the results made in chapter 7. In fact the absence of heat transfer increase (red dotted line) close to the pressure side can be explained by the weak horseshoe vortex leg convecting on this side of the vane and its rapid weakening. Close to the suction side, the dashed line highlights an region with a low-high band of measured heat transfer coefficient that could be the signature of the suction side leg of the horseshoe vortex. A variation of 25% of heat transfer coefficient is measured between the high and low bands.

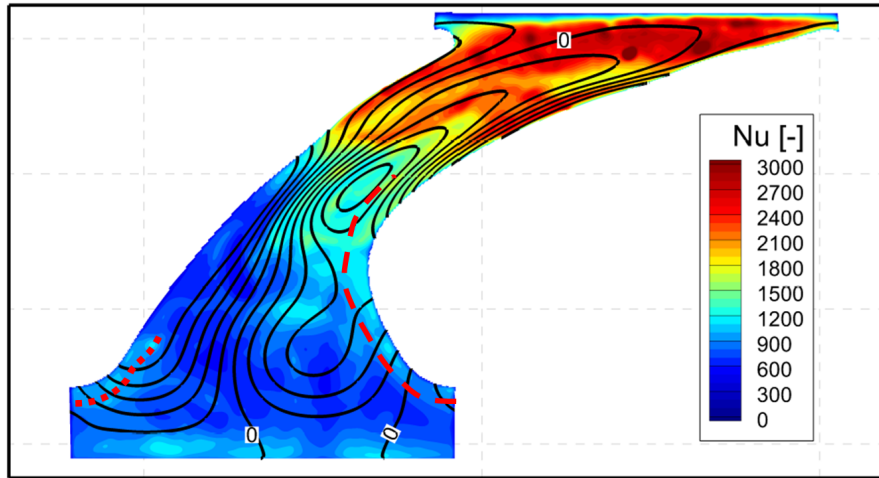


Figure 8.10: Nusselt number contours for the contoured endwall case. The lines show the radial modification of the endwall compared to the cylindrical baseline.

## 8.2 Effect of roughness in the accelerating boundary layer close to the vane pressure side

Figure 8.1 shown at the beginning of this chapter highlighted a region (R2) where the ratio of Stanton number relative to the flat plate Stanton number remains relatively constant and uniform. This suggests an evolution with the local Reynolds number at a power  $-0.2$ , which is typical from a developing boundary layer. In fact, the vortical structures developing at the leading edge are crossing the passage from the leading edge towards the suction side, sweeps the incoming boundary layer and entrains it. The flow present in the region R2 is then coming from different regions. First, the incoming flow at a high radial location is not entrained by the vortex but is deflected towards the hub due to the spanwise pressure gradient. The pressure gradient along the vane span also pushes the boundary layer from the lower spanwise location towards the endwall. Finally the cross passage pressure gradient convects the boundary layer from the pressure side towards the suction side. In addition, the downwash of the pressure side leg of the horseshoe vortex is also influencing the boundary layer thickness.

Datapoints have been extracted for the different configurations and operating conditions at the locations shown in Fig. 8.11 for the cylindrical endwall (similar for the contoured case). The points are separated in two groups, the inlet group, composed of points located in a region unaffected by three dimensional flow structures, and the pressure side (PS) group whose points are located between the "location of the horseshoe vortex" and the vane pressure side. The points from the PS group are approximately taken along inviscid streamlines. The data from both groups will be compared to turbulent flat plate correlation with different starting location.

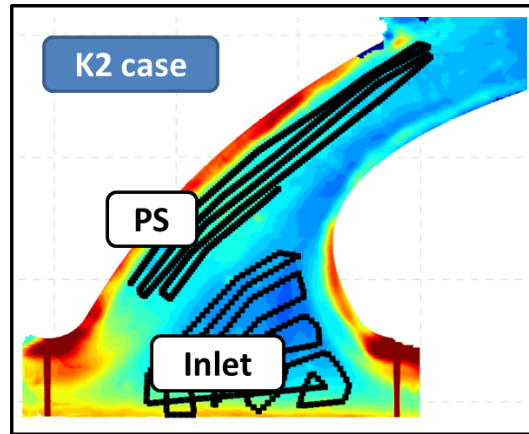


Figure 8.11: Position of the points used to generate Fig. 8.12 and 8.13.

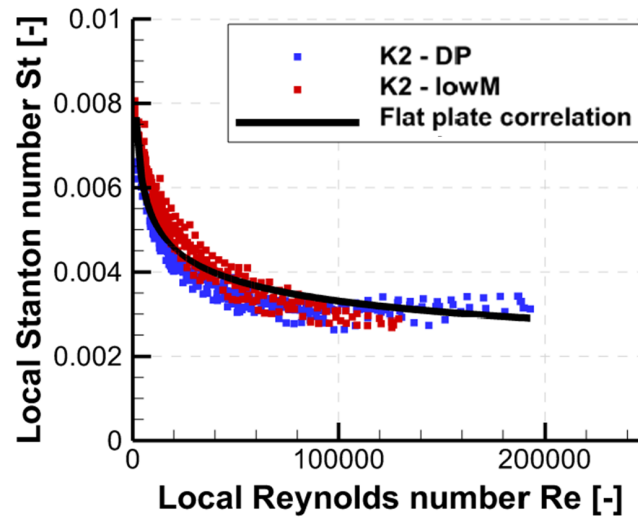


Figure 8.12: Local Stanton number evolution relative to the local Reynolds number at the passage inlet for the cylindrical endwall case, for both operating conditions.

Figures 8.12 and 8.13 shows the local Stanton number evolution with the local Reynolds number. For clarity, the Reynolds number corresponds to a boundary layer with the origin at the beginning of the thermally managed section. Only the correlation curves as affected by a variation of origin.

The measured data at the inlet for both operating conditions are following the turbulent flat plate correlation, as shown in Fig. 8.12. On the other hand, the points of the PS group (Fig. 8.13) have a very different evolution with the local Reynolds number. In fact, the points close to the leading edge follows the correlation with a shift of the origin of 11mm, which is approximately the distance between the start of the thermally managed section and the leading edge of the vane. For the points at high local Reynolds number, the evolution appears to follow a  $Re_x^{-0.2}$  correlation but with a factor 1.8. For these two

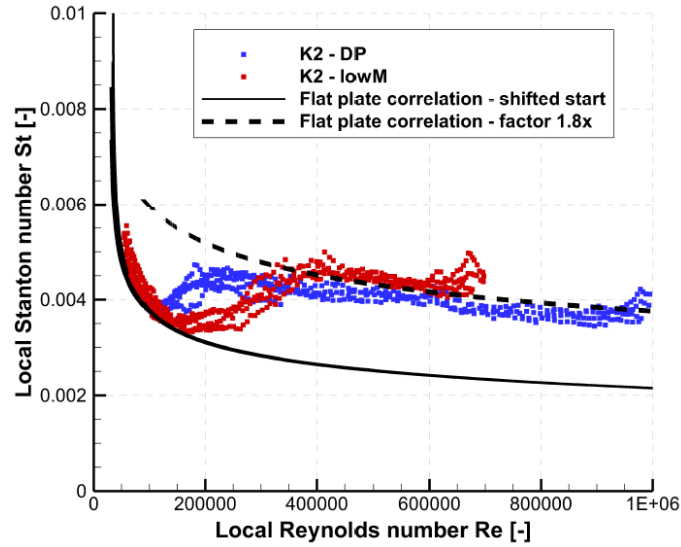


Figure 8.13: Local Stanton number evolution relative to the local Reynolds number close to the vane pressure side for the cylindrical endwall case, for both operating conditions.

extreme cases, the data from both operating conditions follows the same trends. However the points at moderate Reynolds number behaves in a very different manner. A transition between the two correlation curves seems to occur around  $Re_x = 150k$  with a different slope for the two conditions. In the design point case, the transition appears abrupt, while the second operating conditions sees a smooth delayer transition. In the PS region, the fluid close to the wall originates from the vane leading edge or the pressure side and therefore the boundary layers could be considered already turbulent. From the analysis conducted in section 8.1, a difference between the two operating conditions is the location and strength of the vortical structures emanating from the leading edge region. While the two vortices appear separated and with different strength for the low Reynolds number case, the design point case sees an interaction of the two vortices. The high value of heat transfer coefficient at design point suggests that the boundary layer thickness is reduced for this case. The flow acceleration along the passage will then reduce the boundary layer thickness, which will then stabilize and restart growing when the flow velocity becomes constant. Due to the different effect of the vortical structure, the boundary layer in the second operating case (low Reynolds number) is thicker and the effect of the acceleration will occur at a later stage. In section 6.1, the surface measurements showed that the paint coating generated an arithmetic surface roughness level close to  $10\mu m$ . In addition to the effect of the acceleration on the boundary layer thickness, the surface roughness will play also a role and increase the heat transfer coefficient locally, with an increasing effect if the boundary layer is accelerating. The trend observed in Fig. 8.13 is similar to the measurements obtained in turbulent flat plate studies over a rough surface, especially in the flow is in the transitionally rough regime. The work of Blair [14] provides endwall

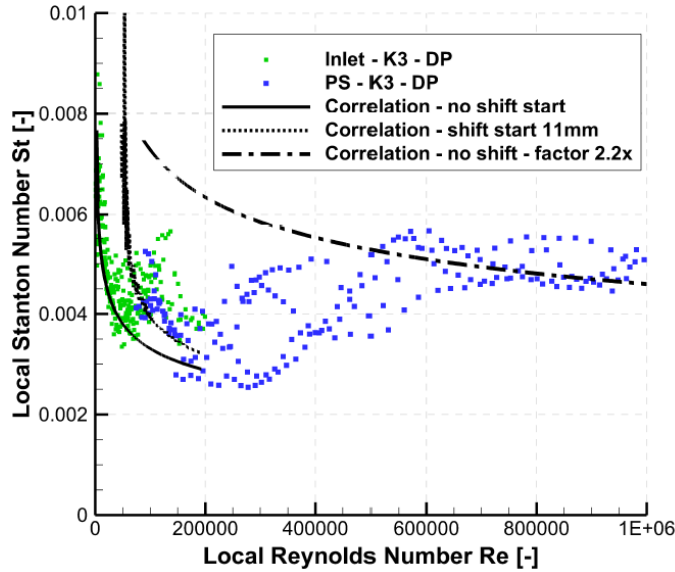


Figure 8.14: Local Stanton number evolution relative to the local Reynolds number for the contoured endwall case, for the design point.

heat transfer data for a turbine blade with different surface roughness. To the author's knowledge, it is the only experimental work providing heat transfer patterns on rough surface in a turbine geometry but, unfortunately the resolution and details provided in the contour plots do not help in the current case. The particular work of Pimenta et al. [71] and later Hosni et al. [42] on flat plates, however exhibit a similar transitioning trend for the variation of Stanton number with Reynolds number. This behavior is observed when the flow is in a transitionally rough regime.

The combined effect of roughness and flow acceleration seems to be the reason for the increased magnitude of the Stanton number at high Reynolds number. The factor 1.8 was estimated to provide a close fit of the data but could not be justified analytically, for example using the correlations of Dippery and Sabersky [27].

Figures 8.14 and 8.15 provides the same comparison for the contoured endwall case. For clarity, the data for the two operating conditions are separated. In fact, the quite homogeneous behavior for the cylindrical endwall case, is now replaced by a more chaotic evolution of local Stanton number with local Reynolds number. While the inlet section appear to follow closely the flat plate correlation, the points in the PS region have very different evolution based on their location. At high Reynolds number, the points appear to follow a trend in  $Re_x^{-0.2}$  but with a multiplication factor 2.2 instead of 1.8 for the cylindrical endwall. In a similar way, the points of the PS group appears to follow a transitional trend between the two curves from flat plate correlations. Because of the similar impact of wall roughness and acceleration, the effects on heat transfer cannot be separated. However the behavior of the local Stanton number suggests that the flow is



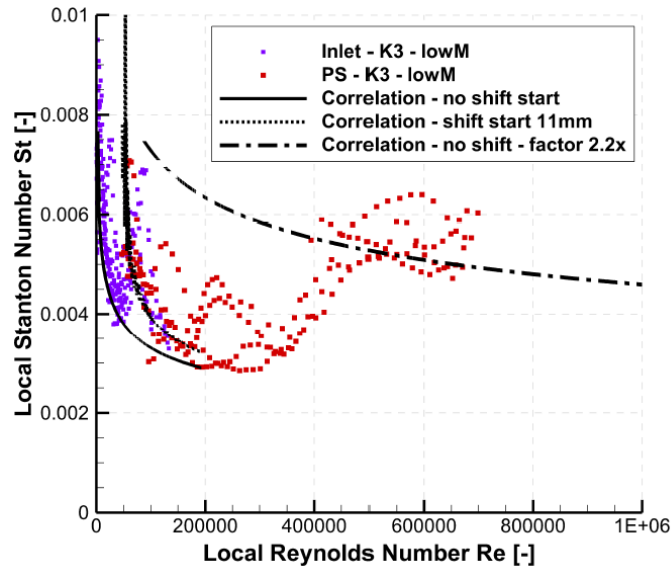


Figure 8.15: Local Stanton number evolution relative to the local Reynolds number for the contoured endwall case, for the lower Reynolds number condition.

in a transitionally rough regime in the middle section of the passage, which corroborates the predictions made using numerical tools and detailed in Chap. 6.

### 8.2.1 Impact of endwall contouring on the pressure side close to the trailing edge

At the end of the the pressure side region investigated in the previous section, the cylindrical and contoured endwall appear to behave significantly different. In fact, the Stanton number ratio shown in Fig. 8.1 for the cylindrical endwall appears to reduce at the exit of the passage, while the measurements for the contoured case remains at a high value in Fig. 8.2.

A zoom of this region is shown in Fig. 8.16. The contour scales have been adjusted to enhance the contrast between the different contour values and be able to observe local variation of the heat transfer coefficient despite the large magnitude difference. In the cylindrical endwall case, the region of high heat transfer coefficient appears rather uniform. Only a small portion close to the suction side experiences a lower, corresponding maybe to the upwash side of the pressure side leg of the horseshoe vortex. For the contoured case however, two regions appear and as it can be seen on the 3D view, the highest values are measured on the ridge located at the exit of the passage. The effect of the hill, directing the flow towards the suction side, may locally increase the wall friction, hence the heat transfer coefficient.

The difference originates in the modification of the flow behavior due to the contouring. In fact, the hill located on the pressure side at the entrance of the passage decrease

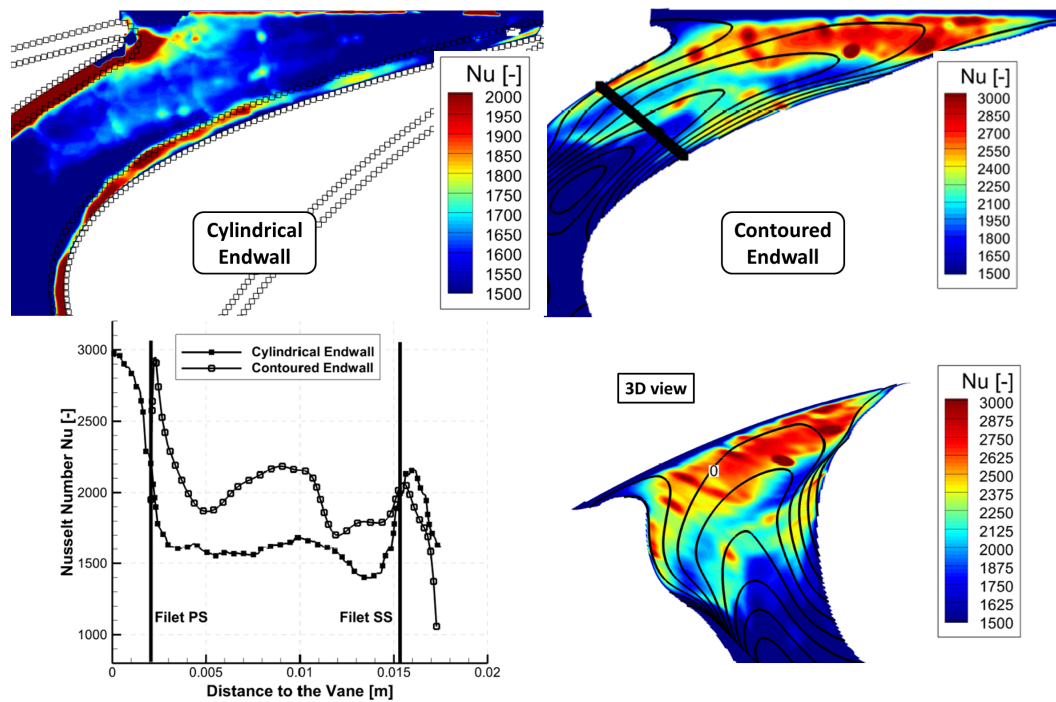


Figure 8.16: Contour of Nusselt number for the two endwall geometries (top and bottom right). Bottom left - extracted profile close to the throat of the passage. The lines represents the variation of the endwall radius.

the local static pressure and the trough on the suction side increases it. The pressure gradient across the passage is reduced. However the endwall shape needs to be recovered at the exit of the passage, and while the transition is done smoothly, the passage pressure gradient becomes stronger. The crossflow across the passage is therefore delayed compared to the cylindrical endwall. In addition, a hill is located on the pressure side close to the trailing edge of the vane which appears to direct the flow circumferentially towards the suction side. The surface streaklines shown in Fig. 8.17 highlights the turning of the lines (green) on the pressure side close to the trailing edge. It also shows two "preferred" region (CF1 and 2) where the cross-flow is directed, a "channel" is defined at those location by a ridge extending in the circumferential direction. In these two regions, the flow is directed towards the suction side, which can lead to an increase in wall shear stress, hence in heat transfer coefficient. Comparing with Fig. 8.2, the two regions showing high Stanton number ratio in the downstream part of the passage corresponds to these two locations upstream of a ridge.

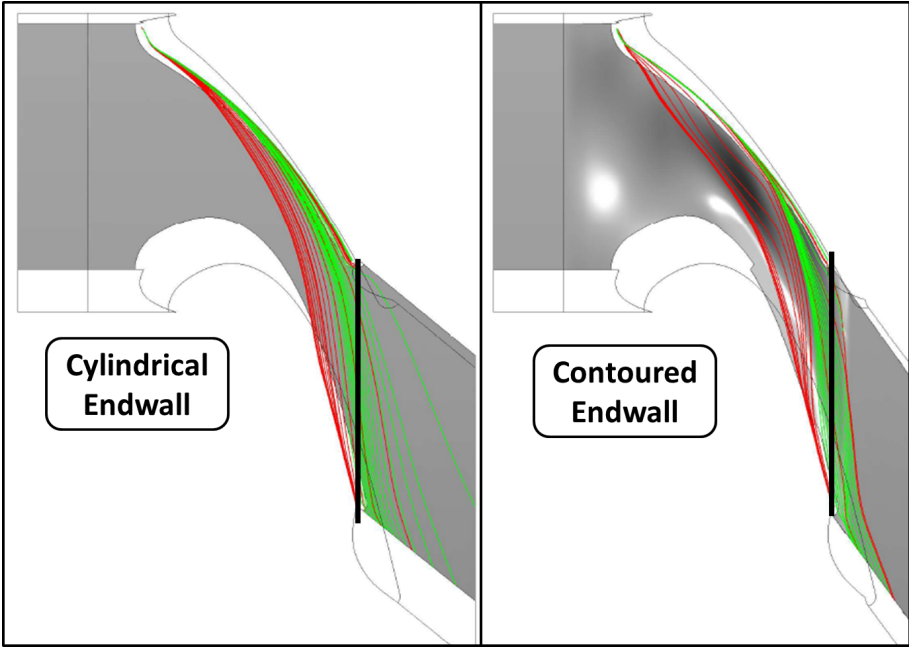


Figure 8.17: Endwall streaklines at the exit of the passage shown for both the cylindrical (left) and contoured (right) cases. The two color identifies streamlines generated across the passage from two different axial locations.



# Chapter 9

## Summary, Conclusions and Outlook

The research objectives envisaged in this work were to design, manufacture and integrate a heat transfer measurements platform on the nozzle guide vane row of the axial turbine facility LISA. In a second step, the impact of endwall contouring on the thermal loads were to be assessed.

The improvement of the flat plate heat transfer measurement technique using isothermal boundary conditions and an infrared camera was a first step towards achieving the first goal. The adaptation of the measurement technique to a vane segment thermally managed using circulating water and providing the optical access through small infrared transparent elements completed the first goal. The successful utilization of the heat transfer platform for different operating conditions of the turbine provided measurements of thermal quantities on the cylindrical endwall. In a second step, the measurements of the same quantities for the same operating conditions on the contoured endwall ensured that both goals were achieved.

In addition numerical predictions of the flow field completed the study to provide more insight on the link between flow behavior and thermal loads.

### 9.1 Contribution of the current work

#### 9.1.1 Experimental Setup and Methods

The experimental study presented in this work was envisaged to extend the measurement capabilities of the Laboratory in an axial turbine environment. The first contribution of this work was therefore the new methodology associated to the design, manufacturing, integration of the measurement platform in the turbine facility. To achieve this goal, modern computational methods were used to develop the mechanical design, ensure the thermal management of the measurement platform. The experimental facility was suitably modified to accommodate the measurement platform. The platform was designed to provide an isothermal boundary conditions achieved using circulating water. The nec-

essary controlling and monitoring electronics and software were also created during the course of this work. The measurement procedure using an infrared camera manipulated with a robotic arm was developed in this study. The camera geometrical calibration procedure was defined in this study and multiple tools required for the alignment of the robot and the segment were manufactured. The accessibility of the endwall surface using multiple view ports was suitably designed and the measurements over a complete vane endwall achieved. The specialized post processing softwares were also developed and continuously improved during the study. The procedure to wrap the insulating Kapton layer was demonstrated on the K2 airfoils and K3 endwall. However micro-air bubbles were trapped underneath in the region of extreme curvature, especially when the curvature is of the same magnitude in two directions (high gaussian curvature). An experimental method was created to experimentally quantify the thermal resistance non-uniformity introduced by the micro bubbles. The procedure used a laser to locally heat the surface for a short period of time while an infrared camera monitored the temperature rise during the heating and cool-down phases. The combination of a new technique to lay down the insulating layer and this in-situ calibration method would be the best solution for more accurate and reliable measurements in the future. The experimental systems and methodology developed in the frame of this work will find further use in the upcoming studies focused on heat transfer in complex environment such as turbomachines.

### **9.1.2 High resolution measurements of heat transfer on cylindrical and contoured endwall**

The heat transfer measurement technique and procedure were successfully improved and adapted to perform the measurements on both cylindrical and contoured endwall configuration on the hub endwall of the NGV row. The measurement platform provided a uniformly controlled solid temperature and an infrared camera was used to measure the endwall surface temperature through infrared transparent elements located on the outer casing. The data were measured over complete passage by using a six axis robot arm traversing the camera to a total of 38 positions. For one measurement day, a total of 30000 infrared pictures of 0.1MPix were acquired and processed to provide a full passage map of heat transfer coefficient and adiabatic wall temperature formed of 20000 points. The current measurement technique provided a resolution of 0.4mm per point on the surface, which is potentially the highest obtained in a full scale axial turbine. The measurement procedure using a variable isothermal boundary conditions provided both heat transfer quantities, namely the heat transfer coefficient and the adiabatic wall temperature, in a single operating run of the facility. The test section is therefore identical for the two quantities. The high resolution data obtained on the cylindrical endwall highlighted the importance of the secondary flow structures on the heat transfer coefficient distribution on the endwall. High levels of heat transfer coefficient were measured close to the leading

edge and along the migration path of the horseshoe vortex towards the suction side. The highest level of heat transfer were predicted at the exit of the passage, where the flow velocity is the highest and the secondary flow structures are impacting the flow in a large proportion of the passage. The effect of Reynolds number on the thermal loads showed an overall increase in heat transfer coefficient following turbulent flat plate estimation, but where the flow acceleration is the highest, the increase in Nusselt number could reach a factor 2 for a 28% increase in Reynolds number. The reduction of the adiabatic wall temperature due to the flow acceleration through the passage was also measured and followed the expected variation.

The measurements of heat transfer quantities were performed for the same conditions as the cylindrical endwall. The endwall design was optimized for a reduction of secondary flow losses downstream of the NGV row and therefore strongly affects the secondary flow structure. In the heat transfer coefficient results, the patterns linked to the secondary flows was not visible in the upstream part of the passage. At the passage exit, increase of Nusselt number close to 50% were measured for the contoured case compared to the cylindrical endwall. The complementary numerical study predicted higher wall shear stress at these locations. Also the roughness of the surface was changing at this location. The combination of both effect could explain the large increase, clearly visible in the laterally averaged data. In the rest of the passage, the laterally averaged Nusselt number measured showed a minor effect of the contouring.

Finally the surface properties were measured and fully characterized using profilometry and 3D surface structure scanning technique. Roughness parameters were obtained to provide a complete set of boundary conditions and results for the assessment of numerical tools.

### 9.1.3 Numerical setup and methods for predictions on rough surfaces.

In such complex configuration with 3D vortical flows dominating the heat transfer process, the use of numerical flow predictions is essential to obtain qualitative indication on the flow behavior or modifications due to change in operating point or geometrical endwall modification. In the current work, the in-house developed URANS solver Multi3 was used to provide flow as well as heat transfer predictions. Guidelines for the geometry discretization and use of the flow solver have been established in this work. A first cell height providing  $y^+$  values below 0.5 should be used and unsteady simulation must be run for approximately 1ms of physical time to obtain converged solution, especially in the low momentum fluid regions. A roughness model was implemented in the flow solver to allow computation of flows on rough surfaces. The modification of the turbulent eddy viscosity at the wall was used to simulate rough surfaces. Based on the measured characteristic of the surfaces used in the experiment, numerical predictions were performed

in terms of aerodynamic losses and heat transfer. The obtained aerodynamic losses are matching the experiments. For heat transfer, the simulations appear to overestimate the heat transfer on rough surfaces. The modifications of the code opened new perspective in terms of development of numerical methods related to roughness modeling and will therefore receive more attention during the future years.

#### 9.1.4 Concluding remarks

In the Chapter 8, the analysis of the heat transfer coefficient patterns in combination with data from literature and CFD predictions have helped in drawing a picture of the secondary flows. In addition, the analysis of the data measured on the contoured endwall combined with advanced CFD predictions have helped defining a design guideline for the gas turbine designer in the challenging task of shaping the endwall.

#### Secondary flow structure based on the measured thermal loads

The model of Kang et al. [90] appears to correlate the flow structure of the cylindrical endwall case with the measured heat transfer coefficient distribution. In this model, two vortical structures are generated upstream of the leading edge and evolves on both sides of the vane. The secondary flow structures are seen to impact the heat transfer coefficient distribution especially in the region of upwash-downwash of the vortices. Downstream of the separation line, where the incoming boundary layer is swept by the vortical structure, a new boundary layer develops. In this region, the heat transfer patterns are mainly influence by the combination of flow acceleration and surface roughness.

#### Mesh resolution requirements for a designer

The high resolution measurements performed in this study have highlighted the strong local effect of secondary flow structure on the endwall thermal loads. For a designer, the local variations can initiate local phenomenon and lead to early failures. The mesh resolution of the FEM model used during the design phase should ensure a correct predictions where sharp local gradients are expected. The current results have been applied to 3D FEM models of the endwall meshed with different resolutions (5mm, 2mm, 1mm, 0.5mm and 0.2mm). The endwall is composed of a TBC coating layer ( $500\mu\text{m}$ ) on a typical base turbine material. The adiabatic wall temperature was estimated using a total inlet temperature of 1400K and the Mach number distribution. The back of the endwall is cooled with impingement cooling ( $h = 10000\text{W}/\text{m}^2/\text{K}$ ). Figure 9.1 shows the results of the temperature profile extracted at the passage throat for the different mesh resolutions and the resulting additional stress due to the incorrect predicted local temperature. The predictions show that mesh resolutions between 1 and 2mm are necessary to limit the additional stress below 5MPa.



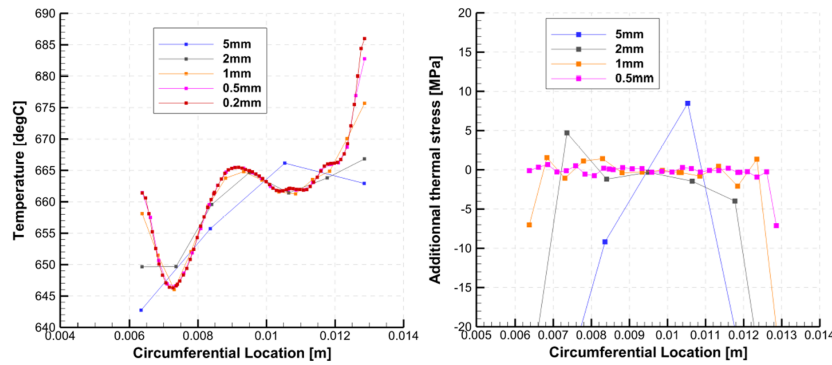


Figure 9.1: Temperature profile on top of the coating extracted at the throat of the passage from an FEM thermal analysis with different mesh resolution (left). On the right, additional thermal stress due to the inaccuracy in predicted temperature using lower resolution meshes.

The combined thermal stress, centrifugal stress and stress due to gas bending can dramatically impact the lifetime of a rotor part and lead to un-explained failure of components. The use of high resolution measurements as boundary conditions for FEM analysis was highlighted in this short study. In particular, high resolution data on the rotor blade and endwall were of particular interest.

### Shaping of the endwall to reduce thermal loads

The topic of shaping the endwall with the purpose of reducing aerodynamics losses has been extensively covered in the literature. However very few studies have looked at optimizing the endwall from a thermal load point of view.

From the current configuration tested, it appears the the suppression of the pressure side leg of the horseshoe vortex using endwall contouring is successful. Therefore the concept of a hill located on the pressure side of the leading edge should be kept. Further increase of the hill height could allow a greater reduction of the pressure side leg.

On the other hand the design of the endwall in the middle of the passage appears to be more chaotic and generates more thermal loads than expected, mainly due to the delay in the establishment of the cross passage pressure gradient and the presence of ridges forcing the flow towards the suction side. In these regions, an increase in wall shear stress is expected from the heat transfer patterns and the numerical predictions. A smoother transition on the pressure side from the hill to the cylindrical endwall, combined with the suppression of the ridge at the trailing edge should provide better results in terms of heat transfer.

The contoured endwall designed investigated in the current study featured multiple hills and trough in both circumferential and axial direction. A more efficient design could be a simpler design, similar to the one investigated by Schuepbach et al. [81], where a single hill and a single trough were used.

## 9.2 Future perspective

The first perspective opened by the current work is the impact of surface roughness on heat transfer and aerodynamic and the modeling of rough surfaces using the current CFD tools. At first an effort should be placed on reducing the levels of surface roughness on the heat transfer measurements platform. This would allow the direct comparison with numerical predictions on smooth surfaces and remove the uncertainty introduced by a single "lump" parameter, the equivalent sand grain roughness. On the other hand, real engines are experiencing substantial variation of roughness during the life cycle, especially the parts downstream of the combustion chamber. The 3D numerical tools are currently not able to provide high accuracy data on such surfaces. A more systematic approach would be to first characterize the roughness ( $R_a$ ,  $R_z$ , 3D surface scan, shape factor,...) of the surface and then measure the aerodynamic and heat transfer quantities on these surface in an accelerating flow with 3D flow structure, for example a linear cascade with symmetric airfoils. With the newly developed roughness capability of Multi3, the predictions on similar configuration would help in understanding which phenomenon is under predicted by the numerical tools.

The present work introduced a new heat transfer measurement platform in the turbine research facility, allowing measurements to be performed on stationary rows, which opens up the perspective of heat transfer measurements in rotating facility. On the NGV row, the design of contoured endwall optimized to reduce heat loads while limiting the aerodynamic losses should be designed and tested. For real engines, a heat transfer optimized design is beneficial for reducing cooling flows. In fact, the stationary rows are often attached to the outer casing and a cavity is present underneath the hub platform. To avoid ingestion of mainstream air, the cavity is pressurized and purge air is injected both upstream and downstream of the stationary row. This introduces a cold film of air ejected upstream of the stator row. The use of endwall contouring to direct this flow to regions where cooling is required would reduce the overall needs in cooling fluid. The investigation of these effects could be performed in the axial turbine LISA by opening a gap upstream the stator and dividing the cavity into two volumes individually fed and controlled.

The LISA 1.5 stage turbine can be equipped with a heat transfer measurement platform on the second stator, where multiple effect are then introduced. The high resolution of the measurements and the use of high speed imaging technique would allow investigations on the effect of the unsteady flow field at the exit of the rotor row on the hub endwall heat transfer.

The most relevant studies that can follow this work are linked to the measurement of heat transfer quantities on the rotor platform. In fact, most rotor blade geometries are tested in linear cascades where the swirl and the unsteadiness coming from the upstream vanes, in the relative frame of reference, cannot be reproduced. The use of water to control the rotor temperature is rather risky and a different setup could be used such as the

generation of an iso-energetic boundary condition using in-house made heater, as demonstrated in Chen [21]. The use of electrically based heaters would require the power to be brought using a slip-ring arrangement and the solid temperature data monitored with an on-board acquisition system. In order to achieve high resolution instantaneous measurements of the surface temperature, the use of extremely sensitive infrared detectors, such as MCT type, is required to limit the integration time and prevent image blurring. In addition to the influence of flow feature on heat transfer patterns, the investigation of the use of purge flow as a cooling medium for the hub platform is of interest. In fact the temperature of the flow injected in the cavity between the NGV and the rotor can be reduced. The cool air becomes first a tracker to identify its trajectory on the hub surface, or it can be used as a coolant whose performance can be studied in a similar way as film cooling jets.

For turbine designer, the thermal loads are required over the complete passage surface including both endwalls and the airfoil. Due to the very high level of heat transfer present on the leading edge and the combination of thermal loads and mechanical stress close to the trailing edge, these two locations are of particular interest. For complex 3D airfoil shape, the accessibility is not guaranteed in the present configuration using a view port on the outer casing and an infrared camera. The use of indirect measurement technique, such as imaging a mirror reflecting the surface, are necessary. An infrared probe is currently under development in the Laboratory and allows a scan of the airfoil surface using a set of optics and a 45-degree mirror. The Figure 9.2 is the outcome of the work of Marti [63]. With this tool and the already developed heat transfer platform, the heat transfer quantities could be determined using multiple solid temperatures, in a similar way to the camera measurement technique. A modification of the probe tip could allow a larger change in the redirection angle and the outer casing would become accessible. With the airfoil surface accessible, the study of hot streak impact on thermal loads would receive particular interest.

In a last phase, the facility could be modified to allow a fully cooled turbine to be tested. The aerothermal performance of a fully film cooled turbine stage could be investigated using the aerodynamic probe technology already established, including the Fast Entropy probe, and the heat transfer measurements could be performed on the endwall and airfoil surfaces using the technique presented in the current work and in the previous paragraph.

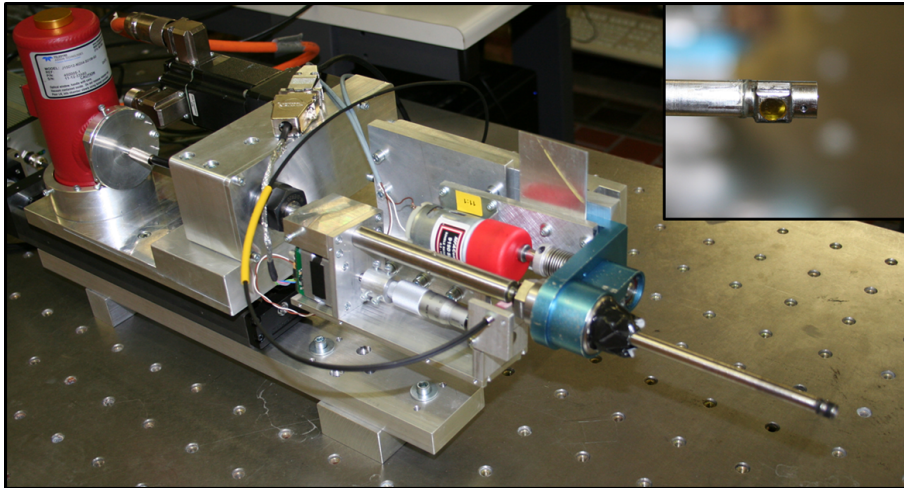


Figure 9.2: Overview of the infrared probe system mounted on a traversing system. The close up view shows the tip of the probe where the view is redirected at 90degree.

# Bibliography

- [1] Iriss website - [www.iriss.com](http://www.iriss.com).
- [2] Texstan boundary layer code - [www.texstan.com](http://www.texstan.com).
- [3] Thorlabs website - [www.thorlabs.com](http://www.thorlabs.com).
- [4] R. S. Abhari and A. H. Epstein. An Experimental Study of Film Cooling in a Rotating Transonic Turbine. *ASME J. Turbomachinery*, 116:63–70, January 1994.
- [5] V. Aga. *Experimental Investigation of the Influence of Flow Structure on Compound Angled Film Cooling Performance*. PhD thesis, ETH Zurich, 2009.
- [6] V. Aga and R. S. Abhari. Influence of flow structure on compound angled film cooling effectiveness and heat transfer. *ASME J. Turbomachinery*, 133(3), 2011.
- [7] V. Aga, M. Mansour, and R. S. Abhari. Aerothermal performance of streamwise and compound angled pulsating film cooling jets. *ASME J. Turbomachinery*, 131(4), 2009.
- [8] A. M. Anderson and R. J. Moffat. The adiabatic heat transfer coefficient and the superposition kernel function: Part 1 - data for arrays of flatpucks for different flow conditions. *Journal of Electronic Packaging*, 114(1):14–21, 1992.
- [9] S. Baldauf, A. Schulz, and S. Wittig. High Resolution Measurements of Local Effectiveness from Discrete Hole Film Cooling. *ASME J. Turbomachinery*, 123:758–765, 2001.
- [10] D. N. Barlow, Y. W. Kim, and L. W. Florschuetz. Transient liquid crystal technique for convective heat transfer on rough surfaces. *ASME J. Turbomachinery*, 119(1):14–22, January 1997.
- [11] A. Basol and R.S. Abhari. Gpu acceleration of a rans solver: Effect of the memory coalescence of the performance. In *Proceedings of the ASME Turbo Expo, GT2014-26753*, Düsseldorf, 2014.
- [12] T. Behr. *Control of Rotor Tip Leakage and Secondary Flow by Casing Air Injection in Unshrouded Axial Turbines*. PhD thesis, ETH Zürich, 2007. Diss. ETH No. 17283.

- [13] S. Bernsdorf. *Experimental Investigation of Film Cooling Flow Structure*. PhD Thesis, ETH Zürich, 2005. Diss. ETH No. 16355.
- [14] M.F. Blair. An experimental study of heat transfer and film cooling on large-scale turbine endwalls. *Journal of Heat Transfer*, 96:524–529, 1974.
- [15] M.F. Blair. An experimental study of heat transfer in a large-scale turbine rotor passage. *ASME J. Turbomachinery*, 116(1):1–13, 1994.
- [16] J. P. Bons. St and Cf augmentation for real turbine roughness with elevated freestream turbulence. *ASME J. Turbomachinery*, 124(4):632–644, 2002.
- [17] J. P. Bons. A review of surface roughness effects in gas turbines. *ASME J. Turbomachinery*, 132(2):021004, 2010.
- [18] J-Y. Bouquet. Camera calibration toolbox for matlab - [www.vision.caltech.edu/bouquetj/](http://www.vision.caltech.edu/bouquetj/).
- [19] G. Brennan, N. W. Harvey, M. G. Rose, N. Fomison, and M. D. Taylor. Improving the efficiency of the trent 500-hp turbine using nonaxisymmetric end walls—part i: Turbine design. *ASME J. Turbomachinery*, 125(3):497–504, 2003.
- [20] A. Burdet. *A computationally efficient feature-based jet model for prediction of film-cooling flows*. PhD Thesis, ETH Zürich, 2005. Diss. ETH No. 16163.
- [21] N. Chen. Convective heat transfer measurement on a blade-endwall configuration using an iso-energetic setup. Master’s thesis, ETH Zürich, 2012.
- [22] V. Chiron. Convective heat transfer predictions for a turbine blade passage with endwall contouring. Technical report, ETH Zürich, 2013.
- [23] James E. Danberg and Asher Sigal. Analysis of turbulent boundary-layer over rough surfaces with application to projectile aerodynamics. Technical report, Army Ballistic Research Lab Aberdeen, 1988.
- [24] T. Dauch. Computation of advanced gas turbine endwall heat transfer. Master’s thesis, ETH Zürich, 2013.
- [25] J.D. Denton. Some limitations of turbomachinery cfd. In *Proceedings of ASME Turbo Expo, GT2010-22540*, Glasgow, 2010.
- [26] W.J. Devenport and R.L. Simpson. Time-dependent and time-averaged turbulence structure near the nose of a wing-body junction. *J. of Fluid Mechanics*, 210:23–55, 1990.

- [27] R.B. Dippery and R.H. Sabersky. Heat and mass transfer in smooth and rough tubes at various prandtl numbers. *Int. J. Heat Mass Transfer*, 6:329–353, 1963.
- [28] P. A. Eibeck and J. K. Eaton. Heat transfer effects of a longitudinal vortex embedded in a turbulent boundary layer. *Journal of Heat Transfer*, 109(1):16–24, 1987.
- [29] R. E. Gaugler and L. M. Russell. Comparison of visualized turbine endwall secondary flows and measured heat transfer patterns. *ASME Journal of Engineering Gas Turbines and Power*, 106:168–172, 1984.
- [30] J. Gengenbach, S. Kabelac, and L.R. Koirala. Measurement of directional spectral emissivities of microstructured surfaces. *ECTP Paper*, 2005.
- [31] T. Germain, M. Nagel, I. Raab, P. Schüpbach, R. S. Abhari, and M. Rose. Improving efficiency of a high work turbine using nonaxisymmetric endwalls - part i: Endwall design and performance. *ASME J. Turbomachinery*, 132(2):021007, 2010.
- [32] P. W. Giel, G.J. Van Fossen, R.J. Boyle, D.R. Thurman, and K.C. Civinskas. Blade heat transfer measurements and predictions in a transonic turbine cascade. *NASA/TM*, (209296), 1999.
- [33] R.J. Goldstein and R.A. Spores. Turbulent transport on the endwall in the region between adjacent turbine blades. *ASME Journal of Heat Transfer*, 110:862–869, Nov 1988.
- [34] R. A. Graziani, M. F. Blair, J. R. Taylor, and R. E. Mayle. An experimental study of endwall and airfoil surface heat transfer in a large scale turbine blade cascade. *Journal of Engineering for Power*, 102(2):257–267, 1980.
- [35] Satoshi Hada, Kenichiro Takeishi, Yutaka Oda, Sejiro Mori, and Yoshihiro Nuta. The effect of leading edge diameter on the horse shoe vortex and endwall heat transfer. In *Proceedings of the ASME Turbo Expo, GT2008-50892*, pages 813–823, Berlin, 2008.
- [36] Charles W. Haldeman, Michael G. Dunn, John W. Barter, Brain R. Green, and Robert F. Bergholz. Aerodynamic and heat-flux measurements with predictions on a modern one and one-half state high pressure transonic turbine. *ASME J. Turbomachinery*, 127(3):522–531, 2005.
- [37] J.C. Han, S. Dutta, and S. Ekkad. *Gas Turbine Heat Transfer and Cooling Technology*. Taylor & Francis, 2013.
- [38] S Han and R. J. Goldstein. Influence of blade leading edge geometry on turbine endwall heat (mass) transfer. *ASME J. Turbomachinery*, 128(4):798–813, 2005.

- [39] S. Harrison. The influence of blade lean on turbine losses. *ASME J. Turbomachinery*, 114:184–190, 1992.
- [40] J. C. Hartland, N. W. Harvey, M. G. Rose, and D. G. Gregory-Smith. Nonaxisymmetric turbine end wall design: Part ii - experimental validation. *ASME J. Turbomachinery*, 122(2):286–293, 1999.
- [41] N. W. Harvey, S. Shahpar, J. Hartland, D.G. Gregory-Smith, M. G. Rose, and M. D. Taylor. Nonaxisymmetric turbine end wall design: Part i: Three-dimensional linear design system. *ASME J. Turbomachinery*, 122(2):278–285, 1999.
- [42] M. H. Hosni, H. W. Coleman, and R. P. Taylor. Heat transfer measurements and calculations in transitionally rough flow. *ASME J. Turbomachinery*, 113(3):404–411, 1991.
- [43] G. Ingram, D.Gregory-Smith, M. Rose, N. Harvey, and G. Brennan. The effect of end-wall profiling on secondary flow and loss development in a turbine cascade. In *Proceedings of the ASME Turbo Expo, GT2002-30339*, volume 2002, pages 135–145. ASME, Amsterdam, 2002.
- [44] Switzerland. International Organisation for Standardisation Geneva, editor. *ISO: Guide to the Expression of Uncertainty in Measurement (Gum)*. 1995.
- [45] P. Jenny. *Interaction Mechanisms between Rim Seal Purge Flow and Profiled End Walls in a Low-Pressure Turbine*. PhD thesis, ETH Zürich, 2012. Diss. ETH No. 20429.
- [46] Jinhee Jeong and Fazle Hussain. On the identification of a vortex. *Journal of Fluid Mechanics*, 285:69–94, 2 1995.
- [47] M. B. Kang, A. Kohli, and K. A. Thole. Heat transfer and flowfield measurements in the leading edge region of a stator vane endwall. *ASME J. Turbomachinery*, 121(3):558–568, 1999.
- [48] W. Kays, M. Crawford, and B. Weigand. *Convective heat and mass transfer*. 2004.
- [49] S. J. Kline and F. A. McClintock. Describing Uncertainties in Single-Sample Experiments. *J. Mech. Eng.*, pages 3–8, 1953.
- [50] L.S. Langston. Secondary flows in axial turbines - a review. *Annals of the New York Academy of Sciences*, 934(1):11–26, 2001.
- [51] L.S. Langston, M.L. Nice, and R.M. Hooper. 3-dimensional flow within a turbine cascade passage. *Journal of Engineering for Power*, 99(1):21–28, 1977.



- [52] B. Laveau and R. S. Abhari. Influence of flow structure on shaped hole film cooling performance. In *Proceedings of the ASME Turbo Expo, GT2010-23032*, Glasgow, 2010.
- [53] J. J. Lee, J. C. Dutton, and A. M. Jacobi. Application of temperature-sensitive paint for surface temperature measurement in heat transfer enhancement applications. *Journal of Mechanical Science and Technology*, 21(8):1253–1262, 2007.
- [54] A. T. Lethander, K. A. Thole, G. Zess, and J. Wagner. Vane-endwall junction optimization to reduce turbine vane passage adiabatic wall temperatures. *Journal of Propulsion and Power*, 20 (6):1096–1104, 2004.
- [55] D.J. Lewis and R.L. Simpson. An experimental investigation of heat transfer in three-dimensional and separating turbulent boundary layers. *Technical Report*, 1996.
- [56] M. Lorenz, A. Schulz, and H.-J. Bauer. Experimental study of surface roughness effects on a turbine airfoil in a linear cascade - part i: External heat transfer. *ASME J. Turbomachinery*, 134(4):041006, 2012.
- [57] S. Lucchini. Design and commissioning of a traversing system to conduct heat transfer studies in lisa using an infrared camera. Technical report, ETH Zürich, 2012.
- [58] S. P. Lynch, N. Sundaram, K. A. Thole, A. Kohli, and C. Lehane. Heat transfer for a turbine blade with nonaxisymmetric endwall contouring. *ASME J. Turbomachinery*, 133(1):011019, 2011.
- [59] J.W. Maclachlan Spicer, W.D. Kerns, L.C. Aamodt, and J.C. Murphy. Measurement of coating physical properties and detection of coating disbonds by time-resolved infrared radiometry. *Journal of Nondestructive Evaluation*, 8(2):107–120, 1989.
- [60] G. I. Mahmood and S. Acharya. Measured endwall flow and passage heat transfer in a linear blade passage with endwall and leading edge modifications. In *Proceedings of the ASME Turbo Expo, GT2007-28179*, Montreal, 2007.
- [61] Xavier P. Maldague. *Theory and Practice of Infrared Technology for Nondestructive Testing*. Wiley-Interscience, 2001.
- [62] M. Mansour. *A 48kHz Bandwidth, 1.8mm Diameter Entropy Probe for Aerothermal Loss Measurements in Turbomachinery Flows*. PhD thesis, ETH Zürich, 2008. Diss. ETH No. 18087.
- [63] A. Marti. Measurement of heat transfer on endwalls in a cascade using an infrared probe. Master’s thesis, ETH Zürich, 2012.

- [64] S. T. McClain, B. K. Hodge, and J. P. Bons. Predicting skin friction and heat transfer for turbulent flow over real gas turbine surface roughness using the discrete element method. *ASME J. Turbomachinery*, 126(2):259–267, 2004.
- [65] R. J. Moffat. Describing the Uncertainties in Experimental Results. *Expt. Therm. Fluid Sc.*, 1:3–17, 1988.
- [66] R.J. Moffat. What’s new in convective heat transfer? *International Journal of Heat and Fluid Flow*, 19(2):90–101, 1998.
- [67] J.C. Murphy, L.C. Aamodt, and J.W. Maclachan Spicer. *Principle of photothermal detection in solids*, pages 41–94. Elsevier, New York, 1992.
- [68] J. Nikuradse. *Laws for Flows in Rough Pipes*, volume 361, Series B, Vol. 4. VDI-Forschungsheft, 1933.
- [69] D. O. O’Dowd, Q. Zhang, L. He, P. M. Ligrani, and S. Friedrichs. Comparison of heat transfer measurement techniques on a transonic turbine blade tip. *ASME J. Turbomachinery*, 133(2):021028, 2011.
- [70] Robert Osiander and Jane W.M. Spicer. Time-resolved infrared radiometry with step heating - a review. *Revue Générale de Thermique*, 37(8):680 – 692, 1998.
- [71] M. Pimental, R.J. Moffat, and W.M. Kays. The turbulent boundary layer: an experimental study of the transport of momentum and heat with the effect of roughness. Technical Report HMT-21, Stanford University, 1975.
- [72] T. J. Praisner and C. R. Smith. The dynamics of the horseshoe vortex and associated endwall heat transfer - part i: Temporal behavior. *ASME J. Turbomachinery*, 128(4):747–754, 2005.
- [73] T. J. Praisner and C. R. Smith. The dynamics of the horseshoe vortex and associated endwall heat transfer - part ii: Time-mean results. *ASME J. Turbomachinery*, 128(4):755–762, 2006.
- [74] K. Regina, A.I. Kalfas, and R.S. Abhari. Experimental investigation of purge flow effects on a high pressure turbine stage. In *Proceedings of the ASME Turbo Expo, GT2012-69466*, Copenhagen, 2012.
- [75] M. G. Rose. Non-axisymmetric endwall profiling in the hp ngvs of an axial flow gas turbine. In *Proceedings of the ASME Turbo Expo, 94-GT-249*, The Hague, 1994.
- [76] A. K. Saha and S. Acharya. Computations of turbulent flow and heat transfer through a three-dimensional nonaxisymmetric blade passage. *ASME J. Turbomachinery*, 130(3), 2008.

- [77] H. Sauer, R. Müller, and K. Vogeler. Reduction of secondary flow losses in turbine cascades by leading edge modifications at the endwall. *ASME J. Turbomachinery*, 123(2):207–213, 2000.
- [78] P.W. Schilke. Advanced gas turbine materials and coatings. Technical Report GER-3569G, GE Energy, 2004.
- [79] J. Schlienger. *Evolution of Unsteady Secondary Flows in a Multistage Shrouded Axial Turbine*. PhD thesis, ETH Zürich, 2003. Diss. ETH No. 15230.
- [80] P. Schüpbach. *Influence of Rim Seal Purge Flow on the Performance of an End Wall Profiled Axial Turbine*. PhD thesis, ETH Zürich, 2009. Diss. ETH No. 18458.
- [81] P. Schüpbach, R. S. Abhari, M. G. Rose, T. Germain, I. Raab, and J. Gier. Improving efficiency of a high work turbine using nonaxisymmetric endwalls - part ii: Time-resolved flow physics. *ASME J. Turbomachinery*, 132(2):021008, 2010.
- [82] P. Schüpbach, R. S. Abhari, M. G. Rose, and J. Gier. Influence of rim seal purge flow on the performance of an endwall-profiled axial turbine. *ASME J. Turbomachinery*, 133(2):021011, 2011.
- [83] O. P. Sharma and T. L. Butler. Predictions of endwall losses and secondary flows in axial flow turbine cascades. *ASME J. Turbomachinery*, 109(2):229–236, 1987.
- [84] R.L. Simpson. Junction flows. *Annu. Rev. Fluid Mechanics*, 33:413–443, 2001.
- [85] C. R. Smith, D. R. Sabatino, and T. J. Praisner. Temperature sensing with thermochromic liquid crystals. *Experiments in Fluids*, 30(2):190–201, 2001.
- [86] M Stripf, A Schulz, and S Wittig. Surface roughness effects on external heat transfer of a HP turbine vane. *ASME J. Turbomachinery*, 127(1):200–208, 2005.
- [87] J. A. van Rij, B. J. Belnap, and P. M. Ligrani. Analysis and experiments on three-dimensional, irregular surface roughness. *Journal of Fluids Engineering*, 124(3):671–677, 08 2002.
- [88] Z. Vidakovic. Estimating The Radiation Correction On Heat Transfer Measurements For A Film Cooling Experiment . Master’s thesis, ETH Zürich, 2007.
- [89] M. Vollmer and K.-P. Mollmann. *Infrared Thermal Imaging: Fundamentals, Research and Applications*. Wiley-VCH, 2010.
- [90] H. P. Wang, S. J. Olson, R. J. Goldstein, and E. R. G. Eckert. Flow visualization in a linear turbine cascade of high performance turbine blades. *ASME J. Turbomachinery*, 119(1):1–8, 1997.

- [91] D. C. Wilcox. Formulation of the k-w turbulence model revisited. *AIAA Journal*, 46(11):2823–2838, 2008.
- [92] G. A. Zess and K. A. Thole. Computational design and experimental evaluation of using a leading edge fillet on a gas turbine vane. *ASME J. Turbomachinery*, 124(2):167–174, 2002.

# Appendix A

## Nomenclature

### Symbols

|               |  |
|---------------|--|
| $C_{ax}$      | Airfoil axial chord [m]                                      |
| $C_p$         | Specific Heat capacity [J/kg/K]                              |
| $h$           | Heat transfer coefficient [ $W/m^2/K$ ]                      |
| $k$           | Fluid or Solid Thermal conductivity [ $W/m/K$ ]              |
| $k_s$         | Equivalent sand-grain roughness [ $\mu m$ ]                  |
| $Ma$          | Mach number[-]   |
| $Nu$          | Nusselt number, $hC_{ax}/k$                                  |
| $P$           | Pressure [Pa]  |
| $PR$          | Compressor Pressure Ratio                                    |
| $Pr$          | Prandtl Number $Pr = \frac{\nu}{\alpha}$                     |
| $q$           | Heat flux [ $W/m^2$ ]  |
| $Ra$          | Arithmetic roughness value [ $\mu m$ ]                       |
| $Re_{C_{ax}}$ | Reynolds number based on axial chord, $V_{\infty}C_{ax}/\nu$ |
| $Re_k$        | Roughness based Reynolds number, $u_{\tau}k_s/\nu$           |
| $Re_x$        | Local Reynolds number based, $U(x)x/\nu$                     |
| $Rku$         | Kurtosis of the roughness distribution [-]                   |
| $Rq$          | Root mean squared roughness value [ $\mu m$ ]                |
| $Rsk$         | Skewness of the roughness distribution [-]                   |
| $R_{th}$      | Thermal resistance, $R_{th} = \sum_i \frac{t_i}{k_i}$        |
| $Rz$          | Peak to peak roughness value [ $\mu m$ ]                     |
| $St$          | Stanton number, $St = \frac{h}{C_p\rho V}$                   |
| $t$           | Layer thickness [m]  |
| $T$           | Temperature [K]  |
| $T_r$         | Recovery Temperature [K]                                     |
| $T_{t_{in}}$  | Flow total inlet temperature [K]                             |
| $Tu$          | Turbulence intensity   |
| $u, v, w$     | Flow velocity [m/s]  |

|            |  |
|------------|--|
| $u_\infty$ | Freestream flow velocity [m/s]                             |
| $u_\tau$   | Friction velocity [m/s]                                    |
| $y^+$      | Non-dimensional wall distance $y^+ = \frac{u_\tau y}{\nu}$ |

### Greek

|             |  |
|-------------|--|
| $\alpha$    | Thermal diffusivity $\alpha = \frac{k}{\rho C_p} [m^2/s]$  |
| $\epsilon$  | Surface emissivity   |
| $\eta_B$    | Brayton cycle efficiency [-]                               |
| $\gamma$    | Ratio of fluid specific heats $\gamma = C_p/C_v$           |
| $\Lambda_s$ | Roughness shape factor [-]                                 |
| $\lambda$   | Radiation wavelength [m]                                   |
| $\mu$       | Fluid dynamic viscosity [Pa.s]                             |
| $\nu$       | Fluid kinematic viscosity [ $m^2/s$ ]                      |
| $\rho$      | Density [ $kg/m^3$ ]                                       |
| $\sigma$    | Stefan-Boltzmann constant, $5.67 \times 10^{-8} W/m^2/K^4$ |

### Subscripts

|          |   |
|----------|---|
| $ad$     | Adiabatic   |
| $adh$    | Adhesive  |
| $amb$    | Ambiant conditions  |
| $cond$   | Conduction  |
| $conv$   | Convection  |
| $DP$     | Design point operating condition                            |
| $iso$    | Isothermal plate  |
| $lowM$   |   |
| $orlowR$ | Reduced massflow or reduced Reynolds number operating point |
| $rad$    | Radiation   |
| $stag$   | Stagnation conditions                                       |
| $t$      | Total or Stagnation conditions                              |
| $w$      | Wall  |

### Abbreviations

|       |                               |
|-------|-------------------------------|
| $PS$  | Pressure side                 |
| $SS$  | Suction side                  |
| $TET$ | Turbine Entry Temperature [K] |

# Appendix B

## List of Publications

### **Journal Publications**

Laveau B., Abhari R.S., Crawford M.E., Lutum E.

High Resolution Heat Transfer Measurement on Flat and Contoured Endwalls in a Linear Cascade.

2013, Journal of Turbomachinery, Vol. 135, No. 4, 041020.

### **Peer-reviewed publications**

Laveau B., Abhari R.S., Crawford M., Lutum E.

High resolution heat transfer measurements on the stator endwall of an axial turbine.

ASME Turbo Expo Düsseldorf 2014, GT2014-26105

This paper is recommended for publication in Journal of Turbomachinery.

Laveau B., Abhari R.S., Crawford M.E., Lutum E.

High Resolution Heat Transfer Measurement on Flat and Contoured Endwalls in a Linear Cascade.

ASME Turbo Expo Copenhagen 2012, GT2012-69737

Laveau B., Abhari R.S.

Influence of Flow Structure on Shaped Holes Film Cooling Performance.

ASME Turbo Expo Glasgow 2010, GT2010-23032





# Appendix C

## Curriculum Vitae

### Personal Data

Benoit Edouard Laveau, born November 28<sup>th</sup>, 1985 in Saint Doulchard, France

### Professional Experience

- 2009 - 2014    Research assistant and doctoral student, Laboratory for Energy Conversion, ETH Zurich, Switzerland
- 2008            Research Project (6 months), Mechanical Engineering Dept., Louisiana State University, Baton Rouge (Louisiana), USA
- 2006 - 2007    Industry project (1 year) in the service in charge the engine nacelle integration of the Powerplant Department, Airbus France, Toulouse, France

### Education

- 2007 - 2008    Master of Research in Fluid Dynamics and Energy Transfer (DET), graduated December 2008
- 2008            Master Degree in Aeronautical Engineering, delivered by ISAE-ENSICA in October 2008
- 2004-2008    Studies at Ecole National Supérieur d'Ingénieurs en Construction Aéronautiques (ISAE - ENSICA), Toulouse, France